UNIVERSITÉ DE STRASBOURG

ÉCOLE DOCTORALE Mathématiques, Sciences de l'Information et de l'Ingénieur

Icube, UMR 7357

THÈSE présentée par :

Noura HAMZE

soutenue le : 21 juin 2016

pour obtenir le grade de : **Docteur de l'université de Strasbourg**

Discipline/ Spécialité : Informatique

Optimisation et planification préopératoire des trajectoires en conditions statiques et déformables pour la chirurgie guidée par l'image

THÈSE dirigée par :

Mme ESSERT Caroline	HDR, université de Strasbourg

RAPPORTEURS :

M JOSKOWICZ Leo	Professeur, Hebrew University of Jerusalem
M PROMAYON Emmanuel	HDR, Université Joseph Fourier

AUTRES MEMBRES DU JURY :

M FICHTINGER Gabor	Professeur, Queen's University

A Thesis presented at Université de Strasbourg
Laboratoire des sciences de l'ingénieur, de l'informatique et de l'imagerie
ICube, UMR 7357

by

Mme Noura HAMZE

for the degree of Doctor of Philosophy of the University of Strasbourg

Discipline : Informatics

Preoperative path planning and optimization in static and deformable conditions for image–guided minimally invasive surgery

---

Presented in public on 21 june 2016 in front of the jury composed of :

- M. Leo Joskowicz, Hebrew University of Jerusalem, external examiner
- M. Emmanuel Promayon, Université Joseph Fourier, external examiner
- M. Gabor Fichtinger, Queen's University, external examiner
- Mme. Caroline Essert, Université de Strasbourg, thesis advisor

Remerciements

Je tiens à exprimer toute ma reconnaissance à ma directrice de thèse, Caroline Essert, d'avoir accepté de m'encadrer. Je te remercie pour ton soutien et tes encouragements, pour ta disponibilité et ta grande gentillesse, et pour la confiance et la liberté de travail que tu m'a laissées tout au long de cette thèse en restant là pour me guider quand je m'égarais. Un grand merci d'avoir veillé tard avec moi les soirs de deadlines, même lorsque tu étais en vacances, et d'avoir relu et corrigé patiemment mon manuscrit et tout ce que j'ai rédigé en français ou en anglais. Je te dois beaucoup.

J'aimerais remercier Prof. Leo Joskowicz et Dr. Emmanuel Promayon d'avoir accepté de rapporter ce mémoire. Leurs remarques pertinentes m'ont permis d'améliorer le manuscrit final. Je les remercie aussi, ainsi que Prof. Gabor Fichtinger, d'avoir accepté de participer au jury de cette thèse et d'avoir permis des moments de réussite et de bonheur inoubliables.

Je souhaite également remercier Pierre Collet d'avoir partagé avec nous son expertise et sa passion pour les algorithmes évolutionnaires. Malgré son emploi du temps trop chargé, il a consacré des heures pour discuter avec nous des directions à prendre dans ce travail. Merci également pour sa présence parmi les membres du jury.

Pendant ces années, j'étais très heureuse de faire partie de l'équipe IGG en tant que stagiaire et ensuite en tant que doctorante. J'ai pu travailler dans une ambiance motivante et agréable tant professionnellement qu'humainement. Je remercie donc tous les membres de l'équipe : Arash, Basile, Caroline, David C., Dominique, Isabelle, Fréderic, Fred, Gabriel, Hyewon, Jean-Michel, Jérôme, Julien, Karim, Nicolas, Olivier, Pascal M., Pascal S., Pierre K., Rémi, Sylvain, Thierry, et Toni.

Je pense particulièrement à Dominique Bechmann, qui m'a accordé sa confiance dès le lendemain de mon arrivée en France en me proposant un stage de Master 2 en IGG. Merci pour ton écoute, tes conseils et tes pensées. Ta présence fut un soutien inestimable. Je suis également très reconnaissante à Rémi Allègre qui m'a encadrée durant mon stage de six mois. Merci Rémi de m'avoir patiemment guidée, j'ai apprécié ta méthode d'encadrement très professionnelle. Ce que tu m'as appris m'a beaucoup aidé dans la suite de mon parcours.

Un grand merci à Olivier et à Sylvain qui étaient toujours là pour répondre à mes questions techniques, pour m'aider à décrypter les messages d'erreur sur le terminal de Linux, pour me débloquer lors de la compilation d'une bibliothèque ou pour remplacer mon disque dur crashé deux semaines avant la date de la soutenance !

Merci Basile de m'avoir permis de voir les choses d'une façon différente en écoutant tes idées très intéressantes pendant les déjeuners. Merci Arash pour ta gentillesse et pour ton aide durant mon poste d'ATER. Merci Karim de m'avoir proposé très volontairement de relire et de corriger mon manuscrit.

Et bien sûr, la bande de thésards (ou docteurs) avec laquelle j'ai partagé des moments moins sérieux au labo ou même en dehors : Amir, Guo, Vasyl, Alex, Pierre, Thomas, David, Olga, Christoph, Etienne, Lionel, Kenneth, Jonathan, et Rémi. Merci Vasyl pour les pauses "Earl Grey", et aussi pour les 45 minutes d'échange quotidien après les longues journées de travail en rentrant en tram. Une petite pensée à Nadine : malgré ton court séjour à Strasbourg, j'ai passé des moments agréables avec toi, tu m'as appris de belles choses : Gracia !

Durant cette thèse, j'ai eu la chance de collaborer avec plusieurs personnes en dehors de notre équipe, notamment dans le cadre du projet "ACouStiC". Les réunions qui ont eu lieu dans une ambiance à la fois scientifique et amicale m'ont permis d'avoir un point de vue d'ensemble sur ma recherche et de comprendre les défis majeurs de l'informatique graphique pour la chirurgie mini-invasive. Je remercie donc tous les membres de ce projet : le directeur du projet Pierre Jannin, Tiziano, Sarah, Eric, Jérôme, Sonia, Stéphane, Christian et Alexandre Bilger avec qui nous avons réalisé la partie de recherche concernant la déformation du cerveau.

Je tiens également à remercier Stéphane Cotin et Igor Peterlik pour le travail que nous avons réalisé au sein du projet "Haystack". Igor, merci de m'avoir introduit à SOFA, de m'avoir expliqué comment lire une scène de simulation, d'avoir pris beaucoup de ton temps pour trouver les bugs et pour répondre à mes e-mails. Merci Stéphane pour tout effort déployé pour ce projet.

Merci à Dr. Jimmy Voirin du département de neurochirurgie à l'Hôpital civil de Strasbourg pour son aide à la validation clinique de nos méthodes.

Dans cette aventure, j'ai aussi eu l'occasion de découvrir l'enseignement. Je voudrais exprimer ma gratitude à toutes les personnes qui m'ont encouragée à relever ce défi et qui ont partagé avec moi leurs expériences. Je pense notamment à tous les collègues au département d'informatique de l'UFR Math-Info de l'Université de Strasbourg. Je profite aussi de cette occasion pour adresser mes remerciements à l'équipe administrative (Anne-Sophie et les autres) et aux équipes téchnique et informatique du laboratoire ICube.

En dehors du labo, je voudrais remercier les personnes qui m'ont rendu la vie plus agréable dans la belle ville de Strasbourg. Je m'adresse à mes chères voisines : merci pour votre tendresse quotidienne, pour les gâteaux que vous m'avez fait goûter. Grâce à vos "Bonjour Noura !", j'ai pu commencer mes journées avec un sourire.

Maroua, ma meilleure amie, qui m'a aidée à surmonter les moments de doute, et qui a brisé ma solitude positivement. Merci pour toutes les sorties gourmandes proche-orientales, pour les cadeaux, les voyages, mais surtout pour les larmes de rire que nous avons versées sans cesse. Par contre, il faut avouer que ce n'était pas efficace de "bosser" quand nous nous retrouvions ensemble à la BNU ;)

Merci à ceux qui ont pensé à moi sans que je le sache ...

Enfin, je garde mes pensées les plus sincères pour ma famille, en premier lieu pour mes chers parents - mais comment pourrait-on trouver des mots pour remercier ses parents ? Ma sœur Dia et sa famille adorable (tam tum, tin tin, et milou), mon frère Muhammad et Sophie, et je termine par celle qui est au plus profond de mon cœur, ataa , à qui je dédie ce travail.

Acknowledgements

This work was funded by the French National Research Agency (ANR) through the ACouStiC project grant (ANR 2010 BLAN 0209 02), and by the Institut Hospitalo-Universitaire de Strasbourg (IHU) through Haystack project.

Preoperative path planning and optimization in static and deformable conditions for image–guided minimally invasive surgery

Noura HAMZE

Submitted for the degree of Doctor of Philosophy in Informatics
June 2016

Abstract

In image-guided minimally invasive surgery, a precise preoperative planning of the surgical tools trajectory is a key factor to a successful intervention. However, an efficient planning is a challenging task, which can be significantly improved when considering different contributing factors.

In this work, we focus on two aspects : Integrating intra-operative deformation to the planning, and investigating novel optimization methods.

Firstly, we present a novel automatic preoperative path planning approach which counts for certain biomechanical deformation. Our methods combine geometric-based optimization techniques with physics-based simulations. It is characterized with a certain level of generality, and is experimented on two different surgical procedures. In percutaneous procedures, for hepatic tumor ablation, we compute a patient-specific preoperative safe non-straight trajectory for the ablation flexible needles ; the planning accounts for both : the deformation of the flexible needle during the insertion process, and the deformation of the punctured soft tissue. The other in Deep Brain Stimulation neurosurgery, to compute a patient-specific preoperative safe straight trajectory for the stimulation electrode ; the planning accounts for the "Brain Shift" phenomenon.

Secondly, we address the optimization approaches in path planning problem. We investigate, implement, and compare many approaches with qualitative and quantitative methods, and we present an efficient evolutionary Pareto-based multi-criteria optimization method which can find optimal solutions that are not reachable via the current state of the art deployed methods.

List of publications

- Noura Hamzé, Igor Peterlék, Stéphane Cotin, and Caroline Essert. Pre-operative Trajectory Planning for Percutaneous Procedures in Deformable Environments, Computerized Medical Imaging and Graphics, Elsevier, page 16–28, Volume 47, January 2016. First Online : 11 Nov. 2015.

  doi :10.1016/j.compmedimag.2015.10.002
- Noura Hamzé, Alexandre Bilger , Christian Duriez , Stṕhane Cotin, Caroline Essert. Anticipation of brain shift in Deep Brain Stimulation automatic planning, 37th Annual International Conference of the IEEE Engineering in Medicine and Biology Society (EMBC'15), Milano, Italy, pages 3635 - 3638, August 2015. doi :10.1109/EMBC.2015.7319180
- Noura Hamzé, Pierre Collet, Caroline Essert. Introducing Pareto-based MOEA to Neurosurgery Preoperative Path Planning, Genetic and Evolutionary Computation Conference (GECCO'16), Denver, United States, July 2016.
- Noura Hamzé, Jimmy Voirin, Pierre Collet, Pierre Jannin, Claire Haegelen, Caroline Essert. Pareto front vs. weighted sum for automatic trajectory planning of Deep Brain Stimulation, Medical Image Computing and Computer Assisted Intervention (MICCAI'16), Athènes, Greece, October 2016.

Table des matières

Acknowledgements iii

Acknowledgements vi

Abstract viii

1 Introduction 2
1.1 Introduction . . . 3
  1.1.1 Minimally invasive neurosurgery . . . 4
  1.1.2 Abdominal percutaneous procedures . . . 8
1.2 Problem statement . . . 11
  1.2.1 Preoperative planning . . . 11
  1.2.2 intra-operative deformations . . . 12
  1.2.3 Optimization . . . 14
1.3 Contributions . . . 15

2 State of The Art 17
2.1 Introduction . . . 18
2.2 Assistance to preoperative path planning . . . 19
  2.2.1 Abdominal percutaneous procedures . . . 19
  2.2.2 Neurosurgery . . . 22
2.3 Modeling and deformation simulation . . . 27
  2.3.1 Soft tissue modeling . . . 27
  2.3.2 Needles path planning with deformation . . . 29
  2.3.3 Brain shift modeling . . . 30
  2.3.4 Path planning with brain shift deformation . . . 31
2.4 Optimization methods . . . 32
  2.4.1 Introduction . . . 32
  2.4.2 Constrained optimization . . . 33
  2.4.3 Multi-objective optimization MOO . . . 34

3 Planning in static environments 39
3.1 Introduction . . . 40
3.2 Surgical rules formalization . . . 40
  3.2.1 Strict (or hard) constraints . . . 40
  3.2.2 Soft constraints . . . 41
3.3 Definitions and notations . . . 43

3.4 The optimization approach 44

4 Preoperative trajectory planning for percutaneous procedures in deformable conditions 47
4.1 Introduction 48
4.2 Planning in deformable conditions 49
4.2.1 Biomechanical modeling and simulation 49
4.2.2 Geometric–based preoperative planning 52
4.3 Experiments and results 58
4.3.1 Description of the Evaluation Scenario 60
4.3.2 Datasets and deformations amplitude 61
4.3.3 Overview of optimization methods 62
4.4 Discussion and conclusion 64

5 Preoperative trajectory planning for Deep Brain Stimulation in deformable conditions 68
5.1 Introduction 69
5.2 Planning in deformable conditions 69
5.2.1 Biomechanical modeling and simulation 70
5.2.2 Geometric–based preoperative planning 73
5.2.3 The system workflow 77
5.3 Experiments and Results 79
5.4 Discussion and conclusion 82

6 Preoperative Path Planning Optimization Strategies 84
6.1 Introduction 85
6.2 Pareto front vs. weighted sum for path planning 86
6.2.1 Initialization phase 86
6.2.2 Method 1 : Pareto front 87
6.2.3 Method 2 : weighted sum exploration 88
6.2.4 Evaluation study 89
6.2.5 Results 92
6.3 Evolutionary-based method for path planning 93
6.3.1 Dominance-based MOEAs 94
6.3.2 Three methods to compare 96
6.3.3 Experimental pipeline 101
6.3.4 Results 104
6.4 Disscussion and conclusions 108

7 Technical Deployment 110
7.1 Introduction 111
7.2 Image modalities and processing pipelines 111
7.2.1 RFA datasets 111
7.2.2 DBS datasets 113
7.3 The planning system components 113

8 Conclusions and Perspectives 118
8.1 Disscussion . . . 119
8.2 Summary of the contributions . . . 121
8.3 Perspectives . . . 122

Appendices 136

A The XML constaints file 137
A.1 RFA constraints file . . . 137
A.2 DBS constraints file . . . 139

B NSGA-II 141

1

INTRODUCTION

"Wherever the art of Medicine is loved, there is also a love of Humanity."
- Hippocrates

In this chapter, we introduce the medical context of the work. We explain the two minimally invasive surgery procedures addressed in this work : the deep brain stimulation and the percutaneous thermal ablation of hepatic tumors. After that, we present the research challenges that we confront, and we conclude by stating the main contributions of this work.

1.1 Introduction

"In September 2001, a hospital in Strasbourg, France, probably broke the record for the most expensive standard surgery in history by removing the gallbladder from a 68 year-old woman for the princely sum of more than 1 million euros. It was the first example of transatlantic telesurgery, with the patient in Strasbourg and both surgeons, Jacques Marescaux of the University of Strasbourg and Michel Gagner of New York City's Mount Sinai Medical Center, in New York. This was not necessarily a medical breakthrough, but rather **a proof of principle** that computer technology, robotics, fiber optics and surgical techniques have advanced sufficiently to overcome the technical problems that previously plagued the approach." stated Vicki Brower in a report [Brower, 2002] on the cutting edge in surgery.

Beyond the cited laparoscopic surgery which attained an eminent reputation, the other means of image-guided surgery (and more generally **C**omputer-**A**ssisted **S**urgery **CAS**) are becoming very common in hospitals today. **M**inimally **I**nvasive **S**urgery (**MIS**) has changed the way people think about risky surgical interventions. Compared to conventional surgery (also known as open surgery) which is usually performed by making large incisions in the patient's body, MIS procedures require small incisions using highly specialized surgical instruments and taking advantage of computer assistance. It is characterized with a number of features which increase its acceptance such as : less skin and tissue trauma, less bleeding, less scarring, faster recovery with shorter hospital stay, earlier return to normal activities, and overall less scare and pain. MIS has opened a vast range of promising medical applications and is widely used in neurosurgery, cardiology, gynecology, urology, and abdominal surgery. Depending on the incision size, different procedures can be distinguished in MIS : laparoscopic or keyhole procedures with typically up to half an inch incision length to insert long and thin instruments, and percutaneous procedures where needles puncture the skin and penetrate into the body.

However, its major difficulties are the reduced visibility inside the body, and the limited maneuvering of surgical tools. Therefore, the success of the image-guided surgery is mainly based on the progress in the imaging technologies. Medical images show the internal anatomy of the patient, and the more information they deliver the more precise the intervention can be. Today, many image modalities exist such as : **C**omputed **T**omography (**CT**), **M**agnetic **R**esonance **I**maging (**MRI**), **P**ositron **E**mission **T**omography **(PET**), Elastography, Tomography, Mammography, Ultrasound, X-Ray, etc. The imaging technique emphasize certain contrast characteristics of anatomical structures, and allow the physician to differentiate the structures and determine which are abnormal. Hence, they differ in their techniques, costs, quality and image contrast that can be acquired, and in their appropriateness to different clinical and surgical purposes. In this work, we will focus on the modalities which are widely used for diagnostic and planning purposes.

— **X-RAY :** X-Ray is the oldest and most commonly used form of medical imaging. This technology produces images of a person's internal anatomy by sending X-ray beams through the body, which are absorbed in different amounts dependiong on the density of the tissue.

— **Computed Tomography :** Computed tomography (CT scanning) is a medical imaging modality that combines many X-ray images taken in different directions with the aid of a computer to generate tomographic images of specific areas of the body. Fig. 1.1a illustrates a CT image slice in the human brain. Three-dimensional images of the internal organs can also be reconstructed.

— **Magnetic Resonance Imaging :** Magnetic Resonance Imaging (MRI) is a medical imaging technology that uses radio waves and a magnetic field to create detailed images of organs and tissues. It is very efficient in diagnosing for its ability to show the difference between normal and diseased soft tissues. Fig. 1.1b illustrates a MR-T1 image slice in the human brain.

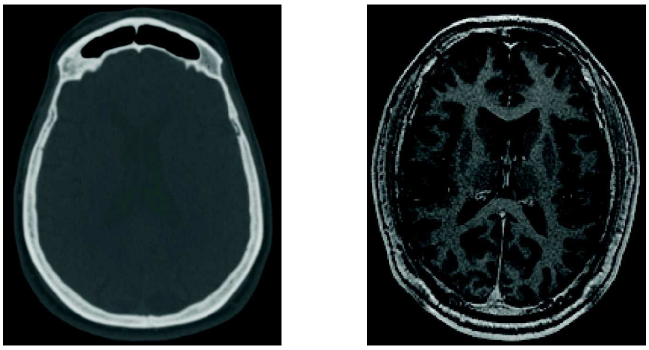
(a) CT image (b) MRI-T1 image

FIGURE 1.1 – Axial images of human brain

1.1.1 Minimally invasive neurosurgery

In neurosurgery, MIS is commonly used for prevention, diagnosis, treatment, stimulation and rehabilitation of disorders which affect the nervous system. These procedures are known as stereotactic surgery or stereotaxy because they make use of a three-dimensional coordinate system to localize any point in 3D space. Two stereotaxy techniques can be distinguished :

— Frame-based stereotaxy : an external mechanical frame is attached to the patient's skull such as Leksell[1] frame [Lek, nd], or Integra CRW [CRW, nd] frame (illustration in Figs. 1.2a, 1.2b). The frame serves as a reference to locate small targets inside the brain in order to perform some surgical action on them. This technique is known to be the gold-standard for diagnostic, for small brain biopsy or functional neurosurgery [Smith et al., 2005].

— Tripod stereotaxy : a starfix platform is fastened in the patient's skull in three or four anchor attachment points (1.2c), and the surgeon selects a target and trajectory on the MR and CT scans with the help of the anchors reference positions. This technology allows relative confort for the patient because the frames are smaller and lighter and patients can slightly move the heads during the intervention.

---

[1] Lars Leksell (1907-1986) was a Swedish physician and Professor of Neurosurgery at the Karolinska Institute in Stockholm, Sweden. He was the inventor of radiosurgery.

(a) Leksell frame [Lek, nd] (b) Integra CRW frame [CRW, nd]

(c) FHC tripod frame [EOS, nd]

FIGURE 1.2 – Stereotactic surgery frames

— Frameless stereotaxy : markers are used as references to locate the coordinates of tools to reach targets. This technique is commonly used for the removal of large brain tumors. However, this technique remains competitive with frame-based stereotaxy for biopsy procedures [Woodworth et al., 2006].

Deep Brain Stimulation DBS is a frame-based stereotaxy in which we are directly concerned in this study. Before stating the research problem we address in this work, we will present this functional intervention and explain its surgical procedure steps.

Deep Brain Stimulation

Deep **B**rain **S**timulation (**DBS**) is a neurosurgery procedure which intends to treat movement disorders such as **P**arkinson's **D**isease (**PD**), dystonia, or essential tremors. It has been first proposed in 1987 by a French medical team (Benabid et al. [Benabid et al., 1987]). Later in 1994 [Benabid et al., 1994], it was successfully applied to treat Parkinson's disease[2]. The procedure also succeeded to treat other pathologies such as chronic pain, obsessive-compulsive disorder, or severe depression, making it more and more popular. The principle of this functional treatment is to electrically stimulate a disorder-specific deep nucleus of the brain in a permanent

---

[2] Parkinson's Disease (PD) is a degenerative disorder of the central nervous system mainly affecting the motor system. The most obvious symptoms are movement-related (shaking, rigidity, slowness of movement and difficulty with walking).

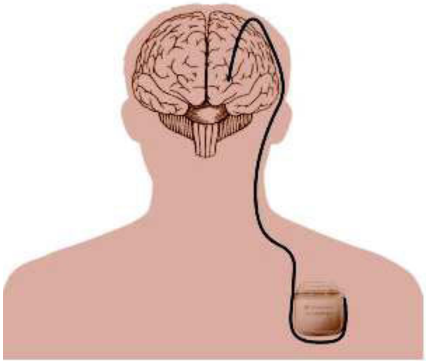

FIGURE 1.3 – Illustration of a DBS system with a neurostimulator, implanted in the chest, sends electrical impulses to the electrode to stimulate a deep brain structure.

manner.

To this end, a frame-based neurosurgery procedure is designed. It consists in implanting one (unilateral) or two (bilateral) permanent electrodes in the target brain tissue through small holes, with diameter of 10 to 14 mm., made at the patient's the skull. Because of the very small size[3] of the targeted structures, commonly the subthalamic nucleus (STN) or the globus pallidus interna (GPI), the insertion of the electrode must be performed with a millimetric accuracy. The electrode is connected by an extension wire that is passed under the skin to a battery-powered stimulator implanted under the skin of the chest. The stimulator emits electrical impulses sent through the extension to the metallic leads located at the tip of the electrode. The DBS electrode has a certain number of leads aligned with 0.5 to 1.5 millimeters depending on the electrode model. After the surgery, the electrode remains inside the patient's brain, and the stimulator can be programmed using the DBS programmer. Fig. 1.4 illustrates Medtronic's DBS system components consisting of the the neurostimulator, the programmer, the lead, and the extension.

(a) programmer (b) neuro stimulator (c) lead (d) extension

FIGURE 1.4 – Medtronic DBS system components [Med, ndb]

---

[3] The STN is a small almond-shaped nucleus with approximative diameters of 8 mm and 6 mm

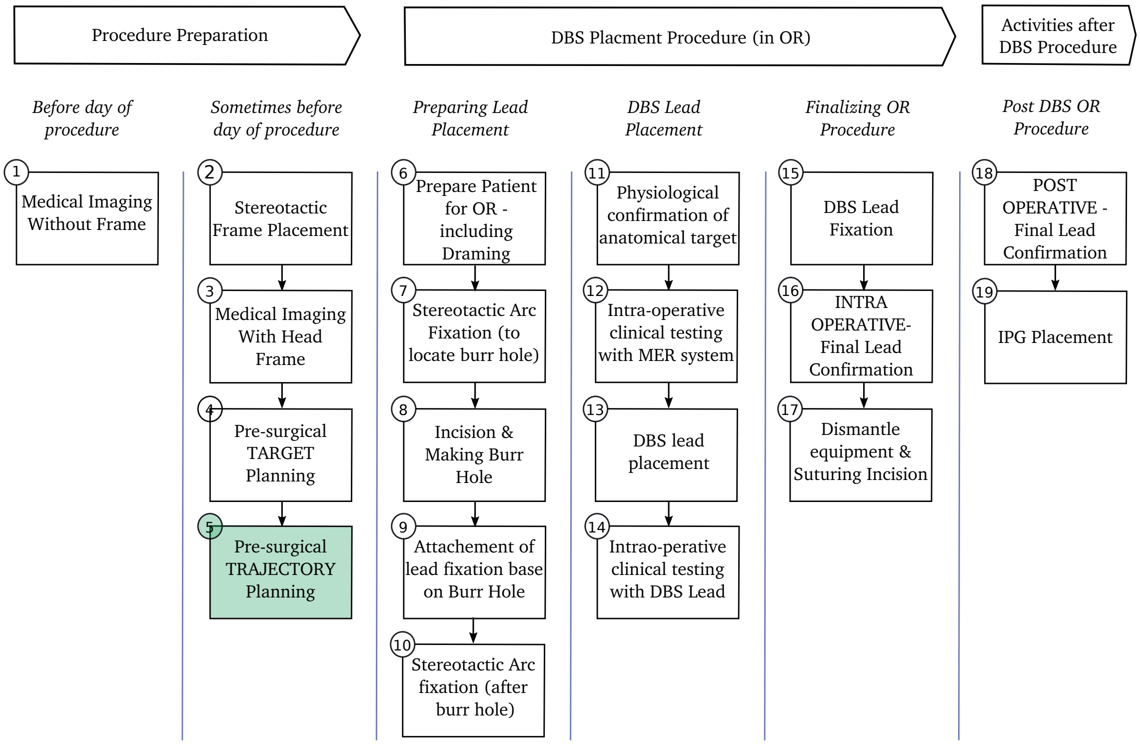

FIGURE 1.5 – DBS steps as presented in [Abosch et al., 2013]

DBS procedural steps

A survey of DBS procedural steps over 143 DBS centers was introduced by Abosch et al. [Abosch et al., 2013]. They identified 19 main steps in DBS surgery workflow and grouped these 19 steps into 3 phases : procedure preparation, DBS placement procedure in **O**perating **R**oom (**OR**), and activities after DBS procedure as illustrated in Fig.1.5. The three phases correspond to : preoperative, intra-operative, and postoperative phases respectively.

The first phase (preoperative) : Prior to surgery, from month to days depending on the neurosurgery center, an inclusion acquisition of the patient brain is done. The modality of the image is mostly an T1-weighted and T2-weighted MRI due to their high contrast on brain tissues.

The day of the surgery, or sometimes the day before, a surgical stereotactic frame is fixed on the patient skull, and a head CT scan is acquired with the frame. The CT image is registered on the MRI image to locate the target in the frame coordinates. Some anatomical or histological atlases may be used at this stage to help the target identification task. After locating the target, the surgeon determines a linear trajectory from an entry point on the patient scalp to the target. (Fig. 1.6a). The choice of the trajectory is carefully made and has to fulfill many constraints which we will discuss in detail in Chapter 5. We highlight that our work mainly concerns this preoperative step.

The second phase (intra-operative) : after the preoperative target and trajectory planning, and once the patient is ready in the OR, the surgeon fixes the stereotactic frame, and adjusts its arc according to the planned entry point and target. The arc piece is removed to incise the scalp skin on the entry point position, and a burr hole is made in the skull under local anesthesia on one or both head sides depending on whether the procedure is unilateral or bilateral. A lead fixation base is mounted on the burr hole, and the stereotactic arc of the frame is put back (Fig. 1.6b). In order to confirm the target coordinates of the preoperative planning, one or several micro-electrodes are inserted through the fixation base opening straight forward to the target anatomical structure (Fig. 1.6c), and the electrophysiological signals of the brain tissue are stimulated and their activities are recorded and compared to their normal electrophysiological activity (Fig. 1.6d). Once the target is confirmed, a stimulation testis done, the tissues are stimulated using microelectrodes, and neurological tests are preformed with the awake patient to see whether the stimulation provides satisfactory effects and reduced side-effects or not (Fig. 1.6f). Finally, when the most satisfactory position is found, a permanent stimulating electrode is inserted (Fig. 1.6e) using a micro-drive robot, the electrode is fixed, and a CT image is acquired just after the fixation.

The third phase (postoperative) : after the surgery, MR images can be taken (depending on the neurosurgical center) to follow-up purposes. The neurostimulator is incised under the skin a few hours after the surgery under general anesthesia, and is regularized using the programmer a few days later. Many visits are required to ensure a permanent benefit of the stimulation and to adjust it when needed.

After describing the DBS procedure as a representative example of path planning in neurosurgery, in the following section, we will study a representative exemple of abdominal path planning procedures.

1.1.2 Abdominal percutaneous procedures

"Percutaneous", via its Latin roots means, 'by way of the skin'. Percutaneous procedure refers to procedures where the access to inner organs or other tissue is done via needle-puncture of the skin. In these image-guided interventions, the role of the imaging techniques is primordial to help guiding the surgical tools inside the body to perform the task. Ultrasound, computed tomography, or magnetic resonance imaging are the familiar modalities for these procedures.

In abdominal surgery, this way of access has become a common alternative for open surgery in biopsy, cholecystectomy, splenectomy, adrenalectomy, appendectomy, and cancer treatment in particular for the treatment of small to medium size abdominal tumors.

Hepatic thermal ablation

Hepatic cancer is one of the most frequent malignant tumors and is responsible for more than one million deaths per year worldwide [Esquivel et al., 1982]. Thermal tumor ablation is becoming increasingly important for treating cancers of the liver. The term “ablation” refers to the destruction of a material, and many ablation techniques are used clinically for destroying malicious cells such as cryotherapy, radio-frequency, and microwave ablation. Despite the different ablation mechanisms, they all rely on the same concept of interventional technique. A needle is inserted into the liver, usually under the guidance of ultrasonography, CT or more recently

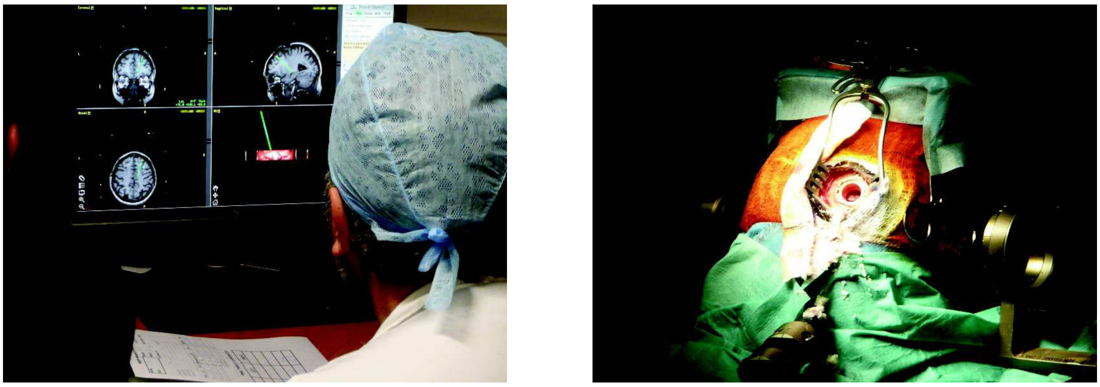

(a) preoperative planning

(b) removing the arc and placing burr hole fixation base

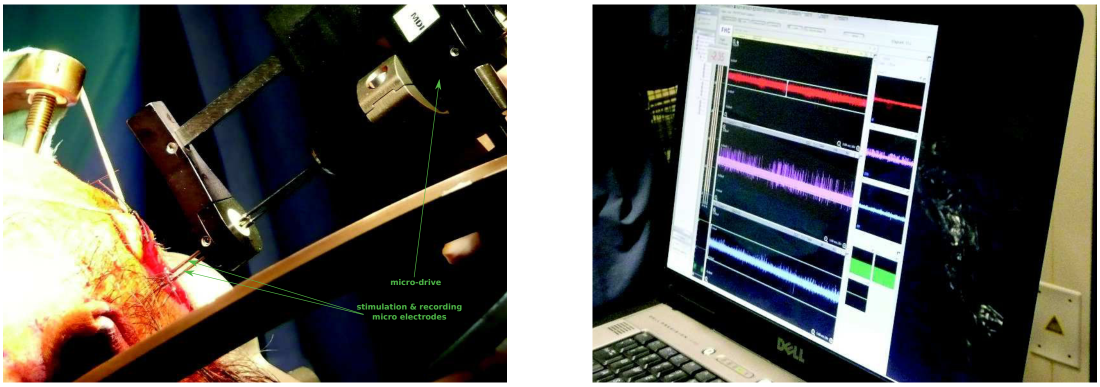

(c) MER stimulation and recording tests using mirco electrodes

(d) recording the brain activity and comparing normal electrophysiological activity

(e) a micro-drive mounted on Leksell frame to insert the permenant electrode

(f) surgeon asks the patient to do neurological tests to check the mouevment disorder

FIGURE 1.6 – Different steps in a DBS protocol during a surgery in the Unit of Functional Neurosurgery, UCL Institute of Neurology, National Hospital for Neurology and Neurosurgery, London and in the neurosurgery unit, Pitié-Salpêtrière Hoslpital, Paris.

MRI. Once placed within the tumor, heat, cold or a pharmaceutical product is locally delivered in the tumor region, triggering the destruction of the tumor on a matter of a few minutes (illustration in Fig. 1.7).

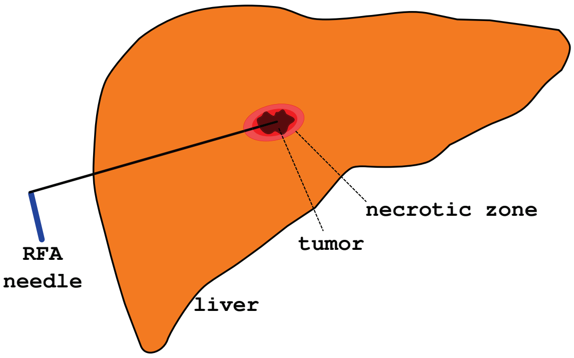

FIGURE 1.7 – Thermal ablation of a hepatic tumor

The three main thermal ablation modalities are :

- Cryotherapy ("cryosurgery" or "cryoablation") which involves cooling the tip of the needle to extremely low temperatures using compressed argon gas. This forms an iceball, which covers the targeted tissue and destroys malicious cells. An illustration of a cryoablation system components is depicted in Fig. 1.8.

(a) system (b) needles with iceballs (c) iceball ablation zone

FIGURE 1.8 – GalilMedical Visual-ICE system [Gal, nd] has a large HD touch screen for managing the procedure and allows for precise delivery of the shape and size ice balls required for each individual case.

- **R**adio**F**requency **A**blation (**RFA**) has become the most popular and widely studied thermal ablation modality for primary and metastatic liver tumors [Garrean et al., 2008]. It consists in passing high-frequency electric currents through the needle electrode, creating heat that destroys the cancer cells. An ellipsoidal ablation zone centered in the needle's tip covers the necrosis zone including a security margin. An illustration of a radio system components is depicted in Fig. 1.9.
- Microwave thermotherapy in which microwaves transmitted through the probe are used to heat and destroy the abnormal tissue. While both RF and microwave energy can heat tissue to cytotoxic levels, the mechanisms of RF and

(a) radiofrequency waves generator (b) RFA ablation needle (c) RFA zone

Figure 1.9 – Covidien Medtronic RFA system [Med, nda]

microwave heating are quite different and must be considered for ablation of different tissue types [Brace, 2009].

Finally, whatever the ablation mechanism is chosen, the preoperative planning, that aims at determining a secure and efficient needle path before the intervention, remains one of the main challenges of this therapy. In the next section we will present the preoperative planning, and state the problems addressed in this thesis.

1.2 Problem statement

In the contexts of DBS keyhole surgery and the percutaneous procedures that we have already presented, a precise preoperative planning to find a safe and adequate path is a key factor to a successful intervention. The provision of computer assistance and decision support systems is essential. Still, many challenges are slowing it down.

1.2.1 Preoperative planning

In the context of this work, we will commonly use the word "planning" to refer to the "preoperative planning". *It consists in calculating in a preoperative phase a safe path of the surgical tool to reach a predefined target.* Depending on the intervention, the target can be either an anatomic structure or a specific point. Planning an intervention is a decisive task. The chances of a successful surgical operation depend strongly on a good preoperative planning strategy. A few days before the intervention, CT or MRI images of the patient are acquired, then the physician elaborates his intervention plan from these sets of preoperative 2D slices. It is a difficult task, as the physician has to build a mental representation of a 3D model of the anatomy of the patient and the position of pathologies, and estimate a secure tridimensional path.

Thanks to nowadays advanced computer graphics techniques, the visibility of the patient's internal anatomy can be significantly enhanced by a volume rendering, or a 3D mesh reconstruction based on CT and MRI data. In addition, semi-automatic computer assistance techniques for preoperative planning can help the surgeons by facilitating navigation and interaction tasks, or by a decision support system.

Furthermore, automatic path planning was addressed by many works and will be discussed in Chapter 2. The proposed algorithms that take advantage of different optimization techniques to calculate automatically a safe path subject to a set of surgical rules depending on the intervention type. Despite the valuable help of the planning algorithms, they still have some limits which we will explain in the next section.

1.2.2 intra-operative deformations

The existing preoperative planning methods can be helpful, but to a certain extent. Many important challenges remain on the behalf of the surgeon such as ensuring the safety of the planned path between the preoperative and the intra-operative intervention phases.

In fact, basing the choice of the path on static preoperative images of a set of deformable anatomical structures, and considering no motion will happen during the surgery raise some issues in terms of precision and reliability of the planning. Multiple sources of intra-operative deformations such as breathing, interaction between surgical tools and soft tissues, or brain shift, can reduce the safety level of the planned path, or even distort the preoperative planning. This challenge encourages a novel planning approach in dynamic conditions.

In the following, we will explain the main intra-operative deformations that can distort the preoperative planning in both DBS and percutaneous ablation procedures for hepatic tumors. Finally, we will evoke the related optimization issues.

Deformations during DBS procedures

DBS preoperative planning is done on the preoperative data of the patient. This planning is based on the configuration of the brain and other structures at the moment the MRI was acquired. During the surgery, as previously explained in 1.1.1, a burr hole is drilled in the patient's skull in order to access the brain tissue at the entry point the surgeons defined earlier. The brain tissue is a deformable material, and when the skull and dura mater are open, and the patient is lying in supine position, **C**erebro-**S**pinal **F**luid (**CSF**) which surrounds the brain may leak through the hole. A leak of CSF causes a change of intracranial pressure and constitutes one of the main reasons of a brain deformation called *brain shift* as illustrated in Fig. 1.10.

According to [Slotty et al., 2012], the *brain shift* phenomenon describes movement and deformation of the brain in terms of its anatomical and physiological position in the skull. This phenomenon is important as brain deformation leads to a displacement of some structures considered during the planning such as the target or the vessels. It results in a difference between the preoperative configuration, based on which the path is planned, and the intra-operative configuration. The magnitude of brain displacement differs depending on the anatomical structure. Usually, the brain shift does not affect a lot the deep tissue, such as the STN. If the target moves, the magnitude of movement remains small enough to keep the target in the activation

FIGURE 1.10 – Brain shift phenomenon [Bilger, 2014]

volume of the DBS electrode [Butson et al., 2007]. However, other structures of low or medium depth such as blood vessels can shift up to 10 mm [Elias et al., 2007]. In the worst possible scenario, if a blood vessel shifts across the path of the electrode, it could lead to hemorrhage and death of the patient.

Various monitoring procedures or precautions are taken in the intra-operative phase as we will discuss in 2, and still not addressed in the preoperative planning phase. Our first objective therefore is to propose a novel preoperative planning method for DBS procedure which takes into account the brain shift phenomenon.

Deformations during percutaneous procedures

In the current practice of percutaneous procedures for tumor ablation, surgeons make their preoperative planning on MR images acquired before the intervention. They localize the tumor, and choose an entry point on the patient's skin, the path for the surgical probe or needle is the linear segment between the entry point and the tumor. This planning is done in a preoperative phase on MR images where no deformation took place. However, during the operation, the some deformation can be produced. In the case of percutaneous procedures, two main intra-operative deformations sources can be distinguished : the interaction between the needle and the tissue, and the respiratory motion.

In the case of hepatic tumor ablation, liver is a highly deformable object with low stiffness as shown by [Kemper et al., 2010, Kemper et al., 2013]. Therefore, the forces applied due to the interaction with the needle result in important deformations, mainly in the areas close to the needle trajectory. The forces can exceed 1 N according to a survey of the experiments aiming at quantifying phenomena related to the needle–tissue interaction [van Gerwen et al., 2012]. In addition, flexible needles bend during the insertion and do not follow a linear path. As consequence, they may deviate from the preoperative planned trajectory and miss the target tumor. Fig. 1.11 illustrates this kind of limitation.

As for the deformations due to the respiratory motion, Rohlfing et al. quantified the motion of liver due to breathing [Rohlfing et al., 2004] : after removing the rigid-motion component, a mean residual deformation of 10 mm has been reported.

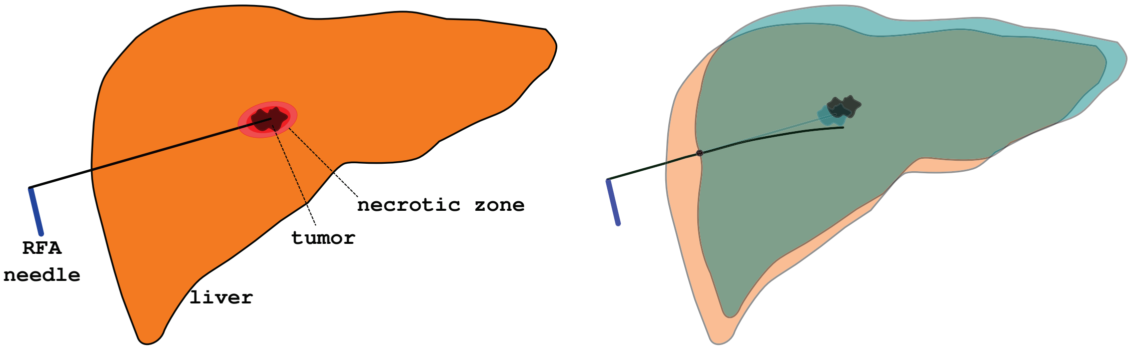

(a) static conditions (b) dynamic conditions

FIGURE 1.11 – flexible needle curvature after penetrating the liver tissues, it deviates from the preoperative planned straight path and target is missed

From the previous reasons, we can say that a planning based on the static preoperative data which does not take into account the deformations of the tissue and tools is not sufficient.

Different intra-operative techniques are applied to mitigate the impact of the needle interaction : for example [Mahvash and Dupont, 2009] proposed to increase the insertion velocity to minimize the tissue deformation mainly during the puncture of the organ surface, while [Kobayashi et al., 2005] introduced an intelligent robotic manipulator driven by an imaging modality capturing the actual deformation of the tissue.

To reduce the deformations caused by the respiration, the needle insertion in clinical routine is done under shallow breathing ; in this case, [Korin et al., 1992] reported deformations which do not exceed 3 mm.

To the best of our knowledge, the intra-operative deformations has not yet been addressed in the existing preoperative planning works. Our second objective is therefore to propose a novel preoperative planning strategy which anticipates intraperative deformations in advance, and propose a more realistic planning trajectory. It can be ensured using control methods during the surgery.

1.2.3 Optimization

Besides the anticipation of possible deformations, automatic planning also requires an efficient optimization technique to find an optimal path within the search space. The choice of the optimization approach strongly depends on the nature of the search problem, its size, and mainly the criteria to optimize.

Preoperative path searching problems involves satisfying a set of surgical rules (such as keeping far from risky structures) which we will discuss in detail in Chapters [3, 4, 5]. Yet, satisfying all the criteria is non trivial because they are often conflicting, and it is not possible to improve one without degrading at least one of the others. Thus, a trade-off between the objectives is required to make an optimal decision in such cases.

The presented DBS and percutaneous hepatic ablation procedures falls into this category of multi-objective optimization. This problem can be addressed by translating it to a mono-objective optimization by combining all the surgical rules into a single rule and solving it using an certain optimization algorithm. Many approaches can be used for aggregating the rules. The weighted sum method, which consists in assigning importance values to the different criteria, and constituting a representative function by summing up all the criteria with their related importance values (which are usually called weights) is the most well known. This approach is intuitive, and sounds close to the current decision making process.

However, there is a consensus in the optimization community that using single criterion approaches for solving multi-criteria optimization problems through aggregation of criteria can lead to an under-detection of the optimal solutions in a given search space. In the same way, we pretend that using merely mono-objective approaches in preoperative path planning may result in an under-detection of a number of optimal solutions. Even though this problem is theoretically well-known, no study has shown the importance of this problem, and the impact of missing some solutions. In the medical domain, the problem impact has not been enlightened yet, and no quantitative or qualitative tests proved its importance.

Our third objective is therefore a multi-criteria optimization approach that we believe able to reveal new interesting solutions for safe and efficient path planning strategies.

1.3 Contributions

The previous Section 1.2 presented the difficulties that can affect the accuracy of the preoperative planning in DBS procedures because of the brain shift phenomenon, in percutaneous procedures represented by the needle-tissue interaction deformation, and the limits of the current optimization techniques. In the following we summarize briefly our contributions to improve the accuracy and efficiency of the preoperative path planning face of the preceding challenges.

1. We present a novel automatic preoperative path planning approach which accounts for certain biomechanical deformation. Our methods combine geometry-based optimization techniques with physics-based simulations. We experimented our methods on two different surgical procedures :
   - In DBS neurosurgery, to compute a patient-specific preoperative safe straight trajectory for the stimulation electrode ; the planning accounts for the "Brain Shift" phenomenon. This contribution will be detailed in Chapter 5.
   - In percutaneous procedures, for hepatic tumor ablation, we compute a patient-specific preoperative safe non-straight trajectory for the ablation flexible needles ; the planning accounts for both : the deformation of the flexible needle during the insertion process, and the deformation of the punctured soft tissue. This contribution will be detailed in Chapter 4.

   We highlight the fact that our method is characterized by a certain level of generality, so it can be adapted to similar procedures.
2. We present a Pareto-based multi-criteria optimization method which can find

optimal solutions that are not reachable via the current state of the art deployed methods. This contribution will be detailed in Chapter 6.

2

STATE OF THE ART

> *"Those who do not read history are doomed to repeat it."*
> *- George Santayana*

In this chapter, we present the relevant literature. We explain the multidisciplinary nature of our work, and we summarize the related works of the most connected disciplines : the assistance to preoperative path planning for percutaneous procedures and neurosurgery for modeling and simulation of deformations, and the related optimization approaches. At the end, we position our work in relation to the related works, and we highlight its distinction.

2.1 Introduction

In its most recent incarnation, image-guided surgery is only about 20 years old. Since its relatively recent appearance, it captivates the researchers by the persistent needs in many related domains.
This work is at the interface of multiple disciplines illustrated in Fig. 2.1.

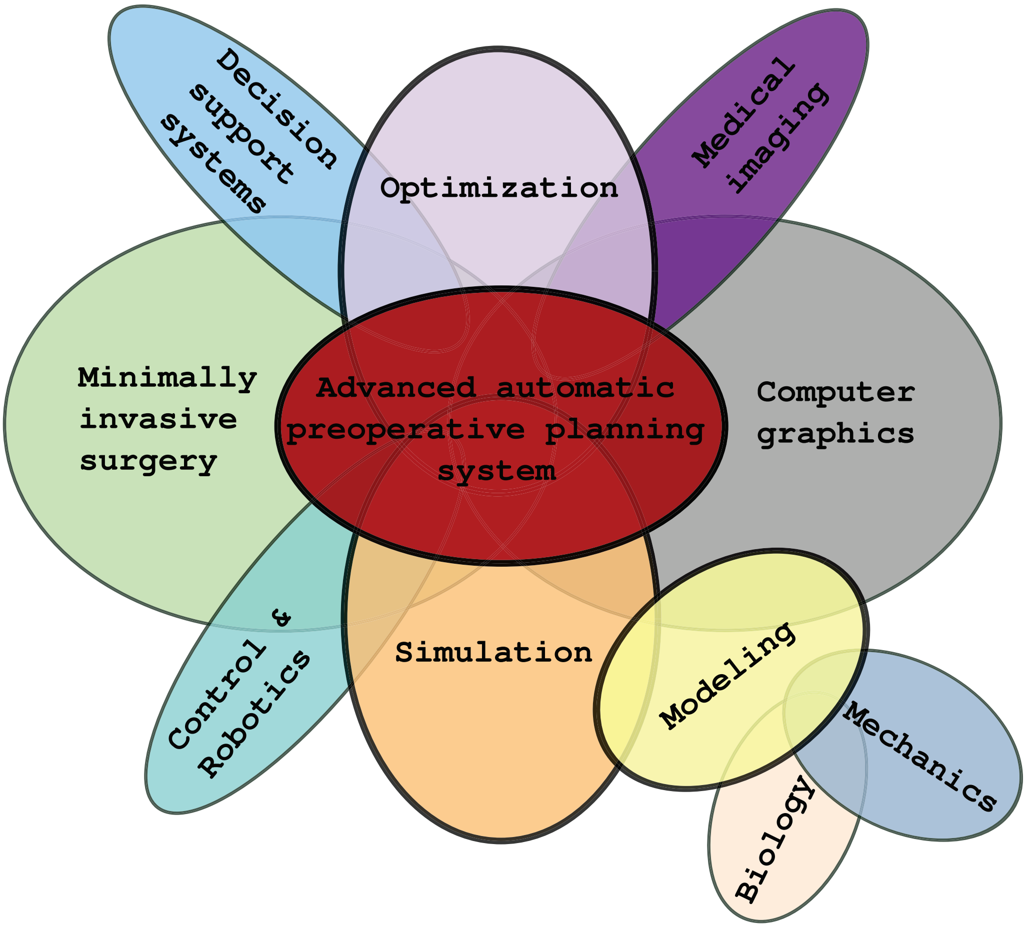

FIGURE 2.1 – related domains

Basically, it takes place between two vast highly connected domains : **minimally-invasive surgery** and **computer graphics**. **Imaging** techniques are closely related as well since the multimodality imaging systems provide primary data on which the planning is performed. At the same time, preoperative planning is regarded as a **decision support system** to help surgeons making their planning strategy. Certainly, the **optimization** techniques play a key role in finding the best planned trajectory. However, to consider real world deformation, physically-based **simulation** is required. **Biology** sciences intersect with **mechanics** rules, together with certain numerical **models** to perform biomechanical **simulations**. The connection of the simulations with the **planning** represent the core of our work. Finally, some other complementary domains such as **robotics** may intervene to ensure the control of the planning during the intervention.

Let us highlight that our work concerns basically the integration of biomechanical deformation simulations with the preoperative planning, and the investigation and integration of efficient preoperative optimization techniques. In the following, we present the related literature. We start by the preoperative path planning techniques in percutaneous and neurosurgery procedures. Then we go through the biomechanical modeling and deformation simulation for abdominal and brain tissue. Afterwards, we discuss the optimization approaches used in the domain. Finally, we position our approach in relation to the existing work.

2.2 Assistance to preoperative path planning

Decision support systems as depicted in Fig. 2.1 play a significant role in nowadays image-guided surgery. They can be integrated into the medical platforms to provide the surgeons with valuable elements in order to make a decision on a planning strategy. As in percutaneous or in neurosurgery procedures, the therapy strategy has to be planned and needs to fulfill multiple clinically relevant criteria to a certain extent.

2.2.1 Abdominal percutaneous procedures

The assistance to preoperative planning in abdominal percutaneous procedures involves choosing a safe trajectory for the surgical tool from the entry point on the patient's skin to the target cells to perform a biopsy procedure or to destroy malicious cells. In the case of thermal ablation of tumors, many issues should be considered in the planning. First of all, the whole tumor should be destroyed in addition to a minimal surrounding safety margin of healthy cells to avoid tumor recurrence. Furthermore, bony structures such as ribs cannot be penetrated. Sensible anatomical structures such as blood vessels should not be crossed by the path to avoid serious complications during the surgery or after it. Indeed, larger distances from the access path to risky anatomical structures are preferred, and shorter paths are desirable to reduce the risk of deviation from the planned path, or to subject to some needles length constraint. In this section we present the works related to the two main planning issues addressed in the literature (path planning and thermal effect simulation), and we give an overview of the existing clinical platforms for planning assistance.

Path planning

Several works addressed improving the planning process for minimally-invasive percutaneous procedures. Many of them offered methods for the segmentation and 3D visualization of the patient's anatomical structures. In intuitive approaches, the trajectory planning was performed in an iterative manner : the surgeons adjusted the trajectories (represented by common applicator geometric models) interactively until the surgical rules were satisfied [Butz et al., 2000, McCreedy et al., 2006, Zhai et al., 2008, Rieder et al., 2009, Weihusen et al., 2007, Stoll et al., 2012].

In some of them, optimization methods were used to automatically or semi-automatically generate suitable access paths : the pioneer work of [Butz et al., 2000] for different types of tumor ablation enabled surgeons to assess the probe placement in a 3D scenes containing the reconstructed anatomy of the patient. In addition, the system performed a semi-automated optimization by minimizing the volume of the safe ablated tissues while destroying all the cancerous cells with a safety margin, the obstacles avoidance is on behalf of the surgeon. In a similar interactive planning approach for percutaneous hepatic microwave ablation [Zhai et al., 2008], surgeons adjusted the trajectories iteratively. Meanwhile, the corresponding necrosis field was predicted depending on a cumulative thermal model for the tissue and the necrosis field, then the 3D model of the necrosis zone was reconstructed and superimposed onto the patient's anatomy to help the surgeon making a decision. In [Wang et al., 2013], authors proposed a mathematical model with a geometric optimization of the needle puncture placements and the ablation frequencies. Their method was designed for treating large liver tumors with multiple needles.

However, the above methods only optimize the applicator position with respect to the thermal ablation zone, and the surgeons still need to verify that the selected trajectories satisfy other related criteria along the access path.

Other approaches addressed methods that incorporate multiple clinically relevant criteria with fully-automatic planning approaches. The first works in this direction were presented by [Villard et al., 2003, Baegert et al., 2007a, Baegert et al., 2007b], they proposed a fully-automatic path planning method based on multiple criteria. They formalized the rules into two types of geometrical constraints (strict and soft) on a 3D reconstructed anatomy. After solving the strict constraints, an aggregative optimization approach based on the weighted-sum method was used to optimize the soft constraints after combining them in a single representative function and assigning importance value to each rule. The results were represented by risk color maps on the scalp where the color intensity represents the risk degree of the insertion point. Let us note that the present study is based on those early works of our research group that will be detailed in Chapter 3. In the same way, [Seitel et al., 2011] calculated trajectories which satisfy a set of strict and soft constraints on patient's 3D reconstructed structures. The system determines possible insertion zones based on the strict constraints and rates the quality of the feasible insertion zones according to their qualities in satisfying soft constraints. In [Schumann et al., 2010], authors proposed a fast automatic method that computes a list of path proposals for a given target point inside the liver with respect to multiple criteria that affect safety. The planning include segmented masks of the relevant anatomical structures.

When considering multiple criteria, many works use an aggregative optimization approach by combining the surgical rules in a single representative function after assigning importance value to each rule, and optimizing this function to find an optimal path [Essert-Villard et al., 2009, Schumann et al., 2010]. Others calculate a list of optimal trajectories by finding a compromise between multiple clinical criteria depending on Pareto optimality as in [Seitel et al., 2011] and recently in [Schumann et al., 2015].

Nevertheless, all the above mentioned works assume that both the tissue and the surgical tool do not deform, which is a significant over simplification given the highly deformable environment and the flexibility of certain ablation needles.

Thermal effect simulation

In addition to the access path, other important aspects arise in thermal ablation planning procedures. For example, destroying all cancerous cells while preserving most of the healthy tissue. To this end, accurate information about the thermal effect volume or ablation zone are required. While some approaches approximated the thermal effect volume by ellipsoids [Butz et al., 2000, Dodd et al., 2001, Trovato et al., 2009, Wang et al., 2013] and proposed planning strategies depending of the approximated necrotic volumes, other works addressed the accurate simulation of heat propagation soft tissue including cooling effects [Kröger et al., 2006, Altrogge et al., 2007, Chen et al., 2009, Wang et al., 2013, Haase et al., 2012]. In this kind of approach, numerical methods such as the finite element method can be used to simulate a more realistic ablation zone. These simulations rely usually on bioheat models such as "Pennes" equation in [Altrogge et al., 2007]. Fast approximation based on the aforementioned simulations was proposed in [Kroger et al., 2010, Rieder et al., 2011] as a compromise between accuracy and practical feasibility. Certainly, approximation approaches make the simulation fast, but it remains a simplification and lacks precision. On the other hand, the use of simulation methods may perhaps result in unpractical computation times in the range of hours, especially when multi probes are required in a single therapy procedure. Finally, let us note that thermal volume optimization is out of the scope of this research.

Percutaneous procedures planning platforms

Despite the permanent need of percutaneous ablation procedures, and the increasing researches addressing the improvement of the existing preoperative planning methods for abdominal thermal percutaneous procedures, to the best of our knowledge, a commercial surgery planning platform has not yet been proposed. Still, some ongoing research prototypes can be pointed out being possessing a certain level of completion, we cite as examples two of them :

- **Siemens AG :** implemented by [Stoll et al., 2012], a percutaneous ablation planning prototype which involves simulation and rendering of the ablation zone, and assistance to define a needle path in an interactive way with a visual illustration on the patient's medical images (Fig. 2.2b).
- **Safir Fraunhofer :** presented by Haase et al. [Haase et al., 2012] to assist radiologists in their interactive preoperative planning. The platform incorporates a realistic representation of the thermal necrosis including heating effects for RFA procedures with a 3D volume rendering of the patient anatomy (snapshot of the interface in Fig. 2.3). Recently, a Pareto-based multi-criteria optimization approach with a navigation interface has been integrated in the platform by [Schumann et al., 2015].

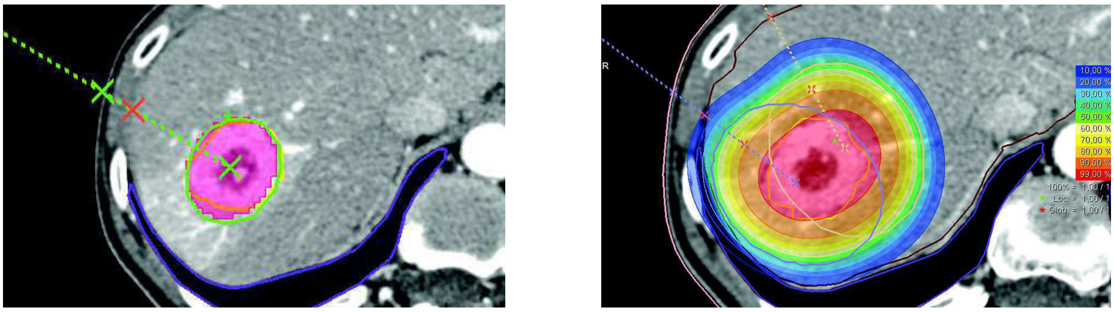

(a) Needle path definition (b) Probabilistic ablation zone

FIGURE 2.2 – Illustration from Siemens AG platform [Stoll et al., 2012]

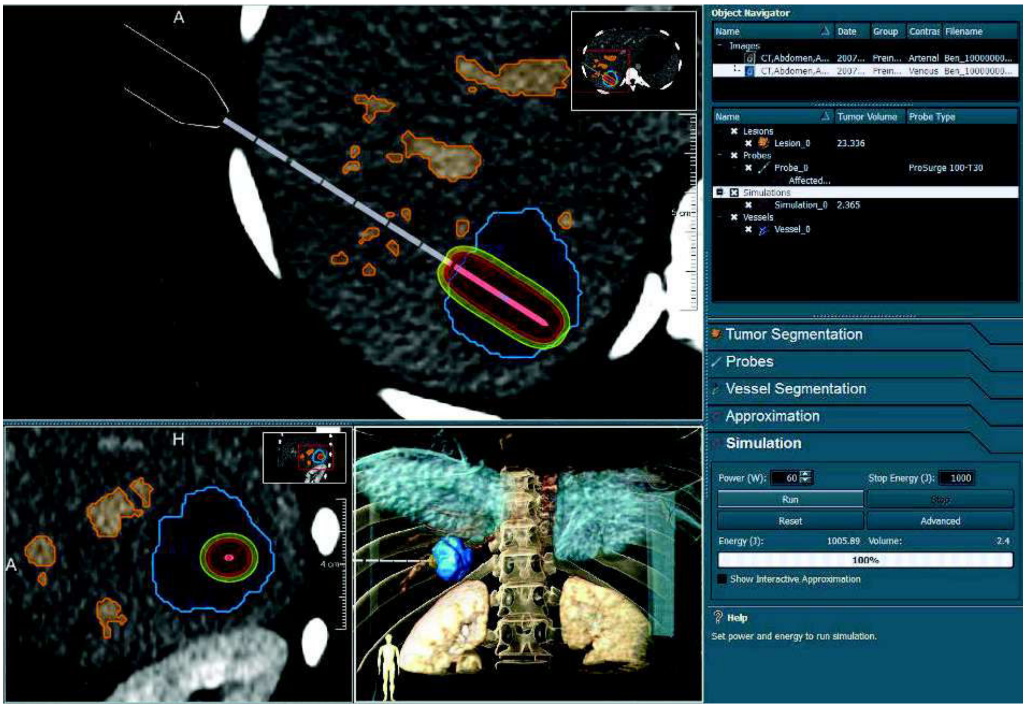

Name	Date	Group	Contras	Filename
Images				
CT,Abdomen,A...	2007...	Prein...	Arterial	Ben_10000000...
CT,Abdomen,A...	2007...	Prein...	Venous	Ben_10000000...

Name	Tumor Volume	Probe Type
Lesions		
Lesion_0	23.336	
Probes		
Probe_0		ProSurge 100-T30
Affected...		
Simulations		
Simulation_0	2.365	
Vessels		
Vessel_0		

Power (W): 60
Stop Energy (J): 1000
Energy (J): 1005.89
Volume: 2.4
100%
☐ Show Interactive Approximation
Set power and energy to run simulation.

FIGURE 2.3 – Safir Fraunhofer platform planning interface [Haase et al., 2012]

2.2.2 Neurosurgery

Assistance to image-guided neurosurgery planning and the plenty of advantages in terms of time and effort saving that fully automatic solvers deliver has attracted many research groups who tried to automate the process. A recent study [Trope et al., 2014] highlighted the role of computer-based surgical trajectory planning tools in improving the potential safety of image-based stereotactic neurosurgery.

The planning is performed after an appropriate brain images acquisition phase and involves mainly two important issues : targeting and path planning. While "targeting" consists in accurately locating the brain area to reach for stimulation in functional neurosurgery, tumor removal, or epilepsy diagnosis, path planning is required to find safe trajectories for the surgical instrument from an entry point to the located target. Surgeons are used to plan their interventions manually on 2D image slices. They have to locate the target and choose a secure path by mentally assessing possible trajectories inside the brain anatomy. Besides being a difficult and a time consuming task, the planning decision is very surgeon dependent. The previous reasons motivated the work in computer-assisted preoperative planning, i.e : the need of accurate targeting and safe trajectories. Both issues come with the need of a clear display with meaningful data.

In this section, we will present the related works in path planning and targeting, and we will discuss the existing neurosurgery planning platforms.

Path planning

Neurosurgery path planning has been addressed in the literature using different approaches varying from interactive to semi-automatic or fully-automatic methods.

The interactive approach consists in defining the path in an iterative manner by the neurosurgeon on 2D slices of the patient's images. After locating the target cells, the surgeon has to choose an entry point on the head boundary, and to assess the safety of the linear segment connecting the entry to the target by examining the path on the successive slides. This interactive planning can be done on 2D slices images as in the early work of [Nowinski et al., 2002] for example, as well as on 3D reconstructed models of the brain which is the case in [Lee et al., 2002].

The second approach is a semi-exhaustive one. Here again, the neurosurgeon first locates the target point interactively. Then, all possible paths on the head boundary are examined automatically and assigned a quality value, leaving the decision to the surgeon to choose the convenient path. Some works integrate solvers capable of proposing a candidate trajectory which optimize certain surgical constraints. An early work on preoperative automatic path planning for a variety of neurosurgical procedures was proposed in [Vaillant et al., 1997]. Firstly, a risk value of each structure of the brain was defined by the surgeon on the atlas segmented structures at an early stage. All the pixels on the segmented structure were assigned the same risk value. The path planning method involved registering the patient's MR images on a brain anatomical atlas. Afterwards, the risk values were mapped from the atlas to the corresponding patient image pixels, and the solver tries to find the best entry point result of an optimization of a cost function minimizing the number of crossed risky structures. A similar work was introduced by [Fujii et al., 2002], the proposed method involved a voxel based 3D atlas which contained a structural part including the geometrical information with respect to each tissue, and a knowledge part generated based on experiences of doctors, with a numeric value provided as an importance value for each tissue by a neurosurgeon in an early stage. The trajectory was calculated automatically by a solver based on the minimization of the importance values for all pixels along with the path. Later, the same group extended their work "Neuropath planner" by integrating a technique to minimize the distance to blood vessels depending on vessel's centerlines diameters [Fujii et al., 2003]. The process was time consuming as the vessels were delineated by the surgeon slide by slide. The aforementioned risk values interpolation method was implemented on images as well on 3D reconstructed mesh as in the work proposed by [Bourbakis and Awad, 2003] for searching an optimal path in brain tumor removal. In their fully automatic preoperative planning, all the pixels on the atlases were assigned a risk value similarly to [Fujii et al., 2002], and mapped to the patient reconstructed meshes. The solver evaluated the possible entry points to the target tumor, and minimized the cost function which calculates the damage to surrounding healthy tissue and the penetration area. However, the mentioned optimization techniques path planning algorithms required manual assignment of tissue importance values which was a time consuming and non trivial task.

Fully-automatic path planning solvers in neurosurgery appeared in the literature some years after those of percutaneous ablation, and could have been influenced by similar planning strategies. Even though the therapy, the intervention techniques, and the objectives are not the same, both search for a safe path inside the body.

So far, alike the automatic path planning method suggested in [Villard et al., 2003], [Brunenberg et al., 2007] proposed an automatic solver to calculate safe paths for DBS procedures without demanding manual settings of a complex cost function. Their method computed distance maps thresholded by 3 mm along the path, and the trajectories which did not respect the distance were considered non safe and therefore rejected, while the remaining trajectories were ordered in a list according to their minimal distance to risky structures, with a possibility offered for the surgeon to choose among them. Another work [Tirelli et al., 2009] proposed a planner for general neurosurgery path planning. In their method, the shortest probe path that caused the least damage was determined by registering the patient's images on multiple atlases (anatomical, vascular, and functional), and the corresponding risk was calculated. A heuristic search was deployed to refine the entry point which is constrained on allowed areas. A general neurosurgery path planning approach was proposed [Shamir et al., 2010, Shamir et al., 2012]. In their system, targeting was done manually on CT/MR preoperative images, then risky structures (vessels and ventricles) were segmented once by an expert, and risk values were assigned to the segmented structures according to the damage importance when crossing the corresponding structure. A risk volume was built by assembling voxels risks, and the outer head surface is colored according to the entry point quality to constitute a risk map. The results were represented visually by the color map, quantitative risk information are provided in the form of risk cards assigned to every trajectory, a risk card contains a summary of geometrical parameters regarding critical structures and planned trajectories. These cards facilitate assessing the quality of trajectories and comparing them before making a definitive choice. The advantage of this work over Brunenberg's was the significant reduction of the number of possible trajectories, and the quantitative feedback of the path quality. However, a considerable amount of manual input was still required before running the solver. The same year, [Essert et al., 2010, Essert et al., 2012] proposed a generic fully automatic path planning approach where a set of surgical rules were formalized into two groups of geometric constraints (hard and soft), and a single aggregative cost function was formed from the different surgical rules with an assigned weights, and optimized to obtain the best trajectories. Alike in [Shamir et al., 2010], and in their previous works in RFA [Villard et al., 2003], the planning results were then represented using color maps on the scalp, and the interface allowed surgeons to choose different trajectories and to assess the quality of each of them relatively to the surgical rules.

Similarly to [Essert et al., 2010], [Bériault et al., 2011] also implemented an optimization method based on the weighted sum approach and the distinction of surgical rules into two constraints types. A platform dedicated to DBS preoperative planning was presented. It gathered an image segmentation pipeline with an optimization method minimizing an aggregative cost function. In a recent work for the same group, the depth optimization for multiple electrodes implantation in epilepsy has been investigated by Zelmann et al. [Zelmann et al., 2014]. They kept the same path planning algorithm, and added the maximization recording coverage of the target volume by estimating the EEG recorded from each contact.

Investigations in the same field are still ongoing, a recent work [Cuevas et al., 2015] formulated surgical criteria based on fuzzy logic rules and an aggregative approach is used to propose a number of best trajectories for keyhole neurosurgery.

Nevertheless, brain shift information has not been taken into account yet by any of the aforementioned works, even thought some of them [Bourbakis and Awad, 2003] highlighted the importance of incorporating them in the planning algorithms for more safety and realism.

Targeting

Surgeons depend on their expertise to locate a target : they identify its coordinates on the 2D slices of the patient's preoperative images taking advantages from the existing 3D medical visualization and interaction softwares. However, using atlases in their different types (anatomical, functional, histological, etc.) can help in locating the target. The physician may rely on a single or multiple atlases at the same time along with the patients images to locate the target. In [Nowinski et al., 2002, Vaillant et al., 1997] for instance, the authors proposed an interactive targeting based on anatomical atlases for image-guided neurosurgery targeting in general.

Automatic inclusion of atlas information into the patient's image is a common approach which can be done via registration and mapping techniques.

Using atlases can be done in the preoperative phase as in [Dawant et al., 2003] who proposed a fully automatic DBS targeting based on anatomical atlases and non-rigid registration, and in [D'Haese et al., 2005b], where electrophysiological atlases were integrated to raise the accuracy of the electrode placement. It can also be used for a second targeting refinement intraoperatively : some works were based registration techniques, [D'Haese et al., 2005a] registered MR images on atlases, others used 3D probabilistic functional maps built from a set of intra-operative data [Guo et al., 2006, Guo et al., 2007] to increase the targeting accuracy. In DBS interventions, using neuro physiological microelerode recoding MER can be done to ensure the maximal coverage of the target tissue before the definitive placement of the DBS electrode [Miocinovic et al., 2007].

The research in this domain resulted in some clinical prototypes varying in the level of assistance and readiness to clinical use. One of the most advanced prototypes is the "CranialVault" for DBS planning presented in [D'Haese et al., 2012] which is the successor of a previous attempt "VU-DBS" developed in [Dawant et al., 2007]. Besides, a number of commercial platforms providing different functionalities are already in use.

Neurosurgery planning platforms

In neurosurgery departments, many commercial planning software are available to help clinicians create treatment plans for everyday procedures. They support the use of multiple common imaging modalities, efficient volume visualization, automatic segmentation and registration techniques. Moreover, some of them enable post-processing of specific datasets turning them into clinically relevant information for pre-planning. We list below the four major commercial platforms :

- **BRAINLAB** platform [BRA, 1988] with its Stereotactic Planning software *"iPlan"* allows clinicians to customize a confident trajectory planning. It supports multiple imaging modalities and enables automatic image fusion, and automatic segmentation of the deep brain structures. The user locate the target, and the software can then define margins around the target. A suggestion of some entry points for a given target point can be made, and a guided entry point planning is performed interactively by the surgeon.
- **Medtronic StealthStation** surgical navigation system [Med, ndc] which combines hardware and software to help the surgeon in the operating room. A set of intra-operative registration techniques are included in addition to tracking technologies to ensure the preoperative planning achievement. However, it is a general navigation-aid system, and the preoperative planning itself remains a surgeon task by defining the target point, and assessing possible entry points interactively.
- **Leksell SurgiPlan** neuro-surgical planning software [Sur, nd] specifically designed for use with Leksell stereotactic system. It includes measurements functions, target localization, manual interactive 3D path planning on patients images.
- **ClearPoint** neurosurgical platform [CLE, nd]. A DBS dedicated integrated hardware and software package with a customized smart frame to perform accurate electrode implantation in STN. Fig.The overall system is illustrated in Fig. 2.4. A smart grid assists the surgeon in identifying the entry point on the patient's scalp for a DBS procedure, and an interactive interface enables the navigation in the MR image slices to localize the target and to assess the trajectories of the different grid entry points.

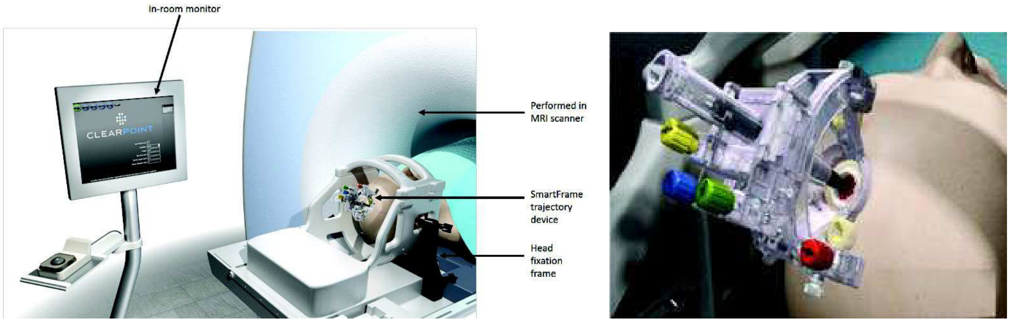

(a) (b)

FIGURE 2.4 – ClearPoint system for DBS

Despite the fact that the commercial platforms offer a lot of features, and facilitate the planning task, still neither automatic path planning algorithm is available, nor intra-operative deformations are considered.

2.3 Modeling and deformation simulation

Most of the aforementioned preoperative planning systems are based on geometric representations of anatomical structures that do not take into account of their physical nature. The realistic modeling of soft tissue to represent physical phenomenon such as presented in 2.2 will increase the credibility of neurosurgery and percutaneous procedures planning addressed in this work. Soft tissue deformation can be represented thanks to complex mathematical models of biomechanics, and the computation efficiency of nowadays computers. In order to achieve realistic tissue deformation, it is essential to combine the geometric representation with the biomechanical models. In the following, we survey the existing models of deformation simulations for soft tissues.

2.3.1 Soft tissue modeling

Soft tissue modeling is a key element to raise the accuracy of deformation simulations. It involves the biomechanical behavior model of the tissue, the interaction between the tissue and rigid objects like surgical tools, and the real time deformation integration.

The simplest model to represent the tissue behavior or displacement due to some applied forces is the linear elastic model where tissue has a linear stress/strain or force/displacement relationship, and the deformation of points under a certain load are straight lines. This model is valid for small displacements, and deformations can be computed fast. Larger displacements require more complex non-linear models where the stress/displacement relationship is not linear. Many models have been introduced to represent these displacements such as Mooney-Rivlin [Mooney, 1940, Rivlin, 1948] or Venant Kirchoff models. A third type of deformation is plastic deformation which are not reverse. Furthermore, to represent the interaction between tissue and rigid objects, collision detection is required, and the resulting interaction forces which leads to displacements should be computed. However, the interaction between tools and tissue not only occurs at their extremity, but also along their length. Therefore the instrument is considered as a rigid moving body penetrating a soft deformable body, and we have to integrate time for computing displacements : if we denote $\mathbf{X_t}$ the position of the tissue model at time iteration t, we have to compute the new position $\mathbf{X_{t+1}}$ at time $t+1$. To describe the behavior of tissue over time, we need a motion law, which we call a constitutive law. Two motion laws can be distinguished : static and dynamic laws according to whether $\mathbf{X_{t+1}}$ depends on the previous position $\mathbf{X_t}$ or not. However, static laws are not able to model realistic deformations while dynamic lows of motion can model more accurate deformations but are more difficult to handle and computationally more expensive. An extensive description of the constitutive laws used to model tissue-behavior would fall outside the scope of this study. A detailed survey on soft tissue modeling in medical simulation could be found in [Delingette, 1998].

After we explained the major constraints involved in soft tissue modeling, we present briefly the most common models used in the domain.

1. **Finite Element Methods FEMs**

   Principle : FEM is a numerical technique to solve the differential equation of continuum mechanics that has been widely used in soft tissue modeling. It consists in representing an object by a set of basic elements such as triangles, tetrahedra, etc. This way, a continuous representation of the objects is attained.

   Advantages : FEMs are efficient to model complex geometries, as they can represent accurate deformation of soft tissue. Moreover, graphics hardware is well adapted for visualizing finite elements (FEs).

   Limits : FEMs are time consuming, and using them for real-time simulations remains a challenge. Contrary to mass-spring techniques, topological changes such as cutting and suturing are more complicated and costly with FEMs because remeshing process is required.

   Related works : FEMs are convenient for deformations contingent upon mechanical constraints. Indeed, they are well suited to model the brain due to its complexity, and most of the work on brain models use this technique ([Duriez et al., 2009] is an example). Indeed, all the works which will be presented in Section 2.3.2 are implemented using FEMs.

2. **Mass-Spring models**

   Principle : it consists of a set of points (vertices or nodes) each of them representing a mass. They are linked together by springs and dampers. A spring returns a force for a given displacement, while a damper returns a force for a given velocity.

   Advantages : the main advantages of mass-spring models are their ease of implementation and their low computation time. In addition, they are suitable to model cutting and suturing simply by removing or adding connections between vertices.

   Limits : a major limit for mass-spring models is the difficulty of designing a complex topology composed of a large number of springs and masses. This results in a restriction of the geometric representation. In addition, they are less accurate in representing deformations because springs do not rely on continuum mechanics. For slight deformations they behave similarly to FEMs while for important ones they are not valid nonlinear elastic models. Finally, they are less convenient to represent high stiffness models which is the case for soft tissues.

   Related works : the mentioned issues make mass-spring models convenient for medical simulation training systems. The approach of [De Paolis et al., 2009] is an example of mass-spring dampers virtual model of the human brain that could be used in a neurosurgical simulation for both educational and preoperative planning purposes.

3. **Other methods**

> Alternative methods have been proposed to model soft deformable bodies. Even though most of them have rarely been applied in the medical domain, a few is relevant to soft-tissue modeling. A recent example [Pan et al., 2015] of metaballs-based physical approach was used by for modeling and deforming the human liver in a virtual surgery platform. In their approach, meshes represent the organ's surface, while the meta-balls occupying organ's interior. Another approach is implicit surfaces defined by potential fields attached to skeletons are well suited for modeling very soft objects. However, this category is not convenient enough to be used for brain modeling where stability and accuracy are two main factors, and further investigation should be carried out before implementing them to the surgical domain.

The computation efficiency and physical accuracy are the two main factors to be considered in the model. In our application, it is preferable to use a more accurate model. Real time not being necessary for preoperative planning, computational time is less important, but still it should remain compatible for clinical usage. In the following we focus on the existing works in soft tissue modeling and deformation simulation for the case of percutaneous ablation procedures and brain shift phenomenon.

2.3.2 Needles path planning with deformation

Percutaneous procedures as explained in Chapter 1, consists in inserting thin surgical tools through the skin to internal zones in the patient's body for diagnosis and therapeutic purposes. A preoperative path planning is not able to predict intra-operative deformation and hence physical models are necessary to implement realistic planning. With advances in computational hardware, the use of the finite element method for tissue deformation has become a de-facto standard due to its physically-based continuum mechanics representation.

When a needle is inserted into soft tissue, interaction forces are developed at the needle tip and along the needle shaft. The needle tip force is due to cutting of the tissue, and the force along the needle shaft is due to friction between needle and tissue. To model the interaction between tools and tissue, the surgical instrument is considered as a rigid moving body penetrating a soft deformable body.

Needle insertion and path planning in deformable environments have been studied by multiple groups in different contexts, for multiple needles types (rigid, flexible, with beveled tip), and in various environments (2D or 3D, with or without obstacles, in synthetic soft tissue phantoms).

Many works addressed the needle trajectory planning when inserted inside soft tissue. The pioneer work on needle insertion in soft tissue is [DiMaio and Salcudean, 2005] who simulated needle insertion in PVC phantoms using a local search method for the needle configurations based on potential fields attraction to the goal and repulsion from obstacles. Linear elastostatic model approximations for both tissue and needle with a discretization for both tissue and needle. [Alterovitz et al., 2005, Alterovitz et al., 2008] proposed a planning algorithm for insertion of flexible bevel-tip needles into soft tissue with obstacles and a target segmented in a 2D medical image. Using dynamic programming, the planner computes optimal steering actions to maximize the probability that the needle will reach the desired target. The authors in [Park et al., 2010] proposed a stochastic optimization approach for the steering of fexible needles with a bevel tip in the presence of uncertainties for the case when there are no obstacles in the environment.

To simulate the interaction between soft tissue and needles, constraint-based modeling which is independent from the needle and tissue models was proposed by [Duriez et al., 2009]. Their approach has been experimented by comparing the results of needle insertion in a biomechanical simulator framework SOFA with results conducted on needles insertions in prostate phantoms [Moreira et al., 2013]. The work of [Misra et al., 2010] presented a complex behavior model of flexible bevel-tip needles based on the Timoshenko formulation. steering is conducted into soft tissue simulants (gels). In [Goksel et al., 2011] flexible needles were simulated using an angular springs model, composed of a set of rigid rods connected by spring-loaded joints.

Because of uncertainty in needle motion due to patient differences and the difficulty in predicting needle/tissue interaction, many works shifted the problem to a real-time control problem. Authors in [Patil et al., 2011] proposed a unified approach for motion planning under uncertainty in 2D deformable environments that maximizes probability of success by accounting for uncertainty in deformation models. In a more precise scenario, intra-operative modification of the needle trajectory to compensate the target's motion was addressed : in [Bernardes et al., 2011], a method coupled a robotic assisted system for 2D needle steering with image feedback. Other groups [Abayazid et al., 2013] proposed a closed-loop control to steer flexible needles using US in 2D space without obstacles. A work by [Wang et al., 2013] proposed a dynamic path planning with obstacles in a synthesis environment.

2.3.3 Brain shift modeling

Brain models have been mainly used for three purposes : medical training systems, medical images registration, and brain shift compensation. In this section we describe some representative works for brain shift phenomenon modeling.

In medical training systems, mass-spring-damper were used [De Paolis et al., 2009] due to their computation efficiency. Finite element modeling is the most suitable method to estimate the extent of brain shift, because of its accuracy in modeling detailed anatomical structures which is a key element in neurosurgery. Therefore, most of the works which addressed brain shift phenomenon used FEMs ; it is the case of all the works that we will cite in this section.

However, they differ in the behavior laws. The majority of them approximated deformations to a linear elastic model considering brain tissue as a homogeneous linear visco-elastic material [Škrinjar et al., 1998, Ferrant et al., 2002, Hu et al., 2007]. Some others proposed non-linear hyperelastic constitutive law accounting for different stress-strain and compression variations [Miller and Chinzei, 2002, Wittek et al., 2010].

The detecting brain shift can be performed using prediction techniques in the preoperative phase, this is usually done depending on templates or biomechanical simulations [Hu et al., 2007, Chen et al., 2011, Bilger et al., 2012]. Another approach addressed brain shift detection during the intervention using registration techniques where intra-operative images were registered to preoperative ones [Ferrant et al., 2002, Pallavaram et al., 2009, Wittek et al., 2010].

2.3.4 Path planning with brain shift deformation

The first evaluation of brain shift was presented in [Winkler et al., 2005]. A deformation field analysis of pre and postoperative MR images reported a brain movement of 2 mm in the deep region of the target STN. By the obtained quantification, they highlighted the need to reduce brain shift complication while performing the planning. Another work re-emphasized the importance of accounting for brain shift [Khan et al., 2007] by measuring its possible amplitude on registered intra-operative 3D MR scans to preoperative ones. According to their tests, a brain shift of up to 8 mm has been recorded.

Consequently, multiple groups investigated better surgical techniques to compensate or to alleviate this deformation. As for the compensation approaches, [Khan et al., 2007] presented a preliminary study to detect brain shift intraoperatively and potentially to correct it. The study was performed using the "CranialVault" platform on multiple stereotactic frames. It depends on registration between intra-operative data and functional atlases. They also investigated methods to minimize its effect on the electrode placement error estimation [D'Haese et al., 2010]. Another compensation approach for detecting brain shift [Mercier et al., 2010] was introduced in IBIS, the Interactive Brain Imaging System. The system involves freehand ultrasound measurements used to update patient-to-preoperative image alignment.

Authors in [Bilger et al., 2012] suggested a preoperative planning strategy which avoid risk of any potential brain shift in DBS procedures. To this end, they used biomechanical simulations to predict the different potential intensities of brain shift to produce an enhanced risk map that takes into account all possible displacements of vessels (Fig.2.5). After that, they adapted their preoperative path planning to account for the brain shift aware risk map (Fig.2.5).

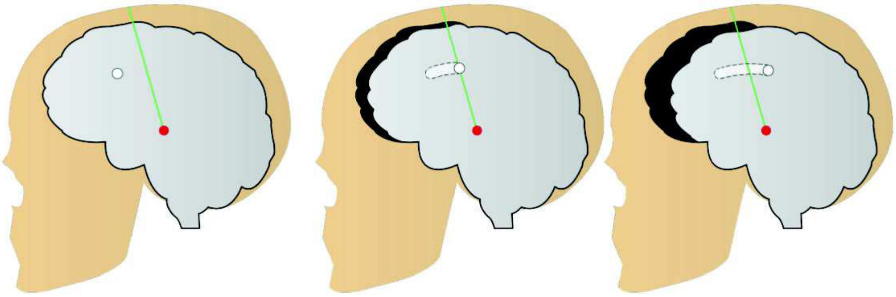

FIGURE 2.5 – Different brain shift intensities : target in red, trajectory in green, and a vessel in white, with all possible positions that it could take in case of brain shift.

Other centers adopted a different philosophy to deal with the problem. Instead of compensation approaches, they believe that it is possible to avoid the brain shift phenomenon. A research team in the neurosurgical center at UCL university [Petersen et al., 2010] considered that there was no need to do Microelectrode Recording MER if a quick MRI-based implantation in STN was done for for Parkinson's Disease. A study has been carried out at the same center [Zrinzo et al., 2012] and has explained how to reduce hemorrhagic complications in functional neurosurgery. Another brain shift avoidance technique was proposed [Slotty et al., 2012] where they stated that CSF loss during a later phase of surgery could be effectively averted by burr hole closure using bone wax during the surgery as illustrated in Fig.2.6a

However, few work addressed the electrode path changes due to brain shift. Among them, a significant work on the electrode curvature induced by the brain shift has been introduced in [Sillay et al., 2012] : authors estimated preoperatively the deformations on both the electrode and the potential displacement of the target. Fig.2.6b illustrates the curvature.

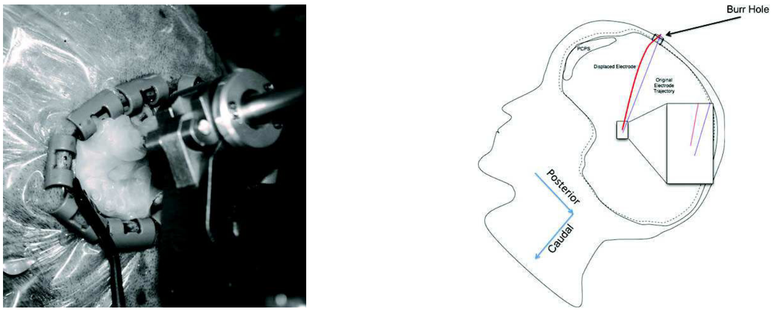

(a) Bone wax closure

(b) Electrode curvature and displacement inside the target

FIGURE 2.6 – Left : Slotty et al. [Slotty et al., 2012] Right : Sillay et al. [Sillay et al., 2012]

2.4 Optimization methods

In preoperative trajectory planning, the quality of the path strongly depends on the initial entry point location on the patient's skin. Finding the good entry point can be regarded as an optimization problem in which an optimal point is inspected in a given solution space. Optimization techniques are vast to allow handling the uncountable search problems around us. They can be categorized in different ways depending on the problem nature, size, conditions, etc.

In this section, we tackle path planning in the optimization context. We start by a general introduction about optimization approaches in order to position our problem in the context. At the same time, we classify the related works according to their optimization techniques.

2.4.1 Introduction

Firstly, optimization problems can be classified according to the **feasible solution space** into two main categories :

- Combinatorial problems in which the feasible solution space is a discrete finite (or countable) set.
- Continuous variable problems where the solution space is not a discrete set, but it is constrained by some defined conditions, and is known as *constrained optimization*.

Trajectory planning of surgical tools by its nature falls into the continuous variable category because the solution space is a skin patch where the number of points constituting it is uncountable.

Nevertheless, the problem is sometimes shifted to a combinatorial one by a discretization of solution space. Some planning strategies are based on an exhaustive search of the finite solution space, others use some optimization techniques to converge to the best trajectory without examining all candidate solutions.

The aforementioned works of [Brunenberg et al., 2007, Bériault et al., 2012, D'Haese et al., 2010, Shamir et al., 2012, Momi et al., 2014, Cuevas et al., 2015] for example implement a coarse discretization of the feasible search space according to the resolution of the available MRI images, and pick the best point after examining all the points.

In the case of optimization approaches, local, global, or hybrid methods can be distinguished. On the first hand, local methods tend to converge quickly but they risk falling in a local minimum. An example of using this methods for path planning in hepatic tumor ablation was presented in [Baegert et al., 2007b] where the derivative-free Nelder-Mead simplex algorithm (known also as downhill) was implemented, or in [Bourbakis and Awad, 2003] where the tool path in brain surgery was calculated in an intelligent manner by testing safe trajectories on the 2D slices from the tumor volume to the skin without irrelevant and redundant path calculation. Others searches the minima by applying a Gaussian smoothing on the segmented slices [Schumann et al., 2010]. On the other hand, global methods require long computation times and they are able to better investigate the solution space avoiding falling into local minima. Some hybrid method could be implemented to arrive a compromise between computation efficiency and solutions variance. Indeed, the choice of the appropriate approach depends mainly on the problem nature and on the allowed computation resources and time, and the required quality of the solution.

Let us explain the mathematics of interpreting criteria to the optimization approach.

2.4.2 Constrained optimization

Constrained optimization problems consist in finding the maximum or the minimum of a function $f(\mathbf{x})$ in presence of some constraints on its variables.

A general constrained optimization problem can be expressed as follows :

$$\begin{aligned}
&\mathit{minimize} \quad f(\mathbf{x}) \quad , \quad \mathbf{x} \in \mathbb{R}^N \\
&\text{subject to :} \\
&\qquad\qquad G_i(\mathbf{x}) \leq 0 \quad , \quad i = 1,..,n \quad , \quad G_i(\mathbf{x}) \in \mathbb{R}^n \\
&\qquad\qquad H_j(\mathbf{x}) = 0 \quad , \quad j = 1,..,m \quad , \quad H_i(\mathbf{x}) \in \mathbb{R}^m
\end{aligned}$$

where $\mathbf{x}$ is the variable vector of length N to be optimized, $G_i(\mathbf{x})$ and $H_i(\mathbf{x})$ are the sets of inequality and equality constraints respectively with their numbers n and m

Another classification for optimization problems according to the **objective function** is the following :

- Mono-objective (Mono-criteria) optimization in which we search to optimize the solution for a single objective.
- Multi-objective (Multi-criteria) optimization where a satisfaction of two objectives at least is required.

Multi-objective optimization arise naturally in most real-world problems. Yet, satisfying all the criteria is nontrivial because they are often conflicting, and there is no way to improve one without degrading at least one of the others. Thus, a trade-off between the objectives is required to make an optimal decision in such cases.

Our work falls into the multi-objective optimization category since preoperative trajectory planning involves multiple surgical rules that should be optimized simultaneously.

2.4.3 Multi-objective optimization MOO

By an extension of the constrained single objective optimization formalization, a multi-objective problem can be expressed as follows :

$$\begin{aligned}
&\textit{minimize} \quad F(\mathbf{x}) = (f_1(\mathbf{x}), f_2(\mathbf{x}), ..., f_k(\mathbf{x}))^T, \quad \mathbf{x} \in \mathbb{R}^N \\
&\text{subject to :} \\
&\qquad\qquad G_i(\mathbf{x}) \leq 0 \quad , \quad i = 1, .., n \quad , \quad G_i(\mathbf{x}) \in \mathbb{R}^n \\
&\qquad\qquad H_j(\mathbf{x}) = 0 \quad , \quad j = 1, .., m \quad , \quad H_i(\mathbf{x}) \in \mathbb{R}^m
\end{aligned}$$

where $\mathbf{x}$ is the variable vector of length N, $k \geq 2$ is the number of objectives f_i, n and m are the number of inequality and equality constraints respectively, and $G_i(\mathbf{x})$, $H_i(\mathbf{x})$ are the set of inequality and equality constraints.

Apart from the optimization search approach (local, global, hybrid), a multi-objective optimization problem should be addressed from the objective treatment manner. The most common approaches are :

1- Aggregating approaches
2- Independent objectives optimization
3- Dominance-based approaches

Aggregating approaches

In these approaches, optimizing a combination of the objectives is done by transforming a multi-criteria problem into a mono-criteria optimization. The principle is to substitute all the objective functions by a single representative aggregative function called *cost function*. Many different techniques exist among which the most commonly used in our field is the *weighted sum* method. The cost function is a linear combination of all the objective functions, and a weight value w_i is assigned to each f_i. The aggregative cost function f is expressed by the following equation to minimize :

$$f = \sum_{i=1}^{n} w_i . f_i(\mathbf{x}), \quad \mathbf{x} \in \mathbb{R}^N \tag{2.4.1a}$$

where $0 < w_i < 1$, and $\Sigma w_i = 1$.

After that, a classical optimization technique can be applied to find an optimum. This method is straightforward, and can always find a solution. However, it is weights dependent.

The popularity of this method in path planning studies is due to its intuitiveness, as surgeons usually have a reasonable idea of priorities between the rules and this approach enables to associate weights to priorities and get the corresponding solution instantly. Many works opted for this optimization choice either for RFA procedures like [Baegert et al., 2007b, Schumann et al., 2010] or in DBS like [Brunenberg et al., 2007, Shamir et al., 2010, D'Haese et al., 2012, Essert et al., 2012, Bériault et al., 2012].

Independent objectives optimization approaches

With these approaches, objective functions are treated separately to find the optimal solution. We summarize two significant techniques in this area :

- Lexicographic ordering, which was proposed in [Ben-Tal, 1980], consists in assigning different priorities to all the objectives at first. After that, the feasible solutions are compared according to the objective with the highest priority. Whenever the optimums set is found, the next objective function is considered and an optimization process is performed again on the optimum set only. The process is continued according to the importance ordering until all the objectives are considered. The main disadvantage of this approach is that the first objective is privileged, and many good solutions for other objectives might be exhibited if they do not fit well the first objective.
- Vector Evaluated Genetic Algorithm (VEGA) VEGA is an early evolutionary technique implemented in [Schaffer, 1985] following a theoretical suggestion made by Rosenberg in 1967. VEGA uses a genetic method to optimize a multi-criteria problem. Having n objective functions and i feasible solutions, n sub populations are created by selecting i/n best individuals for each objective n. After that, parents are chosen from two different sub populations (every parent is optimal according to a certain objective), and some crossover and mutation operators are applied to create offspring populations as in any classical genetic algorithm. In spite of the interesting results of VEGA, the drawback of this method is that the individuals which are very good for one objective are privileged at the expense of the individuals which are good for all the objectives and not for one of them. In fact, these exhibited individuals are the ones we search for in multi-criteria optimization.

To the best of our knowledge, this approach was not used in MIS path planning problems.

Dominance-based approaches

Contrary to the previous approaches, in which the weights assignment (in the first one) or objectives ordering (in the second), can significantly affect the optimization results. Dominance-based approach consider treating all the objectives at the same time without a subjective importance bias. The concept has been introduced by the italian economist *Vilfredo Pareto*[1] [Pareto, 1919], and is called *Pareto-based* approach after his name. Pareto suggested that : *for multi-criteria problems, a single optimal solution does not exist. Instead, a set of optimal solutions could be found.* Let us introduce some definitions followed by an example to clarify Pareto optimality :

Definition 2.4.1 Dominance

We define *dom* as the dominance relationship between two individuals x and y of the solution space $\mathcal{S}$ for a set of n objective functions f_i as follows :

$$\begin{aligned}&\forall \quad x, y \in \mathcal{S}\\ &x \quad dom \quad y \quad \Longleftrightarrow\\ &(\quad \forall i \in [1..n] \quad , \quad f_i(x) \leq f_i(y) \quad \vee \quad \exists i \in [1..n] \quad , \quad f_i(x) < f_i(y) \quad)\end{aligned}$$

Definition 2.4.2 Strict dominance

The dominance is considered as strict when :

$$\begin{aligned}&\forall \quad x, y \in \mathcal{S}\\ &x \quad dom \quad y \quad \Longleftrightarrow \forall i \in [1..n] \quad , \quad f_i(x) < f_i(y)\end{aligned}$$

Definition 2.4.3 Pareto optimal solution

A solution x is Pareto optimal if it is not dominated by any other in the solution space $\mathcal{S}$

$$x \in \mathcal{S} \quad \text{is Pareto optimal} \quad \Longleftrightarrow \quad \forall \quad y \in \mathcal{S} \quad , \quad \neg(y \quad dom \quad x)$$

Definition 2.4.4 Pareto front $\mathcal{F}$

We call the set of all Pareto optimal solutions a Pareto front $\mathcal{F}$. Inside the front, no solution dominates another.

$$x \in \mathcal{F} \quad \Longleftrightarrow \quad \forall \quad y \in \mathcal{F} \quad , \quad \neg(y \quad dom \quad x) \quad \vee \quad \neg(x \quad dom \quad y)$$

Example 2.4.1 Let's consider the problem of choosing a bike depending on two criteria (for simplicity reasons) : cost and weight. We would like to have a light bike with a low price, so the objective functions need to be minimized in this example.

Bikes made of titanium are lighter than those made of steel. Consequently, they are more expensive. According to Pareto, a trade-off between the price and the weight should be established. Fig. 2.7 illustrates the choices which are Pareto optimum, located on an imaginary line which is called Pareto front $\mathcal{F}$.

This different approach of optimization has been used in many domains such as economics, finance, optimal control, electronics, chemical engineering, etc. Nevertheless, it has been less practiced in the surgical domain for preoperative planning. In RFA, [Seitel et al., 2011] opted for a Pareto-based method to remove the bias

---

[1] Vilfredo Federico Damaso Pareto : an Italian engineer and economist who introduced the concept of Pareto efficiency in 1896.

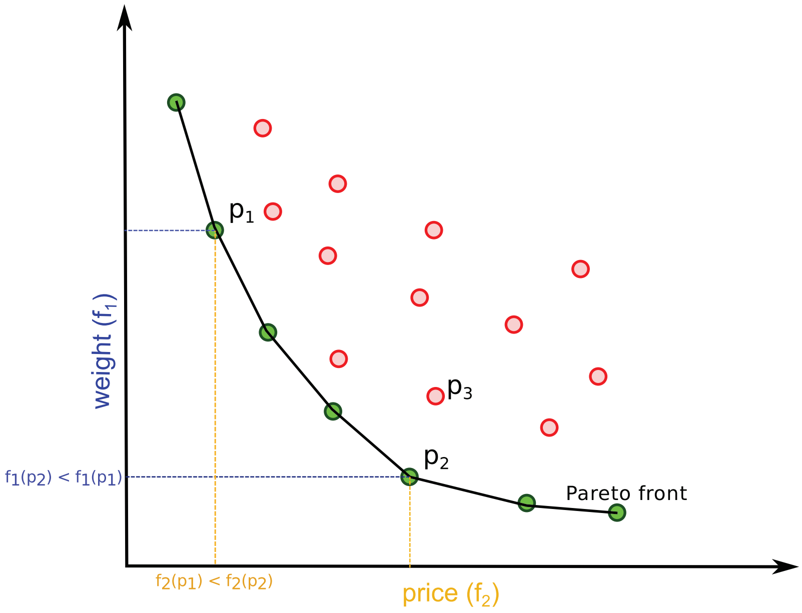

FIGURE 2.7 – Circles represent all the available bikes, among which the most optimal ones are located on the Pareto front (green points). Points p_1 and p_2 are both considered as optimal because none of them dominates the other : While p_1 is better for the price, it is worse for the weight and conversely. Point p_3 is not on the front because it is dominated by several points on the front including p_2.

of the common weighted-sum approach. They proposed a number of optimal trajectories and the definitive choice is in the hands of the surgeon. Another recent study proposed by [Schumann et al., 2015] introduced Pareto approach as well. To the best of our knowledge, dominance-based methods have not been yet addressed in the neurosurgery domain, and no study compared the quantitative or qualitative difference of using them in this field.

Discussion

We conclude this chapter by recalling the main focus of this work. In the presented literature for preoperative path planning, we observe that there are still many challenges to be addressed in order to increase the safety and efficiency of the different procedures, and consequently, obtaining better outcomes.

Basically, we are interested in the problems introduced in Section 1.2. We recall the two issues : intra-operative deformation, and multi objective optimization.

Firstly, we propose an automatic patient-specific preoperative path planning methods in MIS which accounts for different type of intra-operative deformation. The planning is designed for a 3D environment containing obstacles, and for both rectilinear and curved paths.

Secondly, we propose a multi-objective optimization approach based on Pareto optimality and efficient evolutionary algorithms, and a study to compare the methods.

Finally, we highlight that in this work, we address two interventions, the RFA of hepatic tumors, and the DBS neurosurgery procedure on which we performed all our test. At the same time, our methods are not restricted to them.

3

PLANNING IN STATIC ENVIRONMENTS

"Well begun is half done."
- Aristotle

In this chapter, we will briefly explain an existing preoperative planning solver in static conditions, and on which we have been relied in this work. We emphasize that the work presented in this chapter is not conducted during this thesis, but it is essential to enable us introducing our methods later. We present the preoperative path planning in static environments : the formalization of the surgical rules, the optimization approach, and a set of definitions/notations employed over the entire work.

3.1 Introduction

The approaches presented in this manuscript are based on early works published by Essert et al. in our research group between 2003 and 2011. In this chapter, we briefly introduce them and the basic notions for a better understanding of the next chapters.

Surgeons usually constitute their planning strategy by applying a number of surgical rules. When asked about how they plan, they express the rules in a natural language. Therefore, a knowledge formalization is required to represent the rules for the machine. Formalizing the rules based on geometric terms and operations is a convenient approach to such problems since that the patient's information are expressed as a 3D geometric model constructed from the patient's images. In their work, Essert et al. proposed a generic approach to formalize surgical rules using a set of geometric types (points, lines, forms, etc), combined with a set of operators (boolean, numeric, geometric, or other operators specific to the problem), and terms. Known for its flexibility, efficiency, and popularity, the XML language has been chosen to formulate the surgical rules using the terms, types, and operators. Appendix A is an example of constraint files.

At first, the studies were conducted on RFA for hepatic tumors in order to find the optimal path for the ablation probes. The method being generic, they have extended it later to the neurosurgery domain for DBS interventions. However, their work was implemented in static conditions assuming that no deformation will happen during the intervention.

3.2 Surgical rules formalization

Depending on the targeted intervention, a number of interviews were held with the surgeons in order to get a description about the rules they apply when making a path planning in their appropriate ways. The surgical knowledge was formalized based on geometric constraints that translate the intervention rules to a meaningful machine language. The surgical constraints were classified into two main categories : *"strict"* or *"hard"* when they should be completely fulfilled, and *"soft"* when they should be satisfied at best.

3.2.1 Strict (or hard) constraints

Among the hard constraints, the main ones concern the safety of the intervention, and involve the avoidance of surrounding anatomical structures, or subjection to a maximal length allowed for the tool's path.

In the case of thermal ablation of hepatic tumors the formalized hard constraints were the following :

- the trajectory length, which is the distance between the target center and the needle entry point, must be smaller than the needle length.
- the thermal ablation zone of the tip of the needle should cover the tumor shape in addition to a security margin of healthy tissue to avoid recurrence.
- the needle can not penetrate a rib.

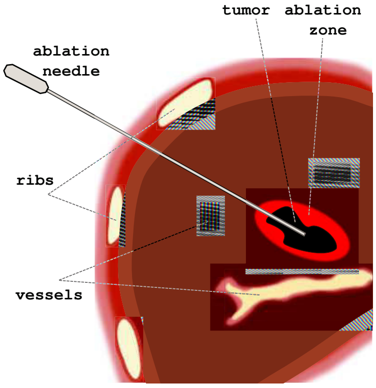

Figure 3.1 – A sagittal slice in a human liver illustrates : the vessels, the ribs, a tumor, and a thermal ablation needle with a theoretical ellipsoidal ablation zone.

- the needle path should not cross a vessel.

Figure 3.1 illustrates a needle trajectory which fulfills the aforementioned hard constraints.

Respectively, in the case of DBS procedures the hard constraints were :

- the trajectory length, which is the distance between the target center and the electrode entry point, must be smaller than the electrode's length.
- the trajectory should not cross any vessel (vessels are embedded in sulci).
- the trajectory should not cross the ventricles.

Figure 3.2 illustrates an electrode trajectory which fulfills the mentioned hard constraints.

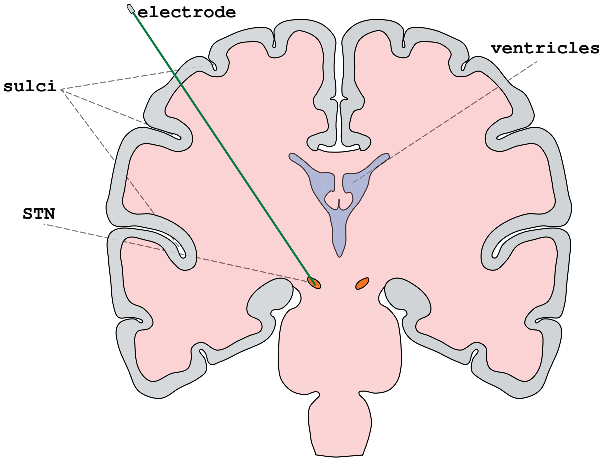

Figure 3.2 – An axial slice in a human brain illustrates : the sulci, the ventricles, the subthalmic nuculus, and a DBS electrode.

3.2.2 Soft constraints

Soft constraints are to optimize at best : keeping the trajectory as far as possible from the risky anatomical structures, and minimizing the insertion depth.

In the case of thermal ablation of hepatic tumors the following constraints have to be optimized :

1- Maximizing the distance between the needle path and the vessels.

$$f_{D_V}(\mathbf{T}) = \text{Max}\left[\frac{D_{minV} - dist(\mathbf{T}, V)}{D_{minV}}, 0\right] \tag{3.2.1a}$$

where D_{minV} is $5mm$, T is the evaluated trajectory, V is the portal vein, and $dist(\mathbf{T}, V)$ is the distance between the needle path and the vessels.

2- Maximizing the distance between the needle path and the ribs.

$$f_{D_R}(\mathbf{T}) = \text{Max}\left[\frac{D_{minR} - dist(\mathbf{T}, R)}{D_{minR}}, 0\right] \tag{3.2.1b}$$

where D_{minR} is $5mm$, T is the evaluated trajectory, R refers to the ribs, and $dist(\mathbf{T}, R)$ is the distance between the needle path and the ribs.

3- Minimizing the volume of ablated healthy tissue while destroying all the malicious tissues in addition to a security margin of healthy tissue (illustration in 3.3).

$$f_{ablation}(\mathbf{T}) = \frac{volume(ablation) - volume(tumor)}{val \times volume(tumor)} \tag{3.2.1c}$$

where $volume(ablation), volume(tumor)$ are the volumes of the ablation and the tumor, and $val = 3$ is an empirical value which ensures a good coverage of the tumor.

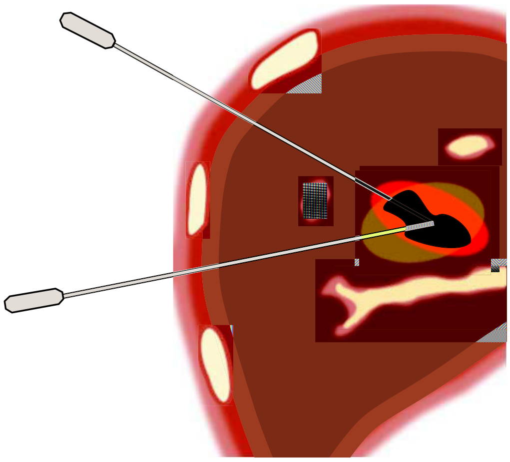

FIGURE 3.3 – The red ablation volume is preferred to the yellow one because both of them cover the tumor with a security margin, but the red volume preserves more healthy cells than the yellow.

In the case of DBS procedures, the following constraints have to be optimized :

1- Proximity to a “Standard Trajectory” : the orientation of the electrode, computed as the proximity to a standard trajectory defined by expert neurosurgeons and commonly used in the commercial platforms (illustration in Fig. 3.4).

$$f_{ST}(\mathbf{T}) = \frac{angle(\mathbf{T}, ST)}{90} \tag{3.2.1d}$$

where $angle(\mathbf{T}, ST)$ is the angle between the candidate trajectory $\mathbf{T}$

2- Distance from the electrode to the vessels, computed as the distance to the closest cortical sulci in which the vessels usually are located.

$$f_{D_S}(\mathbf{T}) = \text{Max}\left[\frac{D_{minS} - dist(\mathbf{T}, S)}{D_{minS}}, 0\right] \tag{3.2.1e}$$

where D_{minS} is $5mm$, $\mathbf{T}$ is the evaluated trajectory and S the sulci.

3- Distance from the electrode to the ventricles.

$$f_{D_V}(\mathbf{T}) = \text{Max}\left[\frac{D_{minV} - dist(\mathbf{T}, V)}{D_{minV}}, 0\right] \tag{3.2.1f}$$

where D_{minV} is $35mm$, T is the evaluated trajectory and V the ventricles.

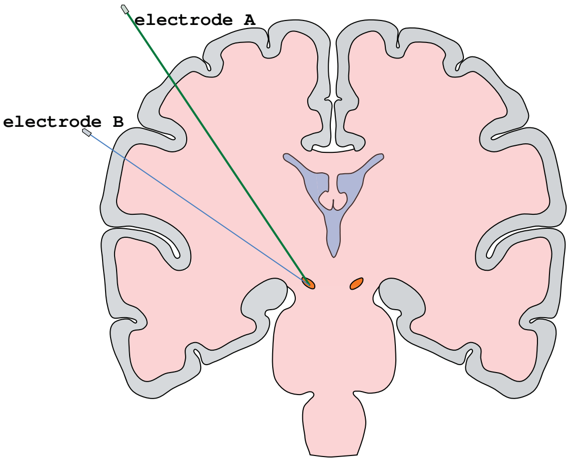

FIGURE 3.4 – Two possible paths which fulfill the hard constraints : while electrode A satisfies better the standard trajectory soft constraint, electrode B satisfies better the distance from ventricles.

In addition, an initial insertion zone can be provided to restrict the search space for practical, medical, or aesthetic reasons.

3.3 Definitions and notations

In the following, we give some definitions with a list of vocabulary and notations that will be extensively used in this work :

strict or hard constraint is denoted by HC, H stands for "hard".

soft constraint is denoted by SC.

obstacle is denoted by $\mathcal{O}$, it is defined as an anatomical structure which should not be crossed by the trajectory of the surgical tool.

planning refers to the automatic definition of an optimal *planning strategy* for the surgical tool before the intervention.

static conditions or *static environment*, denoted E_S, refers to the solving process which is performed on a static 3D geometric scene reconstructed from still preoperative images assuming that no deformation will happen during the intervention.

dynamic conditions or *dynamic environment*, denoted E_D, refers to the solving process which predicts the intra-operative deformation and takes it into account during the preoperative planning phase.

planning strategy or *insertion settings*, denoted IS and is composed of three entities : an insertion point P on the skin represented by a vector of coordinates $\mathbf{x}$, a direction $\mathbf{v}$ represented by a pair of angles (α, β), and an insertion depth d. The depth d can be deduced from the entry point and the target, therefore the planning strategy is represented by a pair $(P, \mathbf{v})$ containing an entry point and an insertion direction. These parameters constitute the strategy the surgeon determines preoperatively during the planning phase, to use as starting indications to insert the surgical tool towards the target.

trajectory, denoted T, is defined by the geometry of the surgical tool inside the body/brain after its insertion when following a given set IS. The word *"path"* is used alternately in this work.

feasible trajectory is a safe trajectory which goes from an entry/insertion point on the skin to the center of the target, and satisfies all the hard constraints HC.

feasible insertion settings are a pair $(P, \mathbf{v})$ that leads to a feasible trajectory.

initial solution space, denoted $\mathcal{U}_{init}$, is the union of all the insertion settings.

feasible solution space, denoted $\mathcal{U}$, is the union of all the feasible insertion settings. For the sake of simplicity, when *solution space* is mentioned in this manuscript, it refers to the *feasible solution space.*

initial insertion zone, denoted $\mathcal{I}_{init}$ is the union of all the entry points of all the insertion settings in $\mathcal{U}_{init}$, $\mathcal{I}_{init}$ is a continuous space. It is a projection of $\mathcal{U}_{init}$ on a surface represented by an initial skin portion on the patient.

feasible insertion zone, denoted $\mathcal{I}$ is the union of all the entry points of the feasible insertion settings, $\mathcal{I}$ is also a continuous space. For the sake of simplicity, when *insertion zone* is mentioned in this manuscript, it refers to the *feasible insertion zone.*

search space, denoted $\mathcal{S}$ is a discretization of $\mathcal{I}$, in which we search the optimal entry point(s).

3.4 The optimization approach

In order to optimize the set of soft constraints explained above either in the case of RFA or of DBS, the multi-criteria optimization problem is translated to a mono-criteria one using an aggregative approach : the weighted sum. So far, the multiple soft constraint are aggregated in a single cost function f to be optimized. For n soft constraints, f is expressed by the equation :

$$f = \frac{\sum_{c=1}^{n} w_c . f_c}{\sum_{c=1}^{n} w_c} \tag{3.4.1g}$$

Where c denotes a soft constraint, f_c its objective function, and w_c its corresponding weight value. The weights reflect the importance of the associated surgical rules, and are fixed after discussions with surgeons.

Afterwards, the geometric constraints are solved within a scene containing 3D triangular meshes reconstructed from the patient's MR and/or CT images. The objective is to locate a feasible, safe and optimal position for a *ray* from the skin to the target representing the trajectory of insertion of the electrode in DBS case or of the needle in RFA.

In a formal way, the purpose of the optimization is to automatically find $\mathbf{x}_{Sopt}$ and $\mathbf{v}_{Sopt}$ such that the resulting trajectory T_{Sopt} is feasible and $f(\mathbf{x}_{Sopt}, \mathbf{v}_{Sopt})$ is minimal. S refers to static conditions. To this end, the solver uses an optimization process in three phases. Basically, phase 1 ensures the feasibility of the trajectory and phases 2 and 3 minimize $f(\mathbf{x}_{Sopt}, \mathbf{v}_{Sopt})$. The three phases are described below :

1. **Computation of the feasible solution space**. In this phase, the hard constraints are solved to keep only the *feasible solution space* $\mathcal{U}$ containing all the IS leading to feasible trajectories. The solution space is stored and displayed as a *feasible insertion zone* $\mathcal{I}$, which is a subset of the surface of the skin representing the *feasible insertion points* (intersections between the feasible trajectories and the skin). An illustration of $\mathcal{I}$ is shown in Fig.3.5a and Fig.3.6a for RFA and DBS examples respectively.
2. **Initialization of the optimization**. In this phase, a rough estimation of objective function f is performed on a search space $\mathcal{S}$ computed on $\mathcal{I}$. The result is shown as a color map on $\mathcal{I}$, where the points are colored using a gradient from blue for the best point P_{min} (with a minimal evaluation of f) to red for the worst point P_{max} (with a maximal evaluation of f). Afterwards, m connected components CC_k are extracted from $\mathcal{I}$, containing only insertion points $P_{CC} \in \mathcal{I}$ such that $f(P_{CC}) < f(P_{min}) + \varepsilon_1$, where ε_1 is a small threshold computed so that several (2 to 5) small-sized connected components are obtained. In other words, the m most interesting areas of $\mathcal{I}$ are chosen.
3. **Optimization**. In this last phase, starting from m initial candidates IS_k in which points P_k are located at the barycenter of each CC_k, a local optimization algorithm (Nelder–Mead [Nelder and Mead, 1965]) is applied to refine $\mathbf{x}$ and $\mathbf{v}$, in order to obtain one optimal pair $(\mathbf{x}_{Sopt_k}, \mathbf{v}_{Sopt_k})$ minimizing f per connected component k. Each pair represents a locally optimal set of insertion settings IS_{Sopt_k} leading to an optimal trajectory T_{Sopt_k}. An illustration of the resulting color maps for both RFA and DBS is given in Fig.3.5b and 3.6b respectively.

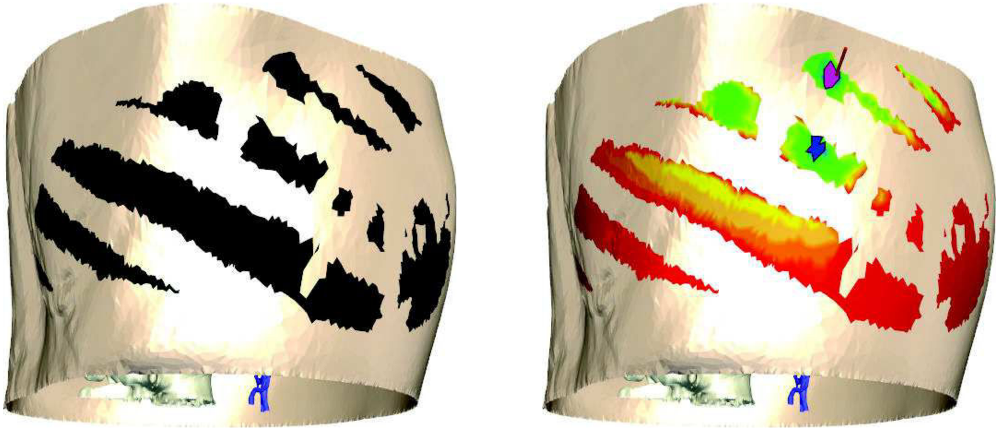

(a) feasible insertion zone $\mathcal{I}$ (b) color map

FIGURE 3.5 – The different phases of planning in static conditions. In (a) the insertion zone $\mathcal{I}$ is delineated. In (b), the color map shows the best locations of $\mathcal{I}$ in blue, medium in a gradient from green to orange, and worst in red. Two connected components CC_1 and CC_2 are delineated on $\mathcal{I}$ and represent the most interesting areas. The red cylinder represents the optimal IS.

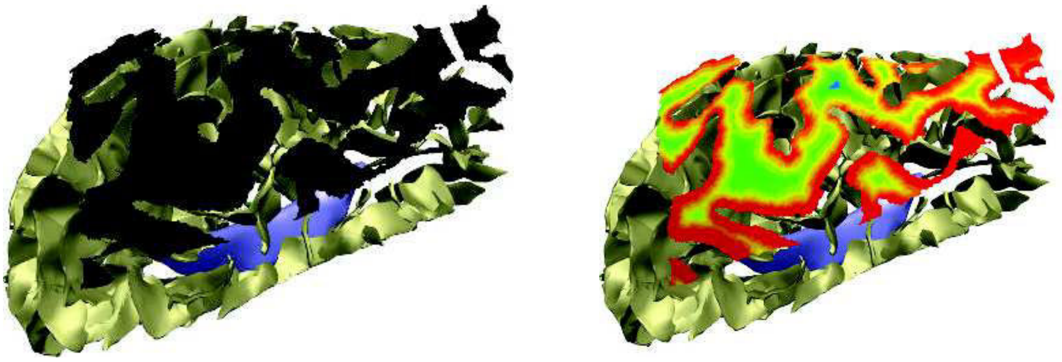

(a) feasible insertion zone $\mathcal{I}$ (b) color map

FIGURE 3.6 – Illustration of the different phases of planning in static conditions. In (a) the insertion zone $\mathcal{I}$ is delineated, containing only feasible entry points satisfying the hard constraints In b), the color map showing the degree of satisfaction of the soft constraints by each feasible entry point with the best zones are in blue and the worst in red.

To summarize

The planning algorithm described above was conducted in our research team [IGG, nd]. In fact, it was implemented for planning in static conditions. However, it is characterized by a high level of generality which enabled us to take it a reliable start point for our work in this thesis. We chose to dedicate a small chapter to it to avoid mixing between our own and this one. In the rest of this manuscript, we will present the our proper methods in both dynamic conditions and optimization techniques. Let us finally note that the definitions and notations presented in 3.3 will be reused throughout the rest of the manuscript.

4

PREOPERATIVE TRAJECTORY PLANNING FOR PERCUTANEOUS PROCEDURES IN DEFORMABLE CONDITIONS

> *"All art is a question of selection whereby one exctracts the needle of truth from the haystack of experience."*
> *- Thomas Rogers*

In this chapter, we present a novel approach of preoperative path planning for percutaneous procedures. Our approach is based on physics and geometry. We describe the two main parts : the biomechanical simulator and the planning solver. Then, we explain our dedicated algorithm *"Haystack"*, and compare its performance with two other search techniques. We describe the experimental scenario and tests, and we report the results with a discussion.

4.1 Introduction

Percutaneous needle insertion is one of the most common minimally invasive procedure. As well for diagnostic such as biopsy or therapeutic such as tumors ablation in its different forms (RFA, cryablation, radiofrequency waves), they rely on the same concept of interventional technique. A surgical tool is inserted inside the body with a planning strategy to reach a target, usually under the guidance of an image modality (US, CT, or MR).

There exists different types and models of surgical needles that differ in their materials, dimensions, tip shapes, the shape and volume of the ablation zone effect they can generate in case of RFA or the iceballs in cryoablation, etc.

The shape of the tip influences the behavior of the needle while penetrating inside the body. When using symmetric or beveled tip needles, needle naturally deflects from a straight path during insertion. This deflection is due to the interaction forces generated between the needle and the surrounding tissue, but also to the inhomogeneity of the penetrated tissues.

Thin flexible needles were introduced later basically to reduce patient discomfort [Grant and Neuberger, 1999]. Their flexibility enables curved needle paths and allows reaching locations which are unreachable by rigid needles. Tissue deformation may be reduced thanks to the flexibility, but planning their paths is much more challenging. Fig. 4.1 illustrates a commercial flexible needle from [Ang, 1988].

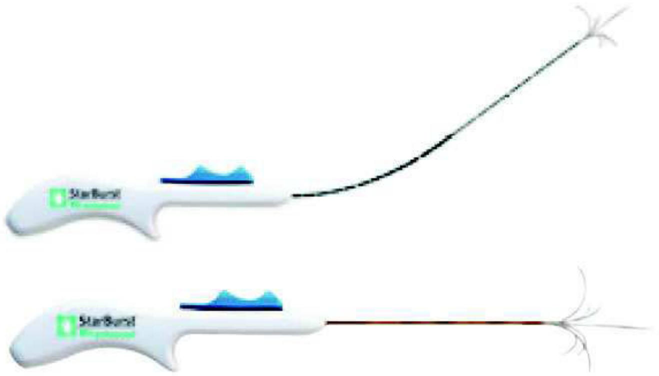

FIGURE 4.1 – StarBurst Xlie RFA flexible needle available with lengths 12 and 25 cm. with a bending capacity up to 90° from [Ang, 1988].

After introducing the main characteristics of surgical needles, let us note that our study focuses on flexible needles with a symmetric tip. We recall that path planning in static conditions has some limitations which were explained earlier in Chapter 1, Section 1.2.2. Indeed, using flexible needles makes it more challenging since that the planning is based on the analysis of preoperative images with the assumption that the needle is rigid and that it will follow a straight path to the target with the absence of soft tissue deformation. However, the flexible needle bends during the insertion and follows a curved path, causing the tissue to deform as well. We confront this problem by introducing a novel preoperative planning approach for flexible needles in dynamic conditions.

4.2 Planning in deformable conditions

We propose a preoperative path planning based on both geometric and physical models. We anticipate the deformation by running biomechanical simulations of the flexible needle insertion inside the abdomen, and we iteratively inject this valuable physics information into an optimization solver to perform a more realistic planning compatible with dynamic conditions. Basically, our planning approach involves two main aspects : the biomechanical modeling and simulation, and the planning algorithm.

4.2.1 Biomechanical modeling and simulation

Performing realistic simulations requires an efficient physical model of the concerned objects. In percutaneous procedures, the needle is regarded as a dynamic moving body penetrating a soft deformable body. We introduce a numerical modeling based on finite element method for both the soft tissue and the needle, with a constraint-based modeling to simulate the interaction between them.

It should be emphasized that in the biomechanical modeling and simulation field (unlike in planning), *by "constraint" we mean a physical coupling between two deformable objects (e. g. tissue and needle) which is a mathematical representation of mechanical interactions.* This should not be confused with the hard and soft constraints that formally represent the surgical rules.

The deformed models of the liver and needle in this section were developed by *Igor Peterlik* during this work based on his previous approach [Peterlik et al., 2011].

Soft tissue model

A dynamic system is mathematically represented by :

$$\mathbf{M}\ddot{\mathbf{q}} = \mathbf{f}(\mathbf{q}, \dot{\mathbf{q}}) + \mathbf{H}^{\top}\lambda \tag{4.2.1a}$$

where $\ddot{\mathbf{q}}, \mathbf{q}, \dot{\mathbf{q}}, \mathbf{f}$ are respectively the acceleration, position, velocity and force vectors and $\mathbf{M}$ stands for the mass matrix. Since a constraint-based dynamics is considered to represent the interaction between the objects as will be explained later in Section 4.2.1, vector λ stands for Lagrange multipliers which represent the unknown response forces, and $\mathbf{H}^T$ provides the direction of the interaction constraints.

The chosen temporal integration is based on implicit backward Euler scheme [Baraff and Witkin, 1998] :

$$\dot{\mathbf{q}}^{t+h} = \dot{\mathbf{q}}^{t} + h\ddot{\mathbf{q}}^{t+h} \tag{4.2.1b}$$

$$\mathbf{q}^{t+h} = \mathbf{q}^{t} + h\dot{\mathbf{q}}^{t+h} \tag{4.2.1c}$$

where the acceleration $\ddot{\mathbf{q}}^{t+h}$ is computed as the solution of a non-linear system :

$$\mathbf{M}\ddot{\mathbf{q}}^{t+h} = \mathbf{f}(\mathbf{q}^{t+h}, \dot{\mathbf{q}}^{t+h}) + \mathbf{H}^{T}\lambda. \tag{4.2.1d}$$

In Eq. 4.2.1d, $\mathbf{f}$ is most generally a non-linear function that represents the sum of internal and external forces.

Nevertheless, the forces applied due to mechanical interactions are not included in $\mathbf{f}$. Therefore, the first order approximation ,which is a single linearization per time step, is applied based on Taylor series expansion :

$$\mathbf{f}(\mathbf{q}^{t+h}, \dot{\mathbf{q}}^{t+h}) \approx \mathbf{f}(\mathbf{q}^{t}, \dot{\mathbf{q}}^{t}) + \mathbf{K}(\mathbf{q}^{t+h} - \mathbf{q}^{t}) + \mathbf{B}(\dot{\mathbf{q}}^{t+h} - \dot{\mathbf{q}}^{t}) \tag{4.2.1e}$$

where $\mathbf{K}$ is the *stiffness* matrix and $\mathbf{B}$ the *damping* matrix.

In both tissue and needle, the computation of the stiffness matrix is based on a corotational FE formulation which allows for large displacements [Felippa and Haugen, 2005]. In the case of the tissue, the global stiffness matrix $\mathbf{K}_t$ is assembled from local element stiffness matrices $\mathbf{K}_{te}$:

$$\mathbf{K}_{te} = \mathbf{R}_{te}^{\top}\{\int_{V_{te}} \mathbf{C}_{te}^{\top}\mathbf{D}_{te}\mathbf{C}_{te} dV\}\mathbf{R}_{te} \tag{4.2.1f}$$

where for each tissue element te : $\mathbf{B}_{te}$ is the strain-displacement matrix, $\mathbf{D}_{te}$ is the stress-strain matrix and $\mathbf{R}_{te}$ is a rotation matrix derived in the co-rotational formulation. While both $\mathbf{B}_{te}$ and $\mathbf{D}_{te}$ are constant during the simulation, $\mathbf{R}_{te}$ must be updated in each step. In our simulations, the domain of tissues is discretized with a mesh composed of P1 tetrahedral elements, each having four nodes with three degrees of freedom (DoF). Therefore, $\mathbf{K}_{te}$ is a 12×12 matrix organized in 3×3 blocks. Further details about the computation of each component can be found in [Nesme et al., 2005].

Flexible needle model

Similarly, the needle stiffness matrix $\mathbf{K}_n$ is assembled from local matrices $\mathbf{K}_{ne}$:

$$\mathbf{K}_{ne} = \mathbf{R}_{ne}^{\top}\{\int_{V_{ne}} \mathbf{C}_{ne}^{\top}\mathbf{D}_{ne}\mathbf{C}_{ne} dV\}\mathbf{R}_{ne} \tag{4.2.1g}$$

where $\mathbf{R}_{ne}$, $\mathbf{C}_{ne}$ and $\mathbf{D}_{ne}$ are respectively rotational, strain-displacement and stress-strain matrices computed for each needle element ne. The needle model is based on Timoshenko beam formulation which accounts for positional as well as rotational degrees of freedom. Therefore, each needle element is composed of two nodes, each having 6 DoFs. Thus, $\mathbf{K}_{ne}$ is a 12×12 matrix composed of two 6×6 blocks located on the main diagonal.

For both needle and tissue, the damping matrix $\mathbf{B}$ in Eq. 4.2.1e is approximated using *Rayleigh damping* computed as $\mathbf{B} = r_M\mathbf{M} + r_K\mathbf{K}$ where r_M and r_K are Rayleigh mass and Rayleigh stiffness coefficients.
Substituting (4.2.1b) and (4.2.1e) into (4.2.1d) provides the final linearized system :

$$\underbrace{\left(\mathbf{M} - h\mathbf{B} - h^2\mathbf{K}\right)}_{\mathbf{A}} \mathbf{d}\dot{\mathbf{q}} = \underbrace{h\mathbf{f}(\mathbf{q}^{t}, \dot{\mathbf{q}}^{t}) + h^2\mathbf{K}\dot{\mathbf{q}}^{t}}_{\mathbf{b}} + \mathbf{H}^T\lambda \tag{4.2.1h}$$

where $\mathbf{d}\dot{\mathbf{q}} = h\ddot{\mathbf{q}} = \dot{\mathbf{q}}^{t+h} - \dot{\mathbf{q}}^{t}$.

Needle–tissue interaction

Constraint-based approach is an efficient method for modeling the interaction independent from the needle and tissue models, and which does not require remeshing to calculate the deformation. Two different types of constraints must be considered for correct modeling of needle–tissue interaction [Peterlik et al., 2011]. First, before entering the tissue, the needle tip is in contact with its surface. Mathematically, this interaction is represented by a unilateral constraint $\Psi(\mathbf{q}_n, \mathbf{q}_t) \geq 0$. As soon as the needle enters the tissue, bilateral sliding constraints are created along the trajectory of the needle : $\Phi(\mathbf{q}_n, \mathbf{q}_t) = 0$. Both Ψ and Φ depend on actual positions of both needle and tissue nodes ($\mathbf{q}_n$ and $\mathbf{q}_t$, respectively) and can be non-linear, e. g. when friction is considered. Moreover, they depend on additional parameters such as coefficient of friction and force thresholds needed to puncture the tissue surface and to advance the needle inside the tissue.

To impose these constraints to the behavior of both needle and tissue, we use Lagrange multipliers and a single linearization per time step. A new value of the multipliers needs λ is to be computed during each simulation step. However, for interaction including deformations, there is often a temporal coherency on the multipliers values. Thus, we can provide an estimate $\tilde{\lambda}$ at the beginning of each time step and compute a correction $\Delta\lambda$ so that $\lambda = \tilde{\lambda} + \Delta\lambda$. For both interacting components, equation 4.2.1h is then replaced by :

$$\begin{aligned} \mathbf{A}_t \mathbf{d}\dot{\mathbf{q}}_t &= \mathbf{b}_t + \mathbf{H}_t^T(\tilde{\lambda} + \Delta\lambda) \\ \mathbf{A}_n \mathbf{d}\dot{\mathbf{q}}_n &= \mathbf{b}_n + \mathbf{H}_n^T(\tilde{\lambda} + \Delta\lambda) \end{aligned} \tag{4.2.1i}$$

where :

$$\mathbf{H}_t = [\frac{\delta\Phi}{\delta\mathbf{q}_t} \ ; \ \frac{\delta\Psi}{\delta\mathbf{q}_t}] \qquad \mathbf{H}_n = [\frac{\delta\Phi}{\delta\mathbf{q}_n} \ ; \ \frac{\delta\Psi}{\delta\mathbf{q}_n}]. \tag{4.2.1j}$$

Given the equations above, the behavior of the constrained system composed of the tissue and needle is modelled in three steps :

Step 1, predictive motion : interacting objects are solved independently while setting $\Delta\lambda = 0$ (i.e. $\tilde{\lambda} = \lambda^t$). We obtain what we call a *predictive motion* $\mathbf{d}\dot{\mathbf{q}}_t^{\mathrm{p}}$ and $\mathbf{d}\dot{\mathbf{q}}_n^{\mathrm{p}}$ for each object. After the integration, we obtain $\mathbf{q}_t^{\mathrm{p}}$ and $\mathbf{q}_n^{\mathrm{p}}$. In this step, each object is solved independently using a dedicated solver which assembles the system matrices $\mathbf{A}_t$ and $\mathbf{A}_n$ and computes their factorizations.

Step 2, constraint solving : the constraint laws Φ and Ψ are linearized as follows :

$$\underbrace{\begin{bmatrix} \Phi(\mathbf{q}_t^{t+h}, \mathbf{q}_n^{t+h}) \\ \Psi(\mathbf{q}_t^{t+h}, \mathbf{q}_n^{t+h}) \end{bmatrix}}_{\boldsymbol{\delta}^{t+h}} = \underbrace{\begin{bmatrix} \Phi(\mathbf{q}_t^{\mathrm{p}}, \mathbf{q}_n^{\mathrm{p}}) \\ \Psi(\mathbf{q}_t^{\mathrm{p}}, \mathbf{q}_n^{\mathrm{p}}) \end{bmatrix}}_{\boldsymbol{\delta}^{\mathrm{p}}} + h\mathbf{H}_t \mathbf{d}\dot{\mathbf{q}}_t^{\mathrm{c}} + h\mathbf{H}_n \mathbf{d}\dot{\mathbf{q}}_n^{\mathrm{c}} \tag{4.2.1k}$$

With $\mathbf{d}\dot{\mathbf{q}}_t^{\mathrm{c}}$ and $\mathbf{d}\dot{\mathbf{q}}_n^{\mathrm{c}}$ being the unknown corrective motions when solving equation 4.2.1i with $\mathbf{b}_t = \mathbf{b}_n = \tilde{\lambda} = 0$. By gathering equations 4.2.1i and 4.2.1k, we have :

$$\boldsymbol{\delta}^{t+h} = \boldsymbol{\delta}^{\mathrm{p}} + \underbrace{h \left[\mathbf{H}_t \mathbf{A}_t^{-1} \mathbf{H}_t^T + \mathbf{H}_n \mathbf{A}_n^{-1} \mathbf{H}_n^T \right]}_{\mathbf{W}} \Delta\lambda \tag{4.2.1l}$$

We obtain the value of $\Delta\lambda$ using a projected Gauss-Seidel algorithm that iteratively checks and projects the various constraint laws contained in Φ and Ψ (see [Duriez et al., 2009]). During needle insertion, three main types of constraints are defined : first, a *surface puncture* constraint is used to penalize insertion through the surface (membrane) of the organ. The constraint allows for emulation of a membrane which is an anatomical feature of several abdominal organs, and is parametrized by a *puncture force* which is needed to penetrate the surface. Second, a *needle tip* constraint is defined in the tip of the needle as soon as it penetrates into the tissue. The constraint is parametrized by a *cutting force* which is must be applied as long as the needle tip is creating a new path inside the tissue. Finally, *needle shaft* constraint defined in the nodes of the needle along the shaft. This constraint guarantees that the shaft is following the trajectory created by the advancing tip. It is parametrized by *friction force* which is needed in order to overcome a static friction between the needle and the surrounding tissue.

Step 3, corrective motion : when the value of $\Delta\lambda$ is available, the corrective motion is computed as follows :

$$\begin{aligned} \mathbf{q}_t^{t+h} &= \mathbf{q}_t^{\mathrm{p}} + h\mathbf{d}\dot{\mathbf{q}}_t^{\mathrm{c}} \quad \text{with} \quad \mathbf{d}\dot{\mathbf{q}}_t^{\mathrm{c}} = \mathbf{A}_t^{-1}\mathbf{H}_t^T\Delta\lambda \\ \mathbf{q}_n^{t+h} &= \mathbf{q}_n^{\mathrm{p}} + h\mathbf{d}\dot{\mathbf{q}}_n^{\mathrm{c}} \quad \text{with} \quad \mathbf{d}\dot{\mathbf{q}}_n^{\mathrm{c}} = \mathbf{A}_n^{-1}\mathbf{H}_n^T\Delta\lambda \end{aligned} \tag{4.2.1m}$$

Although the Eq. 4.2.1l and 4.2.1m involve the inverses $\mathbf{A}_t^{-1}$ and $\mathbf{A}_n^{-1}$, which change at every time step because of the corotational formulation, we do not calculate the inverses explicitly, but we perform a back-substitution for each constraint using the factors of $\mathbf{A}_t$ and $\mathbf{A}_n$ computed in the predictive motion. Since this process is independent for each constraint, it can be parallelized or accelerated using CUDA as presented in [Courtecuisse et al., 2014].

This part of the work has been done in collaboration with Strasbourg University-Hospital Institute (IHU), during the IHU project *Haystack*. A biomechanical simulation module has been designed according to the above described methods, and implemented using the SOFA biomechanical simulation platform [Faure et al., 2012].

4.2.2 Geometric–based preoperative planning

Our planning algorithm is based on a *"generate and test"* approach. It is characterized by repeated, varied attempts which are continued until success, or until stop trying. In this heuristic approach of problem solving, we use tuning, repairing or obtaining knowledge to guide the method, such an approach is known also as *"guided empiricism"*.

Optimization algorithms have a wide spectrum to fit the enormous optimization problems around us. In general, any optimization algorithm requires a certain number of iterations to converge, and the choice of the appropriate method depends of many elements such as the nature of the problem and the allowed resources like time and precision. In our proposed planning, many biomechanical simulations have to be performed. A single simulation of the insertion process in a deformable environment requires a few seconds in our simulation module. To include estimations of deformations in the planning, a simulation has to be performed at each iteration of the optimization. This is relatively expensive in terms of time consuming. Therefore, the choice of a classic optimization algorithm would not allow for an overall process to be performed in a reasonable time compatible with clinical routine. This reason justifies our choice of a "generate and test" approach. After conducting some empirical tests, our design converged to a dedicated search algorithm capable of converging in a relatively low number of iterations to reduce the optimization global time.

Our search algorithm (so–called *"Haystack"* inspired from the well-known problem of finding a needle in a haystack and which is used to refer to something that is difficult to locate in a large space) is described in Algorithm 2. Its principle is to guide the new propositions of insertion settings IS at each iteration by tracking the movement of the target caused by deformation until reaching it.

We start by explaining the evaluation mechanism of the soft constraint concerned by the optimization algorithm.

Evaluation of the optimization functions

The search criteria concerned by the optimization are :

1- maximize the distance between the path and the vessels
2- maximize the distance between the path and the ribs
3- minimize the volume of ablation to preserve a maximum of healthy tissue

So far, for each soft constraint c, we associate a cost function $f_c : \mathbb{R}^5 \rightarrow [0,1]$ which means that for a given *feasible insertion setting* consisting of a pair $(P, \mathbf{v})$ and leading to a *feasible trajectory* that fulfills the hard constraints, f_c expresses the corresponding constraint as a numerical value to minimize. We note that when the constraint expresses a maximization problem, we formulate the function such that the problem is translated into a minimization problem.

After evaluating all the soft constraints, an *optimal trajectory* which is the *feasible trajectory* that minimizes an objective function $f : \mathbb{R}^5 \rightarrow [0,1]$ is formulated by aggregating all soft constraints. To each f_c we assigned a weighting factor w_c describing the importance given to a constraint c with respect to the others. Thus, f is expressed by the weighted sum :

$$f = \frac{\sum_{c=1}^{n} w_c . f_c}{\sum_{c=1}^{n} w_c} \tag{4.2.1n}$$

where $\sum_{c=1}^{n} w_c = 1$. For any trajectory T, the value of $f(T)$ expresses the quality of T : a lower $f(T)$ means a better T.

In the formalization of the soft constraints above, the evaluation of a constraint consists in applying a set of geometric operators with a number of operands representing the manipulated object.

For example, the constraint which represents the distance between the surgical tool and an obstacle (vessels or ribs) is formalized as follows :

```
<soft_constraint name="risk_obstacle"
    label="sc_risk1"
    minValue="0"
    maxValue="1" >
```

```
    max(divide(minus(security_distance,
                     distmin(toolTrajectory,obstacle)),
               security_distance),
        0 )
</soft_constraint>
```

The evaluation of the constraint is done based on a geometric solver. Geometrically, an *obstacle* is represented by a 3D polygonal mesh, and the $toolTrajectory$ is represented by a *ray* in the case of rigid needles which lead to a straight path, and the *distmin* operator calculates the euclidean distance between a ray and a set of triangles and returns the value to the solver.

In the case of flexible needles which bend during the insertion in dynamic conditions. Therefore, we oughted to define a "curve" model in the geometric server, and to re-implement some geometric operators concerning the curves.

Introducing new data structures

We model flexible needles by a number of 3D points representing a curved path (illustration in Fig.4.2). We introduced to the solver the geometric operators to be applied to a curved geometry. For a curved trajectory T modeled by k point p ; given an obstacle $\mathcal{O}$, the *distmin* operator which calculates the minimal distance between a $toolTrajectory$ and an *obstacle* is defined as :

$$distmin(T,\mathcal{O}) = Minimum[dist(p_i,\mathcal{O})] \tag{4.2.1o}$$

for $i : 1 \rightarrow k$, and *dist* calculates the distance between a point p_i and the nearest triangle in $\mathcal{O}$ using an Euclidean metric in the 3D space.

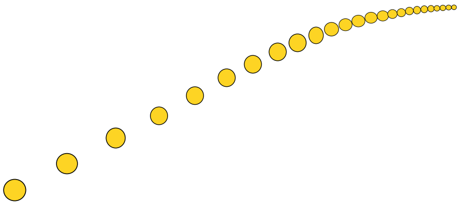

FIGURE 4.2 – Geometric representation to a flexible needle curved path by a set of 3D points

Now that, the needle geometric model with its operators are ready, Let us introduce the planning algorithm.

Haystack algorithm

Haystack algorithm is dedicated for path planning in a dynamic environment E_D. It extends the initial optimization algorithm for static environment E_S. Fig. 4.6 illustrates the complete optimization pipeline.

A first optimization is performed in static using the three phases 1, 2 and 3 described in Section 3.4, and optimal $\mathbf{x}_{Sopt}$ and $\mathbf{v}_{Sopt}$ leading to an optimal theoretical

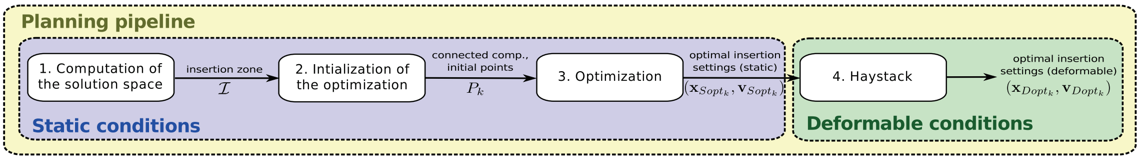

FIGURE 4.3 – Planning pipeling : the position of *Haystack* algorithm.

straight trajectory T_{Sopt} are calculated for the geometrical model G_S which is a surface mesh model reconstructed from the segmented images of the patient. However, in a deformable environment E_D, using $\mathbf{x}_{Sopt}$ and $\mathbf{v}_{Sopt}$ as insertion settings would lead to the deformation of G_S into a deformed geometry G_D and to a deformed trajectory T_D which could be curved and either miss the target or hit an obstacle.

The inputs of *Haystack* algorithm are $\mathbf{x}_0 = \mathbf{x}_{Sopt}$ and $\mathbf{v}_0 = \mathbf{v}_{Sopt}$, and the initial geometry G_S used as an initial model in the simulation module. At each iteration i, new candidate $\mathbf{x}_i$ and $\mathbf{v}_i$ are sent by the solver to the simulation module which computes the needle and tissue motions. The simulation module sends back the corresponding deformed anatomy G_{Di} and curved trajectory T_{Di}. The principle is to iteratively modify $\mathbf{x}_i$ and $\mathbf{v}_i$ by following the target movement until converging to $\mathbf{x}_{Dopt}$ and $\mathbf{v}_{Dopt}$ resulting in a deformed trajectory T_{Dopt} optimizing the soft constraints within E_D while being part of the feasible deformed paths. So, at each iteration the objective function f needs to be evaluated for the curved trajectory T_{Di} on the deformed anatomy G_{Di} and the hard constraints need to be checked.

When receiving a deformed model G_{Di}, the *Haystack* algorithm proposes the next candidates depending on the situation :

1. **Target tracking phase** : if T_{Di} could not reach the target (Fig. 4.4), then the objective is to reach it ; in this case, we iterate over translations of the insertion point or rotations of the insertion direction according to the distance or angle between T_{Di} and the target in the deformed model to compensate the movement, until the target is reached.

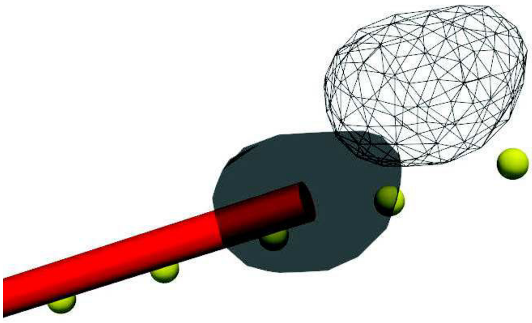

FIGURE 4.4 – deformed trajectory missed the deformed target (in wireframe)

2. **Refinement phase** : when T_{Di} could reach the target (Fig. 4.5), then the objective is to optimize the soft constraints ; in this case, we iterate over small translations of the insertion point or rotations of the insertion direction in order to stay within the target while optimizing the soft constraints in the deformed model. We stop when the improvement of the evaluation falls under a threshold ε_2, i.e. $f(T_{Di-1}) - f(T_{Di}) < \varepsilon_2$ or the number of simulations reached a maximum $iter_{max}$. Then T_{Di} is considered as the optimal trajectory T_{Dopt}.

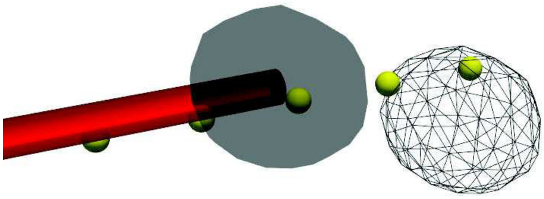

FIGURE 4.5 – deformed trajectory reached the deformed target (in wireframe)

It can happen that T_{Di} does not satisfy the hard constraints, *i.e.* is not a feasible deformed trajectory. For instance, T_{Di} may hit a vessel. In this case, T_{Di} is discarded by adding a penalty to $f(T_{Di})$ and the iterations continue. This is done within the *evaluate* function of the algorithm.

The interest of distinguishing these two phases is to reduce the number of iterations as much as possible by allowing to reach the target faster before refining precisely the trajectory. However, in both phases we consider two possible ways of moving — translations or rotations — because depending on the configuration of the surrounding anatomical structures, they can converge and/or be evaluated differently. At new attempt $i+1$, the *Haystack* algorithm proposes two new candidate pairs $(\mathbf{x}_{Tr}, \mathbf{v}_i)$ and $(\mathbf{x}_i, \mathbf{v}_{Rot})$ corresponding respectively to a translation and a rotation of the previously proposed solution $(\mathbf{x}_i, \mathbf{v}_i)$, and leading respectively to deformed geometries G_{Di_1} and G_{Di_2} and curved trajectories T_{Di_1} and T_{Di_2} (as illustrated in Fig.4.2.2). These propositions are issued thanks to function *compute_displacements* :

— Insertion point P_{Tr} represented by the vector of coordinates $\mathbf{x}_{Tr}$ is computed with the following formula :

$$\mathbf{x}_{Tr} = \mathbf{x}_i + p(\mathbf{x}_{C_{Di}} - \mathbf{x}_{E_{Di}})$$

where C_{Di} of coordinates $\mathbf{x}_{C_{Di}}$ is the center of the target ; E_{Di} of coordinates $\mathbf{x}_{E_{Di}}$ is the point of the deformed trajectory T_{Di} which is the closest to C_{Di} ; p is a parameter allowing a progressive movement towards the target. Fig.4.6b illustrates this case and the proposition of a new candidate insertion point P_{Tr}.

— $\mathbf{v}_{Rot}$ is computed similarly. If we denote θ the oriented angle between points $\widehat{E_{Di}P_iC_{Di}}$, then we can obtain $\mathbf{v}_{Rot}$ by rotating $\mathbf{v}_i$ by angle θ weighted by p for a progressive movement. Fig.4.6c illustrates this case and the proposition of a new candidate insertion direction $\mathbf{v}_{Rot}$.

Factor p is chosen according to the phase of convergence. If we are at the target tracking phase (1), p is initialized to 1, whereas when in refinement phase (2) p is initialized to 0.1. Whatever the phase, due to the inhomogeneity of the tissues, we can not ensure that translating the insertion point by a vector $\vec{v}$ or rotating the insertion direction by an angle θ will lead to a placement of the tip of the deformed needle at the exact expected position. This is why, in the case where using the proposed translation or rotation does not lead to any improvement, we propose more attempts within a search range δ around the theoretical movement by modifying p until an improvement is found. If no improvement is found within δ, we extend δ to explore a larger solution space. This modification is represented by function *modify_p* in Algorithm 2.

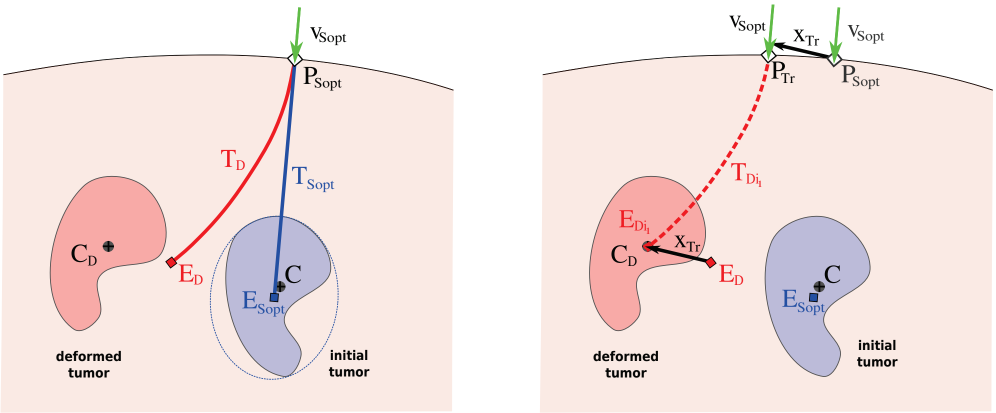

(a) using P_S and $\mathbf{v}_S$, T_D would not reach the deformed target.

(b) a new entry point P_{Tr} is proposed based on the movement of $\mathbf{C}$.

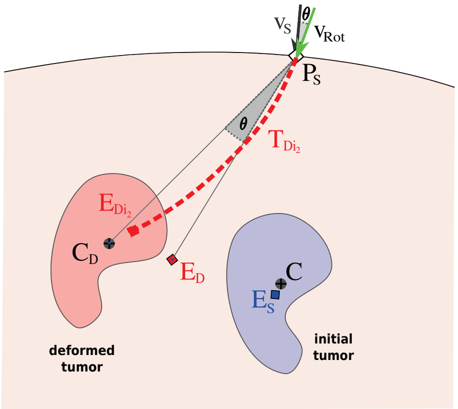

(c) a new direction $\mathbf{v}_{Rot}$ is proposed based on angle $\boldsymbol{\theta}$ ($\widehat{\mathbf{E}_D P_S \mathbf{C}_D}$).

In Fig. 4.2.2, an illustration of the new propositions of : (b) insertion point P_{Tr}, and (c) direction $\mathbf{v}_{Rot}$ in the neighborhood of the previous candidate P_{Sopt} and $\mathbf{v}_{Sopt}$ leading to T_{Sopt} (blue line), in case the deformed trajectory T_D (red line) would not reach the target in the deformed model $\mathbf{G}_D$ (see (a)). On the three images, the blue shapes are the target in the initial model $\mathbf{G}_S$, and the red shapes are the target in the deformed model $\mathbf{G}_D$. The red dotted lines in (b) and (c) are the deformed trajectories T_{Di_1} and T_{Di_2} issued by the two propositions.

Integrating the simulations into the solver

The planning software and simulation module were designed to work separately and communicate using the *Boost* serialization library [Boo, nd], as shown in Fig. 4.6. This figure illustrates the process of proposing new candidate insertion points and directions, simulating the insertions of the needle and the deformations of the anatomical model using the proposed candidates, and looping according to the quality of the resulting deformed trajectory.

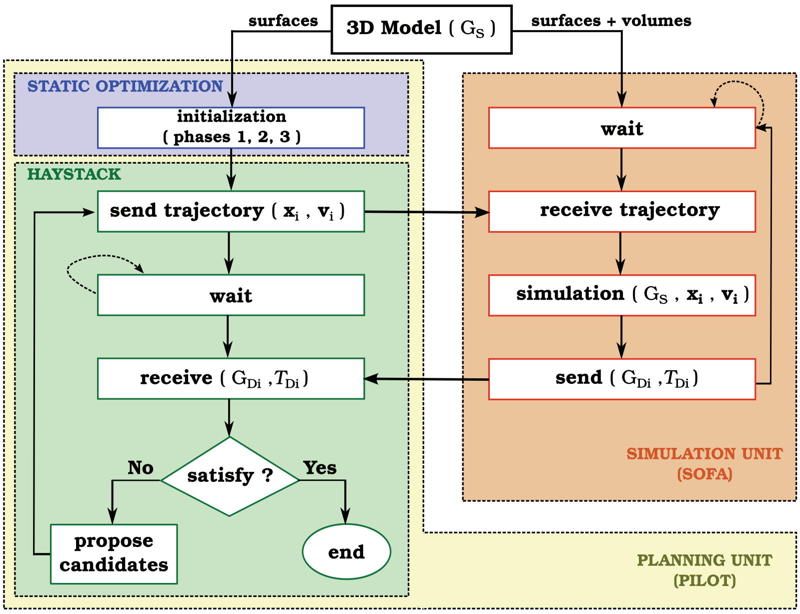

FIGURE 4.6 – Communication pipeline between the planning and simulation units.

4.3 Experiments and results

The tests described in this section have two main objectives. The first one is to underline the importance of accounting for deformations in a preoperative planning. The second one is to assess the efficiency of the *Haystack* algorithm by comparing it to two classical optimization methods.

Algorithm 1: *Haystack* algorithm

```
Data: $IS_{Sopt}(\mathbf{x}_{Sopt}, \mathbf{v}_{Sopt})$ : Optimal insertion settings in static environment $E_S$
      $G_S$ : Initial 3D geometry of patient's anatomy
Result: $IS_{Dopt}(\mathbf{x}_{Dopt}, \mathbf{v}_{Dopt})$ : Optimal insertion settings in deformable environment $E_D$

$(T_D, G_D, C_D) \leftarrow simulation(\mathbf{x}_{Sopt}, \mathbf{v}_{Sopt})$;
$dist \leftarrow compute\_distance(T_D, C_D)$;
$p \leftarrow 1$;
$i \leftarrow 0$;
while $(\ (i < iter_{max})$ and $(tip_{T_D} \notin target_{G_D})\ )$ do
    $(\mathbf{x}_{Tr}, \mathbf{v}_{Rot}) \leftarrow compute\_displacements(\mathbf{x}_i, \mathbf{v}_i, p)$;
    $(T_{Di_1}, G_{Di_1}, C_{Di_1}) \leftarrow simulation(\mathbf{x}_{Tr}, \mathbf{v}_i)$;
    $(T_{Di_2}, G_{Di_2}, C_{Di_2}) \leftarrow simulation(\mathbf{x}_i, \mathbf{v}_{Rot})$;
    $dist_1 = distance\_min(T_{Di_1}, C_{Di_1})$;
    $dist_2 = distance\_min(T_{Di_2}, C_{Di_2})$;
    if $(\ (dist_1 < dist)$ or $(dist_2 < dist)\ )$ then
        $(\mathbf{x}_i, \mathbf{v}_i) \leftarrow keep\_candidate\_with\_min\_dist((\mathbf{x}_{Tr}, \mathbf{v}_i), (\mathbf{x}_i, \mathbf{v}_{Rot}))$;
        $dist \leftarrow min\_distance(dist_1, dist_2)$;
    else
        $p \leftarrow modify\_p(T_{Di_1}, T_{Di_2})$;
    $i \leftarrow i + 1$;
$p \leftarrow 0.1$;
$eval \leftarrow evaluate(T_S, G_S)$;
while $(\ (i < iter_{max})$ and $(eval_{best} - eval < \varepsilon_2)\ )$ do
    $(\mathbf{x}_{Tr}, \mathbf{v}_{Rot}) \leftarrow compute\_displacements(\mathbf{x}_i, \mathbf{v}_i, p)$;
    $(T_{Di_1}, G_{Di_1}, C_{Di_1}) \leftarrow simulation(\mathbf{x}_{Tr}, \mathbf{v}_i)$;
    $(T_{Di_2}, G_{Di_2}, C_{Di_2}) \leftarrow simulation(\mathbf{x}_i, \mathbf{v}_{Rot})$;
    $eval_1 = evaluate(T_{Di_1}, G_{Di_1})$;
    $eval_2 = evaluate(T_{Di_2}, G_{Di_2})$;
    if $(\ (eval_1 < eval)$ or $(eval_2 < eval)\ )$ then
        $(\mathbf{x}_i, \mathbf{v}_i) \leftarrow keep\_candidate\_with\_min\_eval((\mathbf{x}_{Tr}, \mathbf{v}_i), (\mathbf{x}_i, \mathbf{v}_{Rot}))$;
        $eval \leftarrow min\_evaluation(eval_1, eval_2)$;
    else
        $p \leftarrow modify\_p(T_{Di_1}, T_{Di_2})$;
    $i \leftarrow i + 1$;
$\mathbf{x}_{Dopt}, \mathbf{v}_{Dopt}) \leftarrow (\mathbf{x}_i, \mathbf{v}_i)$
```

4.3.1 Description of the Evaluation Scenario

Our approach has been evaluated on a particular percutaneous procedure, the *radiofrequency ablation (RFA) of hepatic tumors*, Let us note that the volume of the RFA, which is delimited by the 60°C isotherm surface defining the lethal temperature for the cells, can be either computed by methods such as Pennes equation to simulate bioheat propagation like in [Jaberzadeh and Essert, 2015], or approximated by an ellipsoid. The simulation of bioheat propagation has the advantage of allowing to account for the presence of vessels in the vicinity of the tumor, that may reduce the efficiency of the treatment, however, it is computationally expensive. In order to keep the time needed for the optimization in reasonable terms, we opted for the method based on the approximated ellipsoid which defines the safety margin as presented in [Baegert et al., 2007b].

To mimic the intervention scenario by the mechanical simulation, we have created a simulation scene in SOFA composed of four objects, as illustrated in Fig. 4.7 :

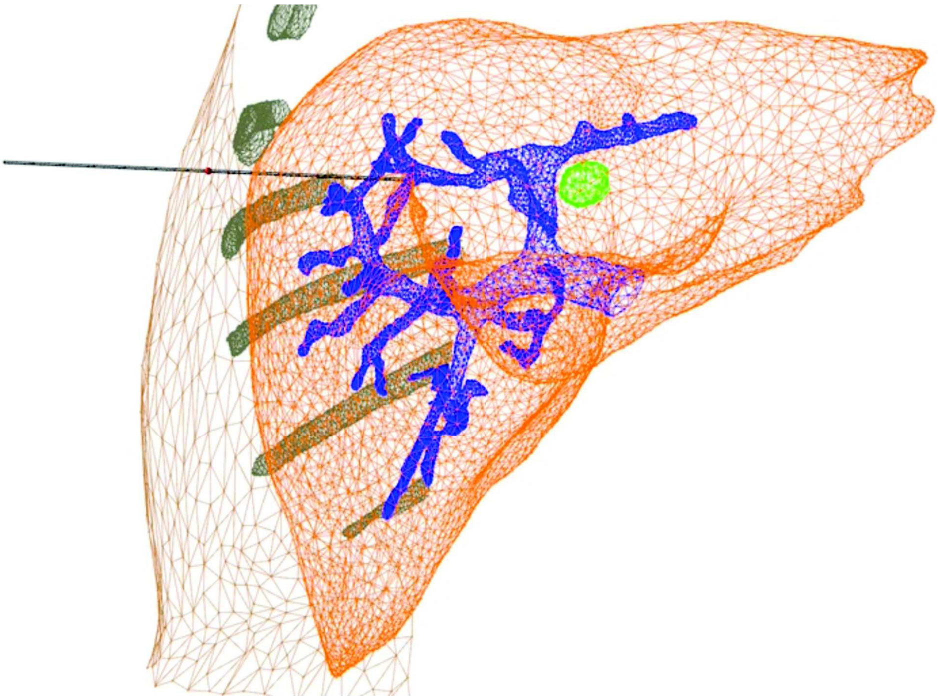

FIGURE 4.7 – Example of a simulation scene consisting of a deformable needle, the abdominal wall, the rib cage, the liver, the vessels and the target (in green). The scene is visualized in SOFA platform.

- *Deformable needle* modeled with Timoshenko beams (see Section 4.2.1). In order to match the properties of a real needle, we set the needle diameter to 1.27 mm. (approx. 18 gauge) and its length to 17 cm. with a Young's modulus equals to 75 GPa.
- *Abdominal wall* modeled with linear FE method : only local deformations in the vicinity of the needle entry were modeled and the FE mesh was fixed by homogeneous Dirichlet boundary conditions in a distance of approximately 10 cm

from the entry point. In order to achieve a reasonable amount of deformation, we set the Young's modulus of the wall to 5 kPa.

— *Rib cage* modeled only as a geometrical obstacles without any mechanical function.

— *Liver* modeled with co-rotational FE method which accounts for large deformations as described in Section 4.2.1. In this scenario, we supposed that the behavior of the organ is simulated by a homogeneous isotropic model : the Young's modulus was set to 1 kPa. The value approximates the average moduli reported for healthy liver in the literature [Kemper et al., 2010]. As for the boundary conditions, the liver was anchored in the space using homogeneous Dirichlet conditions in the areas corresponding to the entry of important vessels (hepatic and portal vein and the aorta) and location of ligaments. In this evaluation, the surrounding organs were not simulated.

— *Vascularization and tumor* modeled as geometrical objects. Nevertheless, unlike the rib cage, they were mapped to the FE model of the liver parenchyma. Therefore, as the liver model gets deformed, both vessels and the target follow this deformation and therefore move.

In each step of the optimization, the needle is inserted from the outside of the abdominal wall at a constant velocity of 4 cm/s. First, it penetrates the abdominal wall and then, the needle punctures the surface of the liver and continues penetrating the parenchyma. The insertion is stopped when the maximal insertion depth is achieved or the needle has hit and now exits the target lesion.

4.3.2 Datasets and deformations amplitude

The datasets on which we performed our tests were prepared based on real patients models from the "3D-IRCADb" database [3Di, nd]. This database includes several sets of anonymized medical CT images of patients and the manual segmentation of the various structures of interest performed by clinical experts. The representation of segmented zones is provided as surface meshes in VTK format. Based on the surface meshes of 4 patients data, we prepared 12 different datasets (referenced as DS1 to DS12) for both the geometric model scene required for the planning module and the physic model scene for the simulation module. Each consists of 3D triangular surface meshes of the abdominal organs and the body contour generated from preoperative CT-scans. The surface triangulations were used to generate volume meshes composed of linear tetrahedral elements ; the average size of a mesh used for the abdominal wall and the liver was 25,000 and 15,000 elements, respectively.

For each dataset, we generated three versions of the tumor each having different size, form, and position, in order to quantify the impact of the tumor attributes on the planning. (See Table 4.1).

The average size of a tumor was 12×10×7 mm (typical tumor diameters for RFA are inferior to 3.0 cm [Livraghi et al., 1999]). The details for each variation are given in Table 4.1. Fig.4.9 shows how deep in the vascular system the target can be located.

The euclidean distance between the initial position C of the tumor's center of mass and its position C_D after a simulation reached up to 25 mm, while the euclidean

Table 4.1 – Description of the tumors geometric properties and relative locations in the 12 experimental datasets.

Dataset	**Diameter** (mm)	**Volume** (mm^3)	**Close to vessels**	**Close to skin**
DS1	14	180	no	yes
DS2	16	397	no	no
DS3	16	397	yes	no
DS4	14	198	no	no
DS5	14	147	yes	no
DS6	25	885	yes	yes
DS7	18	335	no	no
DS8	13	128	yes	yes
DS9	17	525	yes	yes
DS10	17	275	yes	no
DS11	16	372	no	no
DS12	13	218	yes	yes

distance between the needle tip's planned position in static condition N_{Sopt} and its simulated position N_D reached up to 9 mm. This means that in the worst case the target would be missed by 16 mm according to our simulation. Fig.4.8 shows the connection between the displacements of the needle's tip and the tumor's center in each dataset. Fig.4.9 shows an example of amplitude of liver deformation and target displacement.

4.3.3 Overview of optimization methods

To evaluate the performances of our algorithm, we experimented three optimization techniques : an Exhaustive search (EX), the Nelder-Mead Downhill method (DH), in addition to our proposed *Haystack* optimization technique (HST).
These three techniques were applied after an identical initialization phase in static conditions using Nelder-Mead method where T_{Sopt} is computed, so that their performances are compared only for the deformable phase. The planning algorithms were performed on a PC with Intel Core i7 running at 2.67 GHz and 8 GB RAM.

Exhaustive method EX

We have used the EX method in the following way : a first simulation is performed with T_{Sopt} as an input. Then a search range around the initial proposed trajectory T_{Sopt} is defined based on the simulation. For the translations, $\Delta\mathbf{x} = \lambda|\mathbf{x}_{C_D} - \mathbf{x}_C|$ is defined. Similarly, an angle of $\lambda.\theta$ is used as maximum rotations. Parameter λ has been experimentally set to 2, in order to be sure to include the moved target within the range. At each iteration of the EX algorithm, $\mathbf{x}$ and $\mathbf{v}$ are modified by randomly choosing values within the defined range, with a precision of 10^{-5}mm for the coordinates of $\mathbf{x}$ and 10^{-5} degree for angles α and β of direction $\mathbf{v}$.

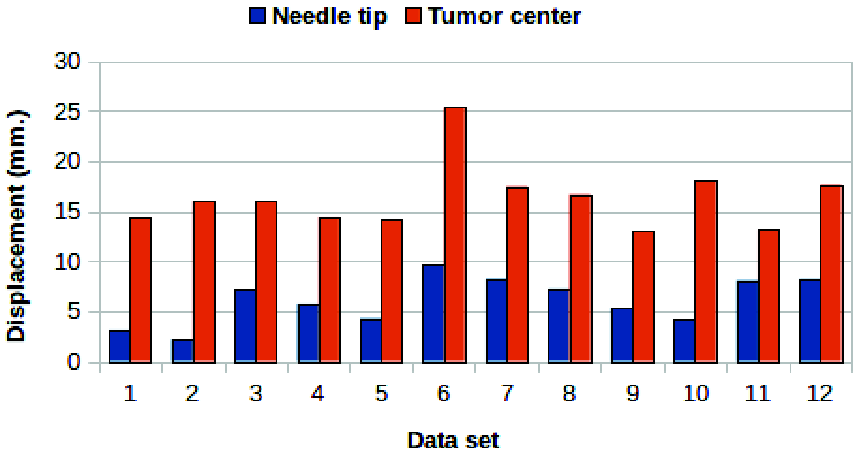

Figure 4.8 – Connection between needle tip and tumor center displacements

Nelder–Mead Downhill method DH

DH [Nelder and Mead, 1965] is a derivative-free numerical method suitable to our non-derivable optimization function, which has proven in previous works to be able to converge to a minimum of f [Baegert et al., 2007b].

Haystack method HST

HST algorithm is the algorithm we described in Section 4.2.2. It is in some way inspired by DH, and could be considered as an adaptation of the latter by replacing the "blind search" on the simplex vertices in DH by a "context-aware" search by integrating information from the simulations feedback. The interest is, as we ensured earlier, to reduce as much as possible the number of simulations while preserving an acceptable precision.

Evaluation of efficiency : The results are summarized in Table 4.2, where we first present the results of the initial static phase. For each dataset (column 1), we report the result of the initial deformed trajectory T_D computed from the simulation of insertion following IS_{Sopt} in static condition, as one of : miss target / hit target / or hit obstacle (column 2), and the value of cost function $f(T_D) \in [0, 1]$ in static condition (column 3). It can be noticed that in case of hitting the target or an obstacle, the evaluation is assigned its worst value ($= 1$), while a value < 1 is computed in case when the target has been already hit but the trajectory is not optimal. We also report in the table the number of simulations (column 5) for each dataset using the three techniques with the corresponding computation time (column 6). For EX method, the number of simulations was limited to 1,000 for each dataset. For the other two methods, the simulations were stopped when the improvement of f fell under a threshold of 10^{-3}. Finally, we report the value of $f(T_{Dopt}) \in [0, 1]$ in the deformable environment (column 7). It can be also noticed that the values in this column are all < 1, which means that all methods converged to a curved path

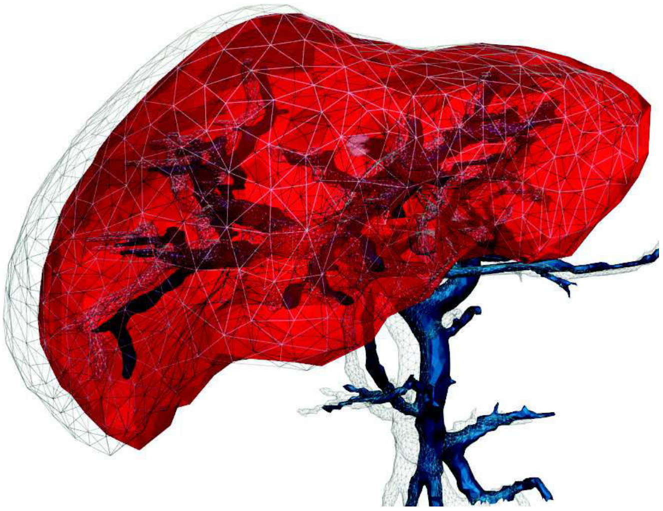

FIGURE 4.9 – 3D models for a liver with portal vein an tumor inside : in static (wireframe) and dynamic (color surfaces) conditions.

hitting the tumor for all datasets.

Figure 4.10 shows the comparison of the performances of the three methods in terms of required number of simulations needed to converge, and Figure 4.11 shows the comparison in terms of the quality of the optimal trajectory reflected by the value of $f(T_{Dopt})$ which had to be minimized in order to optimize the soft constraints.

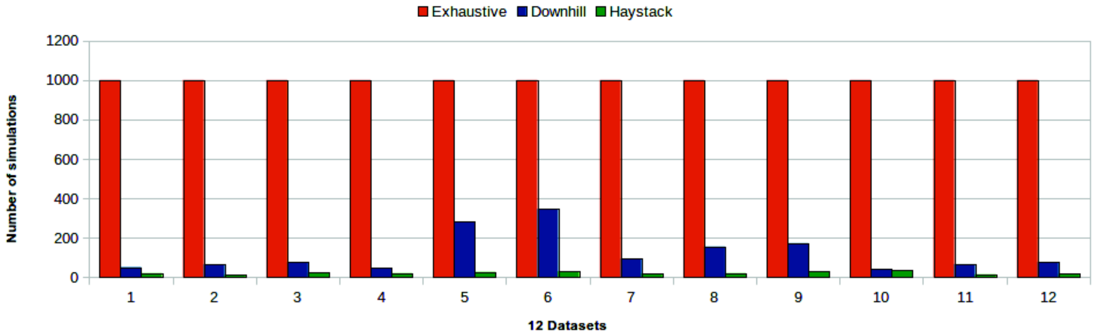

FIGURE 4.10 – Comparison of the number of simulations for the three methods : EX (orange), DH(blue), and HST (green). HST method requires a smaller number of simulations to converge than EX and DH.

4.4 Discussion and conclusion

The amplitude of the deformations measured after the simulations shows that by performing a mere static planning, the target could be missed by up to 16mm. This observation highlights the interest of a planning accounting for the deformable

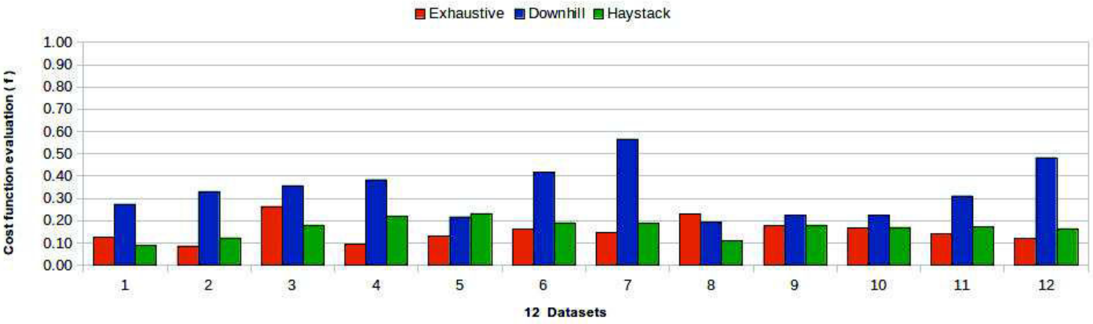

FIGURE 4.11 – Comparison of the values of $f(T_{Dopt})$ for the three methods : EX (orange), DH(blue), and HST (green). HST method obtained a precision close to EX and 2 times better than DH in average.

environment.

The proposed optimization algorithm *Haystack* has been compared to two searching methods. The results show that the three presented methods are capable of finding some insertion settings leading to a feasible and optimal trajectory in a deformable environment, but the *Haystack* algorithm is always the fastest, as it requires the smallest number of simulations to converge. Since the simulation of insertion performed at each step of the optimization process is time consuming, this is an important feature of the proposed algorithm.

Although the proposed deformable approach is more time consuming than a simple rigid planning, it remains computationally efficient with an average computation time of 373 s. and an average of 23 simulations. This is significantly better when compared to the DH method, which completed in an average of about 27 minutes : HST is more than 4 times faster than DH in average.

Furthermore, HST algorithm converges to a good minimum value of the cost function.The average value of $f(T_{Dopt})$ obtained with HST (0.169) is quite comparable to the one obtained with EX (0.15), with only 1.9% of quality loss within the value range $[0, 1]$. Comparatively, the average value of $f(T_{Dopt})$ obtained with DH (0.33), is twice higher than HST with 18% of quality loss within the same value range. This means that the quality of the trajectory obtained with HST is much better than with DH.

In addition, the results show that even when T_{Sopt} can already hit the target (as in DS3, DS4, DS8, and DS12 datasets), the optimizations in deformable environment can enhance the quality of T_D (compare column 3 and column 7), which is also an interesting outcome.

Validity of the physical simulations : In the current implementation, the simulation code used by the planning algorithm relies on a geometrically non-linear constitutive soft tissue model accounting for large deformations. The interaction between the flexible needle and different tissue layers is modeled using advanced constraints solved at each step of the simulation. Although the accuracy of the simulation has not been clinically validated yet, the method has been verified by a comparison with a commercial FE package [Faure et al., 2012]. In this current work, the personalization of the model was limited to the geometry, while material parameters were based on generic values taken from the literature. Nevertheless, it has been shown previously that patient-specific parametrization of such models is straightforward and additional advanced properties of tissues such as heterogeneity and anisotropy can be added while keeping its performance [Livraghi et al., 1999]. As a consequence, updating the parameter choice or constitutive model of the planning algorithm could improve the accuracy of the planning without requiring any particular change in the method. Obviously, the choice of model and parameters is problem-dependent.

It is also important to keep in mind that any simulation remains an approximation of the real world. The promising results presented in this article illustrate the feasibility of biomechanically-inspired advanced planning, and could be further applied to real-world problems when completed by an intra-operative guidance. Nonetheless, we believe that such an advanced planning offers the advantage to propose better insertion settings than a simple planning in static conditions. By anticipating the deformations, it can reduce the need for manual adjustments usually required during the intra-operative guidance.

To summarize : this work shows that it is possible to include information from soft tissue deformations and needle bending in the planning process for percutaneous interventions. A dedicated optimization algorithm named *Haystack* able to converge quickly towards precise optimal insertion settings has been introduced. Tests on 12 different datasets have showed that *Haystack* algorithm converges in a reasonable time (less than 7 minutes with our experimental setup) to a safe and efficient curved trajectory that is close in precision to an exhaustive method.

Table 4.2 – Comparison between the three optimization techniques in a deformable environement in terms of required number of simulations, computation time, and cost function value.

Dataset	T_D	$f(T_D)$	**Algorithm**	**#Simu.**	**Time s.**	$f(T_{Dopt})$
DS1	Miss target	1	EX	1000	16908	0,12
			DH	52	768	0,27
			HST	21	381	0.09
DS2	Hit obstacle	1	EX	1000	15823	0,0860
			DH	66	1345	0,33
			HST	13	241	0,123
DS3	Hit target	0,62	EX	1000	18980	0,26
			DH	77	1512	0,36
			HST	25	241	0,18
DS4	Hit target	0,79	EX	1000	21473	0,094
			DH	47	806	0,38
			HST	21	384	0,221
DS5	Miss target	1	EX	1000	18262	0,13
			DH	281	3018	0,22
			HST	27	433	0,232
DS6	Miss target	1	EX	1000	22411	0,162
			DH	347	4163	0,42
			HST	31	493	0,191
DS7	Miss target	1	EX	1000	15331	0,15
			DH	94	1618	0,57
			HST	19	330	0.19
DS8	Hit target	0,42	EX	1000	12776	0,23
			DH	156	2349	0,19
			HST	21	346	0,11
DS9	Miss target	1	EX	1000	16864	0,18
			DH	173	2672	0,23
			HST	29	437	0,18
DS10	Miss target	1	EX	1000	23026	0,17
			DH	41	387	0,23
			HST	37	455	0,17
DS11	Hit obstacle	1	EX	1000	27885	0,14
			DH	67	693	0,31
			HST	15	284	0,172
DS12	Hit target	0,89	EX	1000	20751	0,12
			DH	78	632	0,48
			HST	17	310	0,164
Average			EX	1000	19208	0.15
			DH	123	1664	0.33
			HST	23	373	0.169

5

PREOPERATIVE TRAJECTORY PLANNING FOR DEEP BRAIN STIMULATION IN DEFORMABLE CONDITIONS

"If the human brain were so simple that we could understand it, we would be so simple that we couldn't."
- Emerson M. Pugh

In this chapter, we present a patient-specific method to automatic trajectory planning in DBS procedures. Our approach takes into account brain deformation, namely, the brain shift phenomenon. After an introduction, we detail the physical model of the brain, and we present a dedicated planning algorithm in dynamic conditions. We describe the performed experiments and the obtained results. Finally, we conclude with a discussion.

5.1 Introduction

Deep brain stimulation (DBS) is a surgical procedure for treating motor-related neurological disorders. It consists in implanting electrodes in a deep area (the basal ganglia) in the patient's brain, and delivering high-frequency electric pulses to the surrounding. Some of the common structures that undergo a stimulation are the Subthalamic Nucleus (STN) or the Globus Pallidus (GPI). Fig. 5.1 illustrates the basal ganglia structures.

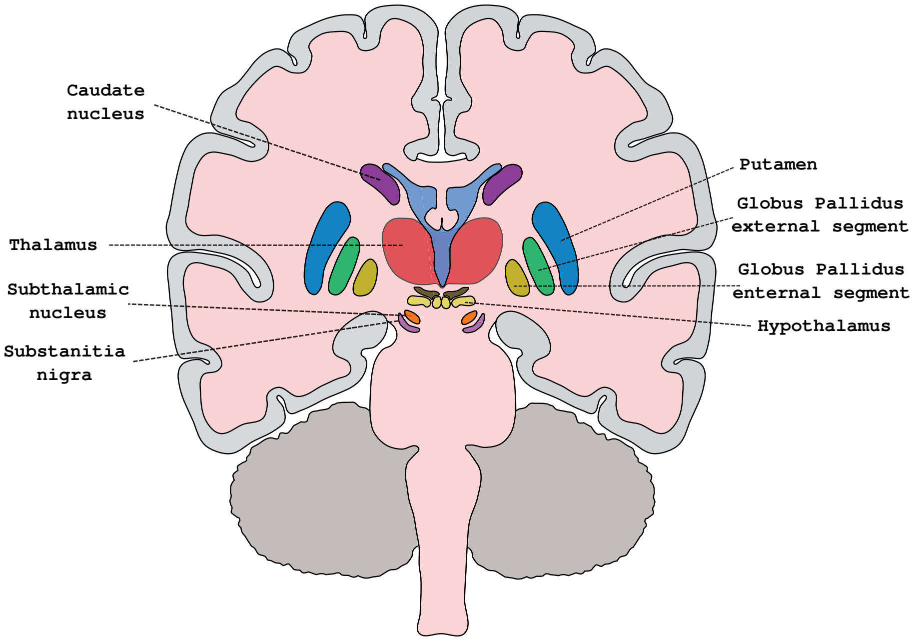

Figure 5.1 – Basal Ganglia structures in the brain

The success of the intervention relies on the electrode placement accuracy [York et al., 2009]. The electrode path is decided in a preoperative phase on the patient's medical images. However, intra-operative brain deformation, called brain shift, might invalidate the planning as described in Chapter 1, Section 1.2.2. In this chapter, we address the trajectory planning for DBS electrode implantation in deformable conditions.

5.2 Planning in deformable conditions

Similarly to the case of percutaneous procedures, we rely on physics and geometry to achieve a deformation-aware preoperative planning. We introduce a method that combines a brain deformation model with a dedicated geometric solver, and we evaluate its usability on a patient-specific model with a comparison between planning in static and dynamic conditions.

The work has been done in collaboration with members from Shacra team, INRIA, Lille/Strasbourg as part of the ANR ACouStiC project. The deformed models of the brain were generated thanks to an approach developed by Alexandre Bilger in his PhD [Bilger, 2014] during the project. We included the brain deformations in our planning process.

5.2.1 Biomechanical modeling and simulation

The physical behavior the human brain is complex. Many elements should be considered to have a realistic model which is a patient-specific challenging task.

We take advantage of physical modeling and numerical methods to simulate the brain shift deformation. The first aspect is how the mechanical behavior of the brain tissue is modeled. Then, we focus on the boundary conditions which have an influence on the brain motion and deformation, and in particular the action of the cerebro-spinal fluid.

Brain deformation modeling

The brain is considered as a soft body subject to the laws of continuum mechanics. One of the numerical methods to solve the governing equations of motion is the Finite Element Method (FEM). In this theory, the continuum is partitioned into smaller disjoint cells called *elements*. We use $\mathcal{P}_1$ Lagrange tetrahedral elements, composed of four nodes, each with three degrees of freedom (see an example in Figure 5.2). The equation of motion is solved for the nodes of the element, and the values inside the element are obtained with a interpolation function defined for each node.

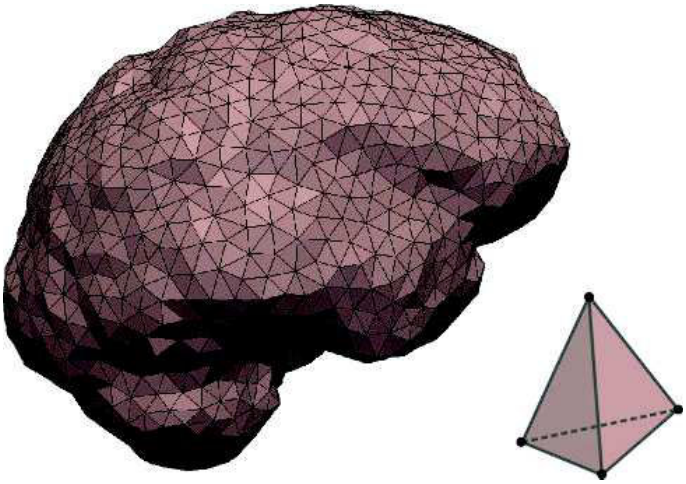

FIGURE 5.2 – Sagittal view of the tetrahedral mesh of the right hemisphere.

As the brain shift process takes place at a very low velocity, we consider the problem as quasi-static and only look for the configuration of the brain at that equilibrium, disregarding the dynamic transient effects. Finally, the discrete equation to solve is

$$\mathbf{f}(\mathbf{x}) = 0 \tag{5.2.1a}$$

where $\mathbf{x}$ and $\mathbf{f}$ are respectively the position and the force vectors on the nodes. Here, $\mathbf{f}$ is a non-linear function of the position of the nodes $\mathbf{x}$, and represents the sum of the internal and external forces. In order to solve this non-linear equation, we use the following first-order linearization at each time step :

$$\mathbf{f}(\mathbf{x} + d\mathbf{x}) = \mathbf{f}(\mathbf{x}) + \mathbf{K}(\mathbf{x})d\mathbf{x} \tag{5.2.1b}$$

where the Jacobian matrix $\mathbf{K}(\mathbf{x}) = \frac{\partial \mathbf{f}}{\partial \mathbf{x}}$ depends on the nodes position. This matrix is called *stiffness matrix* for the internal forces. The solution of Equation 5.2.1a is then approximated with the first iteration of the Newton-Raphson algorithm :

$$\mathbf{f}(\mathbf{x_n}) + \mathbf{K}(\mathbf{x_n})d\mathbf{x} = 0 \tag{5.2.1c}$$

where $d\mathbf{x} = \mathbf{x} - \mathbf{x_n}$ is unknown and $\mathbf{x_n}$ is the current position. Equation 5.2.1c is a linear system solved with a Conjugate Gradient algorithm. This process is applied iteratively until reaching equilibrium.

Regarding the application of the simulation, brain deformation can be considered small. This allows us to use the Hooke's law to define the tissue behavior. It defines a linear relationship between strain σ and stress ε. For an isotropic material such as the brain, the behavior is defined by the Lamé coefficients λ and μ :

$$\sigma = 2\mu\varepsilon + \lambda \mathrm{tr}(\varepsilon) \tag{5.2.1d}$$

From this law, we can write the local (relative to an element e) stiffness matrix $\mathbf{K_e}$:

$$\mathbf{K_e} = \int_{v_e} \mathbf{J_e}^T \mathbf{D_e} \mathbf{J_e} dV \tag{5.2.1e}$$

where v_e is the volume of the element e, $\mathbf{J_e}$ denotes a matrix providing strain-displacement relationship and $\mathbf{D_e}$ stands for the strain-stress relation ship. In our case, with the Hooke's law, $\mathbf{J_e}$ and $\mathbf{D_e}$ are constant.

To handle large displacements (while maintaining small deformation), we use a co-rotational formulation [Felippa and Haugen, 2005], where the geometric non-linearities are approximated with the rotation of the element with respect to its initial configuration. With this approach, the stiffness matrix $\mathbf{K_e^r}$ of the element e is defined as :

$$\mathbf{K_e^r} = \mathbf{R_e}^T \mathbf{K_e} \mathbf{R_e} \tag{5.2.1f}$$

where $\mathbf{R_e}$ is the rotation matrix of the element e. Finally, the global matrix $\mathbf{K}$ is assembled from the local element stiffness matrices $\mathbf{K_e}$.

Interaction with bony structures

When the brain deforms and moves, it may collide the skull, in particular the endocranium, which is the inner surface of the skull. Once they have been detected, contacts are solved using Signorini's law :

$$0 \leq \delta \perp \lambda \geq 0 \tag{5.2.1g}$$

It establishes an orthogonal relationship between the contact response force λ and the interpenetration distance δ. We ensure the Signorini's condition is fulfilled at the end of each time step by adding a term of constraints in the equation 5.2.1a :

$$\mathbf{f}(\mathbf{x}) = \mathbf{H}^T \lambda \tag{5.2.1h}$$

where **H** is a matrix containing the constraints directions and λ is Lagrange multipliers and contains the constraint force intensities. In Equation 5.2.1h, λ is unknown and have to be computed. A linear complementary system is obtained, and is solved using a Gauss-Seidel algorithm. More details on the overall constraint solving process are given in the work [Duriez et al., 2006].

Cerebro-spinal fluid

The main cause of brain shift is due to a Cerebro-Spinal Fluid loss. That is why it is indispensable to model the action of CSF on the brain. CSF is a fluid surrounding the brain, which the density is similar to water ($\rho = 1007$ kg/m^3). The loss of CSF leads to a change of the pressure inside the skull and allows the brain to deform. The action of CSF on the brain is modeled with a hydrostatic pressure :

$$\mathbf{f}_{CSF} = \int_{S_e} \Big(\rho\, g\, h + p(z_0)\Big) \mathrm{d}\mathbf{S} \tag{5.2.1i}$$

where S_e is the surface of a submerged element belonging to the surface of the brain. g denotes the gravitational acceleration. h stands for the height from a point to the fluid surface, and $p(z_0)$ is the pressure of the point z_0 located on the fluid surface. The amount of brain shift is controlled by the fluid level. A loss of CSF corresponds to a decrease of the fluid level, therefore h decreases also, so is the fluid forces. Fig. 5.3 illustrates the different components of the simulation.

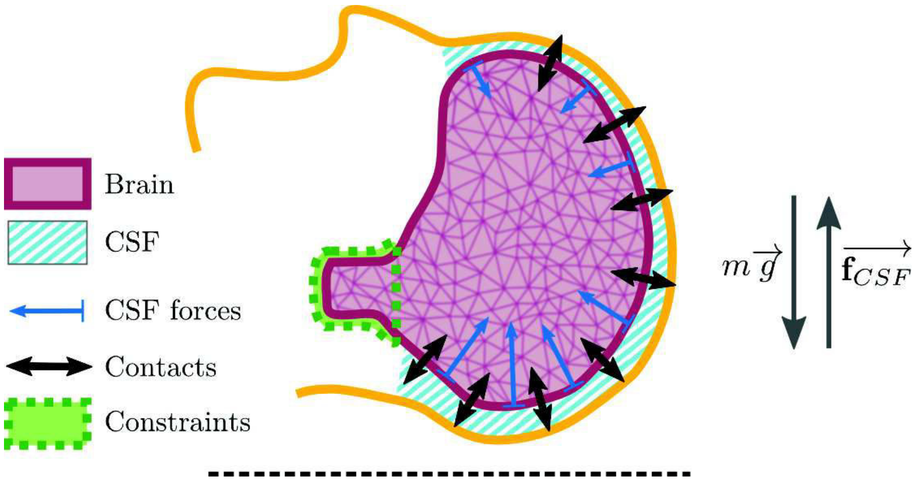

FIGURE 5.3 – Illustration showing the different components of the simulation : brain tissue is simulated with a FEM mesh, brain tissue near brainstem is anatomically constrained, CSF pressure is acting on the brain tissue and contact response in case of collision with the skull.

Thanks to the presented model, we are able to use it to anticipate the brain shift in case of DBS procedure. In the following, we will explain how do we inject the information of brain shift deformation in a geometric–based solver for DBS path planning.

5.2.2 Geometric–based preoperative planning

We propose a planning algorithm based a preventive approach. The reasoning about this choice is the uncertainty of the extent of the deformation which could happen during the operation. Many factors may affect the simulation results : the patient-specific tissue parameters, the position of the patient, the surgical techniques, the operation time, the burr-hole closing ways, etc.

Firstly, we had to define a working hypothesis to anticipate the brain shift intensity. Once we simulate the deformations, we can integrate them into the planner to obtain a safe planning strategy in a preoperative phase.

Working hypothesis

An important aspect to understand in this work is that the extent of the final deformation is hard to anticipate : for now it is not possible to determine preoperatively if the patient's brain will deform or not and what will be the exact magnitude of the deformation.

In more intuitive words, when the patient lies in a supine position on the table, a burr hole close to the forehead generally produces no brain shift, whereas a burr hole in the middle of the skull is more likely to produce a maximal brain shift (as illustrated in Fig.5.4), but may also produce any intermediary magnitude of brain shift. However, because of the presence of vital anatomical structures, neurosurgeons will never choose an entry point posterior to the middle of the skull.

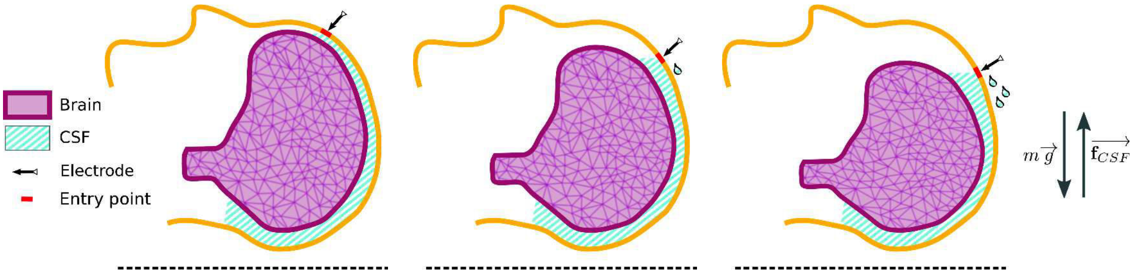

(a) High entry point (b) Medium entry point (c) Low entry point

FIGURE 5.4 – Schematic representation of the influence of the location of the entry point (red) on the loss of CSF and the possible magnitude of brain shift.

However, it is possible to estimate, for a specific entry point, what would be the minimal brain shift BS_0 (corresponding to no brain shift) and maximal possible brain shift BS_{max} (corresponding to full CSF loss through the entry point), with a full range of intermediary possible deformations BS_i. Examples of possibilities are shown on Fig.5.5.

Our hypothesis is to account for all possible magnitudes of brain shift that may occur based on the candidate positions of the entry point, in order to be sure to avoid the vital structures whatever their final position. Therefore, several simulations with different degrees of deformation are required, and for the evaluation of a particular candidate entry point, the corresponding maximum possible deformation and all intermediary deformations will be used.

FIGURE 5.5 – Deformation of the cortical sulci of the left hemisphere due to brain shift. Only 3 deformation intensities are shown : gray mesh : no brain shift, green mesh : medium brain shift, and orange mesh : maximum brain shift. For readability reasons, intermediate deformed meshes are not shown. Note that the difference between maximal deformed mesh and not deformed mesh is more important at the anterior part that at the posterior part.

Introducing new distance metrics

We recall the search criteria concerned by the DBS path planning optimization as described earlier in Chapter 3, Section 3.2.2 are :

1- Proximity to a "Standard Trajectory" : the orientation of the electrode, computed as the proximity to a standard trajectory defined by expert neurosurgeons and commonly used in the commercial platforms.
2- Distance from the electrode to the blood vessels.
3- Distance from the electrode to the ventricles.

Both constraints 2 and 3 require a geometric operator to calculate the distance between $\mathcal{O}$ (the anatomical obstacles vessels or ventricles), and the electrode trajectory T which is a *"ray"* in the DBS case. We suggest to apply different ways for distance calculation depending on the geometric form of the obstacle and its location corresponding to the trajectory path.

A discretization contains np points is done on the trajectory line segment from the tip of the electrode to the entry point on the scalp (with a precision equal to $1mm$ between two successive points).

— when $\mathcal{O}$ is the vessels (embedded in the sulci), the distance is the minimal distance to $\mathcal{O}$ from T.

$$distance(T, \mathcal{O}) = minimum(dist(p_1, \mathcal{O}), dist(p_2, \mathcal{O}), ..., dist(p_{np}, \mathcal{O})) \quad (5.2.1j)$$

— when $\mathcal{O}$ is the ventricles, the distance is the average distance to $\mathcal{O}$ along T.

$$distmin(T, \mathcal{O}) = Average(dist(p_1, \mathcal{O}), dist(p_2, \mathcal{O}), ..., dist(p_{np}, \mathcal{O})) \quad (5.2.1k)$$

for $i : 1 \rightarrow np$, and $dist$ is euclidean distance between p_i and the nearest point on $\mathcal{O}$.

The reason of distinguishing these two cases is that the anatomical structure of the sulci is close to the outer surface of the brain, and the closest point on T to the sulci is found usually closer to the entry point position on the scalp rather than to the electrode tip. In the case of the ventricles, they are located deep in the brain in the area of basal ganglia, and the common targets in DBS stimulation (STN or GPI) are included in the cavity of the ventricles. Since that the electrode's tip should be placed inside the target, the nearest point to the ventricles is always located on T near the tip and far from the entry point. This causes a false positive because there would be no differences between trajectories having different entry points (illustration in Fig. 5.6).

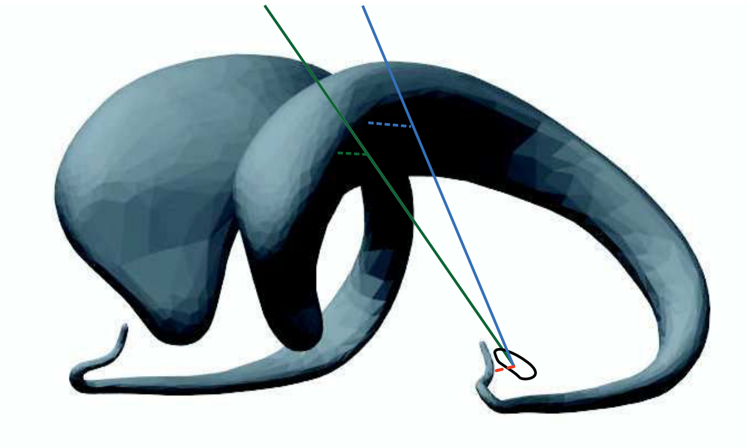

FIGURE 5.6 – calculating the distance between the electrodes and the ventricles using Equation 5.2.1j would result that T_1(blue) and T_2 have the same distance to $\mathcal{O}$ (represented by the red dotted segment), while using Equation 5.2.1j would results in T_1 is further from $\mathcal{O}$ than T_2.

Planning Algorithm

The planning algorithm relies on the existing geometric solver to evaluate the quality of the insertion settings proposition at each iteration. In deformable conditions, the cost function evaluation should be performed on a deformed 3D model instead of the initial model reconstructed from the patient's medical images M_S. Since that the suggested working hypothesis implies performing a number of simulations for a single entry point, several deformed models $M_{D_{CSF}}$ exist, each one corresponding to a different value of CSF loss. Each possible entry point p_i is linked to a model $M_{D_{CSF}}$ relatively to its height h on the head of the lying patient. Thanks to an interpolation with boundaries $hmax \leftrightarrow BS_0$ and $hmin \leftrightarrow BS_{max}$, it is possible to retrieve the maximum possible brain shift BS_h corresponding to height h, and therefore to the deformed model M_{D_h} that can be used with p_i. Deformed model M_{D_h} is constituted by the union of all brain shift models from BS_0 to BS_h. Due to our hypothesis, all points p_i lying at the same height are supposed to lead to the same possible maximum brain shift BS_h, as illustrated in Fig.5.7.

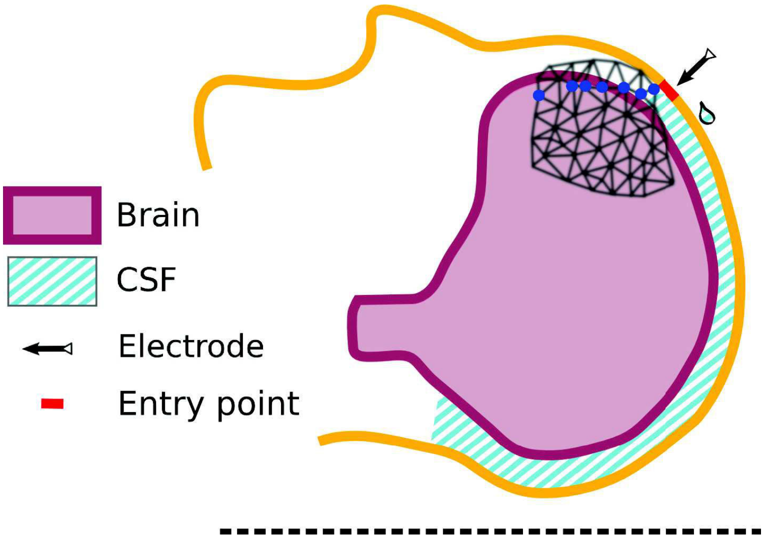

Figure 5.7 – Schematic representation of the entry points (blue) of the initial skin mesh S lying at the same height and likely to lead to the same possible maximal brain shift BS_h.

Calculating a number of simulations for every entry point is a time consuming task regarding the time required for a single simulation (around 1 minute). Therefore, we opted for pre-computation of a high number of simulations for every patient, the simulations are stored in a patient-specific database which is accessed during the planning iterations. Once the deformation data base is ready, the dynamic planning approach can be run. It consists in two steps :

1. Delineation of the *insertion zone in dynamic condition* IZ_D from the skin surface mesh S by solving the HC. For each point $p_i \in S$ we check whether it satisfies all HC on the updated deformed model M_{D_h} corresponding to its height h and containing all possible positions of the obstacle meshes. This is done thanks to an algorithm looking for the intersection between the ray X from p_i to the target point and each obstacle mesh of M_{D_h}, accelerated by the use of the oriented bounding box (OBB) trees [Gottschalk et al., 1996].
2. Compute optimal trajectory by solving the SC. We first evaluate function f for each $p_i \in IZ_D$ using its corresponding deformed model M_{D_h}. Then we color IZ_D according to the values of $f(p_i)$ to obtain a dynamic risk map Map_D. In the same way, the evaluation of SC is done on the updated model M_D. Finally, we identify the most interesting point in IZ_d, and optimize it more accurately using a local derivative-free optimization algorithm (Nelder-Mead method).

> At each iteration of the optimization algorithm, a new candidate trajectory is proposed. Its deformed model M_{D_h} is determined based on its corresponding insertion point, and function f is evaluated. The optimization algorithm stops when the improvement of f falls under a threshold ε.

The overall algorithm including the two steps is detailed in Algorithm 2.

Algorithm 2: DBS Planning Algorithm

```
Data: $M_S$ : Initial 3D model of patient's brain
      $S$ : Initial skin mesh
      $Sim_{DB}$ : Patient's simulations file
      $HC$ and $SC$ : Hard and Soft constraints
Result: $T$ : Optimal trajectory in $E_D$
$Map_D$ : Dynamic risk color map

$IZ_d \leftarrow \emptyset$ ; $Map_d \leftarrow \emptyset$ ; $ST \leftarrow \emptyset$ ;
/*Resolution of Hard Constraints HC*/
foreach $p_i \in S$ do
    $h \leftarrow getHeight(p_i)$;
    $M_{D_h} \leftarrow \bigcup_{i=0 \to h} BS_i$;
    if $satisfy(p_i, HC, M_{D_h})$ then
        $IZ_D \leftarrow IZ_D \cup p_i$;
/*Resolution of Soft Constraints SC*/
/*Computation of Color Map*/
foreach $p_i \in IZ_D$ do
    $h \leftarrow getHeight(p_i)$;
    $M_{D_h} \leftarrow \bigcup_{i=0 \to h} BS_i$;
    $eval\_table \leftarrow evaluate(p_i, SC, M_{D_h})$;
$Map_D \leftarrow color\_insertion\_zone(IZ_D, eval\_table)$;
/*Computation of Optimal Trajectory*/
$T \leftarrow extract\_best\_solution(Map_D)$;
$prev\_eval = 1$;
$h \leftarrow getHeight(T)$;
$M_{D_h} \leftarrow \bigcup_{i=0 \to h} BS_i$;
$eval \leftarrow f(T)$;
while $prev\_eval - eval > \varepsilon$ do
    $T \leftarrow propose\_new\_candidate(NelderMead, IZ_D)$;
    $prev\_eval \leftarrow eval$;
    $h \leftarrow getHeight(T)$;
    $M_{D_h} \leftarrow \bigcup_{i=0 \to h} BS_i$;
    $eval \leftarrow f(T)$;
```

5.2.3 The system workflow

The presented DBS planning system is composed of two main units : planning and simulation, and uses other third-party frameworks : pyDBS, SOFA, and MITK.

First of all, we use pyDBS pipeline [D'Albis et al., 2014] to reconstruct a patient-specific 3D surface model of the brain from intra-operative MRI scans of the head. The tetrahedral meshes of the structures involved in the brain shift deformation are generated using CGAL library [cga, nd]. The biomechanical simulations are performed within the SOFA Simulation Open Framework Architecture (SOFA) framework [Faure et al., 2012]. For each input patient model, a set of deformed brain models is precomputed using simulations. They correspond to the different magnitudes of possible brain shift from a minimum to the maximum. We store all the intermediary deformed models and consider them as a patient-specific simulations database. The interest of using precomputed simulations is to save computational time during the optimization process, and to allow to run several successive constraint resolutions with different settings without the need to perform new simulations. On the planning side, the solver we implemented to optimize the electrode trajectories takes as an input a set of surgical rules described by neurosurgeons and formalized as geometric constraints in XML syntax (HC and SC). The constraints file is not patient-specific, and is only related to the description of the DBS intervention, which makes it easy to upgrade in case new rules are discovered. The other inputs of the planning unit are the surfaces from pyDBS, and the corresponding simulations database.The planning unit computes a patient's color map accounting for possible deformations, and proposes it to the surgeon in an interactive interface with many display facilities. The DBS surgical planning plugin is developed based on the The Medical Imaging Interaction Toolkit (MITK) framework [Wolf et al., 2005]. All the rules have been described in collaboration with an expert neurosurgeon from the neurosurgery department of Rennes University Hospital (Pontchaillou).

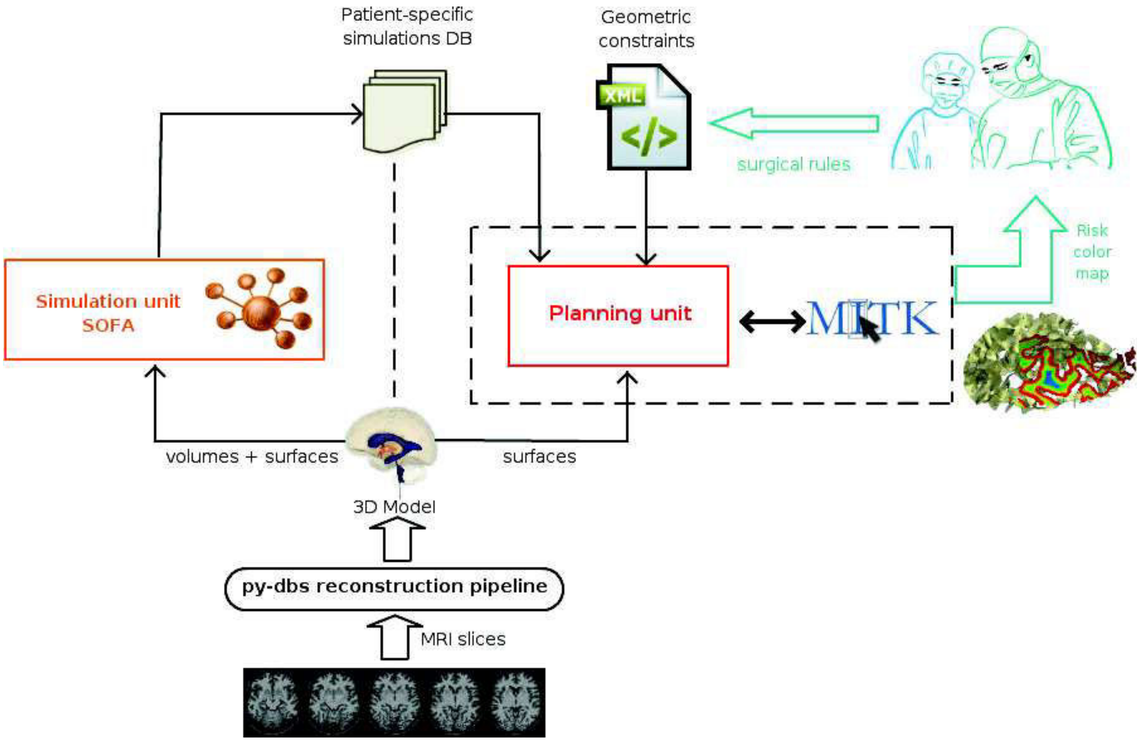

FIGURE 5.8 – Overview of the system

5.3 Experiments and Results

Our experiments consists in comparing our method for planning in deformable environment E_D with the previous planning method in static conditions E_S. Mainly on two aspects : to compare the feasible insertion zones resulting from the application of hard constraints HC, and the efficiency of the optimization approach in the presence of brain shift deformation.

Experimental data

We tested our approach on a single patient-specific 3D model from a retrospective case. The model consists of 3D triangular surface meshes of the sulci where blood vessels are usually embedded, ventricles, subthalamic nucleus, and a skin patch of the scalp.

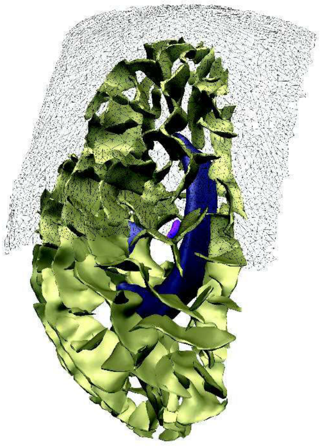

FIGURE 5.9 – Initial 3D model for the geometric solver

The sulci contain most of the blood vessels which are difficult to segment, and therefore they are considered as a geometric obstacle to be avoided during the planning. The ventricles represent another risky anatomical structure which should be avoided as well, while the center of the subthalamic nucleus is the anatomical target. During the planning phase, the skin patch is our initial solution space. The number of elements in the complete surface model is 83k., and the dimensions of the bounding box of the target mesh are 12 × 9 × 4 mm. The planning was performed on an Intel Core i7 running at 2.67 GHz with 8GB RAM workstation.

Physical model

In order to perform simulations, a volume mesh is required. The tetrahedral mesh of the brain is generated from the binary images, where intensities indicate if the voxels belong to the brain tissue. In addition, the simulation needs the surface mesh of the interior of the skull which has been extracted from a preoperative CT scan acquired in a preoperative phase. The number of tetrahedral elements and associated nodes are 8001 tetrahedra and 1975 nodes. The mechanical parameters are set to $\lambda = 1291$ Pa and $\mu = 1034$ Pa according to [Ferrant et al., 2002].

The patient-specific simulations DB contains 20 simulated brain shift levels, and all the simulations are generated on an Intel Core i7 running at 2.7 GHz with 8GB RAM laptop.

Test scenario

The test consists in applying the planning algorithms in both environments E_D and E_S, and comparing the obtained planning results :
As for the resulting feasible insertion zones IZ_S and IZ_D in E_S and E_D respectively, Table 5.1 shows the insertion zones sizes, computation times, and the ratio of the size of the insertion zone compared to the initial skin patch S.

Table 5.1 – Computation of the insertion zones : resulting size and computation times

	S	IZ_S	IZ_D
# Triangles	67920	17408	7868
Comp. time (s)	-	12	36
S coverage %	100	25.6	11.6

First of all, we notice that as we expected IZ_D is smaller than IZ_S which is due to the larger space occupied by the obstacles in deformable condition. Fig.5.10 shows the initial skin patch S, with the two insertions zones (static IZ_S and dynamic IZ_D). It can also be noticed that the percentage of IZ_D to IZ_S is equal to %45.2 which means that the feasible insertion zone is reduced by %54.8. This means that if the possible deformation due to brain shift is not taken into account in the planning, up to one half of the insertion zone mesh actually contains dangerous entry points in case of brain shift.

The reported time to build IZ_D is around 36 s which is 3 times higher than the time required to build IZ_S, but still keeps the approach compatible with clinical use. The time needed to build the color map is equal to 5 s in E_S and to 31 s in E_D.

In this experiment, we experimented different refinements of the initial mesh S. Finally, in the tested model the number of triangles was increased from 4245 to 67920 by implementing a deep subdivision to obtain a more precise color map.

The average time of a single simulation is equal to 1 minute. This emphasizes the interest of precomputing the simulations, to avoid to slow the planning down and allow for several runs with different settings.

Nelder-Mead optimization analysis

We opt for the aggregative approach, the weighted sum to solve the planning problem. The Nelder–Mead algorithm is used to calculate the optimal insertion settings in both conditions. Table 5.2 summarizes the performance of Nelder–Mead optimization algorithm in both E_S and E_D. We report the value of the evaluation of cost function f, the distance between the optimized ray and the obstacle meshes (ventricles and sulci), then we show the number of iterations and convergence time.

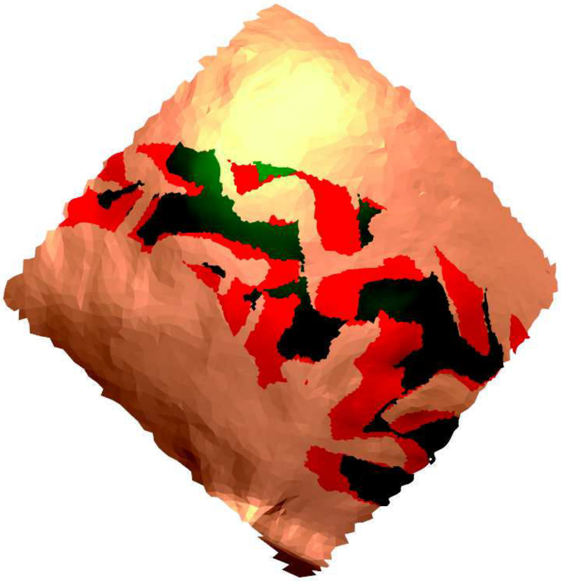

FIGURE 5.10 – S is the large orange patch, IZ_S is a subset of S and is the union of red and green shapes, and IZ_D is a subset of IZ_S and is the green mesh.

At last, the number of maximum deformation levels employed by the optimizer within the candidate points range.

TABLE 5.2 – Nelder-Mead performance in E_s and E_d

Nelder-Mead	E_S	E_D
eval(f) $[0,1]$	0.28	0.38
dist. from ventricles (mm)	11.87	7.39
dist. from sulci (mm)	5.13	3.12
# of iterations	31	21
time (s)	0.034	0.258
# of h levels used	-	3

The values in Table 5.2 show that the optimization algorithm used in E_S could also converge in E_D, and give an acceptable proposition for trajectory T that is sufficiently safe for DBS even in case of brain shift. The optimized trajectory in E_D was closer to the obstacles than the one in E_S but it could remain far enough from them according to surgeons standards. The resulting optimal trajectory in E_D is shown in Fig.5.11d.

Consequently, the best evaluation value in E_D (0.38) was not as good as the best one in E_S(0.28) but still acceptable. The optimization time is negligible in both cases.

Another interesting outcome we obtain after optimization is the fact that the best insertion regions (blue zones) in Fig.5.11 in static condition are not necessarily

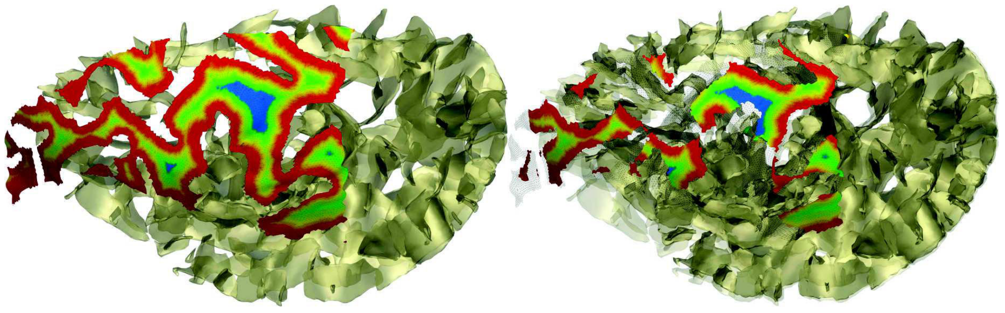

(a) E_S : Map_S on IZ_S (b) E_D : Map_S on IZ_D

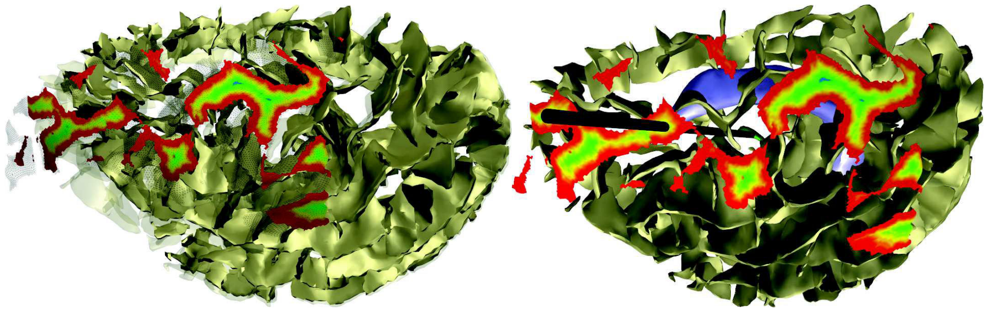

(c) E_D : Map_D on IZ_D (d) E_D : Optimal trajectory

FIGURE 5.11 – A risk map built in a static environment and superimposed on a static insertion zone (a) does not remain correct when it overlays on a dynamic insertion zone (b). The dynamic risk map is shown in (c), and the optimal electrode placement in (d).

the best insertion regions in the dynamic one, which means that the safest zones found when planning on still images will not necessarily remains the safest when taking the brain shift deformation into account.

5.4 Discussion and conclusion

We proposed a preoperative path planning method for DBS rigid electrode implantation which counts for possible intra-operative brain shift. In our approach, we coupled physical simulations with geometric constraint-based optimization to help the surgeon to anticipate the possible deformation during the planning in order to obtain more safe planning strategies.

We tested the feasibility of the method on a patient-specific clinical case. The obtained results firstly showed the variation of the safe feasible insertion zones for DBS interventions between the static and the dynamic conditions. This variation highlighted the interest of including the brain shift deformation during the planning phase, as it removes dangerous entry points that would not be detected otherwise. Secondly, although avoiding a sum of deformations from no brain-shift to a maximum possible brain-shift causes a high restriction of the feasible insertion zone, the remaining insertion zone could still provide an optimized entry point which is safe and efficient. Furthermore, Nelder-Mead optimization algorithm performed well in our test and succeeded to converge quickly to good solution in both cases. We also point out an advantage of our modular system 5.2.3 is that the simulations time is kept aside from the optimization time. In clinical routine, they could be precomputed just after acquiring the patient's MRI, and before the surgeon interacts with the planning software.

However, we are aware that the results presented on a single clinical case are not enough to completely validate the proposed method. The planning method should be applied on a larger series of patients to validate its performance.

Other further work could be also done to improve the system : on the first hand, the investigation of different optimization techniques to reveal safer solutions seems interesting for us, we will address this aspect in the next Chapter. On the second hand, further improvements could be done to raise the accuracy of the brain shift model by using more complex deformation such as a non-linear soft tissue model. For the moment, the co-rotational approach used in our model is a good trade-off between accuracy and computation time.

Finally, clinical validation is required to test the accuracy and robustness of the overall system, and the usability of the method in clinical routine.

6

PREOPERATIVE PATH PLANNING OPTIMIZATION STRATEGIES

"It is not the strongest of the species that survive, nor the most intelligent, but the one most responsive to change."
- Charles Darwin

In this chapter, we propose a new approach based on multi-objective dominance. We compare it to a classical aggregative weighted sum of the multiple constraints using a retrospective study performed by a neurosurgeon on 14 DBS cases. Then, we present an efficient Pareto dominance technique based on evolutionary algorithms, and we investigate three different optimization approaches by making a quantitative study on 30 cases. Finally, we summarize with a conclusion.

6.1 Introduction

Preoperative path planning for minimally invasive surgery is a multi-objective optimization problem consisting in searching the best compromise between multiple placement constraints. As summarized in the literature in Chapter 2 Section 2.4, its automation is usually addressed by turning the problem into mono-objective thanks to the aggregative approaches. Despite its intuitiveness, this approach is known for its incapacity to find all optimal solutions.

Our study on multi-objective optimization consists of two aspects :

1. The first aspect aims at highlighting the importance of using multi-objective approaches for surgical preoperative path planning. This is done by a comparison between a mono-objective aggregative approach (the weighted sum), and a multi-objective Pareto-based method.
2. The second aspect includes a proposition of an efficient Pareto-based evolutionary approach, followed by a quantitative comparison to two other planning techniques in order to materialize the benefit of proposed method.

In this chapter, in a first step we introduce a preoperative path planning approach based on Pareto dominance. Having obtained encouraging results, we go further in the MOO by investigating more efficient techniques based on evolutionary algorithms. Let us underline that the MOO techniques were investigated in static conditions as we will present in the rest of this chapter. First of all, we highlight the interest of a dominance-based method over a weighted sum using concrete values.

Why dominance-based methods ?

Having a problem with two objectives f_1 and f_2, weighted sums aggregate them into a single f_{ws} that can then be optimized by a mono-objective optimization algorithm.

Let's suppose a weighted sum function f_{ws} which aggregates f_1 and f_2 with weights values equal to 6 and 1 respectively. Thus, f_{ws} can be expressed by the equation : $f_{ws}(x) = 6 * f_1(x) + f_2(x)$. Having four points : $a(7, 330)$, $b(22, 171)$, $c(35, 148)$, $d(38, 75)$ in the solution space, their evaluations values are : $f_{ws}(a) = 372$, $f_{ws}(b) = 303$, $f_{ws}(c) = 358$, $f_{ws}(d) = 303$.

The limit of this method is that if the weights are constant, an aggregation creates a virtual affine hyperplane against which distances are measured to determine the best solutions (illustration in Fig. 6.1).

So far, a weighted sum optimizer minimizing f_{ws} will possibly present points b or d to the surgeon, because their weighted sum value 303 is the lowest of all (a ratio represented by the slope of line L). However, points a and c will not be presented to the surgeon because they have higher evaluation, even though they may be of high interest to the surgeon : indeed, point a minimizes f_1 much more, which could be very important if f_1 is distance to a blood vessel.

For a Pareto-based optimization algorithm, all the points of the curve (called a Pareto Front) are as good as points b or d because none of these points is dominated

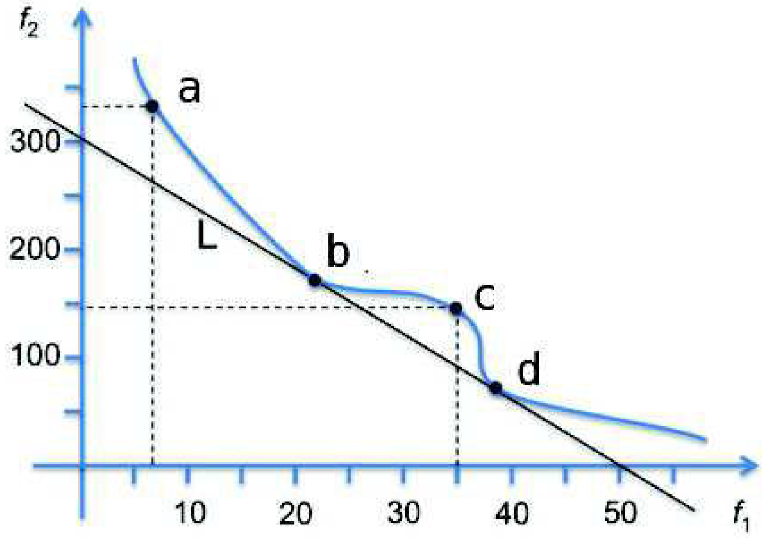

FIGURE 6.1 – Weighted sum method will detect b, d and miss a, c, while all the points lay on the Pareto front.

by any other points of the curve, *i.e.* there is no point of the curve that is better than a on both f_1 and f_2, *irrespective of any ratio.*

Pareto–based methods are already known and used in many fields such as economics, finance, optimal control, electronics, chemical engineering, etc. However, they are less known in the surgical domain. Even if there exists two related works in the domain of RFA [Seitel et al., 2011, Schumann et al., 2015] or radiotherapy planning [Craft, 2013], there has not been any study demonstrating the interest of using Pareto-based over weighted sum methods. To our knowledge, they are totally new to DBS planning. Therefore, the first phase of our work in optimization involves a thoughtful comparison between these two approaches.

6.2 Pareto front vs. weighted sum for path planning

The purpose of this work is to better understand and quantify the capacities and limits of different approaches to detect optimal solutions in the particular case of preoperative path planning. We propose a new optimality quantification approach based on dominance with the computation of a Pareto front. We compared it to a classical aggregative method based on a weighted sum. In this section, we detail both quality quantification approaches which were compared. Experiments were performed on the case study of DBS, but could be done in the same way for RFA for instance.

6.2.1 Initialization phase

Once $\mathcal{S}$ is delineated from the initial insertion zone IZ by applying the hard constraints, we perform an initialization phase involving the discretization of $\mathcal{S}$.

Usual automatic trajectory planning techniques, as explained before in this manuscript, involve the search of the best entry point thanks to an optimization phase converging to solutions optimizing the chosen quality measurement. However, the choice of an optimization method would differ for mono- and multi-objective cases : classical derivative-free optimization techniques are appropriate for mono-objective, while evolutionary approaches are more suitable and most frequently used for multi-objective techniques. The choice of such different optimizers could bias the comparison of the quality measurement method, as their convergence may differ. In order to have a fair comparison, we chose to avoid the use of optimizers at this stage, and focused on comparing only the quality measurement methods on a selection of candidate entry points.

To do so, we computed a discretization of the solution space by choosing a uniform distribution $\mathcal{S}$ of points over the surface of the feasible entry points, i.e. the points leading to a safe trajectory not crossing any forbidden anatomical structure or zone. The precision of the distribution was chosen such that we have one candidate trajectory per degree, if the center of rotation is the center of the targeted structure, which corresponds to approximately to one entry point every millimeter. This precision was assessed as sufficiently spaced by our expert neurosurgeon. An example of a distribution of candidate points over a surface of feasible points is shown in Fig. 6.2.

Figure 6.2 – Initial distribution of points on the feasible solution space $\mathcal{S}$

6.2.2 Method 1 : Pareto front

Method $\mathcal{M}_{PF}$ that we propose is a multi-objective method based on a Pareto ranking scheme. It consists in analyzing the mutual non-dominance of candidate entry points in an initial set $\mathcal{S}$. We define the *strict dominance* relationship *dom* between two individuals x and y of the solution space $\mathcal{S}$ for a set of n objective functions f_i as follows :

$$\forall \quad x, y \in \mathcal{S} \quad x \quad dom \quad y \quad \iff \forall i \in [1..n] \quad , \quad f_i(x) < f_i(y)$$

A solution x is *Pareto-optimal* if it is not dominated by any other solution in the solution space $\mathcal{S}$.

$$x \in \mathcal{S} \quad \text{is } \textit{Pareto} \text{ optimal} \quad \Longleftrightarrow \quad \forall \quad y \in \mathcal{S} \quad , \quad \neg(y \quad dom \quad x)$$

The set of all Pareto-optimal solutions is called a *Pareto front*. Let us denote $\mathcal{S}_{PF}$ the subset of points of $\mathcal{S}$ that belong to the Pareto front. Inside the front, no solution dominates another.

$$x \in \mathcal{S}_{PF} \quad \Longleftrightarrow \quad \forall \quad y \in \mathcal{S}_{PF} \quad , \quad \neg(y \quad dom \quad x) \quad \wedge \quad \neg(x \quad dom \quad y)$$

$\mathcal{S}_{PF}$ represents the Pareto-optimal points of $\mathcal{S}$ that can be reached using $\mathcal{M}_{PF}$. They are computed by comparing the points of the sampling in pairs and keeping only the points that satisfy the above property. Fig. 6.3 illustrates the Pareto-optimal solutions.

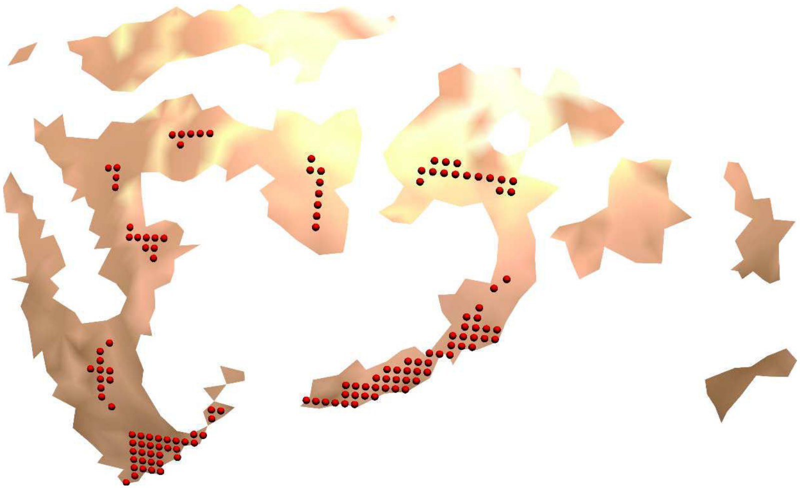

FIGURE 6.3 – Pareto front set $\mathcal{S}_{PF}$

6.2.3 Method 2 : weighted sum exploration

The weighted sum $\mathcal{M}_{WS}$ is a mono-objective approach for quantifying the quality of a solution based on the representation of all of the n objective functions f_i by a single aggregative cost function f to minimize. A weight w_i is associated to each f_i as follows :

$$f(\mathbf{x}) = \sum_{i=1}^{n} w_i . f_i(\mathbf{x}), \quad \mathbf{x} \in \mathbb{R}^N$$

where : $0 < w_i < 1$ and $\varSigma w_i = 1$ *(weights condition)*, and $\mathbf{x}$ represents the trajectory associated to a candidate entry point.

After that, a classical mono-criteria optimization technique is applied, in our case the *Nelder-Mead* method [Nelder and Mead, 1965], to find an optimum over the space of possible candidate trajectories. This method is straightforward and can always find a solution, but may prematurely converge to a local optimum. This problem can be overcome, for instance by using an initialization phase to start the optimization process close to a known approximated optimum, or close to j different optima to obtain j most optimal solutions, as explained for instance in [Essert et al., 2012].

Because surgeons have seen that this approach was limited, the state of the art in the domain implements an interactive weight exploration technique, that allows the surgeon to interactively change the weights to see possible alternative points. But even by changing the weights, points in concave Pareto fronts such as point c of Fig.6.1 will not be found. In order to show this, we compute the set of "optimal" points obtained with a weighted sum (WS) approach exploring automatically the possible weights combinations. For a fixed combination of weights $W = w_1, ..., w_n$, we can quantify the quality of each candidate entry point $p_j \in \mathcal{S}$ of the initial set by evaluating $f(\mathbf{x_j})$, where $\mathbf{x_j}$ is the trajectory corresponding to p_j. Then, the optimal entry point for combination W is the point of $\mathcal{S}$ with a minimal evaluation of f.

When varying weights w_i in W, different entry points of $\mathcal{S}$ minimizing f can be obtained. An exploration by varying systematically a high number of different combinations of weights is the most widely-used approach to approximate a Pareto front : the maximal coverage of method $\mathcal{M}_{WS}$ is the subset $\mathcal{S}_{WS}$ of all the points of $\mathcal{S}$ that can be found as optimal with this method (illustration in Fig. 6.4).

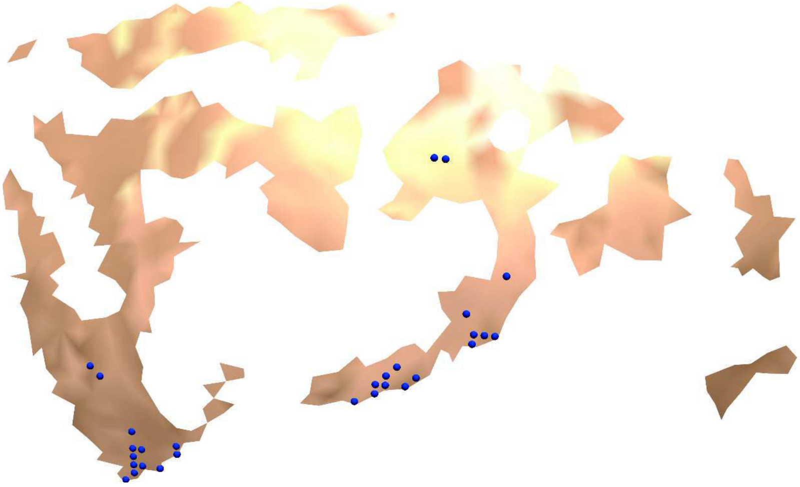

FIGURE 6.4 – Optimal point set in weighted sum $\mathcal{S}_{WS}$

To achieve this, a stochastic sampling of the n weights w_i satisfying the above-mentioned *weights condition* is built. A *Dirichlet* distribution [Ng et al., 2011] allows to obtain a uniform sampling of k different combinations of weights. Note that different combinations can lead to the same optimal entry point within a predefined finite set of candidate entry points, and this explains why from a large number of combinations(Fig. 6.5), few optimal points can be found(Fig. 6.4).

6.2.4 Evaluation study

The objective of the test is to compare the two methods on their coverage over the surface of candidate entry points, and their ability to find the maximal set of optimal solutions, and to check whether the points found as optimal by one method and not by the other one were likely to be chosen by neurosurgeons.

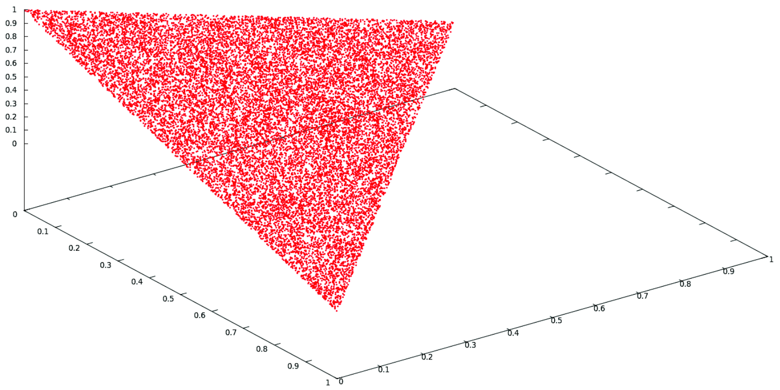

FIGURE 6.5 – Uniform sampling of $20,000$ combinations of parameters w_i using a *Dirichlet* distribution for $n = 3$ weights and associated objective functions.

To this end, we perform a retrospective study on 14 datasets from 7 patients who underwent a bilateral Deep Brain Stimulation of the Subthalamic Nucleus (STN) to treat Parkinson's disease.

Experimental datasets and preprocessing

Each dataset was composed of preoperative 3T T1 and T2 MRI with a resolution of 1.0mm x 1.0mm x 1.0mm, and a 3D brain model containing triangular surface meshes of the majority of cerebral structures, segmented and reconstructed from the preoperative images using the pyDBS pipeline described in [D'Albis et al., 2014], further description about the experimented data will be presented in Chapter 7. Among the 3D structures, we have the STN, a patch delineated on the skin as a search area for the entry points, the ventricles and the sulci that neurosurgeon try to avoid. The T1, T2 and 3D meshes were registered in the same coordinates system.

A second pipeline was implemented and executed on the 3D scene of each case to prepare the test. First a discretization $\mathcal{S}$ of the search space, as described in Section 6.2.1, was performed. The distribution contained between 0.93 and 1.29 point per mm^2 (average 1.07), representing an average of 2,320 sample points per case on an average surface of 2,158 mm^2. Then we computed the subsets $\mathcal{S}_{WS}$ and $\mathcal{S}_{PF}$ of points labeled as optimal respectively by methods $\mathcal{M}_{WS}$ and $\mathcal{M}_{PF}$, as described in Sections 6.2.2 and 6.2.3. Examples of subsets of optimal points proposed by both methods are presented in Figs. 6.3 and 6.4. We marked for each case the *difference set* $\mathcal{D}$ of points found by one method and not by the other $\mathcal{D}_{WS} = \mathcal{S}_{WS} - (\mathcal{S}_{WS} \cap \mathcal{S}_{PF})$ and $\mathcal{D}_{PF} = \mathcal{S}_{PF} - (\mathcal{S}_{WS} \cap \mathcal{S}_{PF})$, and computed their cardinality.

Experimental pipeline

An experienced neurosurgeon was asked to perform a test in 4 steps.

- **Step 1 : "Manual planning $\mathcal{M}_{MP}$".** This phase consisted in selecting interactively the target point and the entry point on the 2D T1/T2 slices. The chosen trajectory T_{MP} could be visualized and assessed in the 3D view to check if the position was satisfying. Let's denote this method $\mathcal{M}_{MP}$.

- **Step 2 : "Planning using method $\mathcal{M}_{WS}$".** In this phase, the target point chosen in step 1 was kept, and the surgeon had to choose an entry point among the ones proposed by method $\mathcal{M}_{WS}$. The color map and sliders could be used to assist the choice of trajectory T_{WS}.
- **Step 3 : "Planning using method $\mathcal{M}_{PF}$".** In this phase, the target point chosen in step 1 was also kept, and the surgeon had to choose an entry point among the ones proposed by method $\mathcal{M}_{PF}$. The sliders could be used to assist the choice of trajectory T_{PF}.
- **Step 4 : "Trajectories ranking".** This phase consisted in ranking the three trajectories T_{MP}, T_{WS} and T_{PF} chosen in steps 1-3. The ranking was blind as the three trajectories were randomly assigned a color, and the surgeon ranked the colors. An illustration of this step is shown in Fig. 6.6, where the colors have been set to match Figs. 6.3 and 6.4 for readability purposes. The ranking could be zero if the trajectory was finally marked as being really worse than the others and rejected. Trajectories could be equally ranked if they were identical or estimated to have a similar quality.

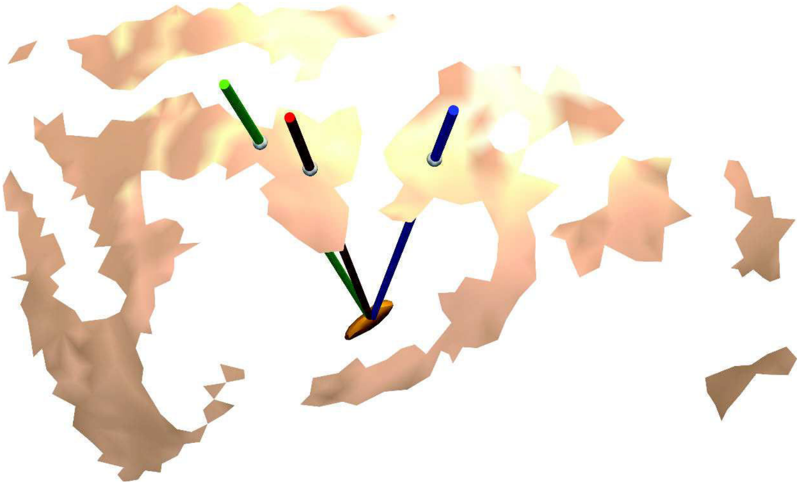

FIGURE 6.6 – Ranking step

The optimized criteria

The trajectory planning is submitted to a number of surgical rules. We have chosen to represent three of them, that seemed to be among the most commonly accepted rules, as objective functions for our experiment. Function f_1 represents the proximity to a standard trajectory defined by expert neurosurgeons and commonly used in the commercial platforms : 30° anterior and 30° lateral. Function f_2 represents the distance from the electrode to the sulci where the vessels are most often located, and that the surgeons try to avoid at best. Function f_3 represents the distance from the electrode to the ventricles, to avoid as well.

Experiments have been performed on an Intel Core i7 running at 2.67 GHz with 8GB RAM workstation. For all cases, the positions of the target/entry points, the final ranking, and the times required for each step were recorded.

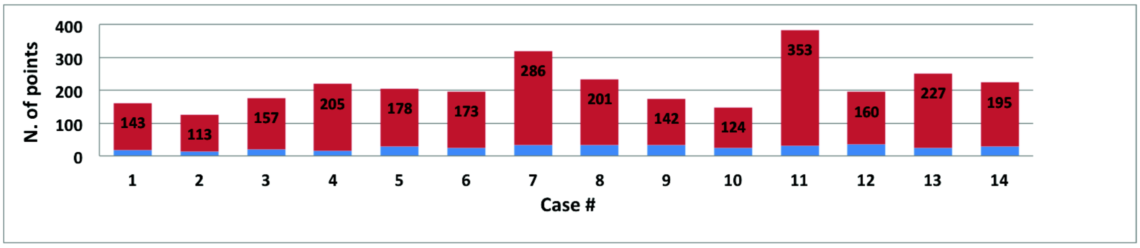

FIGURE 6.7 – Number of points in $\mathcal{S}_{WS}$ and $\mathcal{S}_{PF}$ for the 14 cases

6.2.5 Results

For all the cases, $\mathcal{S}_{WS} \subset \mathcal{S}_{PF}$. Average cardinalities are $|\mathcal{S}_{WS}| = 26$ and $|\mathcal{S}_{PF}| = 190$. Difference set $\mathcal{D}_{WS}$ was always empty, which means that all points found as optimal by $\mathcal{M}_{WS}$ were also proposed by $\mathcal{M}_{PF}$. On the contrary, method $\mathcal{M}_{PF}$ always found more points than method $\mathcal{M}_{WS}$. The chart in Fig.6.7 shows the number of points in $\mathcal{S}_{WS}$ and $\mathcal{S}_{PF}$. The average cardinality of the difference $\mathcal{D}_{PF}$ is 164, which represents 86.41% of the average number of points of $\mathcal{M}_{PF}$.

In order to determine if the points missed by $\mathcal{M}_{WS}$ were interesting points likely to be chosen by a surgeon, we analyzed the data recorded during the test. First, we could observe that $\mathcal{M}_{MP}$ ranked first in 2/14 cases, method $\mathcal{M}_{WS}$ ranked first in 5/14 cases, and method $\mathcal{M}_{PF}$ ranked first in 6/14 cases. In the remaining case, the entry points chosen using $\mathcal{M}_{WS}$ and $\mathcal{M}_{PF}$ coincided, so both methods were equally ranked in first position.

As $\mathcal{S}_{WS} \subset \mathcal{S}_{PF}$, for all cases where $\mathcal{M}_{WS}$ ranked first, the chosen point had also been proposed by $\mathcal{S}_{PF}$. Conversely, when $\mathcal{M}_{PF}$ ranked first, none of the entry points were also part of $\mathcal{M}_{WS}$. Presumably, the best possible solution was not available in $\mathcal{S}_{WS}$ so a sub-optimal alternative was chosen.

In order to see whether, in these kind of cases, reasonably close alternatives would be available in $\mathcal{S}_{WS}$, we computed the distances between entry points selected in $\mathcal{S}_{PF}$ and the closest point of $\mathcal{S}_{WS}$. Results are shown on the left part of Table 6.1. It can be observed that in one case over six (#12), the distance is higher than 16 mm, which means that no point was proposed by $\mathcal{S}_{WS}$ within the region of the selected entry point. This case is also the one having the highest difference in terms of coverage of optimal points between the two methods. In two other cases, the distance is higher than 4.8 mm, which is still far from the preferred location. For the other 3 cases, the distance ranges between 1.6 mm and 2.05 mm which may correspond to relatively reasonable alternatives.

TABLE 6.1 – Distances in mm between entry points selected with methods $\mathcal{M}_{PF}$ and $\mathcal{M}_{MP}$ and the closest alternative point in other automatic methods

Distance	$\mathcal{M}_{PF}$ ranked first						$\mathcal{M}_{MP}$ ranked first	
to :	2	6	9	11	12	14	7	13
$\mathcal{S}_{WS}$	2.05	4.83	1.67	1.90	16.05	5.92	2.83	1.49
$\mathcal{S}_{PF}$	-	-	-	-	-	-	1.16	0.87

It is also interesting to observe that for the two cases where $\mathcal{M}_{MP}$ was ranked first (#7 and #13), the distance between the manually proposed entry point and the closest point of $\mathcal{S}_{PF}$ (resp. 1.16 and 0.87 mm) was always lower than the closest point of $\mathcal{S}_{WS}$ (resp. 2.83 and 1.49 mm).

Finally, the average times taken for each of the three methods of selection were respectively 155 s. for $\mathcal{M}_{MP}$, 38 s. for $\mathcal{M}_{WS}$, and 42 s. for $\mathcal{M}_{PF}$. Of course, this measurement is biased because the target selection time is included only in $\mathcal{M}_{MP}$, as steps 2 and 3 consisted in only selecting an entry point. We did not record separately the time required to select the entry point, because in step 1 we chose to let the surgeon go back and forth between target and entry point position refinement to have a good accuracy. However, even considering that planning the target point took half of the time in step 1, steps 2 and 3 were still much faster. Besides, the improvement of speed was not at the cost of accuracy, as the selection of an automatically proposed entry point was ranked first in 12/14 cases.

The recorded times indicated that the automatic assistance was, in 12 cases over 14, both faster and more accurate than a manual planning, which further confirms the overall interest of automatic assistance to preoperative trajectory planning for Deep Brain Stimulation.

We recall that the MOO approach that we applied is merely a discretization method based on dominance rules, and discards any optimization technique to avoid biasing the results. Considering the interest outcomes we get from the tests, we will shift our focus to investigate efficient optimization techniques for multiple objectives.

Known for their performance, evolutionary algorithms seemed a promising approach to try on our planning problem. In the rest of this chapter, we will present the evolutionary based planning approach. We will start by a general introduction about evolutionary algorithms technique, afterwards we present the methods and the comparison.

6.3 Evolutionary-based method for path planning

Evolutionary algorithms (EAs) is a class of stochastic optimization methods for both mono and multi objective optimization problems inspired by Darwin's theory of evolution. They simulate the mechanisms of natural evolution process : start from an initial population pool representing the solution space, and create generations subsequently by a selection mechanism followed by variation techniques of recombination and mutation to mimic the natural capability of creating new living. The process is repeated until convergence to some satisfying offspring generation. Since the 1980s, these methods have proven themselves as a robust and efficient search mechanism in various problem domains such as in economics, biology, weather forecasting, computer sciences, etc. EAs are characterized by several features making them desirable for problems involving multiple conflicting objectives among them the maintenance of good candidate solutions, and the elitism mating selection process which recombines various solutions in an intelligent way to generate better solutions. Despite their performance, they are less known in the surgical domain, therefore, it seemed a promising approach to tackle our preoperative planning problem.

The class of evolutionary algorithms destined to solving multi-objective problems is reffered to as "MOEAs" for Multi Objective Evolutionary Algorithms. MOEAs are currently receiving growing interest from researchers with various backgrounds. Evolutionary algorithms (EAs), however, have been recognized to be possibly well-suited to multiobjective optimization since early in their development. Multiple individuals can search for multiple solutions in parallel, eventually taking advantage of any similarities available in the family of possible solutions to the problem. The ability to handle complex problems, involving features such as discontinuities, multimodality, disjoint feasible spaces and noisy function evaluations, reinforces the potential effectiveness of EAs in multiobjective search and optimization, which is perhaps a problem area where the evolutionary computation really distinguishes itself from its competitors. In MOEAs many approaches can be found : plain aggregating , population-based non-Pareto, Pareto-based, nich induction techniques.

Encouraged by the promising results of Pareto–based methods, and the efficiency of Multi Objective Evolutionary Algorithms (MOEAs) in many fields, we propose a Pareto-based MOEA for preoperative path planning in image-guided surgery.

In the following, we summarize the most well-known dominance-based MOEAs. Afterwards, we present our optimization choice.

6.3.1 Dominance-based MOEAs

Dominance-based MOEAs is a well-established technique of optimization for which an important amount of work was proposed. An extensive literature would perhaps mislead the reader, and would be out of the scope of this study : a detailed survey on MOEAs could be found in [Fonseca and Fleming, 1995].

In order to present our work, we will report some reference points algorithms for their very satisfying and relevant performance :

- Pareto Archived Evolution Strategy PAES [Knowles and Corne, 1999]
- Strength Pareto Evolutionary Algorithm SPEA [Zitzler and Thiele, 1998], and SPEA2 [Zitzler and Thiele, 2001]
- Pareto Envelope-Based Selection Algorithm PESA [Corne et al., 2000], and Region-based selection PESA-II [Corne et al., 2001]
- Non-dominated Sorting Genetic Algorithm NSGA [Srinivas and Deb, 1994], and NSGA-II [Deb et al., 2002]

The main distinction between the listed algorithms is the way they ensure the *elitism* which refers to the quality of a given individual or solution. The non-dominated individuals can be preserved either by maintaining an archive (as in : PAES, SPEA, SPEA2, PESA, and PESA-II), or by using deterministic replacement procedure (as in NSGA and NSGA-II).

Archive-based MOEAs

SPEA is a good a representative example of this algorithms class. Starting with an initial population and an empty archive (external set), an initialization phase is done firstly by copying all non-dominated population members to the archive. Parents are then selected from both the archive and the population by means of binary tournaments, the selection is followed by a variation process to get a child population. When the number of individuals in the archive exceeds the allowed size, similar solutions are removed by means of a clustering technique which preserves the variance in the non-dominated front. The offspring generations are evaluated and the reproduction is repeated until reaching the best generation. So far, the algorithm is dominance-based, it enables a good distribution for the individuals on Pareto front, with an elitism feature by keeping the strong members in the archive. The complexity of SPEA is $O(mN^2)$ with m for the number of objectives and N the archive's size. However, the archive size should be adjusted because even when applying a clustering technique to preserve a spread front, some outer solutions may be lost. In addition, even with the archive member fitness which is higher than its value for the population members, identical fitness values are attributed to all the population members although some of them are better than others.

Non-archive based MOEAs

The non-dominance genetic algorithm with its two versions NSGA and NSGA-II is a representative algorithm for non-archive based methods, they are extensions of classical genetic algorithms (GAs) and designed for continuous function multiple objective optimization problems. The algorithm rely on an evolutionary process with genetic operators including selection, crossover, and mutation. The population is sorted into a hierarchy of sub-populations called fronts based on the ordering of Pareto dominance. Unlikely to true-Pareto optimizers which treat all solutions on the same front as having the same fitness, similarity between members of each front is evaluated using an efficient crowding distance metric to promote a diverse front of non-dominated solutions. Though NSGA results were theoretically pleasant, it suffers from a high complexity level of order $O(mN^3)$ with m for the number of objectives and N the population's size. In the improved version NSGA-II the complexity has been reduced to $O(mN^2)$ making it practically plausible.

Comparison and justification of choice

Now that we summarized the most recognizable methods for multi-objective optimization using evolutionary algorithms, let us highlight the main decision elements which allow to choose the most appropriate method rather than others :

- As for the elitism feature, we think that it is more convenient to go for non-archive based option since using archive assigns the same fitness value for all non-dominated solutions (usually referred to by true-Pareto optimizers).
- Diversity preserving is a key element. Though, reducing the number of the required parameters to maintain a well spread Pareto front is beneficial. One of the key parameters in EAs is called the sharing factor/parameter σ_{share}, it can be considered as radius adjustment inside which all individuals share the same fitness (known as *fitness sharing* in EA literature), it is manually fixed in most of the cases. So, having a technique which enables an automatic fitness assignment without sharing is very valuable.
- The complexity order plays a key role in excluding some algorithms which are not convenient in the practical case. However, MOEAs attained a satisfying level of complexity in the improved versions of many techniques. A practically feasible complexity is of the order $O(mN^2)$ with m for the number of objectives

and N the solution space size.

— The selection and variation techniques should also be carefully used because the main advantage of EAs is their capability of producing new interesting solutions.

Motivated by the reported success of NSGA-II, and by the fact that it satisfies all the above mentioned concerns, in addition to the possibility of adapting it to fit better our search problem, our choice has converged to it. We list the main attracting features of NSGA-II and we refer again to them in detail in the methods section :

- it is designed for continuous MOEAs,
- it has a complexity of $O(mN^2)$,
- diversity preserving with a uniform sampling for all Pareto set,
- it avoids genetic drift. [1],
- it maintain elitism thanks to a new concept of dominance,
- no fitness sharing and no need to specify a sharing parameter σ_{share}.
- fitness and ranking is given for all the population individuals, and the niche [2] size is automatically adjustable thanks to an efficient diversity preserving technique,
- very less manual parameter assignment,
- possibility to use an adapted selection,mating, and mutation techniques.

After making a choice on NSGA-II, the second aspect of this work is to try it in our search problem, and to compare it with other methods.

6.3.2 Three methods to compare

Our purpose is to better understand and quantify the capacity and limits of the different optimization approaches in preoperative path planning. We investigated three of them : an aggregative method using a weighted sum of the multiple constraints, an multi-objective evolutionary method, and an exhaustive dominance-based method considered as a ground truth. For each approach, we extracted the set of all optimal insertion points based on dominance rules, and analyzed the common and differing solutions by comparing their coverage surfaces in the solution space.

Method 1 : weighted sum exploration

We repeat the same method explained in 6.2.3. For each combination of weights, we perform an optimization using Nelder-Mead method on a weighted sum cost function, and we keep the optimal points in a set. In this experiment, and after obtaining the optimal points set, we calculate a Pareto front from it. We denote the method $\mathcal{M}_1$, and $\mathcal{S}_1$ to be the set of optimal points obtained using $\mathcal{M}_1$. Then we filter out the set of optimal points in $\mathcal{S}_1$ by computing its Pareto front $\mathcal{S}_1\mathcal{F}_1$. We decided to do this filtering to compare a the Pareto-front later with the Pareto fronts obtained using the two other methods.

---

[1] See Appendix B for genetic drift phenomenon.

[2] See Appendix B for niching scheme concept in GAs.

Method 2 : NSGA-II

The second method relies on the NSGA-II algorithm with our adaptation for the different genetic operations. We refer to this method by $\mathcal{M}_2$.

Before presenting $\mathcal{M}_2$, we will explain the basic genetic operations we use in making new generations :

Selection

The selection process consists in choosing two or more individuals which are called parents to mate. Many techniques could be implemented to choose the parents. Mainly, the selection could be *non-restrictive* by granting all individuals in the current population an equal chance to participate in the recombination process for the offspring ; or *restrictive* in which only on the individuals that possess good fitness values are selected to mate. In our implementation, we tried two types of selection :

1. Tournament selection : it is a non restrictive selection method which involves running a number of "tournaments" among many individuals chosen randomly from the population. The "winner" individual of every tournament, which has the best fitness value, is then selected for a crossover process.
2. DBX : the Dominance Based Restricted mating is a selection (followed by a crossover process) proposed in [Rudenko and Schoenauer, 2004]. A first mate is chosen using the usual selection procedure of the EA at hand, if the chosen individual is non-dominated and dominates some other individuals in the population, its mate is chosen among those. Otherwise, the mate is chosen using the usual selection procedure.

Recombination or Crossover operators

The crossover operator is independent from the selection strategy (restricted or not). It is also believed to be the main search operator when using genetic algorithms because it decides the way the new solutions are generated. An adequate crossover operator should consider a couple of elements : firstly, the problem variables should be represented tightly. Otherwise, the crossover operator cannot combine two solutions together. Secondly, good parts of the variables should be combined to obtain better offsprings.

In $\mathcal{M}_2$, we used BLX-α [Eshelman, 1993], in which an offspring c_k is generated by a random linear recombination of the parents p_1 and p_2 as follows :

$$c_k = (1 - \gamma_i) p_{1,k} + \gamma_i p_{2,k}$$

where $\gamma_i = (1 + 2\alpha) u_i - \alpha$ with u_i a random number between 0 and 1, and $\alpha = 0.5$ in our experiments.

Mutation operator

Aside with the crossover operator, mutation is a genetic operator which is used to maintain diversity from one generation to another. This operator mimics the biological mutation phenomenon, where a permanent change of the nucleotide sequence of the genome of an organism may occur resulting in a new chromosome. Despite its importance, mutation is less likely to occur than crossover (as it is the case in nature), and this is usually decided by means of a parameter called *mutation rate* r_m which should be fixed for a certain problem. The higher r_m is, the more likely the mutation is to happen. Mutation mechanism is simple, it is done by altering one or more gene values to produce a new individual. Many mutation techniques are proposed in the literature. However, in NSGA-II, a polynomial mutation operator is commonly used and is prone to provide good results.

We used a classical *polynomial mutation* operator defined as follows :

$$c_k = c_k + (c_k^u - c_k^l)\delta_k$$

where $c_k^u = \dfrac{c_k - b^l}{b^u - b^l}$ and $c_k^l = \dfrac{b^u - c_k}{b^u - b^l}$, with b^u, b^l the upper and lower bounds of the solution space $\mathcal{S}$, and their variance represents the maximum permissible change in the child. δ_k is a small random variation calculated via a polynomial distribution.

$$\delta_k = (2r_k)^{\dfrac{1}{\eta_m + 1}} - 1 \text{ , if } r_k < 0.5$$

$$\delta_k = 1 - [2(1 - r_k)]^{\dfrac{1}{\eta_m + 1}} \text{ , if } r_k \geq 0.5$$

where η_m is the mutation distribution index, its experimented good values are usually between 10 and 20, and r_k is an uniformly sampled random number between (0, 1).

Diversity preserving

In addition to the fitness value, a new parameter called *crowding distance* is calculated for each individual. The crowding distance is a measure of how close an individual is to its neighbors. Large average crowding distance will result in better diversity in the population. For each objective function f_i, we evaluate all the individuals by assigning a fitness value (corresponds to the evaluation value of a soft constraint function), and a crowding distance value.

For a given solution i, and a function f_m, the distance value for a single objective function is the absolute normalized difference in the function values of two adjacent solutions.

$$i_{distance} \leftarrow i_{distance} + f_m(i+1) - f_m(i-1))/(f_m^{max} - f_m^{min})$$

where $i_{distance}$ is the crowding distance assigned to the solution i, $f_m(i+1), f_m(i-1)$ are the fitness values of f_m for the successor and predecessor solutions of i on the same front, and f_m^{max}, f_m^{min} are the highest and lowest fitness values on the front.

Fig. 6.8 illustrates the crowding distance for two individuals.

Respectively to sharing techniques, a large average crowding distance will result in better diversity in the population.

To compare different solutions, a crowded-comparison operator $\prec_n$ is designed. For two solutions i and j in $\mathcal{S}$, $\prec_n$ is defined as follows :

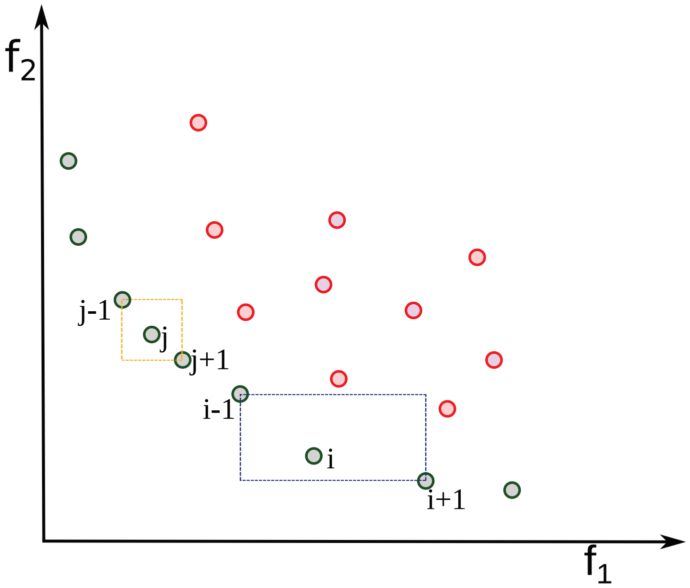

FIGURE 6.8 – Illustration of the crowding distance for two solutions : solution i is considered to be better than j because they are on the same front and i has a bigger crowding distance than j (see rectangle's area).

$$i \prec_n j \text{ if } (i_{rank} < j_{rank}) \text{ or } ((i_{rank} = j_{rank}) \text{ and } (i_{distance} > j_{distance}))$$

This means that when two solutions are on different Pareto fronts, the solution which is situated on a front with a lower index is better, and when both solutions are found on the same Pareto front, the solution with the higher crowding distance value is considered better than the other.

The algorithm

NSGA-II as presented by [Deb et al., 2002] in detailed in Appendix B. Basically, the main algorithm involves two phases : Firstly, an *initialization phase* in which an initial population $\mathcal{P}_0$ of size N is selected randomly from an initial solution space $\mathcal{S}$. All the individuals are evaluated using the three objective functions described in Chapter 3 Section 3.2.2 and ranked on different fronts using the following method : firstly, all individuals on the Pareto front are ranked 1 and removed ; then, all individuals from the new front are ranked 2 and this new front is removed, a.s.o. until there are no more individuals in the population. In the end, the population is ranked in r ranks, corresponding to r Pareto fronts F_1 to F_n as illustrated in Fig. 6.9. For each solution, a *crowding distance* value is assigned as explained in 6.3.2.

Secondly, an *iterative phase* is used to create the new generations.

1. A generational evolutionary engine creates an offspring population $\mathcal{Q}_n$ of size N by selecting two parents using a *DBX* selection on $\mathcal{P}_n$ based on the individuals' rank. Offsprings are created by a BLX-α crossover and a polynomial mutation and all children are evaluated along the three different functions.

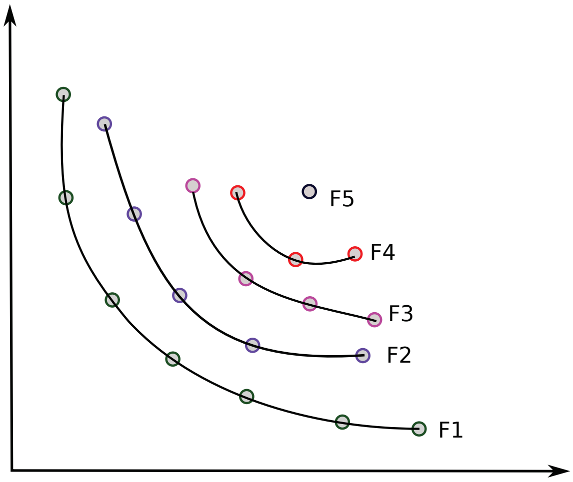

Figure 6.9 – Solutions grouped in different Pareto fronts according to non-dominance sorting algorithm.

2. Then, a new rank is established for population $\mathcal{P}_n + \mathcal{Q}_n$ as described above, and a new population $\mathcal{P}_{n+1}$ is formed by adding solutions from the first, second, third, ... fronts until the population size is reached. The solutions of the last accepted front are sorted according to the crowded distance metric, and a new iteration can start based on population $\mathcal{P}_{n+1}$.

The population is evolved until a pre-determined number of generations is reached. This non-dominance and crowding-comparison approach guides the selection process at the various stages of the algorithm towards a uniformly spread-out Pareto optimal front thanks to a density-estimation metrics without need of a sharing parameter.

Complexity Analysis

For each solution x in the second or higher level front, the domination count n_x can be at most $N-1$. Thus, each solution x will be visited at most $N-1$ times before its domination count becomes zero. At this point, x is assigned a non domination level and $n_x \leftarrow 0$ and will never be visited again. Since there are at most $N-1$ such solutions, the total complexity is $O(N^2)$, and the overall complexity of the procedure is $O(mN^2)$, where m is the number of objectives and N the population's size, making it usable in a reasonable time for our kind of application. If N is really large, other algorithms such as ASREA or G-ASREA [Sharma and Collet, 2010a, Sharma and Collet, 2010b] have been devised that have an $O(maN)$ complexity (where a is an archive of size $10m$) and that can be massively parallelized.

NSGA-II setup

In this method, the initialization is done with a population size of 2,000 individuals selected randomly over the surface of the solution space (Fig. 6.10). It is interesting to note that the surface of the search space being about 2,000 mm^2 in average, we also have an average of approximately one point per mm^2, knowing that the current resolution of usual MRI images is 1 mm^2.

The DBX crossover was applied with a probability equal to 0.9 and a crossover distribution index eta_c =10, while the polynomial mutation function was applied with a probability equals to 0.5 and a mutation distribution index $\text{eta}_m = 5$.

The algorithm is run over 10 generations. The number of generations was determined experimentally : new solutions could not be found anymore in the Pareto front when increasing the number of generations.

FIGURE 6.10 – Initial random population of 2000 points (red) over the search space (triangular mesh).

Method 3 : Quasi-exhaustive dominance-based method

The third method $\mathcal{M}_3$, based on a Monte-Carlo approach, is considered as a ground truth for our experiments. It consists in analyzing the dominance on a very large distribution of randomly sampled points in the solution space. Let us denote $\mathcal{S}_3$ the set of samples. We compute the Pareto front $\mathcal{S}_3\mathcal{F}_1 \subset \mathcal{S}_3$ according to the dominance rule described above. Fig. 6.11 shows the dense sampling of the initial solution space.

6.3.3 Experimental pipeline

The objective of the test was to compare the three methods on their coverage over the surface of candidate entry points, and their ability to find the maximal set of optimal solutions.

FIGURE 6.11 – Initial random population of 20000 points over the search space (triangular mesh).

To this end, we have implemented a pipeline illustrated in Fig. 6.12. Starting from the initial space of candidate entry points $\mathcal{S}$, it proceeds as follows :

Step 1 : Optimal sets

We compute $\mathcal{S}_1$ containing the 60.000 best solutions obtained when running Nelder-Mead optimization $\mathcal{M}_1$. and keeping best three trajectories for 20.000 times on different random combination of weights. We compute $\mathcal{S}_2$ in $\mathcal{M}_2$ using NSGA-II according to the settings described in Section 6.3.2. Finally we compute $\mathcal{S}_3$ containing a sample of 100.000 random entry points with the quasi-exhaustive search method $\mathcal{M}_3$.

Step 2 : Pareto fronts

For $\mathcal{S}_1$, $\mathcal{S}_2$, and $\mathcal{S}_3$, we compute the first Pareto fronts, respectively named $\mathcal{S}_1\mathcal{F}_1$, $\mathcal{S}_2\mathcal{F}_1$, and $\mathcal{S}_3\mathcal{F}_1$, according to the dominance rule. These sets contain the non-dominated solutions from their source sets.

Step 3 : Non-dominance test

In this step, we filter $\mathcal{S}_1\mathcal{F}_1$, $\mathcal{S}_2\mathcal{F}_1$, and $\mathcal{S}_3\mathcal{F}_1$ by eliminating the points that are dominated by points found by another method using a non-dominance (ND) test. By filtering front $\mathcal{S}_i\mathcal{F}_1$ with points of front $\mathcal{S}_j\mathcal{F}_1$, we obtain the set $\mathbf{ND}_{ij}$ of points of $\mathcal{S}_i\mathcal{F}_1$ that are not dominated by points of $\mathcal{S}_j\mathcal{F}_1$. In the rest of the paper, we will call these points *elite points* of $\mathcal{S}_i\mathcal{F}_1$. The results are six subsets named *NDsets* : $\{\mathbf{ND}_{12}, \mathbf{ND}_{13}\} \subset \mathcal{S}_1\mathcal{F}1$, $\{\mathbf{ND}_{21}, \mathbf{ND}_{23}\} \subset \mathcal{S}_2\mathcal{F}1$, and $\{\mathbf{ND}_{31}, \mathbf{ND}_{32}\} \subset \mathcal{S}_3\mathcal{F}1$.

Step 4 : Distance filter

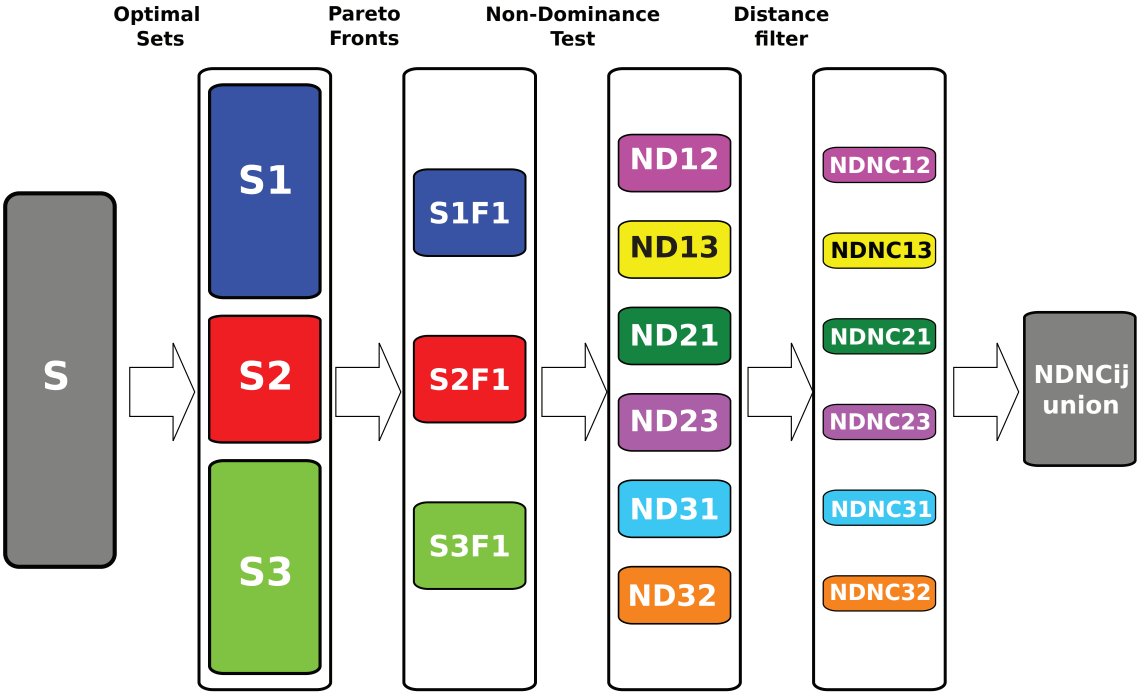

FIGURE 6.12 – Sets pipeline

Finally, we noticed that the $\mathbf{ND}_{ij}$ sets may contain solutions which are very close in terms of locations (and therefore evaluations). Thus, we added another filter keeping only the distinct solutions, using an Euclidean distance metric. The result of the filter is six subsets named *NDNCsets* $\mathbf{NDNC}_{ij} \subset \mathbf{ND}_{ij}$, with $\mathbf{NDNC}_{ij}$ containing points from $\mathcal{S}_i\mathcal{F}1$ that are not dominated by any point of $\mathcal{S}_j\mathcal{F}1$ and that are not located close to a point of $\mathcal{S}_j\mathcal{F}1$(NDNC stands for Not Dominated Not Close). In other words, $\mathbf{NDNC}_{ij}$ covers areas containing elite points found by method $\mathcal{M}_i$ but no elite points found by method $\mathcal{M}_j$. After that the closest points have been clustered in order to highlight the areas of the surface of candidate points where elite points have been found by one method and not by another.

Comparison of the three methods

The number of points in the Pareto fronts is not a good indicator of the ability of a method to discover points where other methods couldn't, as it also strongly depends on the location of the points and their density. We have chosen to compare the coverage areas instead of the number of points.

We have first subdivided the triangular mesh representing the surface of possible candidate entry points on the skin. The level of subdivision has been chosen empirically. The triangles need to be not too small otherwise they would be reduced to the size of a single point and we have no benefit of using surfaces instead of points, and not too large otherwise the precision would be too low. The average size of a triangle has been set to a maximum of 1 mm^2.

For each set, we have located all the triangles containing at least one of its points, and created a surface as the aggregation of all the triangles. The areas of the created surfaces have been computed.

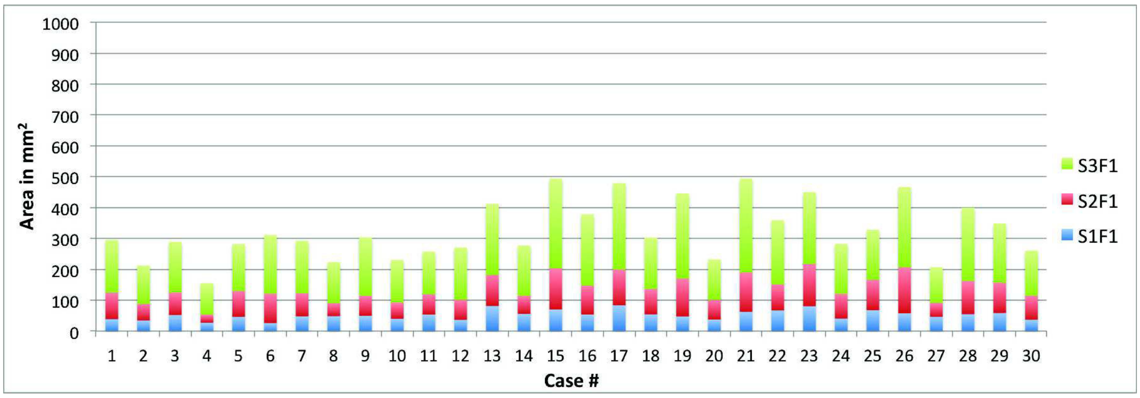

FIGURE 6.13 – Surfaces areas of the Pareto fronts in the three methods

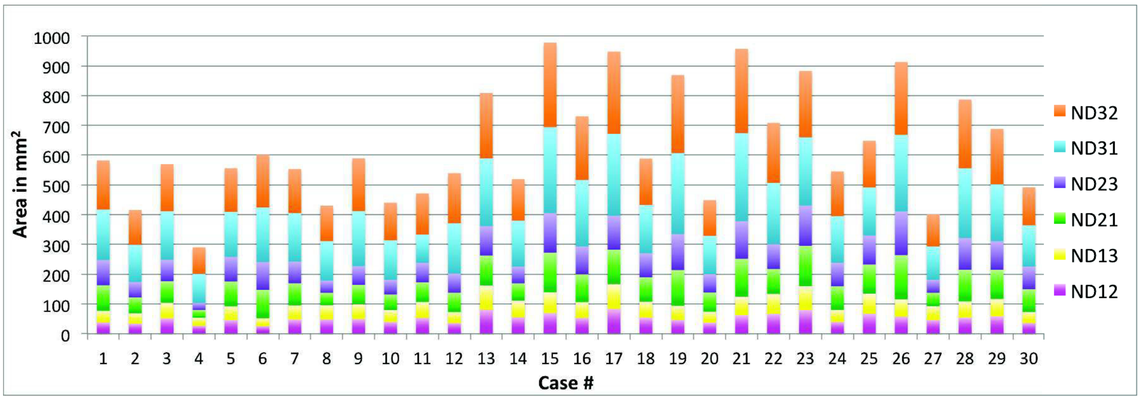

FIGURE 6.14 – The six non-dominated sets for each of the 30 datasets

Use-case and experimental data

We have performed our tests on 30 retrospective datasets of preoperative images of 15 patients from 2 different hospitals who underwent bilateral DBS implant. All were treated for Parkinson's disease, and the target was the subthalamic nucleus. A model consists of triangular surface meshes of the sulci, the ventricles, the subthalamic nucleus, and a skin patch representing the initial solution space $\mathcal{S}$. More details about the experimental datasets will be given in Chapter 7. Experiments have been performed on an Intel Core i7 running at 2.67 GHz with 8GB RAM workstation.

6.3.4 Results

The results on the 30 cases are summarized in the three charts of Fig. 6.13, 6.14, and 6.15 that illustrate the quantitative information about the solution surfaces areas. The snapshots of Figs. 6.16 to 6.19 illustrate the results on case #26.

Fig. 6.13 shows the areas covered by the Pareto fronts for each of the three methods. As expected, the surfaces covered by the reference method $\mathcal{M}_3$ are the largest. Among the two optimization methods, $\mathcal{M}_2$ provides the largest coverage with a mean of 85.23 mm^2 compared to 51.75 mm^2 for $\mathcal{M}_1$. In Fig. 6.16 the three fronts are superimposed over the initial solution space mesh (the zone of the scalp corresponding to feasible entry points). It can be noticed that the solutions of $\mathcal{M}_1$

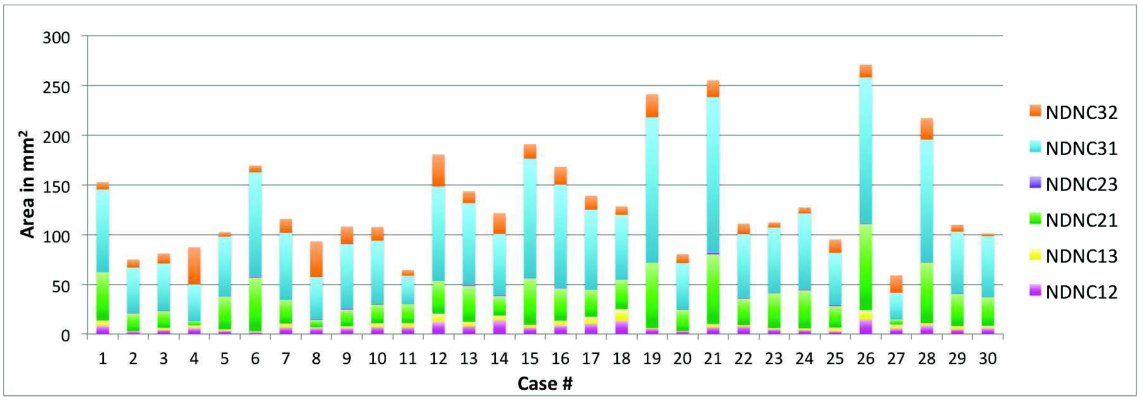

FIGURE 6.15 – The six non-dominanated not-close sets for each of the 30 datasets

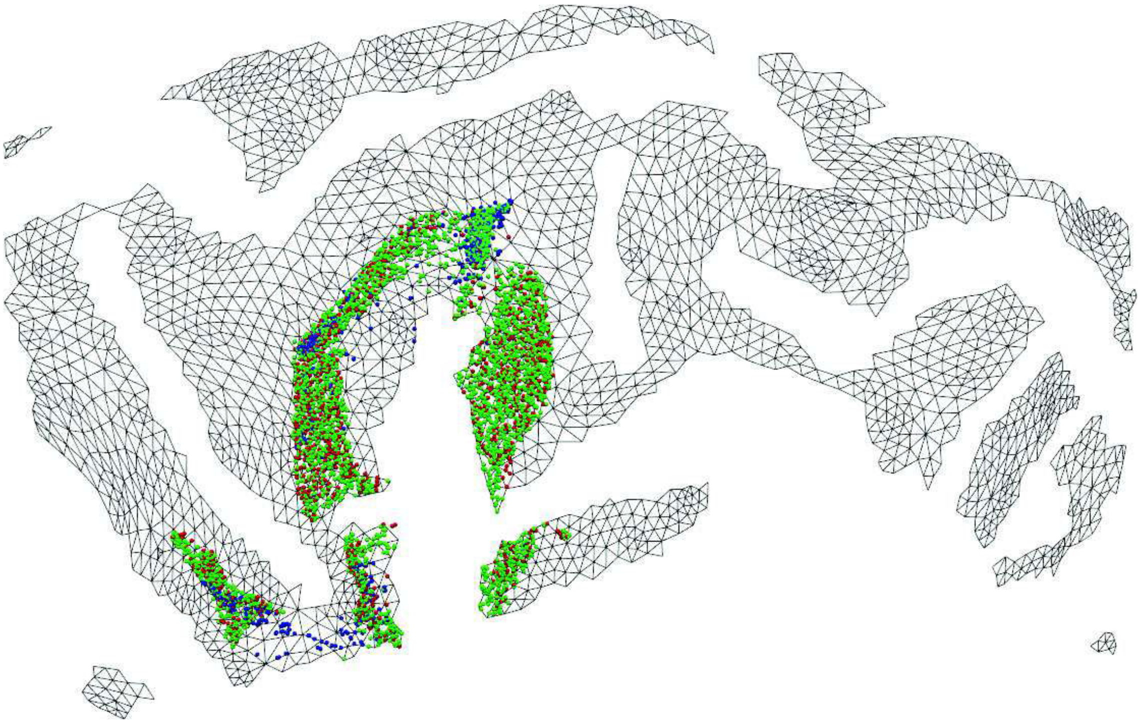

FIGURE 6.16 – Overview of the surface of possible entry points, with the three Pareto fronts : $\mathcal{S}_1\mathcal{F}_1$ in blue, $\mathcal{S}_2\mathcal{F}_1$ in red, $\mathcal{S}_1\mathcal{F}_1$ in green

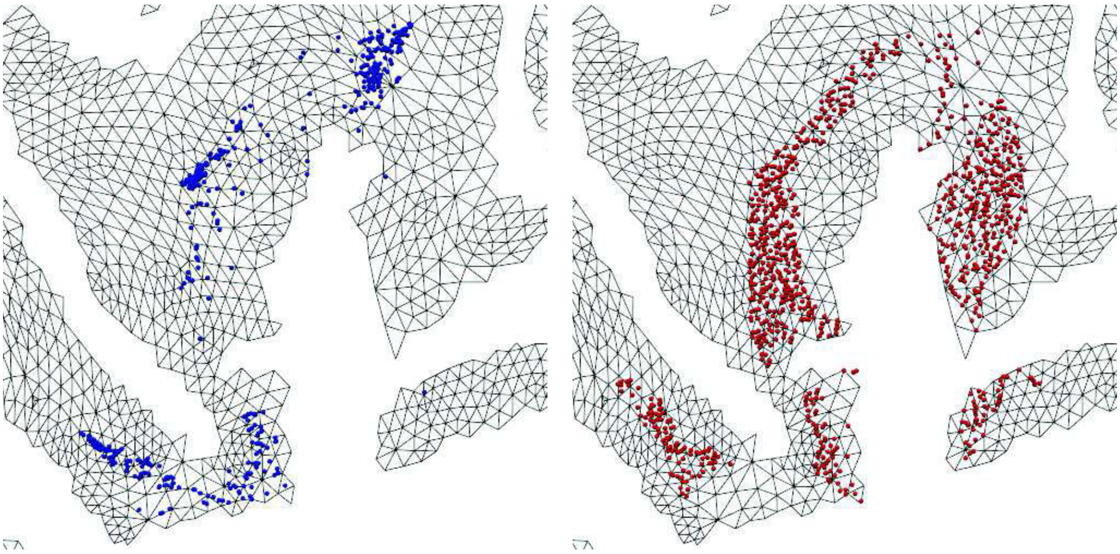

(a) $\mathcal{S}_1\mathcal{F}_1$ (b) $\mathcal{S}_2\mathcal{F}_1$

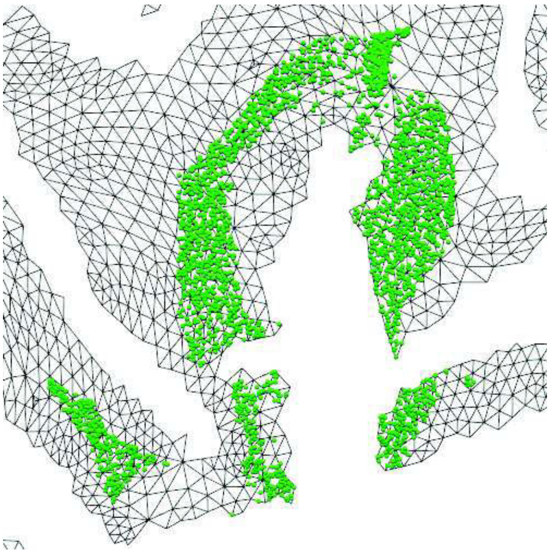

(c) $\mathcal{S}_3\mathcal{F}_1$

FIGURE 6.17 – Zoom on the Pareto fronts of $\mathcal{M}_1$ in blue, $\mathcal{M}_2$ in red, and $\mathcal{M}_3$ in green

and $\mathcal{M}_2$ are different, and they are more or less contained in the solutions of $\mathcal{M}_3$. A zoom on the area of interest is shown in Fig. 6.17 for each of the fronts separately. In Figs. 6.18a and 6.18b, the solutions of $\mathcal{M}_1\mathcal{F}_1$ and $\mathcal{M}_2\mathcal{F}_1$ are superimposed on the solutions of $\mathcal{M}_3\mathcal{F}_1$, allowing to compare visually the coverage of $\mathcal{M}_1$ and $\mathcal{M}_2$ compared to method $\mathcal{M}_3$.

We can see in Fig. 6.14 the areas of the non-dominated solution sets $\mathbf{ND}_{ij}$ surfaces for two methods at a time. It can be noticed that the areas of solutions detected by $\mathcal{M}_1$ and $\mathcal{M}_2$ which are not dominated by solutions in $\mathcal{M}_3$ are relatively small (see $\mathbf{ND}_{13}$ and $\mathbf{ND}_{23}$) since that $\mathcal{M}_3$ is a quasi-exhaustive method and supposed to detect the maximum number of solutions. Despite that, both $\mathcal{M}_1$ and $\mathcal{M}_2$ are able to find a few solutions more interesting than $\mathcal{M}_3$ thanks to the efficiency of opti-

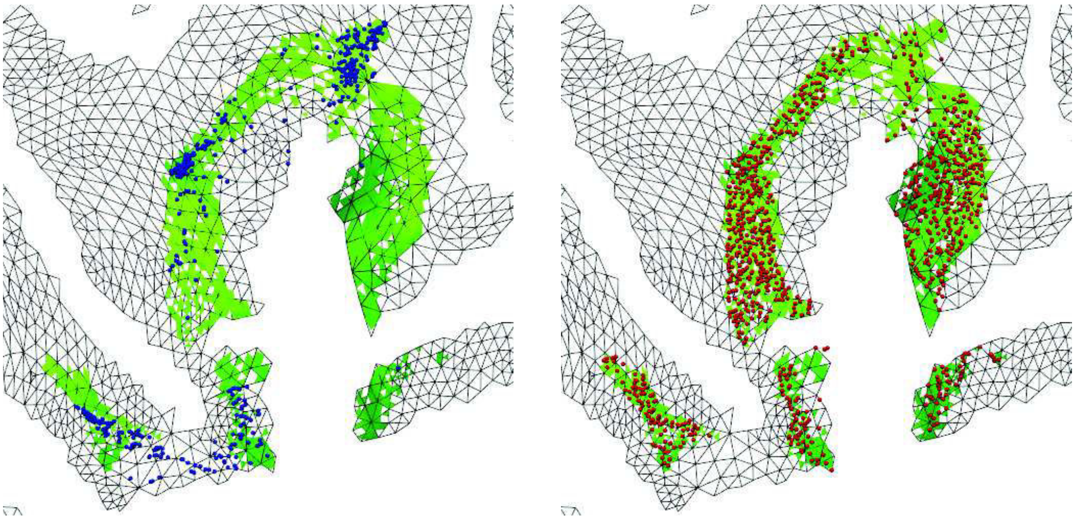

(a) $\mathcal{S}_1\mathcal{F}_1$ points over $\mathcal{S}_3\mathcal{F}_1$ surface (b) $\mathcal{S}_2\mathcal{F}_1$ points over $\mathcal{S}_3\mathcal{F}_1$ surface

FIGURE 6.18 – Coverage of methods $\mathcal{M}_1$ and $\mathcal{M}_2$ compared to $\mathcal{M}_3$

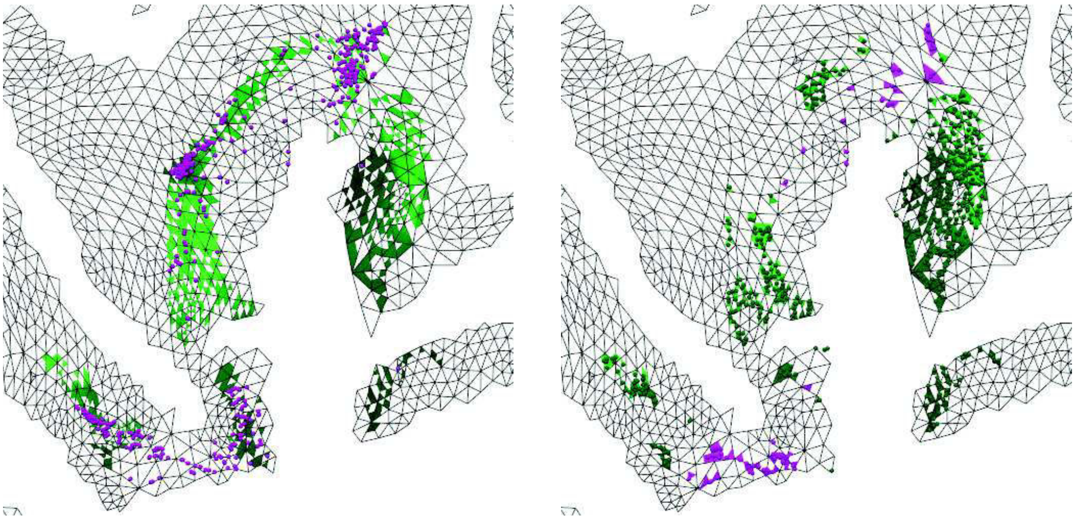

(a) **ND**$_{12}$ points over **ND**$_{21}$ surface (b) **NDC**$_{12}$ and **NDC**$_{21}$

FIGURE 6.19 – Comparison between coverage by elite points of methods $\mathcal{M}_1$ and $\mathcal{M}_2$

mization. When comparing $\mathcal{M}_1$ and $\mathcal{M}_2$, we can observe that both methods could find elite points not discovered by the other (see **ND**$_{12}$ and **ND**$_{21}$, both in Fig. 6.14 and Table 6.2), with a small advantage for method $\mathcal{M}_2$. This can also be observed on the snapshot of Fig.6.19a that displays the coverage of **ND**$_{12}$ over **ND**$_{21}$.

The non-dominated non-close solutions sets (NDNC sets) allow to highlight areas where some methods can propose solutions and others do not. The large areas missed by methods $\mathcal{M}_1$ and $\mathcal{M}_2$ can be visualize in Fig. 6.19b.

The most remarkable information is that the areas of elite points found by $\mathcal{M}_3$ and not by $\mathcal{M}_1$ (corresponding to **ND**$_{31}$ in Fig. 6.14) are very large, which emphasizes the fact that the mono-objective weighted sum approach can miss a large

Table 6.2 – Mean coverage of the solution space by methods 1 and 2 compared to each other and to method 3

	$\mathcal{S}_1\mathcal{F}_1$		$\mathcal{S}_2\mathcal{F}_1$		$\mathbf{ND}_{12}$	$\mathbf{ND}_{21}$	$\mathbf{NDNC}_{12}$	$\mathbf{NDNC}_{12}$
	area	% of $\mathcal{S}_3\mathcal{F}_1$	area	% of $\mathcal{S}_3\mathcal{F}_1$				
AVG	51.75	28.35	85.23	44.96	51.68	84.79	6.84	32.53
STD	15.02	6.67	30.06	8.02	15.01	29.82	3.40	19.57

number of interesting solutions. The zones detected by $\mathcal{M}_3$ and not by $\mathcal{M}_2$ are smaller ($\mathbf{ND}_{32}$ in Fig. 6.14) since that $\mathcal{M}_2$ and $\mathcal{M}_3$ have close concepts. Table 6.2 summarizes coverage for the comparison between $\mathcal{M}_1$ and $\mathcal{M}_2$.

Another important information is that none of the experimented methods were able to find the totality of the solutions. Significant areas are found by each of the methods and not by the others. This is due to several factors. The quasi-exhaustive method does not optimize the solutions and is dependent on the random sorting, which make that it can miss good solutions. The results of the weighted sum confirm again the well-know drawbacks of this method, that leads to an inhomogeneous distribution of the solutions over the Pareto front. Evolutionary method $\mathcal{M}_2$ is a compromise between fast computation time and number of tested points, and a better coverage of the area would be at the price of a higher number of points and longer computations.

The computation times are about 20 mn for method $\mathcal{M}_1$, about 30 sec. for $\mathcal{M}_2$, and 5 mn for method $\mathcal{M}_3$. Even if $\mathcal{M}_3$ is the one providing the best coverage, it is not usable in a reasonable time compatible with clinical routine, whereas method $\mathcal{M}_1$ can provide a single updatable result in a few seconds. This is why we think that hybrid methods for optimization or for display in GUI, or extensions of weighted sum method [Kim and de Weck, 2006] should be investigated.

6.4 Disscussion and conclusions

The automatic trajectory planning techniques that have been proposed for DBS in the literature are based on mono-objective optimization approaches that combine different criteria through weighted sums. Unfortunately, theory shows that such techniques cannot find concavities in Pareto fronts, meaning that some Pareto-optimal solutions cannot be reached.

In a first phase, we demonstrated the interest of using Pareto-based methods in preoperative planning over the weighted sum method by means of clinical validation on 14 use cases. Before this work, there has not been any comparable study demonstrating the interest of using Pareto-based over weighted sum method. This interest was purely theoretical before we concretely measured the extent of missed solutions that could have been preferred by a surgeon. This experiment confirms the overall interest of automatic assistance to preoperative trajectory planning for Deep Brain Stimulation. It shows that methods using a quantification of the trajectories quality based on Pareto-optimality can find more optimal propositions than the current state of the art algorithms using weighted sums. The evaluation study we conducted involving a blind ranking, highlighted that the extra propositions can often be chosen as more accurate by a neurosurgeon, and that some of them did not have any reasonably close alternative proposed by the weighted sum method.

In the second phase, we investigated three different optimization approaches : an aggregative method using a weighted sum of the multiple constraints, an evolutionary multi-objective method, and an exhaustive dominance-based method used as ground truth. In each method, we extract the set of all optimal insertion points based on dominance rules, and analyze the common and differing solutions by comparing the surfaces they cover. We have performed our study on 30 images datasets from patients who underwent a Deep Brain Stimulation electrode implant in the brain, and observed that the areas covered by the optimal insertion points obtained by the three methods differ significantly. The results show again that the traditional weighted sum approach is not sufficient to find the totality of the optimal solutions. The two other approaches provide extra solutions, but neither of them could find the complete optimal solution space. Further works may investigate either hybrid or extended methods such as adaptive weighted sum.

7

TECHNICAL DEPLOYMENT

> *"Technology is just a tool. In terms of getting the kids working together and motivating them, the teacher is the most important."*
> *- Bill Gates*

In this chapter, we explain the technical details of the work implemented in this thesis. We describe the datasets we used in the experiments with their reconstruction pipelines. After that, we describe our planning software components with some GUI illustrations.

7.1 Introduction

The work implemented in this thesis relies on a number of pipelines, and makes use of many libraries and frameworks. In the following we describe the datasets on which our experiments has been implemented, and the preprocessing pipelines that are applied to them before they can be used as an input. Afterwards, we give an overview of our planning system components with a collection of snapshots of the GUI.

7.2 Image modalities and processing pipelines

Our planning algorithms take as an input 3D patient-specific models for any kind of procedure. The models combine surface polygonal meshes with tetrahedral volume elements. We explain below how we obtain such 3D scenes from native preoperative medical images.

7.2.1 RFA datasets

The most commonly used imaging modality for abdominal surgery is CT. In our experiments, we worked on such CT images, however similar kind of preprocessing would be done with MR images.

The datasets on which we performed our tests were prepared based on real patients models from the ”3D-IRCADb” database [3Di, nd]. This database includes several sets of anonymized medical 3D CT-scans of patients and the manual segmentation of the various structures of interest already performed by clinical experts. The images are stroed in DICOM [DIC, nd] format. Segmentation are under the form of binary masks and VTK [VTK, nd] surfaces. As described in Chapter 4 Fig. 4.6, the system includes a planning and a simulation unit : we used the precomputed VTK surfaces for the planning unit 7.3, and we created the required VTK volumes for the simulation. The tetrahedral mesh of the liver shown in Fig. 7.4a is generated as follows : firstly, we convert the vtk surfaces format into *.ply* polygonal file format using the ParaView [Par,] application. Then, we use TetGen [Tet,] to generate a tetrahedral mesh from the polygonal surfaces. TetGen generates exact constrained Delaunay tetrahedralizations, boundary conforming Delaunay meshes, and Voronoi partitions. We generated our meshes with a radius edge ratio of the tetrahedra equal to 1.2mm. The generation was followed by a refinement in some cases to get smaller tetrahedra in order to increase the quality of the simulation at the cost of time. The output of TetGen consists in many files, we used two of them : one describes the nodes (*.node*), and the other describes the triangles elements (*.ele*) of the model. We wrote a piece of code to assemble both files into a single serial vtkUnstructuredGrid file (*.vtu*) which is used in our simulations.

As for the abdominal wall volume skin shown in Fig. 7.4b, which is, contrary to the liver, an open mesh model, which is not provided in [3Di, nd], we firstly segmented it manually using ITK-SNAP [ITK, nd], then we used the CGAL [cga, nd] library to convert the masks from to *.vtu* volumes.

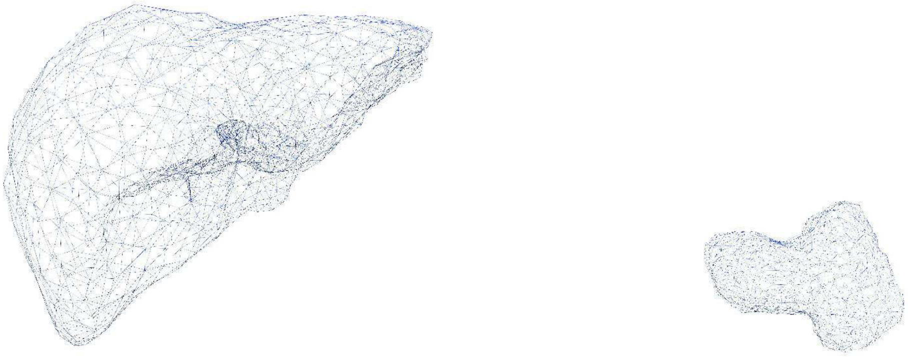

(a) liver (b) tumor

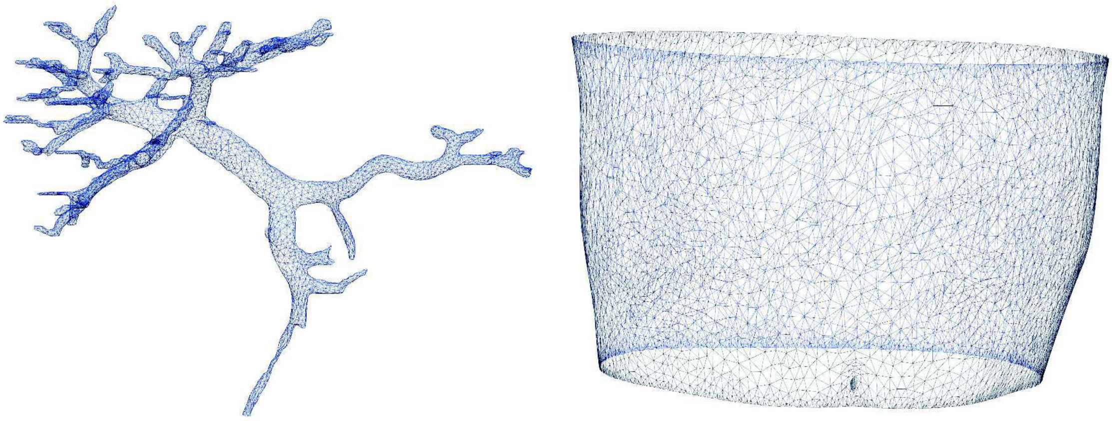

(c) portal vein (d) abdominal wall

FIGURE 7.1 – surface meshes for planning

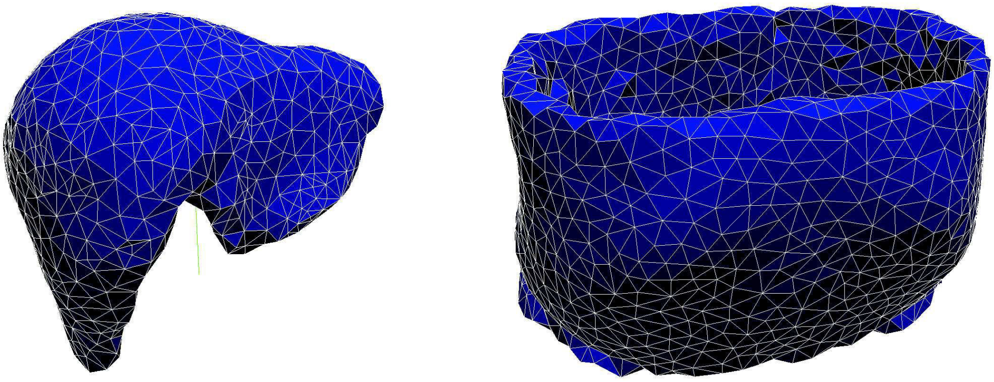

(a) liver (b) abdominal wall

FIGURE 7.2 – volume meshes for needle insertion simulation

The average size of a mesh used for the abdominal wall and the liver was 25,000 and 15,000 elements, respectively.

7.2.2 DBS datasets

Many image acquisitions are made at different stages of the DBS intervention as described in Chapter1, Section 1.1.1. Our datasets were acquired at two French hospital centers : the department of neurosurgery at Pontchaillou University Hospital in Rennes, and the Pitié-Salpêtrière Hospital (UPMC).

Inclusion images are taken months before the surgery, and preoperative images are taken the day of the surgery :

- Inclusion 3T T1-weighted MR image with gadolinium injection ($1mm \times 1mm \times 1mm$, Philips Medical system)
- Inclusion 3T T2-weighted MR image ($1mm \times 1mm \times 1.1mm$,Philips Medical system)
- preoperative CT scan with Leksell stereotactic frame ($0.55mm \times 0.55mm \times 0.6mm$, GE Healthcare VCT 6)

The DICOM image series are imported and converted into NIfTI format. After that, the images underwent a series of image processing and reconstruction algorithms thanks to the pyDBS workflow [D'Albis et al., 2014] which involves three pipelines (inclusion, preoperative, and postoperative).

Two types of segmentation are performed. An intensity-based segmentation is triggered using BrainVISA Morphologist pipeline [Cointepas et al., 2001] is done to get the scalp, brain (gray and white matter), and cortical sulci. The T2-weighted and T1-weighted MR images are then subject to rigid co-registration. All linear registrations are computed by means of the FMRIB's Linear Image Registration Tool (FLIRT).

The T1-weighted image of the brain is registered onto an anatomical atlas [Haegelen et al., 2013] to perform an atlas-based segmentation of the brain ventricles and basal ganglia. The segmentation is followed by a linear and nonlinear registrations in a box volume around the basal ganglia.

In the preoperative pipeline, the CT image which is acquired with the Leksell frame is rigidly registered onto the preoperative T1-weighted MR image of the patient's brain, and an intensity-based segmentation of the patient's skull and the four frame screws is performed, and the frame model is rigidly registered on the CT scan using landmarks points.

Tridimensional polygonal meshes are reconstructed from the segmented images and are exported to us in *.vtk* file format. We gather all the files in a single *.mitk* scene file to treat it using our MITK-based software.

7.3 The planning system components

Our software, named "PILOT" has been developed for a few years in C^{++} under the form of a planning plugin integrated into the Medical Imaging Interaction Toolkit (MITK) [Wolf et al., 2005] platform. It takes advantages of a number of multi-platform libraries, mainly ITK and VTK. In its current version, it is tested to be successfully run on Linux and Mac OS X platforms.

PILOT is composed of a number of modules :

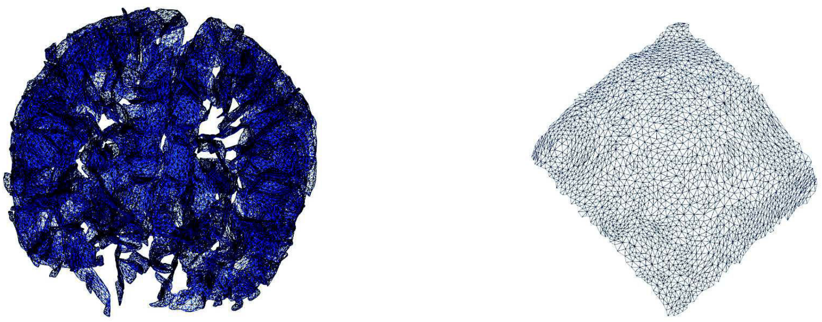

(a) sulci (b) skin patch

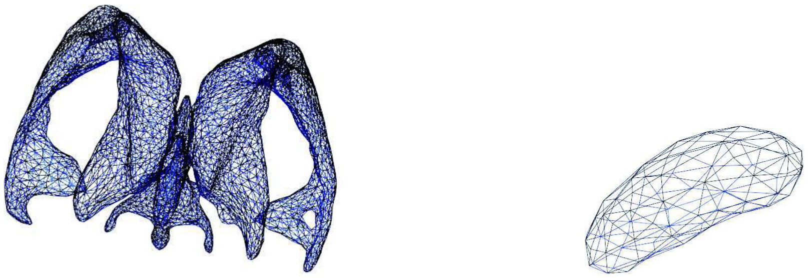

(c) ventricles (d) subthalamic nucleus (STN)

Figure 7.3 – surface meshes for planning

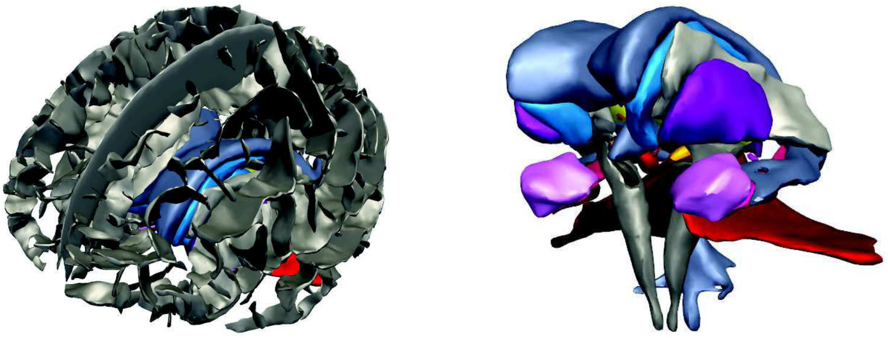

(a) brain (b) basal ganglia

Figure 7.4 – 3D surface mesh models generated by pyDBS and visualized in MITK

- XML interpreter which translates the planning rules described in an XML file to meaningful constraints for the solver.
- The solver, which evaluates the formalized geometric constraints. It involves the optimizers such as Nelder-Mead and *Haystack*.
- 3D scene viewer, which visualizes the images and 3D meshes of the patient, in addition to the geometric models of the surgical tools. Interaction is possible with the different elements contains in the scene.
- The graphical user interface which includes a number of tasks dedicated for the user settings.
- The simulation unit, implemented in SOFA, that communicates with the op-

timizers by means of boost-serialization library.

Software implementation

Our implementation of the methods proposed in this manuscript has been performed in C^{++} inside the PILOT plug-in, and the SOFA Haystack plug-in. The estimated code size for the our contribution presented in this thesis is around $12,000$ lines.

Software copyright protection

PILOT software, with its spin-offs Brain-PILOT and Cryo-PILOT, was filed at the Programs Protection Agency (APP) in Jul. 2015 under file n.
IDDN.FR.001.280006.000.R.P.2015.000.31230
The contribution of this thesis constitutes 20% of the overall software.

PILOT GUI

In this section, we illustrate the GUI with a few snapshots showing the different views and widgets to interact with the system.

Fig. 7.5 shows the overall display of the software. with the three most common slice views and the 3D scene. On the left side a tree view of the different segmented anatomical structures of the brain.

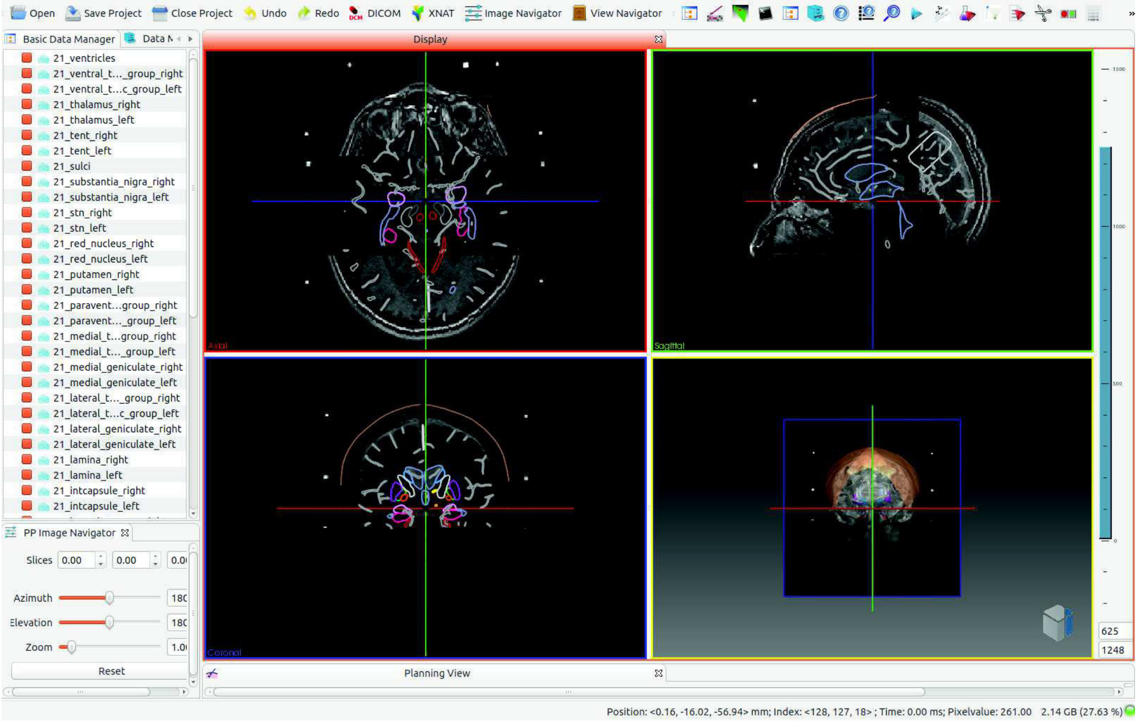

Position: <0.16, -16.02, -56.94> mm; Index: <128, 127, 18> ; Time: 0.00 ms; Pixelvalue: 261.00 2.14 GB (27.63 %)

FIGURE 7.5 – MITK 3D viewer with a brain model in the three views (axial, sagittal, and coronal), with the 3D reconstructed model on bottom left.

Fig. 7.6 illustrates the representation of weighted-sum optimization method planning proposition in our software. Results are represented by a risk color map. The three sliders corresponds to the weights of the constraints : standard trajectory, distance from sulci, and distance from ventricles. When moving the sliders, the weights values are changed, and the final aggregating cost function value will changer according to the new weights values.

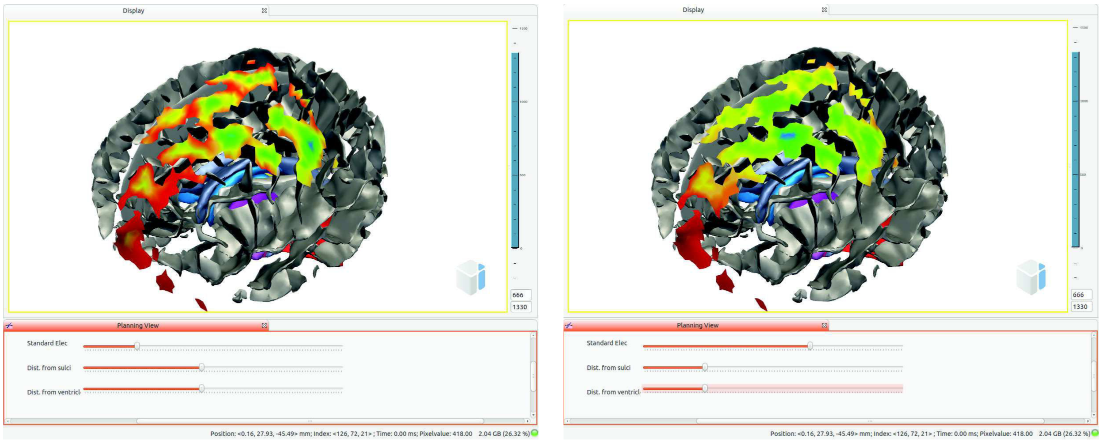

(a) defaut values for weights

(b) favouring the weight "the standard trajectory"

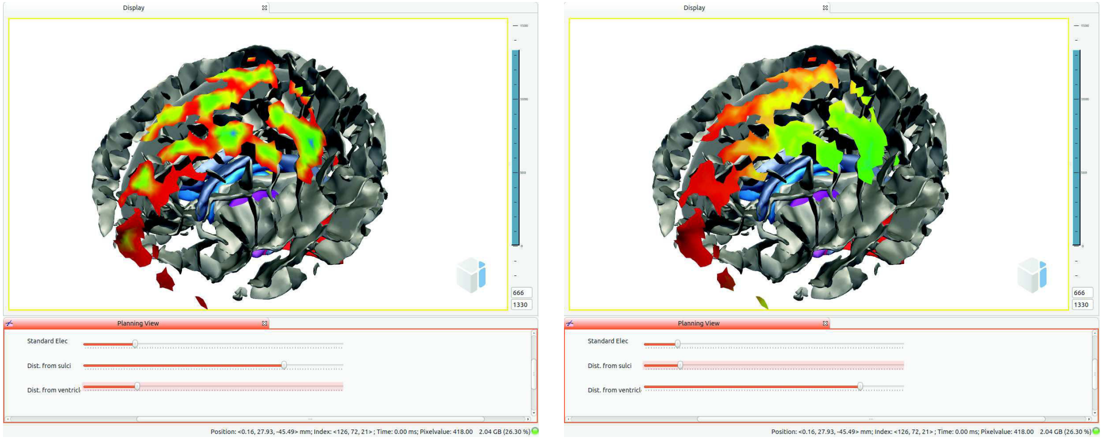

(c) favouring the weight "maximizing the distance from the sulci"

(d) favouring the weight "maximizing the distance from the ventricles"

FIGURE 7.6 – snapshots for different weights values with their corresponding risk maps. Colors grades from blue referring to best region to red in the worst regions depending on the weights values that are modified using the sliders.

Fig. 7.7 illustrates the representation of Pareto optimal solutions. According to Pareto, all the red points have the same quality since that none of them is dominated by any of the others. When the sliders values are set to zeros, all the Pareto optimals are visualized. It is possible to move sliders in order to filter the points in favor of a particular constraint. We recall that no weighted sum cost function is applied.

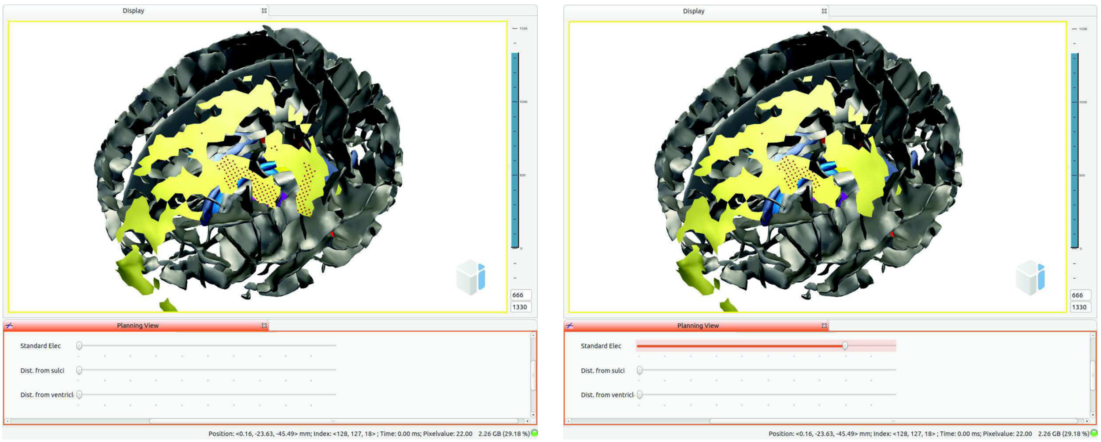

(a) All Pareto optimals

(b) favouring the points which satisfies better "the standard trajectory"

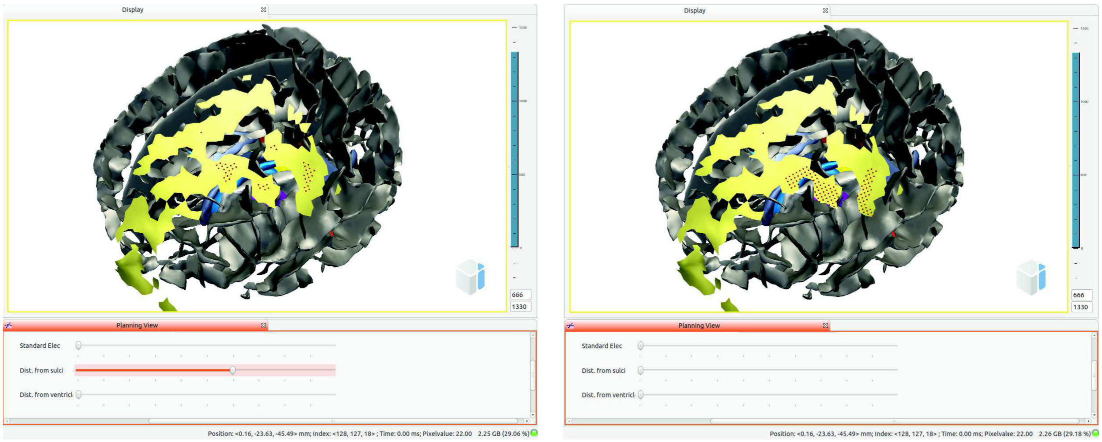

(c) favouring the points which satisfies better "the distance from the sulci"

(d) favouring the points which satisfies better "the distance form the ventricles"

FIGURE 7.7 – snapshots for different visualizations of the Pareto front solutions. All red points are Pareto-optimal. By moving the sliders, a the point set is filtered to favor some solution and hide others.

Conclusion

In this work, we tried to pay attention to the overall ergonomy of the GUI, as the software is aiming at being used by non-specialists of computer science. Therefore, the interaction was designed so that the use feels as natural as possible. Of course, when in use in clinical routine, the GUI will probably have to be improved and proof-tested carefully with the help of ergonomists.

8

CONCLUSIONS AND PERSPECTIVES

"Once we accept our limits, we go beyond them."
- Albert Einstein

In this chapter, we recapitulate and discuss the different parts of the work conducted during this thesis. We go over the strong and weakness points. After that, we report the main contributions, and we conclude by stating some interesting perspectives.

This thesis presents the results of my work realized within the computer graphics research group (IGG) in (ICube) laboratory at the university of Strasbourg. The part of work described in Chapter 4 concerning the percutaneous procedures has been developed in collaboration with the Institut Hospitalo-Universitaire de Strasbourg IHU through the *"Haystack"* project, and the work described in Chapters 5 and 6 concerning the DBS has been developed through the *"ACouStiC"* project in collaboration with participants from four french laboratories : Medicis, INSERM, Rennes, CRICM - UPMC, Paris, Shacra team, INRIA, Lille, and IGG team, ICube, Strasbourg. In addition to two departments of neurosurgery in Pontchaillou University Hospital and in Strasbourg University Hospital.

8.1 Disscussion

One of the motivations of this thesis was associated to the preexisting expertise in the domain of surgical path planning for image-guided surgery in IGG research group, and which addressed the problem using a pure geometric approach in coherence with the activities of the team where the geometry is the core activity.

Besides, the possess of a stable geometric solver in static conditions, and the urged needs of more realistic surgical planners, encouraged further investigation in the domain.

By examining the multidisciplinary literature after familiarization the medical context of the work, we got aware of the diverse attempts that have already and are still addressing the intra-operative deformation problems mainly using robotics and control methods, we realized the increasing interest and progress in biomechanical simulations and which had not been customized for preoperative path planning. We also noticed that optimization was a promising fertile domain which had not been yet intensively investigated in the sense of preoperative path planning. Therefore, we decided to focus on the preoperative planning phase.

Despite the generality of the existing path planning solver which encouraged us to address many procedures, we realized later that when deformations have to be considered, generality becomes more difficult to maintain because deformation sources and nature are different, and the planning algorithms have to be adapted to the type of deformation. However, we could maintain the generality in the way the surgical rules are formalized and expressed by constraints, but the optimization methods that we propose vary between two different interventions : while *"Haystack"* algorithm basis is to follow the tumor movement, in the DBS case the planning focus on the blood vessels movement caused by the brain shift.

We proposed a novel approach which combines geometry-based optimization techniques with physics-based simulations. A dedicated optimization algorithm named Haystack able to converge quickly towards precise optimal insertion settings has been introduced. Tests on 12 different datasets have showed that Haystack algorithm converges in a reasonable time (less than 7 minutes with our experimental setup) to a safe and efficient curved trajectory that is close in precision to an exhaustive method. However, the accuracy of the obtained results depend on the matching degree between the preoperative simulations and the intra-operative conditions. This is a real challenge to overcome. For example, the resulting deformations are computed according to a constant velocity of needle insertion which is difficult be ensured by a manual insertion. Another challenge is attributed to the inhomogeneity and variance of tissue from a patient to another, even though the biomechanical parameters of the simulations are tested in phantoms gels and are close to what is reported in the literature, there is no grantee to reproduce the same deformations during the intervention. Therefore, we think that a possible solution is to combine the planner with a needle robotic system to ensure the simulation conditions, and to compensate the divergence from the theoretical path.

Despite the aforementioned uncertainty, we believe that our planning approach is closer to reality than the existent approaches. In all cases, the final decision is on behalf of the surgeons, so our planning can serve as a decision support system being the first approach which accounts for deformations in the preoperative phase. Moreover, our method is characterized by a modularity level, it is independent of the simulation unit, and it can work if the simulation unit is replaced by another.

We also addressed the planning for DBS, but noticed that it would not be convenient to use Haystack algorithm for DBS because the principle of Haystack is changing iteratively the proposed insertion setting according to the target movement and keeping obstacles avoidance, while in DBS the target is located in a deep area of the brain where the deformation are usually less important than the deformations produced in the blood vessels which are extremely risky and should be better avoided. Since that the CSF leak is not possible to anticipate, we proposed a planning laying on an assumption for CSF loss, with this uncertainty we chose to propose planning solutions which avoid all the possible intermediate deformations. Similarly to the case of percutaneous procedures, deformations were integrated in the solver, and a planning strategy is proposed.

The obtained results were promising in the sense that the planner was able to find safe insertion zones even with brain shift, this increases the safety of the procedure. Nevertheless, the major shortcut of this study is that tests were performed on just one patient-specific case, this is why it just remains as a proof of feasibility, and much more tests are required to strengthen our results.We emphasize that the planning module is independent from the simulations, and the same algorithm can work on more complicated or improved deformation models of the brain.

Finally, we addressed the problem of finding the optimal solutions regardless of the possible intra-operative deformation. We were attracted by the success of the evolutionary optimization techniques in many research domain including multi-objective problems such as the ours. So far, none of the related works of DBS planning used a MOO approach to solve the problem, and only two implementations based on Pareto-front were proposed for RFA(one of them at the same time of this work by [Schumann et al., 2015]). We adapted the NSGA-II algorithm to our research problem, and we were able to find good configurations for the genetic operators and the evolution parameters. The main outcome of our investigation in the optimization techniques is that we could concertize the interest of shifting the existent optimization approaches in similar path planning interventions from the commonly used aggregative approaches to the multi-objectives methods, and more particularly the dominance-based evolutionary approaches. We succeeded in showing it using a clinical validation on 14 cases where our approach outperforms the weighted-sum. In addition, the quantitative information about the solutions surface coverage comparison was the first quantitative study on the differences between the two optimization approaches in the domain of surgical path planning. We believe that in multi-criteria optimization techniques, the GUI plays a key role in surgical planning decision support system, and the final decision depends quite a lot on the way we lay the information in the hands of the surgeon.

Finally, let us note that the main reason for which we investigated the optimization techniques in static conditions is the need of a very large number of simulations to run exhaustive search methods which was not practically possible with our current resources. In addition, we did not want to bias the optimization results by the simulations information. Nevertheless, deformations can be integrated with the new optimizers in a future steps.

In Chapter 7, we enlightened the technical details of the work, and which occupied an important time and effort during this thesis. On the first hand, despite the existence of some reconstructed 3D models, a lot of data preprocessing steps were required before being capable of running the algorithms on the data, and the success of the algorithms rely strongly on the good constrained data models. Low quality data may slow down the work progress especially in the experimental phase of *Haystack* algorithm were a large number of needle insertions should be run and the method were very sensitive to the volume models. This was one of the reasons that prevents performing brain shift simulations on a large number of patients. On the other hand, our software had to communicate with different modules like SOFA, and had to ensure the data exchange interfaces between 3D Slicer and MITK.

8.2 Summary of the contributions

The objectives of this work were firstly to present novel methods in preoperative path planning for image-guided surgery that account for intra-operative deformations, and secondly to introduce new optimization methods which improve the commonly used techniques in related works.

At the end of this thesis, our objectives were globally fulfilled, and the achieved work brings two prime contributions :

1. We presented the first automatic preoperative path planning approach for MIS which combine geometry-based optimization techniques with physics-based simulations.

   We experimented our methods on two different surgical procedures : in DBS neurosurgery, to compute a patient-specific preoperative safe straight trajectory for the stimulation electrode the planning accounts for the "Brain Shift" phenomenon, and in percutaneous procedures for hepatic tumor ablation, we compute a patient-specific preoperative safe non-straight trajectory for the ablation flexible needles, the planning accounts for both : the deformation of the flexible needle during the insertion process, and the deformation of the punctured soft tissue. We highlight the fact that our method is characterized by a certain level of generality, so it can be adapted to similar procedures.

2. An efficient Pareto-based multi-criteria optimization method which can find

more optimal solutions than the current state of the art in weighted sums optimization algorithms.

8.3 Perspectives

The multidisciplinary nature of this work inspired us with a number of future short or long term perspective.

Surgical planning training systems

PILOT software can be customized in the short term to help as a training system. Surgical planning training systems are increasingly demanded in nowadays hospitals training centers. The system can used by trainee students to get experience of path planning, to allow them to make errors without harming a patient before stepping into the operating room. Trainees can plan their trajectories using PILOT, access their qualities, visualize their risks, or compare them with saved trajectories planned by an experienced expert.

More image modalities

In our work, planning was performed on CT and MR images. We think that the employment of neuroradiological techniques (including functional MRI and MR-tractography) is of great help in preoperative neurosurgical planning. In DBS, the diffusion tensor imaging (DTI) is of vital importance for path planning because it enables visualizing tracts and help the localization of some fibres which surgeons may want to avoid with the electrode access path.

Planning with multiple trajectories

Another interesting extension of the planning system is to address the problem of multiple trajectories planning. In the case of tumor cryoablation for example, it is quite common that surgeons place more than one needle to destroy a large size tumor by targeting it from different directions. This extension is challenging, the simulations for each needle insertion should be performed separately because needles will not be inserted simultaneously in the real intervention. Therefore, an optimization method will required a very large number of simulations of paths combinations which is very costly in time and computation resources. In addition, a Pareto-based optimization for a large number of constraints is non trivial, the Pareto-front will have a dimension higher than 3, and the visualization of results in the GUI is a challenging task.

Using expert systems

Despite the existing commercial and research preoperative path planning system (including PILOT), the decision and the execution still stem from humans and depends on the surgeon experience and practice. We believe that if the surgical expertise were fed into a “smart” planning algorithm, the surgery will be moving toward safer milieu. A knowledge-base allows more surgeons to take part in the decision-making thus reducing the potential bias and subjectivity of one surgeon. A possible improvement therefore is to orient the optimization approach in the direction of expert systems which rely on knowledge bases. Case Based Reasoning "CBR" techniques for example, which is a technique of solving new problems based on the solutions of similar past problems, can be investigated by analyzing every new case and comparing it with similar old cases in order to propose a solution depending on the successful postoperative planning strategy of the similar cases. Finally, the application can be also useful for novice medical surgeons to test their plans versus planning strategies retrieved, revised ,and retained from a expertise knowledge base.

Combination with image-guided control system

With the increasing advances in medical robotics, we propose to couple *Haystack* algorithm with a control system to validate its results. Even that a physics-based path planning is more realist than a geometry-based. However, it is not yet sufficient, and to be able to use the present method into a proper surgery protocol, the planned trajectory path should be ensured, the needle insertion should be done in a constant velocity which is not possible by a manual insertion. We believe that needles steering robots if instructed efficiently, can be used to carry out the insertion process with a significant precision compared to manual insertion.

Augmented Reality

Augmented Reality techniques are becoming familiar to the surgical community. They could be used to improve many phases of the surgical procedures. In the proposed training system for example, augmented reality techniques may be introduced to teach the trainees about possible deformations. Calculated deformations can be superimposed on the static images of the patient to give informative and visual information and help the decision making process.

Biomechanical models

Further work could be conducted to raise the efficiency of the biomechanical models : in the current work for RFA, the deformation caused by the breathing has not been taken into account in the simulations. A more complex simulation model may include the respiratory motion. On the other hand, in the brain shift simulation, the accuracy of the brain shift model can be improved by using more complex deformation such as a non-linear soft tissue model. For the moment, the co-rotational model used in this work is a good trade-off between accuracy and computation time. Further improvements could be done by substituting co-rotational approach with a non-linear constitutive equation. Finally, thanks to the modularity of our system, both aforementioned extensions can be implemented independently from the planning unit, and the new models can easily replace the existing simulation model in the planning system.

Bibliographie

[Par,] Data analysis and visualization application. http://www.paraview.org/.

[Tet,] A quality tetrahedral mesh generator and a 3d delaunay triangulator. http://wias-berlin.de/software/tetgen/.

[Ang, 1988] (1988). AngioDynamics. http://www.angiodynamics.com/.

[BRA, 1988] (1988). BRAINLAB neurosurgical platform . https://www.brainlab.com.

[3Di, nd] (n.d.). 3D Image Reconstruction for Comparison of Algorithm Database . http://www.ircad.fr/research/3dircadb/.

[Boo, nd] (n.d.). Boost library. http://www.boost.org.

[CLE, nd] (n.d.). ClearPoint neurosurgical platform . http://www.mriinterventions.com.

[DIC, nd] (n.d.). Digital imaging and communications in medicine. http://dicom.nema.org/.

[ITK, nd] (n.d.). Digital imaging and communications in medicine. http://www.itksnap.org.

[IGG, nd] (n.d.). équipe Informatique Géométrique et Graphique. http://icube-igg.unistra.fr/fr/index.php.

[EOS, nd] (n.d.). Fhc - eos technology for manufacturing of stereotactic platforms for neurosurgery. http://www.eos.info/press/customer_case_studies/fhc.

[Gal, nd] (n.d.). GalilMedical solutions for cryoablation. https://www.galilmedical.com/.

[CRW, nd] (n.d.). Integra CRW system. http://www.integralife.com.

[Lek, nd] (n.d.). Leksell system. http://ecatalog.elekta.com.

[Sur, nd] (n.d.). LeksellSurgiPlan preoperative planning system . http://ecatalog.elekta.com/neuroscience.

[Med, nda] (n.d.a). Medtronic Covidien system for RF ablation. http://www.medtronic.com/covidien/products/ablation-systems.

[Med, ndb] (n.d.b). Medtronic Products for Deep Brain Stimulation. http://professional.medtronic.com/pt/neuro/dbs-md/prod.

[Med, ndc] (n.d.c). StealthStation S7 surgical navigation system . http://www.medtronic.com.

[cga, nd] (n.d.). CGAL, Computational Geometry Algorithms Library.

[VTK, nd] (n.d.). The visualization toolkit. `http://www.vtk.org/`.

[Abayazid et al., 2013] Abayazid, M., Roesthuis, R. J., Reilink, R., and Misra, S. (2013). Integrating deflection models and image feedback for real-time flexible needle steering. *IEEE Transactions on Robotics*, 29(2) :542–553.

[Abosch et al., 2013] Abosch, A., Timmermann, L., Bartley, S., Rietkerk, H. G., Whiting, D., Connolly, P. J., Lanctin, D., and Hariz, M. I. (2013). An international survey of deep brain stimulation procedural steps. *Stereotactic and Functional Neurosurgery*, 91(1) :1–11.

[Alterovitz et al., 2008] Alterovitz, R., Branicky, M., and Goldberg, K. (2008). Motion Planning Under Uncertainty for Image-guided Medical Needle Steering. *The International journal of robotics research*, 27(11-12) :1361–1374.

[Alterovitz et al., 2005] Alterovitz, R., Goldberg, K., and Okamura, A. (2005). Planning for steerable bevel-tip needle insertion through 2d soft tissue with obstacles. In *Proceedings of the 2005 IEEE International Conference on Robotics and Automation*. Institute of Electrical & Electronics Engineers (IEEE).

[Altrogge et al., 2007] Altrogge, I., Preusser, T., Kröger, T., Büskens, C., Pereira, P., Schmidt, D., and Peitgen, H. (2007). Multiscale optimization of the probe placement for radiofrequency ablation. *Academic Radiology*, 14(11) :1310–1324.

[Baegert et al., 2007a] Baegert, C., Villard, C., Schreck, P., and Soler, L. (2007a). Multi-criteria trajectory planning for hepatic radiofrequency ablation. In *proceedings of MICCAI'07*, volume 4791 of *Springer LNCS*, pages 584–592.

[Baegert et al., 2007b] Baegert, C., Villard, C., Schreck, P., Soler, L., and Gangi, A. (2007b). Trajectory optimization for the planning of percutaneous radiofrequency ablation of hepatic tumors. *Computer Aided Surgery*, 12(2) :82–90.

[Baraff and Witkin, 1998] Baraff, D. and Witkin, A. (1998). Large steps in cloth simulation. In *SIGGRAPH '98*, pages 43–54. ACM Press.

[Ben-Tal, 1980] Ben-Tal, A. (1980). *Characterization of Pareto and lexicographic optimal solutions*. Springer Berlin Heidelberg.

[Benabid et al., 1994] Benabid, A., Pollak, P., Gross, C., Hoffmann, D., Benazzouz, A., Gao, D., Laurent, A., Gentil, M., and Perret, J. (1994). Acute and long-term effects of subthalamic nucleus stimulation in parkinson's disease. *Stereotact Funct Neurosurg*, 62 :76–84.

[Benabid et al., 1987] Benabid, A., Pollak, P., Louveau, A., Henry, S., and de Rougemont, J. (1987). Combined (thalamotomy and stimulation) stereotactic surgery of the VIM thalamic nucleus for bilateral parkinson disease. *Stereotactic and Functional Neurosurgery*, 50(1-6) :344–346.

[Bériault et al., 2012] Bériault, S., Subaie, F. A., Collins, D. L., Sadikot, A. F., and Pike, G. B. (2012). A multi-modal approach to computer-assisted deep brain stimulation trajectory planning. *Int J CARS*, 7(5) :687–704.

[Bériault et al., 2011] Bériault, S., Subaie, F. A., Mok, K., Sadikot, A. F., and Pike, G. B. (2011). Automatic trajectory planning of DBS neurosurgery from multi-modal MRI datasets. In *Medical Image Computing and Computer-Assisted Intervention MICCAI 2011*, pages 259–266. Springer Science + Business Media.

[Bernardes et al., 2011] Bernardes, M. C., Adorno, B. V., Poignet, P., Zemiti, N., and Borges, G. A. (2011). Adaptive path planning for steerable needles using duty-cycling. In *2011 IEEE/RSJ International Conference on Intelligent Robots and Systems*. Institute of Electrical & Electronics Engineers (IEEE).

[Bilger, 2014] Bilger, A. (2014). *Patient-specific biomechanical simulation for deep brain stimulation*. Theses, Université des Sciences et Technologie de Lille.

[Bilger et al., 2012] Bilger, A., Essert, C., Duriez, C., and Cotin, S. (2012). Brain-shift aware risk map for deep brain stimulation planning. In *Proc. MICCAI*.

[Bourbakis and Awad, 2003] Bourbakis, N. and Awad, M. (2003). A 3-D visualization method for image-guided brain surgery. *IEEE Transactions on Systems, Man, and Cybernetics, Part B : Cybernetics*, 33(5) :766–781.

[Brace, 2009] Brace, C. L. (2009). Radiofrequency and microwave ablation of the liver, lung, kidney, and bone : What are the differences ? *Current Problems in Diagnostic Radiology*, 38(3) :135–143.

[Brower, 2002] Brower, V. (2002). The cutting edge in surgery : Telesurgery has been shown to be feasible–now it has to be made economically viable. *EMBO Reports*, 3(4) :300–301.

[Brunenberg et al., 2007] Brunenberg, E., Vilanova, A., Visser-Vandewalle, V., Temel, Y., Ackermans, L., Platel, B., and ter Haar Romeny, B. (2007). Automatic trajectory planning for deep brain stimulation : A feasibility study. In *proceedings of MICCAI'07*, volume 4791 of *Springer LNCS*, pages 584–592.

[Butson et al., 2007] Butson, C. R., Cooper, S. E., Henderson, J. M., and McIntyre, C. C. (2007). Patient-specific analysis of the volume of tissue activated during deep brain stimulation. *NeuroImage*, 34(2) :661–670.

[Butz et al., 2000] Butz, T., Warfield, S., Tuncali, K., Silverman, S., Van Sonnenberg, E., and Jolesz, F.A.and Kikinis, R. (2000). Pre- and intra-operative planning and simulation of percutaneous tumor ablation. In *proceedings of MICCAI'00*, volume 1935 of *Springer LNCS*, pages 317–326.

[Chen et al., 2009] Chen, C.-C., Miga, M., and Galloway, R. (2009). Optimizing electrode placement using finite-element models in radiofrequency ablation treatment planning. *IEEE Transactions on Biomedical Engineering*, 56(2) :237–245.

[Chen et al., 2011] Chen, I., Coffey, A., Ding, S., Dumpuri, P., Dawant, B., Thompson, R., and Miga, M. (2011). Intraoperative brain shift compensation : Accounting for dural septa. *Biomedical Engineering, IEEE Transactions on*, 58(3) :499–508.

[Cointepas et al., 2001] Cointepas, Y., Mangin, J., Garnero, L., Poline, J., and Benali, H. (2001). BrainVISA : Software platform for visualization and analysis of multi-modality brain data. *NeuroImage*, 13(6) :98–98.

[Corne et al., 2000] Corne, D., Knowles, J., and Oates, M. (2000). The pareto envelope-based selection algorithm for multiobjective optimization. In Schoenauer, M., Deb, K., Rudolph, G., Yao, X., Lutton, E., Merelo, J., and Schwefel, H.-P., editors, *Parallel Problem Solving from Nature PPSN VI*, volume 1917 of *Lecture Notes in Computer Science*, pages 839–848. Springer Berlin Heidelberg.

[Corne et al., 2001] Corne, D. W., Jerram, N. R., Knowles, J. D., Oates, M. J., et al. (2001). Pesa-ii : Region-based selection in evolutionary multiobjective optimization. In *Proceedings of the Genetic and Evolutionary Computation Conference (GECCO'2001*. Citeseer.

[Courtecuisse et al., 2014] Courtecuisse, H., Allard, J., Pierre, K., Bordas, S. P.-A., Cotin, S., and Duriez, C. (2014). Real-time simulation of contact and cutting of heterogeneous soft-tissues. *Medical Image Analysis*, page 20.

[Craft, 2013] Craft, D. (2013). Multi-criteria optimization methods in radiation therapy planning : a review of technologies and directions. *arXiv preprint arXiv :1305.1546*.

[Cuevas et al., 2015] Cuevas, A. D. L., Tovar-Arriaga, S., Gonzalez-Gutierrez, A., and Aceves-Fernandez, M. A. (2015). Trajectory planning for keyhole neurosurgery using fuzzy logic for risk evaluation. In *2015 12th International Conference on Electrical Engineering, Computing Science and Automatic Control (CCE)*. Institute of Electrical & Electronics Engineers (IEEE).

[D'Albis et al., 2014] D'Albis, T., Haegelen, C., Essert, C., Fernández-Vidal, S., Lalys, F., and Jannin, P. (2014). PyDBS : an automated image processing workflow for deep brain stimulation surgery. *Int J CARS*, 10(2) :117–128.

[Dawant et al., 2007] Dawant, B. M., D'Haese, P.-F., Pallavaram, S., Li, R., Yu, H., Spooner, J., Davis, T., Kao, C., and Konrad, P. E. (2007). VU-DBS project : integrated and computer-assisted planning, intra-operative placement, and post-operative programming of deep-brain stimulators. In Cleary, K. R. and Miga, M. I., editors, *Medical Imaging 2007 : Visualization and Image-Guided Procedures*. SPIE.

[Dawant et al., 2003] Dawant, B. M., Li, R., Cetinkaya, E., Kao, C., Fitzpatrick, J. M., and Konrad, P. E. (2003). Computerized atlas-guided positioning of deep brain stimulators : A feasibility study. In *Biomedical Image Registration*, pages 142–150. Springer Science and Business Media.

[De Paolis et al., 2009] De Paolis, L. T., De Mauro, A., Raczkowsky, J., and Aloisio, G. (2009). Virtual model of the human brain for neurosurgical simulation. *Studies in health technology and informatics*, pages 811–815.

[Deb et al., 2002] Deb, K., Pratap, A., Agarwal, S., and Meyarivan, T. (2002). A fast and elitist multiobjective genetic algorithm : Nsga-ii. *Evolutionary Computation, IEEE Transactions on*, 6(2) :182–197.

[Delingette, 1998] Delingette, H. (1998). Toward realistic soft-tissue modeling in medical simulation. *Proc. IEEE*, 86(3) :512–523.

[D'Haese et al., 2005a] D'Haese, P.-F., Cetinkaya, E., Konrad, P. E., Kao, C., and Dawant, B. M. (2005a). Computer-aided placement of deep brain stimulators : from planning to intraoperative guidance. *IEEE Transactions on Medical Imaging*, 24(11) :1469–1478.

[D'Haese et al., 2010] D'Haese, P.-F., Pallavaram, S., Konrad, P. E., Neimat, J., Fitzpatrick, J. M., and Dawant, B. M. (2010). Clinical accuracy of a customized stereotactic platform for deep brain stimulation after accounting for brain shift. *Stereotact Funct Neurosurg*, 88(2) :81–87.

[D'Haese et al., 2012] D'Haese, P.-F., Pallavaram, S., Li, R., Remple, M. S., Kao, C., Neimat, J. S., Konrad, P. E., and Dawant, B. M. (2012). CranialVault and its CRAVE tools : A clinical computer assistance system for deep brain stimulation (DBS) therapy. *Medical Image Analysis*, 16(3) :744–753.

[D'Haese et al., 2005b] D'Haese, P. F., Pallavaram, S., Niermann, K., Spooner, J., Kao, C., Konrad, P. E., and Dawant, B. M. (2005b). Automatic selection of DBS target points using multiple electrophysiological atlases. *Med Image Comput Comput Assist Interv*, 8(Pt 2) :427–434.

[DiMaio and Salcudean, 2005] DiMaio, S. and Salcudean, S. (2005). Needle steering and motion planning in soft tissues. *IEEE Transactions on Biomedical Engineering*, 52(6) :965–974.

[Dodd et al., 2001] Dodd, G. D., Frank, M. S., Aribandi, M., Chopra, S., and Chintapalli, K. N. (2001). Radiofrequency thermal ablation : computer analysis of the size of the thermal injury created by overlapping ablations. *AJR Am J Roentgenol*, 177(4) :777–782.

[Duriez et al., 2006] Duriez, C., Cotin, S., Lenoir, J., and Neumann, P. (2006). New approaches to catheter navigation for interventional radiology simulation. *Computer Aided Surgery*, 11(6) :300–308.

[Duriez et al., 2009] Duriez, C., Guébert, C., Marchal, M., Cotin, S., and Grisoni, L. (2009). Interactive simulation of flexible needle insertions based on constraint models. In Yang, G.-Z., Hawkes, D., Rueckert, D., Noble, A., and Taylor, C., editors, *Proceedings of MICCAI 2009*, volume 5762, pages 291–299. Springer.

[Elias et al., 2007] Elias, W. J., Fu, K.-M., and Frysinger, R. C. (2007). Cortical and subcortical brain shift during stereotactic procedures. *Journal of neurosurgery*, 107(5) :983–8.

[Eshelman, 1993] Eshelman, Larry J., S. J. (1993). *Real-Coded Genetic Algorithms and Interval-Schemata.*

[Esquivel et al., 1982] Esquivel, C., Keeffe, E., Garcia, G., Imperial, J., Millan, M., and Monge, H.and So, S. (1982). Automatic computation of electrodes trajectory for deep brain stimulation. *Gastroenterol Hepatol*, 14 :27–41.

[Essert et al., 2010] Essert, C., Haegelen, C., and Jannin, P. (2010). Automatic computation of electrodes trajectory for deep brain stimulation. *proceedings of Medical Imaging and Augmented Reality*, LNCS 6326 :149–158.

[Essert et al., 2012] Essert, C., Haegelen, C., Lalys, F., Abadie, A., and Jannin, P. (2012). Automatic computation of electrode trajectories for deep brain stimulation : a hybrid symbolic and numerical approach. *International journal of computer assisted radiology and surgery*, 7(4) :517–532.

[Essert-Villard et al., 2009] Essert-Villard, C., Baegert, C., and Schreck, P. (2009). Multi-semantic approach towards a generic formal solver of tool placement for percutaneous surgery. In *Proceedings of Knowledge Engineering & Ontology Development*, pages 443–446.

[Faure et al., 2012] Faure, F., Duriez, C., Delingette, H., Allard, J., Gilles, B., Marchesseau, S., Talbot, H., Courtecuisse, H., Bousquet, G., Peterlik, I., and Cotin,

S. (2012). SOFA : A Multi-Model Framework for Interactive Physical Simulation. In Payan, Y., editor, *Soft Tissue Biomechanical Modeling for Computer Assisted Surgery*, volume 11 of *Studies in Mechanobiology, Tissue Engineering and Biomaterials*, pages 283–321. Springer.

[Felippa and Haugen, 2005] Felippa, C. and Haugen, B. (2005). A unified formulation of small-strain corotational finite elements : I. theory. *Computer Methods in Applied Mechanics and Engineering*, 194(21) :2285–2335.

[Ferrant et al., 2002] Ferrant, M., Nabavi, A., Macq, B., Black, P. M., Jolesz, F. a., Kikinis, R., and Warfield, S. K. (2002). Serial registration of intraoperative MR images of the brain. *Medical image analysis*, 6(4) :337–59.

[Fonseca and Fleming, 1995] Fonseca, C. M. and Fleming, P. J. (1995). An overview of evolutionary algorithms in multiobjective optimization. *Evolutionary Computation*, 3(1) :1–16.

[Fujii et al., 2002] Fujii, T., Asakura, H., Emoto, H., Sugou, N., Mito, T., and Shibata, I. (2002). Automatic path searching for minimally invasive neurosurgical planning.

[Fujii et al., 2003] Fujii, T., Emoto, H., Sugou, N., Mito, T., and Shibata, I. (2003). Neuropath planner-automatic path searching for neurosurgery. In *proceedings of CARS'03*, volume 1256, pages 587–596. Elsevier.

[Garrean et al., 2008] Garrean, S., Hering, J., Saied, A., Helton, W. S., and Espat, N. J. (2008). Radiofrequency ablation of primary and metastatic liver tumors : a critical review of the literature. *Am. J. Surg.*, 195(4) :508–520.

[Goksel et al., 2011] Goksel, O., Sapchuk, K., and Salcudean, S. (2011). Haptic simulator for prostate brachytherapy with simulated needle and probe interaction. *IEEE Transactions on Haptics*, 4(3) :188–198.

[Gottschalk et al., 1996] Gottschalk, S., Lin, M. C., and Manocha, D. (1996). Obbtree : A hierarchical structure for rapid interference detection. In *Proc. of the 23rd annual conference on Computer graphics and interactive techniques*, pages 171–180. ACM.

[Grant and Neuberger, 1999] Grant, A. and Neuberger, J. (1999). Guidelines on the use of liver biopsy in clinical practice. *Gut*, 45(Supplement 4) :iv1–iv11.

[Guo et al., 2006] Guo, T., Finnis, K. W., Parrent, A. G., and Peters, T. M. (2006). Visualization and navigation system development and application for stereotactic deep-brain neurosurgeries. *Computer Aided Surgery*, 11(5) :231–239.

[Guo et al., 2007] Guo, T., Parrent, A., and Peters, T. (2007). Automatic target and trajectory identification for deep brain stimulation (DBS) procedures. In *proceedings of MICCAI'07*, volume 4791 of *Springer LNCS*, pages 483–490.

[Haase et al., 2012] Haase, S., Patz, T., Tiesler, H., Altrogge, I., and Preusser, T. (2012). Radiofrequency ablation planning beyond simulation. In *Engineering in Medicine and Biology Society (EMBC), 2012 Annual International Conference of the IEEE*, pages 191–194.

[Haegelen et al., 2013] Haegelen, C., Coupe, P., Fonov, V., Guizard, N., Jannin, P., Morandi, X., and Collins, D. L. (2013). Automated segmentation of basal ganglia and deep brain structures in MRI of Parkinson's disease. *Int J Comput Assist Radiol Surg*, 8(1) :99–110.

[Hu et al., 2007] Hu, J., Jin, X., Lee, J. B., Zhang, L., Chaudhary, V., Guthikonda, M., Yang, K. H., and King, A. I. (2007). Intraoperative brain shift prediction using a 3D inhomogeneous patient-specific finite element model. *Journal of neurosurgery*, 106(1) :164–9.

[Jaberzadeh and Essert, 2015] Jaberzadeh, A. and Essert, C. (2015). Pre-operative planning of multiple probes in three dimensions for liver cryosurgery : comparison of different optimization methods. *Mathematical Methods in the Applied Sciences.*

[Kemper et al., 2010] Kemper, A. R., Santago, A. C., Stitzel, J. D., Sparks, J. L., and Duma, S. M. (2010). Biomechanical response of human liver in tensile loading. In *Annals of Advances in Automotive Medicine/Annual Scientific Conference*, volume 54, page 15. Association for the Advancement of Automotive Medicine.

[Kemper et al., 2013] Kemper, A. R., Santago, A. C., Stitzel, J. D., Sparks, J. L., and Duma, S. M. (2013). Effect of strain rate on the material properties of human liver parenchyma in unconfined compression. *Journal of biomechanical engineering*, 135(10) :104503–104503–8.

[Khan et al., 2007] Khan, M. F., Mewes, K., Gross, R., and Škrinjar, O. (2007). Brain shift analysis for deep brain stimulation surgery using non-rigid registration. In Cleary, K. R. and Miga, M. I., editors, *Medical Imaging 2007 : Visualization and Image-Guided Procedures.* SPIE.

[Kim and de Weck, 2006] Kim, I. and de Weck, O. (2006). Adaptive weighted sum method for multiobjective optimization : a new method for pareto front generation. *Structural and Multidisciplinary Optimization*, 31(2) :105–116.

[Knowles and Corne, 1999] Knowles, J. and Corne, D. (1999). The pareto archived evolution strategy : a new baseline algorithm for pareto multiobjective optimisation. In *Proceedings of the 1999 Congress on Evolutionary Computation-CEC99 (Cat. No. 99TH8406).* Institute of Electrical & Electronics Engineers (IEEE).

[Kobayashi et al., 2005] Kobayashi, Y., Okamoto, J., and Fujie, M. (2005). Physical properties of the liver and the development of an intelligent manipulator for needle insertion. In *In IEEE International Conference on Robotics and Automation*, pages 1632–1639.

[Korin et al., 1992] Korin, H. W., Ehman, R. L., Riederer, S. J., Felmlee, J. P., and Grimm, R. C. (1992). Respiratory kinematics of the upper abdominal organs : a quantitative study. *Magnetic resonance in medicine*, 23(1) :172–178.

[Kröger et al., 2006] Kröger, T., Altrogge, I., Preusser, T., Pereira, P. L., Schmidt, D., Weihusen, A., and Peitgen, H.-O. (2006). Numerical simulation of radio frequency ablation with state dependent material parameters in three space dimensions. In *Medical Image Computing and Computer-Assisted Intervention – MICCAI 2006*, pages 380–388. Springer Science + Business Media.

[Kroger et al., 2010] Kroger, T., Patz, T., Altrogge, I., Schenk, A., Lehmann, K. S., Frericks, B. B., Ritz, J.-P., Peitgen, H.-O., and Preusser, T. (2010). Fast estimation of the vascular cooling in RFA based on numerical simulation. *The Open Biomedical Engineering Journal*, 4(2) :16–26.

[Lee et al., 2002] Lee, J., Huang, C., and Lee, S. (2002). Improving stereotactic surgery using 3-D reconstruction. *IEEE Engineering in Medicine and Biology Magazine*, 21(6) :109–116.

[Livraghi et al., 1999] Livraghi, T., Goldberg, S. N., Lazzaroni, S., Meloni, F., Solbiati, L., and Gazelle, G. S. (1999). Small hepatocellular carcinoma : Treatment with radio-frequency ablation versus ethanol injection. *Radiology*, 210(3) :655–661.

[Mahvash and Dupont, 2009] Mahvash, M. and Dupont, P. (2009). Fast needle insertion to minimize tissue deformation and damage. In *In IEEE International Conference on Robotics and Automation*, pages 3097–3102.

[McCreedy et al., 2006] McCreedy, E. S., Cheng, R., Hemler, P. F., Viswanathan, A., Wood, B. J., and McAuliffe, M. J. (2006). Radio frequency ablation registration, segmentation, and fusion tool. *IEEE Trans Inf Technol Biomed*, 10(3) :490–496.

[Mercier et al., 2010] Mercier, L., Maestro, R. F. D., Petrecca, K., Kochanowska, A., Drouin, S., Yan, C. X. B., Janke, A. L., Chen, S. J.-S., and Collins, D. L. (2010). New prototype neuronavigation system based on preoperative imaging and intraoperative freehand ultrasound : system description and validation. *Int J CARS*, 6(4) :507–522.

[Miller and Chinzei, 2002] Miller, K. and Chinzei, K. (2002). Mechanical properties of brain tissue in tension. *Journal of biomechanics*, 35 :483–490.

[Miocinovic et al., 2007] Miocinovic, S., Noecker, A. M., Maks, C. B., Butson, C. R., and McIntyre, C. C. (2007). Cicerone : stereotactic neurophysiological recording and deep brain stimulation electrode placement software system. In *Operative Neuromodulation*, pages 561–567. Springer Science + Business Media.

[Misra et al., 2010] Misra, S., Reed, K. B., Schafer, B. W., Ramesh, K. T., and Okamura, a. M. (2010). Mechanics of flexible needles robotically steered through soft tissue. *The International journal of robotics research*, 29(13) :1640–1660.

[Momi et al., 2014] Momi, E. D., Caborni, C., Cardinale, F., Casaceli, G., Castana, L., Cossu, M., Mai, R., Gozzo, F., Francione, S., Tassi, L., Russo, G. L., Antiga, L., and Ferrigno, G. (2014). Multi-trajectories automatic planner for StereoElectroEncephaloGraphy (SEEG). *Int J CARS*, 9(6) :1087–1097.

[Mooney, 1940] Mooney, M. (1940). A theory of large elastic deformation. *Journal of Applied Physics*, 11(9).

[Moreira et al., 2013] Moreira, P., Peterlík, I., Herink, M., Duriez, C., Cotin, S., and Misra, S. (2013). Modelling prostate deformation : Sofa versus experiments. *Mechanical Engineering Research*, 3(2) :64–72.

[Nelder and Mead, 1965] Nelder, J. and Mead, R. (1965). A simplex method for function minimization. *Computer Journal*, 7(4) :308–313.

[Nesme et al., 2005] Nesme, M., Payan, Y., and Faure, F. (2005). Efficient, physically plausible finite elements. In Dingliana, J. and Ganovelli, F., editors, *Eurographics (short papers)*.

[Ng et al., 2011] Ng, K. W., Tian, G.-L., and Tang, M.-L. (2011). *Dirichlet and related distributions : Theory, methods and applications*, volume 888. John Wiley & Sons.

[Nowinski et al., 2002] Nowinski, W., Yang, G., and Yeo, T. (2002). Computer-aided stereotactic functional neurosurgery enhanced by the use of the multiple brain atlas database. *IEEE Transactions on Medical Imaging*, 19(1) :62–69.

[Pallavaram et al., 2009] Pallavaram, S., D'Haese, P.-F., Remple, M. S., Neimat, J. S., Kao, C., Li, R., Konrad, P. E., and Dawant, B. M. (2009). Detecting brain shift during deep brain stimulation surgery using intra-operative data and functional atlases : A preliminary study. In *2009 IEEE International Symposium on Biomedical Imaging : From Nano to Macro*. IEEE.

[Pan et al., 2015] Pan, J., Zhao, C., Zhao, X., Hao, A., and Qin, H. (2015). Metaballs-based physical modeling and deformation of organs for virtual surgery. *The Visual Computer*, 31(6-8) :947–957.

[Pareto, 1919] Pareto, V. (1919). *Manuale di Economia Politica ; con una Introduzione alla Scienza Sociale*. Milano : Societa Editrice Libraria.

[Park et al., 2010] Park, W., Wang, Y., and Chirikjian, G. S. (2010). Path planning for flexible needles using second order error propagation. In *Algorithmic Foundations of Robotics*, pages 583–595.

[Patil et al., 2011] Patil, S., van den Berg, J., and Alterovitz, R. (2011). Motion planning under uncertainty in highly deformable environments. *Proceedings of Robotics : Science and Systems VII*, pages 241–248.

[Peterlik et al., 2011] Peterlik, I., Nouicer, M., Duriez, C., Cotin, S., and Kheddar, A. (2011). Constraint-based haptic rendering of multirate compliant mechanisms. *IEEE Trans. Haptics, Special Issue on Haptics in Medicine and Clinical Skill Acquisition*, 4 :175–187.

[Petersen et al., 2010] Petersen, E. A., Holl, E. M., Martinez-Torres, I., Foltynie, T., Limousin, P., Hariz, M. I., and Zrinzo, L. (2010). Minimizing brain shift in stereotactic functional neurosurgery. *Neurosurgery*, 67 :ons213–ons221.

[Rieder et al., 2011] Rieder, C., Kroeger, T., Schumann, C., and Hahn, H. K. (2011). GPU-based real-time approximation of the ablation zone for radiofrequency ablation. *IEEE Trans. Visual. Comput. Graphics*, 17(12) :1812–1821.

[Rieder et al., 2009] Rieder, C., Schwier, M., Weihusen, A., Zidowitz, S., and Peitgen, H.-O. (2009). Visualization of risk structures for interactive planning of image guided radiofrequency ablation of liver tumors. In Miga, M. I. and Wong, K. H., editors, *Medical Imaging 2009 : Visualization, Image-Guided Procedures, and Modeling*. SPIE-Intl Soc Optical Eng.

[Rivlin, 1948] Rivlin, R. S. (1948). Large elastic deformations of isotropic materials. i. fundamental concepts. *Philosophical Transactions of the Royal Society of London. Series A, Mathematical and Physical Sciences*, 240(822) :459–490.

[Rohlfing et al., 2004] Rohlfing, T., Maurer Jr, C. R., O'Dell, W. G., and Zhong, J. (2004). Modeling liver motion and deformation during the respiratory cycle using intensity-based nonrigid registration of gated mr images. *Medical physics*, 31(3) :427–432.

[Rudenko and Schoenauer, 2004] Rudenko, O. and Schoenauer, M. (2004). Dominance based crossover operator for evolutionary multi-objective algorithms. In *Parallel Problem Solving from Nature - PPSN VIII*, volume 3242 of *Lecture Notes in Computer Science*, pages 812–821. Springer Berlin Heidelberg.

[Schaffer, 1985] Schaffer, J. D. (1985). Multiple objective optimization with vector evaluated genetic algorithms. In *Proceedings of the 1st International Conference on Genetic Algorithms*, pages 93–100, Hillsdale, NJ, USA. L. Erlbaum Associates Inc.

[Schumann et al., 2010] Schumann, C., Bieberstein, J., Trumm, C., Schmidt, D., Bruners, P., Niethammer, M., Hoffmann, R., Mahnken, A., Pereira, P., and Peitgen, H. (2010). Fast automatic path proposal computation for hepatic needle placement. In *SPIE Medical Imaging*, volume 7625, page 76251J.

[Schumann et al., 2015] Schumann, C., Rieder, C., Haase, S., Teichert, K., Süss, P., Isfort, P., Bruners, P., and Preusser, T. (2015). Interactive multi-criteria planning for radiofrequency ablation. *Int J CARS*.

[Seitel et al., 2011] Seitel, A., Engel, M., Sommer, C., Redeleff, B., Essert-Villard, C., Baegert, C., Fangerau, M., Fritzsche, K., Yung, K., Meinzer, H.-P., and Maier-Hein, L. (2011). Computer-assisted trajectory planning for percutaneous needle insertions. *Medical Physics*, 38(6) :3246–3260.

[Shamir et al., 2010] Shamir, R., Tamir, I., Dabool, E., Joskowicz, L., and Shoshan, Y. (2010). A method for planning safe trajectories in image-guided keyhole neurosurgery. In *proceedings of MICCAI'10*, volume 6363, pages 457–464. Springer LNCS.

[Shamir et al., 2012] Shamir, R. R., Joskowicz, L., Tamir, I., Dabool, E., Pertman, L., Ben-Ami, A., and Shoshan, Y. (2012). Reduced risk trajectory planning in image-guided keyhole neurosurgery. *Med. Phys.*, 39(5) :2885.

[Sharma and Collet, 2010a] Sharma, D. and Collet, P. (2010a). An archived-based stochastic ranking evolutionary algorithm (ASREA) for multi-objective optimization. In *GECCO '10 : Proceedings of the 12th annual conference on Genetic and evolutionary computation*, pages 479–486, New York, NY, USA. ACM.

[Sharma and Collet, 2010b] Sharma, D. and Collet, P. (2010b). Gpgpu-compatible archive based stochastic ranking evolutionary algorithm (g-asrea) for multi-objective optimization. In *PPSN (2)*, pages 111–120.

[Sillay et al., 2012] Sillay, K. A., Kumbier, L. M., Ross, C., Brady, M., Alexander, A., Gupta, A., Adluru, N., Miranpuri, G. S., and Williams, J. C. (2012). Perioperative brain shift and deep brain stimulating electrode deformation analysis : Implications for rigid and non-rigid devices. *Ann Biomed Eng*, 41(2) :293–304.

[Slotty et al., 2012] Slotty, P. J., Kamp, M. A., Wille, C., Kinfe, T. M., Steiger, H. J., and Vesper, J. (2012). The impact of brain shift in deep brain stimulation surgery : observation and obviation. *Acta Neurochirurgica*, 154(11) :2063–2068.

[Smith et al., 2005] Smith, J. S., Quinones-Hinojosa, A., Barbaro, N. M., and McDermott, M. W. (2005). Frame-based stereotactic biopsy remains an important diagnostic tool with distinct advantages over frameless stereotactic biopsy. *J. Neurooncol.*, 73(2) :173–179.

[Srinivas and Deb, 1994] Srinivas, N. and Deb, K. (1994). Muiltiobjective optimization using nondominated sorting in genetic algorithms. *Evolutionary computation*, 2(3) :221–248.

[Stoll et al., 2012] Stoll, M., Boettger, M., Schulze, C., and Hastenteufel, M. (2012). Transfer of methods from radiotherapy planning to ablation planning with focus on uncertainties and robustness. *Biomedical Engineering / Biomedizinische Technik.*, 57(SI-1 Track-C) :901–904.

[Tirelli et al., 2009] Tirelli, P., de Momi, E., Borghese, N., and Ferrigno, G. (2009). An intelligent atlas-based planning system for keyhole neurosurgery. In *Computer Assisted Radiology and Surgery supplemental*, pages S85–S91.

[Trope et al., 2014] Trope, M., Shamir, R. R., Joskowicz, L., Medress, Z., Rosenthal, G., Mayer, A., Levin, N., Bick, A., and Shoshan, Y. (2014). The role of automatic computer-aided surgical trajectory planning in improving the expected safety of stereotactic neurosurgery. *International Journal of Computer Assisted Radiology and Surgery*, 10(7) :1127–1140.

[Trovato et al., 2009] Trovato, K., Dalal, S., Krücker, J., Venkatesan, A., and Wood, B. J. (2009). Automated rfa planning for complete coverage of large tumors. In Miga, M. I. and Wong, K. H., editors, *Medical Imaging 2009 : Visualization, Image-Guided Procedures, and Modeling*. SPIE-Intl Soc Optical Eng.

[Vaillant et al., 1997] Vaillant, M., Davatzikos, C., Taylor, R., and Bryan, R. (1997). A path-planning algorithm for image-guided neurosurgery. In *proceedings of CVRMed-MRCAS'97*, volume 1205 of *Springer LNCS*, pages 467–476.

[van Gerwen et al., 2012] van Gerwen, D. J., Dankelman, J., and van den Dobbelsteen, J. J. (2012). Needle–tissue interaction forces–a survey of experimental data. *Medical engineering & physics*, 34(6) :665–680.

[Villard et al., 2003] Villard, C., Soler, L., Papier, N., Agnus, V., Gangi, A., Mutter, D., and Marescaux, J. (2003). RF-Sim : a treatment planning tool for radiofrequency ablation of hepatic tumors. In *proceedings of Information Visualization*, pages 561–566. IEEE Computer Society Press.

[Škrinjar et al., 1998] Škrinjar, O., Spencer, D., and Duncan, J. S. (1998). Brain shift modeling for use in neurosurgery. *Proceedings of MICCAI'98*.

[Wang et al., 2013] Wang, K.-F., Pan, W., Wang, F., Wang, G.-F., Madhava, P., Pan, H.-M., Kong, D.-X., and Liu, X.-G. (2013). Geometric optimization of a mathematical model of radiofrequency ablation in hepatic carcinoma. *Asian Pacific Journal of Cancer Prevention*, 14(10) :6151–6158.

[Weihusen et al., 2007] Weihusen, A., Ritter, F., Kröger, T., Preusser, T., Zidowitz, S., and Peitgen, H.-O. (2007). "workflow oriented software support for image guided radiofrequency ablation of focal liver malignancies". In Cleary, K. R. and Miga, M. I., editors, *Medical Imaging 2007 : Visualization and Image-Guided Procedures*. SPIE-Intl Soc Optical Eng.

[Winkler et al., 2005] Winkler, D., Tittgemeyer, M., Schwarz, J., Preul, C., Strecker, K., and Meixensberger, J. (2005). The first evaluation of brain shift during functional neurosurgery by deformation field analysis. *Journal of Neurology, Neurosurgery & Psychiatry*, 76(8) :1161–1163.

[Wittek et al., 2010] Wittek, A., Joldes, G., Couton, M., Warfield, S. K., and Miller, K. (2010). Patient-specific non-linear finite element modelling for predicting soft organ deformation in real-time : application to non-rigid neuroimage registration. *Progress in biophysics and molecular biology*, 103(2-3) :292–303.

[Wolf et al., 2005] Wolf, I., Vetter, M., Wegner, I., Böttger, T., Nolden, M., Schöbinger, M., Hastenteufel, M., Kunert, T., and Meinzer, H.-P. (2005). The medical imaging interaction toolkit. *Medical Image Analysis*, 9(6) :594–604.

[Woodworth et al., 2006] Woodworth, G. F., McGirt, M. J., Samdani, A., Garonzik, I., Olivi, A., and Weingart, J. D. (2006). Frameless image-guided stereotactic brain biopsy procedure : diagnostic yield, surgical morbidity, and comparison with the frame-based technique. *Journal of Neurosurgery*, 104(2) :233–237.

[York et al., 2009] York, M. K., Wilde, E. A., Simpson, R., and Jankovic, J. (2009). Relationship between neuropsychological outcome and DBS surgical trajectory and electrode location. *Journal of the Neurological Sciences*, 287(1) :159–171.

[Zelmann et al., 2014] Zelmann, R., Beriault, S., Mok, K., Haegelen, C., Hall, J., Pike, G. B., Olivier, A., and Collins, D. L. (2014). Automatic optimization of depth electrode trajectory planning. In *Clinical Image-Based Procedures. Translational Research in Medical Imaging*, pages 99–107. Springer International Puplishing.

[Zhai et al., 2008] Zhai, W., Xu, J., Zhao, Y., Song, Y., Sheng, L., and Jia, P. (2008). Preoperative surgery planning for percutaneous hepatic microwave ablation. In *Lecture Notes in Computer Science*, pages 569–577. Springer Science + Business Media.

[Zitzler and Thiele, 1998] Zitzler, E. and Thiele, L. (1998). *An evolutionary algorithm for multiobjective optimization : The strength pareto approach*, volume 43. Citeseer.

[Zitzler and Thiele, 2001] Zitzler, E. and Thiele, L. (2001). Spea2 : Improving the strength pareto evolutionary algorithm.

[Zrinzo et al., 2012] Zrinzo, L., Foltynie, T., Limousin, P., and Hariz, M. I. (2012). Reducing hemorrhagic complications in functional neurosurgery : a large case series and systematic literature review. *Journal of Neurosurgery*, 116(1) :84–94.

Appendices

A

THE XML CONSTAINTS FILE

A.1 RFA constraints file

```
<constraint_file>

<data_definition>

<data name="needle length (mm)" label="maxPathLength">
  130
</data>

<data name="obstacles" label="obstacle_organs">
  obstacles( portalvein, ribs )
</data>

<data name="authorized tangency angle" label="tangAngle">
  20
</data>

<data name="distance skin-tumor" label="distTumorSkin">
  distmin( skin, center( target ) )
</data>

<data name="weight of volume constraint" label="w1" show="true">
  divide(3,10)
</data>

<data name="weight of portalvein risk constraint" label="w2" show="true">
  divide(3,10)
</data>

<data name="weight of ribs risk constraint" label="w2" show="true">
  divide(4,10)
</data>

<data name="skin" label="skin" obstacle="false">
</data>

<data name="liver" label="liver" obstacle="false">
</data>

</data_definition>
```

```
<strict_constraints_definition>

<strict_constraint name="initial target volume" impact="targetVolume">
  target
</strict_constraint>

<strict_constraint name="initial ablation volume" impact="ablationVolume">
  target
</strict_constraint>

<strict_constraint name="initial insertion zone" impact="insertionZone">
  skin
</strict_constraint>

<strict_constraint name="accessibility restriction" impact="insertionZone">
  visible( insertionZone, targetVolume, obstacle_organs )
</strict_constraint>

<strict_constraint name="path length restriction" impact="insertionZone">
  lower( distmin ( center( target ), toolInsertionPoint ), maxPathLength )
</strict_constraint>

</strict_constraints_definition>

<soft_constraints_definition>

<soft_constraint name="volume" label="sc_risk_1"
                 minValue="0" maxValue="1">
  divide( minus( volume( toolAblation ), volume( target ) ),
          mult ( 5, volume( target ) ) )
</soft_constraint>

<soft_constraint name="risk_portalvein" label="sc_risk_2"
                 minValue="0" maxValue="1">
  max( divide( minus( 5 , distmin (toolTrajectory, portalvein) ), 5 ), 0 )
</soft_constraint>

<soft_constraint name="risk_ribs" label="sc_risk_3"
                                minValue="0" maxValue="1">
  max( divide( minus( 5 , distmin (toolTrajectory, ribs) ), 5 ), 0 )
</soft_constraint>

<soft_constraint name="final const" label="SCfinal"
                                 minValue="0" maxValue="1">
divide ( plus ( mult( w1, sc_risk_1 ),
                            mult( w2, sc_risk_2 ),
                            mult( w3, sc_risk_3 )),
                plus( w1, w2, w3))
</soft_constraint>
```

```
</soft_constraints_definition>

</constraint_file>
```

A.2 DBS constraints file

```
<constraint_file>

<data_definition>

<data name="needle length (mm)" label="maxPathLength">
  110
</data>

<data name="front axis" label="frontAxis">
  frontAxis( skin )
</data>

<data name="obstacles" label="obstacle_organs">
  obstacles( sillon,ventricules )
</data>

<data name="weight_of_front_constraint" label="w1" show="true">
  0.2
</data>

<data name="weight_of_risk_constraint_ventricles" label="w2" show="true">
  0.4
</data>

<data name="weight_of_risk_constraint_sulci" label="w3" show="true">
0.4
</data>

</data_definition>

<strict_constraints_definition>

<strict_constraint name= "initial target volume" impact="targetVolume">
  target
</strict_constraint>

<strict_constraint name= "initial ablation volume" impact="ablationVolume">
  target
</strict_constraint>

<strict_constraint name= "initial insertion zone" impact="insertionZone">
  skin
```

```
</strict_constraint>

<strict_constraint name="path length restriction" impact="insertionZone">
  lower( distmin ( center( target ), toolInsertionPoint ), maxPathLength )
</strict_constraint>

<strict_constraint name="accessibility restriction" impact="insertionZone">
  visible( insertionZone, targetVolume, obstacle_organs )
</strict_constraint>

</strict_constraints_definition>

<soft_constraints_definition>

<soft_constraint name="risk_front" label="SCfront"
                 minValue="0" maxValue="1">
  divide( angle ( toolTrajectory, frontAxis ), 90.0 )
</soft_constraint>

<soft_constraint name="risk_ventricules" label="SCriskVentricles"
                 minValue="0" maxValue="1">
  max( divide( minus( 35.0 , distminVec ( ventricules, toolTrajectory ) )
                    , 35.0 ), 0 )
</soft_constraint>

<soft_constraint name="risk_sillon" label="SCriskSulci"
                 minValue="0" maxValue="1">
  max( divide( minus( 5.0 , distminVec ( sillon, toolTrajectory ) )
                    , 5.0 ), 0 )
</soft_constraint>

<soft_constraint name="final const" label="SCfinal"
                 minValue="0" maxValue="1">
  divide( plus( mult( w1, SCfront ),
                mult( w2, SCriskVentricles ),
                mult( w3, SCriskSulci )),
          plus ( w1,w2,w3) )
</soft_constraint>

</soft_constraints_definition>

</constraint_file>
```

B

NSGA-II

The Non-dominated Sorting Genetic Algorithm NSGA was firstly introduced in [Srinivas and Deb, 1994], and followed later by an improved version NSGA-II in [Deb et al., 2002].

In this appendix, we describe and comment the main algorithm of NSGA-II, with its salient features over other genetic algorithms techniques. For more details about NSGA-II algorithm, we refer the reader to the original work [Deb et al., 2002].

Pareto fronts ordering

In this phase, for an initial population $\mathcal{S}$ of size N, and m objectives, all the individuals in $\mathcal{S}$ are assigned to different fronts according to a non-dominated sorting approach.

In a classical non-dominated sorting approach, the fronts are built as the following :

In order to retrieve members of the first non-dominated front $\mathcal{F}_1$ (front $\mathcal{F}$ of rank 1), we compare each member with all the population (according to a dominance rule) members which means $O(mN)$ comparison. When $\mathcal{F}_1$ is attained, the complexity reach to $O(mN^2)$. After that, to find the members of the second front $\mathcal{F}_2$, the same process is repeated on $\mathcal{S} \setminus \mathcal{F}_1$, in the worst case the complexity for finding $\mathcal{F}_2$ is $O(mN^2)$. In the same way, the process continues until finding all the fronts. In the worst case where there are N fronts, which means that only one individual in each front, resulting in a complexity for the whole sorting process of order $O(mN^3)$ making this process unsatisfactory for real world problem.

In NSGA-II non-dominated sorting approach, the complexity drawback has been overridden, and the complexity has been reduced to $O(mN^2)$ thanks to a simple and efficient way, the sorting is performed as follows :

For each individual $x \in \mathcal{S}$, two entities are introduced :

- the domination count n_x, the number of individuals which dominate x ;
- and $\mathcal{D}_x$, the set of solutions that x dominates.

All individuals in $\mathcal{F}_1$ have a domination count $n_x = 0$, now for all $x \in \mathcal{F}_1$ with $n_x = 0$, we visit each member y of its $\mathcal{D}_x$ and reduce its domination count by one ($n_y \leftarrow n_y - 1$). Whenever a solution y becomes with n_y equals to zero which means that it is no longer dominated by any solution, we move it to a separate list $\mathcal{T}$. So far, the members of $\mathcal{T}$ constitute the second non-dominated front. The same procedure is continued with each member of $\mathcal{T}$, and the third front is identified, and so on until identifying all the fronts. The sorting algorithm is described in 3, and Fig. 6.9 shows individuals laying on "virtual lines" representing Pareto fronts of different ranks.

Algorithm 3: Non-dominated sorting

```
foreach $x \in \mathcal{S}$ do
    $n_x \leftarrow 0$;
    $\mathcal{D}_x \leftarrow \{\}$;
    $\mathcal{F}_1 \leftarrow \{\}$;
    foreach $y \in \mathcal{S}$ do
        if $(x\ dom\ y)$ then
            $\mathcal{D}_x \leftarrow \mathcal{D}_x \cup y$;
        else if $(y\ dom\ x)$ then
            $n_x \leftarrow n_x + 1$;
    if $n_x = 0$ then
        $x_{rank} \leftarrow 1$;
        $\mathcal{F}_1 \leftarrow \mathcal{F}_1 \cup \{x\}$;
$i \leftarrow 1$;
while $\mathcal{F}_i \neq \{\}$ do
    $\mathcal{T} = \{\}$;
    foreach $x \in \mathcal{F}_i$ do
        foreach $y \in \mathcal{D}_x$ do
            $n_y \leftarrow n_y - 1$;
            if $(n_y = 0)$ then
                $y_{rank} \leftarrow i + 1$;
                $\mathcal{T} \leftarrow \mathcal{T} \cup \{y\}$
    $i \leftarrow i + 1$;
    $\mathcal{F}_i \leftarrow \mathcal{T}$;
```

Complexity Analysis

For each solution x in the second or higher level front, the domination count n_x can be at most $N - 1$. Thus, each solution x will be visited at most $N - 1$ times before its domination count becomes zero. At this point, x is assigned a non domination level and $n_x \leftarrow 0$ and will never be visited again. Since there are at most $N - 1$ such solutions, the total complexity is $O(N^2)$, and the overall complexity of the procedure is $O(mN^2)$ which is one of the strength points of NSGA-II.

Diversity preserving

Diversity preserving is one of the most pertinent features in any EA, and an elitism mechanism is required to prevent the loss of good solutions once they are found.

Sharing techniques are widely used to maintain the population's diversity. In these techniques, a metric to calculate the distance between two individuals is generally introduced, and a sharing parameter σ_{share} (also known as *niche radius*) should be defined. It denotes the maximum value of distance within which any two individuals are considered to have the same quality, and thus share the same fitness value. Roughly speaking, maximizing the distance between individuals is desired to avoid genetic drifts.

However, the sharing technique undergoes two drawbacks :

- firstly, it is difficult to choose the value of σ_{share} automatically, and even that their are some guidance rules to find a suitable value, but this is done manually by the user ;
- and secondly, the complexity of the sharing function is $O(N^2)$ since every individual should be compared with all the population's individuals.

Density estimation

In NSGA-II, the selection process is guided without a sharing parameter, and the diversity is maintained automatically.

To that end, a "*crowding-distance*" metric with a "*crowded-comparison*" operator have been introduced.

1.Crowding-distance : it is a metric which measures how close an individual is to its neighbors. For a given solution, the distance value for a single objective function is the absolute normalized difference in the function values of two adjacent solutions. Fig. 6.8 illustrates the crowding distance for two individuals.

A *crowding-distance* is accorded to all the individuals in a non-dominated set and stored in a list $\mathcal{I}$ using the following algorithm :

Algorithm 4: crowding distance

```
$l \leftarrow |\mathcal{I}|$ ;
foreach $i$ do
    $\mathcal{I}[i]_{distance} \leftarrow 0$;
    foreach objective $m$ do
        $\mathcal{I} \leftarrow sort(\mathcal{I}, m)$;
        $\mathcal{I}[1]_{distance} \leftarrow \infty$;
        $\mathcal{I}[l]_{distance} \leftarrow \infty$;
        for $i = 2$ to $l$ do
            $\mathcal{I}[i]_{distance} \leftarrow \mathcal{I}[i]_{distance} + (\mathcal{I}[i+1]_m - \mathcal{I}[i-1]_m)/(f_m^{max} - f_m^{min})$;
```

Respectively to sharing techniques, a large average crowding distance will result in better diversity in the population.

2.Crowded-comparison operator$\prec_n$: it is designed to compare individuals, after being assigned their crowding distance, in order to decide which of them has a better fitness value.

For two solutions i and j in $\mathcal{S}$, $\prec_n$ is defined as follows :

$$i \prec_n j \text{ if } (i_{rank} < j_{rank}) \text{ or } ((i_{rank} = j_{rank}) \text{ and } (i_{distance} > j_{distance}))$$

Main algorithm

An initialization phase : an initial population $\mathcal{P}_0$ of size N is selected randomly from the initial solution space $\mathcal{S}$, and the individuals are assigned a fitness value for the m objective functions. A first offspring generation $\mathcal{Q}_0$ of size N is then created by a tournament selection on $\mathcal{P}_0$ followed by recombination and mutation processes.

An iterative phase : the populations are combined together for a certain number of generations. So far, for the t^{th} generation, a combined population $\mathcal{R}_t$ of size $2N$ is formed from the current population $\mathcal{P}_t$ and the offspring generation $\mathcal{Q}_t$. Since all the previous and current best individuals are added in the population, elitism is ensured. $\mathcal{R}_t$ is then sorted based on non-dominated and crowding distance sorting. The new generation $\mathcal{P}_{t+1}$ is filled by each front subsequently until the population size exceeds N. If by adding all the individuals in front $\mathcal{F}_j$ the population exceeds N then individuals in front $\mathcal{F}_j$ are selected based on their crowding distance in the descending order until the population size becomes equal to N. The process is repeated until the desired offspring generation is attained. Fig. B.1 illustrates the process, while the main algorithm is described in B.

Algorithm 5: Main algorithm

```
initialization-phase ;
$\mathcal{R}_t \leftarrow \mathcal{P}_t \cup \mathcal{Q}_t$ ;
$\mathcal{F} \leftarrow$ fast-non-dominate-sort($\mathcal{R}_t$) ;
$\mathcal{P}_{t+1} \leftarrow \{\}$ ;
$i \leftarrow 1$ ;
while $|\mathcal{P}_{t+1}| + |\mathcal{F}_i| \leq N$ do
    crowding-distance-assignment($\mathcal{F}_i$);
    $\mathcal{P}_{t+1} \leftarrow \mathcal{P}_{t+1} \cup \mathcal{F}_i$ ;
    $i \leftarrow i + 1$ ;
$sort(\mathcal{F}_i, \prec_n)$;
$\mathcal{P}_{t+1} \leftarrow \mathcal{P}_{t+1} \cup \mathcal{F}_i[1 : (N - |\mathcal{P}_{t+1}|)]$ ;
$\mathcal{Q}_{t+1} \leftarrow$ make-new-population($\mathcal{P}_{t+1}$);
$t \leftarrow t + 1$;
```

Creating a new generation is the core of any GA. As in nature, an offspring generation is created by a selection process between some of the current population individuals, followed by a recombination process (crossover) between the selected ones, and probably a certain mutation to an individual may happen. Fig. B illustrates the three processes.

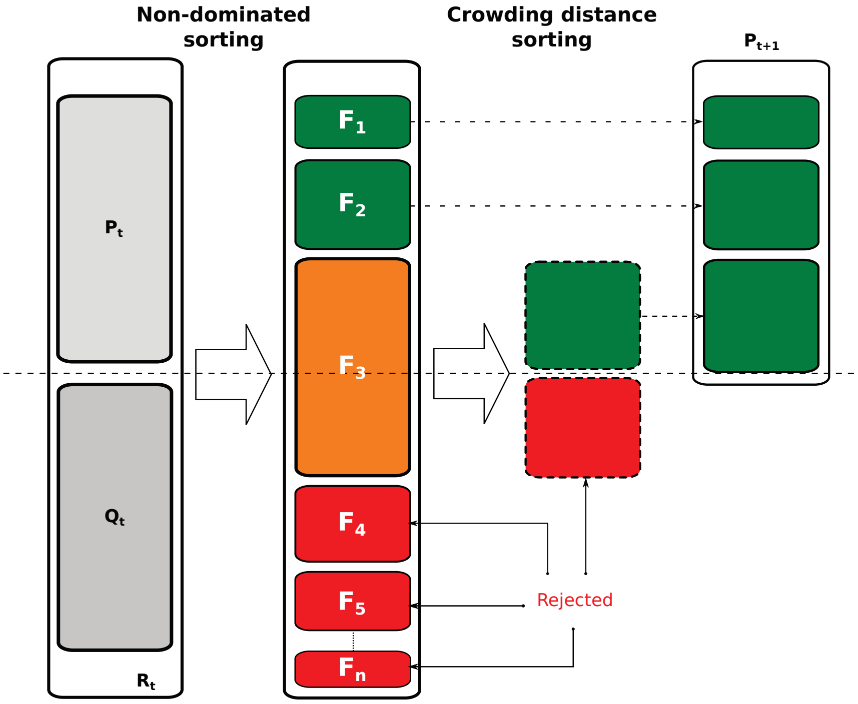

FIGURE B.1 – Population size maintenance through the two sorting phases.

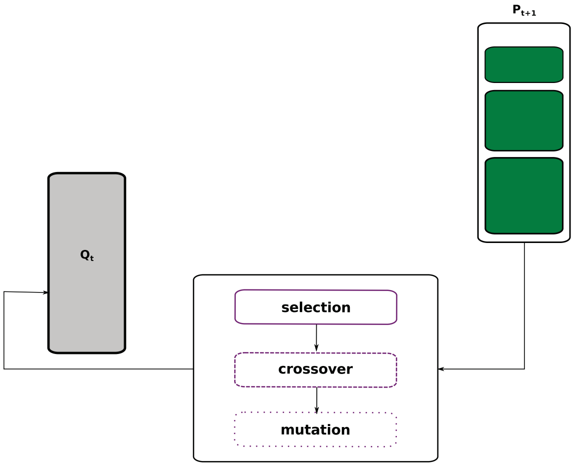

FIGURE B.2 – make new population

Some genetic algorithms concepts

Here are brief definitions of some well-known concepts in genetic algorithms, and which are mentioned in this manuscript.

Genetic drift phenomenon

Genetic drift is a term borrowed from population genetics where it is used to explain changes in gene frequency through random sampling of the population. It is a phenomenon observed in genetic algorithms (GA) due to the stochastic nature of the selection operator, and is one of the mechanisms by which the population converges to a single member.

Niching scheme

Niching is a class of methods that try to converge to more than one solution during a single run. In genetic algorithms, niching is the idea of segmenting the population of the GA into disjoint sets, intended so that there will be at least one member in each region of the fitness function that is "interesting"; generally by this we mean that we cover more than one local optima. Imagine a function like $f(x) = sin(x^2)$

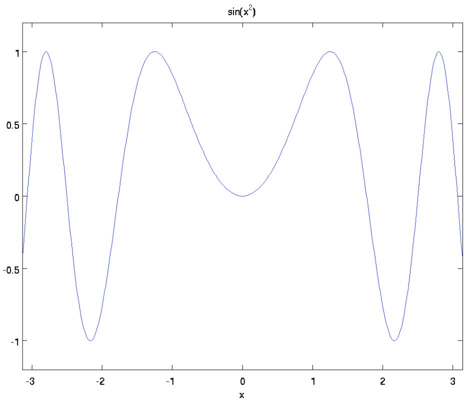

FIGURE B.3 – $sin(x)$

A normal GA will eventually converge towards one of the two global minima. Which one depends on the initial population and the random genetic drift occurring throughout the run, but eventually, we'll get n copies of one individual in one or the other valleys. For example, if we lookd at such a GA when it was almost converged, we might see something like

Niching is a general class of techniques intended to end up with roughly half the population converging in each minima (or possibly even including a few members in the less fit minimum at $x = 0$).

Indeed, niching is not really an algorithm so much as a general class of algorithms. One such method is Goldberg's fitness sharing. In this method, we define a niche radius sigma. Any two individuals closer together than this sigma are considered to be in the same niche, and thus must share their fitness values (we may think of this as being a function that decreases fitness of each member of the niche the more densely populated the niche is). Then we will have the GA operate on the shared fitness values instead of the raw ones.

The idea here is to discourage convergence to a single region of the fitness function by pretending there are limited resources there. The more individuals try to move in, the worse off they all are. The result is that as the GA converges to a single local optimum somewhere, the fitness of that optimum decreases because of the increased

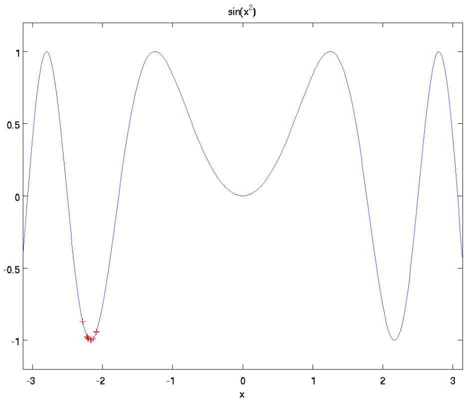

Figure B.4 – $sin(x)$

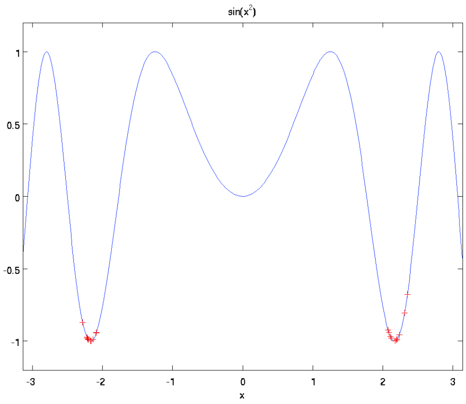

Figure B.5 – $sin(x)$

competition within the niche. Eventually, another region of the fitness landscape becomes more attractive, and individuals migrate over there. The idea is to reach a steady state – a fixed point in the dynamics – where an appropriate representation of each niche is maintained.

Sharing is hard because of the need to manually set the niche radius, and the algorithm is quite sensitive to this choice. Another alternative is crowding. In particular, we might look up "Deterministic Crowding", which was a popular method for a period of time. In crowding based methods, instead of dealing with an explicit radius, we work by limiting the set of individuals that a new offspring can replace to some set of similar solutions, for example an offspring might be allowed to replace only one of its parents. The effect is to try to prevent replacing a unique individual with one that is very similar to a dozen others in the population and thus to preserve diversity that way.

Thèse de doctorat
Laboratoire des sciences de l'ingénieur, de l'informatique et de l'imagerie
ICube, UMR 7357

par

Mme Noura HAMZE

présentée pour obtenir le grade de Docteur de l'université de Strasbourg

Mention : Informatique

Optimisation et Planification Préopératoire des Trajectoires en Conditions Statiques et Déformables pour la Chirurgie Guidée par l'Image

---

UNIVERSITÉ DE STRASBOURG

soutenue publiquement le 21 juin 2016 devant le jury composé de :

- M. Leo Joskowicz, Hebrew University of Jerusalem, rapporteur externe
- M. Emmanuel Promayon, Université Joseph Fourier, rapporteur externe
- M. Gabor Fichtinger, Queen's University, examinateur
- Mme. Caroline Essert, Université de Strasbourg, directrice de thèse

Abstract

En chirurgie mini-invasive guidée par l'image, une planification préopératoire précise des trajectoires des outils chirurgicaux est un facteur clé pour une intervention réussie. Cependant, une planification efficace est une tâche difficile, qui peut être considérablement améliorée en considérant différents facteurs contributifs tels que les déformations biomécaniques intra-opératoires, ou en introduisant de nouvelles techniques d'optimisation.

Dans ce travail, nous nous concentrons sur deux aspects. Le premier aspect porte sur l'intégration de la déformation intra-opératoire dans le processus de planification de trajectoire. Nos méthodes combinent des techniques d'optimisation géométrique à base de simulations biomécaniques. Elles sont caractérisées par un certain niveau de généralité, et ont été expérimentées sur deux types d'interventions chirurgicales : les procédures percutanées pour l'ablation de tumeurs hépatiques, et la stimulation cérébrale profonde en neurochirurgie. Deuxièmement, nous étudions, mettons en œuvre, et comparons plusieurs approches d'optimisation en utilisant des méthodes qualitatives et quantitatives, et nous présentons une méthode efficace d'optimisation évolutionnaire multicritères à base de Pareto qui permet de trouver des solutions optimales qui ne sont pas accessibles par les méthodes existantes.

1 Introduction

La chirurgie mini-invasive est devenue très commune dans les hôpitaux ces dernières années. Par rapport à la chirurgie conventionnelle (également connue comme la chirurgie ouverte), qui est généralement réalisée en faisant de grandes incisions dans le corps du patient, les procédures dans la chirurgie mini-invasive nécessitent de petites incisions à l'aide d'instruments chirurgicaux hautement spécialisés, guidés grâce à l'assistance de l'imagerie médicale. Cette nouvelle chirurgie est caractérisée par un certain nombre des avantages qui augmentent son acceptation telles que : la diminution du traumatisme des tissus, moins de saignements, moins de cicatrices, une récupération plus rapide avec court séjour à l'hôpital, un retour plus rapide aux activités normales, et moins du peur et de la douleur. Par contre, elle présente des défis majeurs, notamment la visibilité réduite, et la manœuvre limitée des outils chirurgicaux à l'intérieur du corps du patient. Cependant, une planification précise est une clé pour une intervention réussite. La chirurgie guidée par l'image est largement utilisé dans la neurochirurgie, la cardiologie, la gynécologie, l'urologie et la chirurgie abdominale. Dans cette thèse nous nous intéressons dans deux procédures : la stimulation cérébrale profonde, et l'ablation des tumeurs abdominales.

1.1 La stimulation cérébrale profonde

La stimulation cérebrale profonde (SCP) ou (DBS) en anglaise pour Deep Brain Stimulation, est une procédure de neurochirurgie destiné à traiter les troubles du mouvement tels que la maladie de Parkinson (PD), dystonie, ou des tremblements essentiels. Il a été proposé en 1987 par une équipe médicale française. Le principe fonctionnel de ce traitement consiste à stimuler électriquement un noyau profond du cerveau d'une manière permanente (Fig.1, droite).

À cette fin, une procédure de neurochirurgie basée sur l'image est conçue. Elle consiste à implanter un (unilatéral) ou deux (bilatérales) électrodes permanent dans le tissu cible du cerveau à travers d'un petit trou avec un diamètre de 10 à 14 mm., fait au crâne du patient. Durant l'intervention, la tête du patient est fixée dans un cadre stéréotaxique comme le cadre de Leksell (Fig.1, gauche).

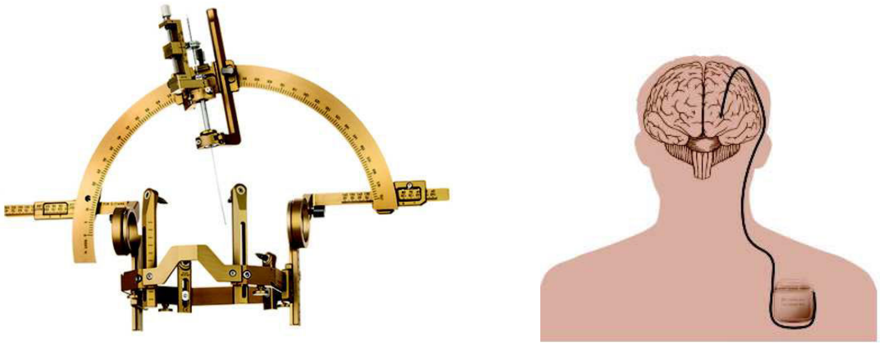

Figure 1 – Le cadre Stereotactique Leksell, et une illustration d'un système de SCP avec un neurostimulateur implanté dans le thorax, envoie des impulsions électriques à l'électrode pour stimuler une structure cérébrale profonde

1.2 L'ablation thermique des tumeurs hépatiques

le cancer hépatique est l'une des tumeurs malignes les plus fréquentes et est responsable de plus d'un million de décès par an dans le monde.

De nombreuses techniques d'ablation sont utilisés en clinique pour la destruction des cellules malveillantes telles que la cryothérapie, la radiofréquence, et l'ablation en utilisant des micro-ondes. Malgré les différents mécanismes d'ablation, ils comptent tous sur le même concept de la technique interventionnelle. Une aiguille est insérée dans le foie, habituellement sous la direction de l'échographie, la CT ou plus récemment l'IRM. Une fois placé dans la tumeur, la chaleur, le froid ou un produit pharmaceutique est localement délivré dans la région de la tumeur, ce qui déclenche la destruction de la tumeur sur une question de quelques minutes. (Fig.4).

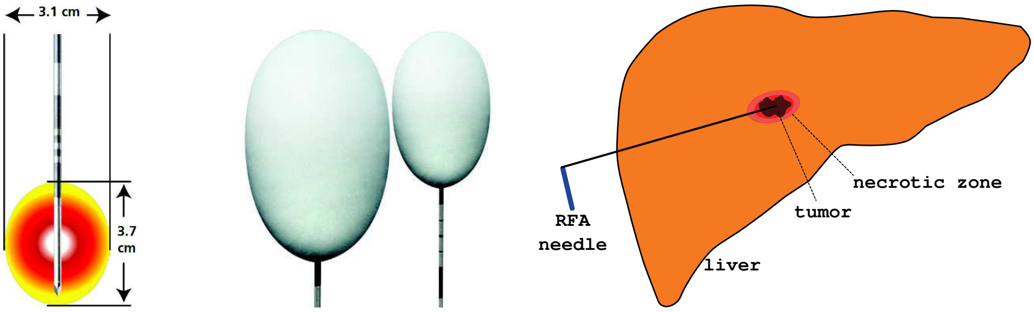

(a) RFA (b) cryoablation (c) tumeur hépatique

FIGURE 2 – Illustration des techniques d'ablation des tumeurs hépatiques

Définition. Dans le cadre de ce travail, nous allons souvent utiliser le mot ≪planification≫ pour faire référence à la ≪planification préopératoire≫.*Il consiste à calculer dans une phase préopératoire un trajectoire sûr de l'outil chirurgical pour atteindre une cible prédéfinie.* En fonction de l'intervention, la cible peut être soit une structure anatomique ou un point spécifique.

1.3 Problème

La planification d'une intervention est une tâche décisive. Les chances d'une opération chirurgicale réussie dépendent fortement d'une bonne stratégie de planification préopératoire. Quelques jours avant l'intervention, des images CT ou IRM du patient sont acquises, le médecin élabore son plan d'intervention de ces ensembles de tranches 2D préopératoires. C'est une tâche difficile, car le médecin doit construire une représentation mentale d'un modèle 3D de l'anatomie du patient et de la position des pathologies, et estimer un trajectoire tridimensionnel sure.

En fait, élaborer une planification de trajectoire basée sur les images préopératoires statiques n'est pas suffisante, car les structures anatomiques sont déformables, et quant on ne se rend pas et compte du mouvement qui va se passer au cours de la chirurgie, cela soulève certaines questions en termes de précision et de fiabilité de la planification. De multiples sources de déformations intra-opératoires telles que la respiration, l'interaction entre les outils chirurgicaux et des tissus mous, ou la déformation du cerveau, peuvent réduire le niveau de la sécurité de la trajectoire, ou même fausser la planification préopératoire. Ces défis encouragent une approche de planification dans des conditions dynamiques.

Dans le cas de la simulation cérébrale profonde, pendant la chirurgie, un trou est percé dans le crâne du patient afin d'accéder au tissu cérébral, ce trou est fait au niveau du point d'entrée défini par un chirurgien. Le tissu cérébral est un matériau déformable, et quand le crâne et la dure-mère sont ouvertes, le liquide cérébro-spinal qui entoure le cerveau peut fuir à travers le trou. Une fuite de ce liquide provoque un changement de la pression intracrânienne et constitue l'une des principales raisons d'une déformation du cerveau appelés *brain shift* comme illustré sur Fig. 3. Cependant, d'autres structures anatomique telle que les vaisseaux sanguins peuvent se déplacer jusqu'à 10 mm. Dans le pire des cas, si un vaisseau sanguin se déplace à travers le trajet de l'électrode, elle pourrait conduire à une hémorragie et à la mort du patient.

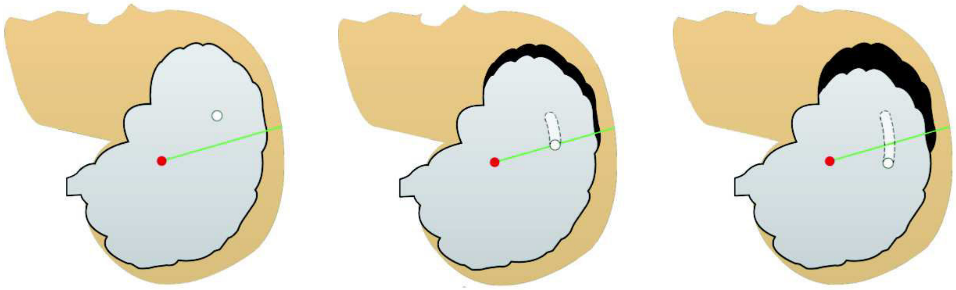

(a) Conditions statiques (b) Conditions dynamiques (c) Conditions dynamiques

FIGURE 3 – La déplacement de vaisseau à cause du "brain shift" peut traverser le trajet de l'électrode.

Dans le cas de l'ablation de la tumeur hépatique, le foie est un objet hautement déformable de faible raideur. Par conséquent, les forces appliquées en raison de l'interaction avec l'aiguille provoquent des déformations importantes, principalement dans le les zones proches de la trajectoire de l'aiguille. Les forces peuvent dépasser 1 N. En outre, les aiguilles souples se plient lors de l'insertion et ne suivent pas une trajectoire linéaire. En conséquence, ils peuvent dévier de la trajectoire préopératoire prévue et ils peuvent manquer la tumeur cible. Fig 4 illustre ce type de limitation.

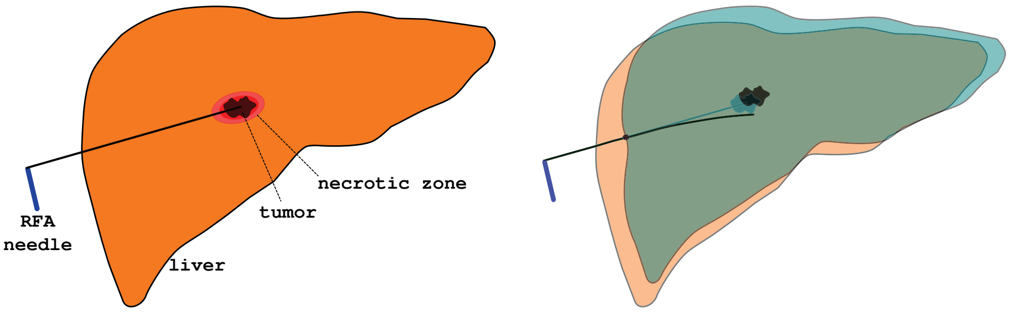

(a) Conditions statiques (b) Conditions dynamiques

FIGURE 4 – La courbure d'une aiguille flexible après avoir pénétrée dans les tissus du foie, elle dévie du trajet droit prévu et la cible est manquée.

1.4 Contribution

Nous présentons une approche de planification préopératoire automatique de trajectoire qui tient en compte certaine déformation biomécanique. Nos méthodes combinent des techniques d'optimisation basées sur la géométrie avec des simulations basés sur la physique. Nous avons expérimenté nos méthodes sur deux interventions chirurgicales différentes : Dans la stimulation profonde du cerveau en neurochirurgie, pour calculer une trajectoire de l'électrode de stimulation, cette trajectoire tient en compte le phénomène de "brain shift". La deuxième procédure est l'ablation thermique des tumeurs hépatiques, on calcule une trajectoire préopératoire non rectiligne pour des aiguilles flexibles, la planification tient en compte la déformation de l'aiguille flexible pendant le processus d'insertion et la déformation du tissu mou perforé.

Ensuite, nous présentons une méthode d'optimisation multi-critères sur la base de Pareto qui peuvent trouver des solutions optimales qui ne sont pas accessibles par les méthodes existantes.

2 Planification pour l'ablation des tumeurs abdominales

Nous proposons une planification de trajectoire préopératoire sur la base à la fois géométrique et physique des modèles. Nous nous attendons à la déformation en exécutant des simulations biomécaniques de la insertion de l'aiguille flexible à l'intérieur de l'abdomen, et nous injectons itérativement cette précieuse l'information de la physique dans un solveur d'optimisation pour effectuer une planification plus réaliste compatible avec les conditions dynamiques. Fondamentalement, notre approche de planification implique deux aspects principaux : la modélisation et de simulation biomécanique, et la planification algorithme.

2.1 Modélisation biomechanique et simulation

Effectuer des simulations réalistes nécessite un modèle physique efficace des objets.Nous présentons une modélisation numérique basée sur la méthode des éléments finis pour les tissus mous et l'aiguille, avec un modèle de contraints pour simuler l'interaction entre eux. Le modèle des tissus mous se base sur la méthode des éléments finis (modèle linéaire co-rotationnel) Le modèle d'aiguille est basée sur la formulation de Timoshenko de poutre qui tient en compte les degrés de liberté de position, ainsi que de la rotation. Par conséquent, chaque élément d'aiguille est composée de deux nœuds, chacun ayant 6 DoFs. L'interaction tissu-aiguille basé sur la résolution de contraints. Une illustration d'un modèle

(a) Modèle de simulation

(b) Modèle géometrique

FIGURE 5 – Les deux modèle physique et géométrique requis pour la planification.

2.2 L'algorithme Haystack

Nous avons mis en place une méthode d'optimisation pour le calcul de trajectoires courbes qui peuvent atteindre la cible dans un milieu déformable. Notre algorithme de planification est basée sur une approche ≪générer et tester".

notre méthode se situe dans un pipeline illustré sur la figure (Fig.6).

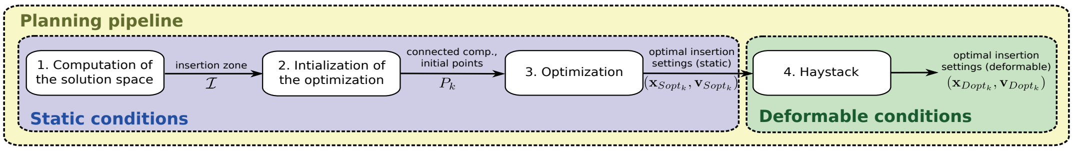

FIGURE 6 – Le pipeline de planification en conditions statiques et déformables.

l'algorithme consiste en deux phases : une phase de suivi de cible, et une phase de raffinement dès que la cible est atteinte. Ces deux phase sont illustrés dans la figure (Fig.7).

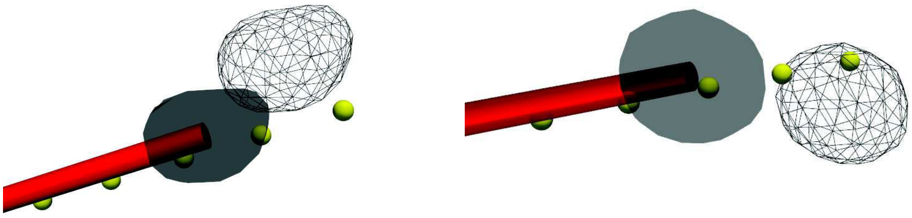

(a) Phase de suivi

(b) Phase de raffinement

FIGURE 7 – Les phases de l'algorithme Haystack

Pour tester l'efficacité de cet algorithme, nous avons le comparé avec deux autres méthode d'optimisation : une méthode de Nelder-Mead (Downhill), et avec une recherche quasi-exhaustive. Les tests sont fait sur 12 modèles de patients spécifiques préparé avec des variations de tailles et de positions des tumeurs. Les résultat obtenus montrent que quand une simulation de déformations est fait en se basant sur une trajectoire planifiée dans des conditions statiques, la cible va être loupé dans six cas parmi les 12 cas, alors que dans 4 cas la cible va être atteinte, et dans deux cas un obstacle va être touché. Le tableau résume les moyennes de nombre d'itérations, le temps, et la valeur de la fonction de coût pour les trois algorithmes.

Method	iterations nb.	time *mn*.	f
EX	1000	320	0.15
DH	123	27	0.33
HST	23	6	0.169

3 Planification pour la stimulation cérébrale profonde

3.1 Modèle du cerveau

Le cerveau est considéré comme un corps mou soumis aux lois de la mécanique des milieux continus. Une des méthodes numériques pour résoudre les équations de mouvement est la méthode des éléments finis (FEM). Dans ce travail, nous utilisons $\mathcal{P}_1$ Lagrange tétraèdres. Alors que le processus de "Brain shift" se produit à une vitesse très faible, on considère le problème comme quasi-statique et ne cherchons la configuration du cerveau à l'équilibre, sans tenir compte des effets transitoires dynamiques. Enfin, l'équation discrète à résoudre est :

$$\mathbf{f}(\mathbf{x}) = 0 \tag{1}$$

où $\mathbf{x}$ and $\mathbf{f}$ sont respectivement la position et la force vecteurs sur les noeuds des éléments tétraédriques. En ce qui concerne l'application de la simulation, la déformation du cerveau peut être considérée comme faible. Cela nous permet d'utiliser la loi de Hooke pour définir le comportement des tissus. Elle définit une relation linéaire entre la contrainte et le stress. Pour gérer de grands déplacements (tout en maintenant petite déformation), nous utilisons une formulation de co-rotation, où les non-linéarités géométriques sont estimés avec la rotation de l'élément par rapport à sa configuration initiale.

Interaction avec les structures osseuses : Quand le cerveau se déforme et se déplace, il peut entrer en collision avec l'endocrâne. Une fois les collisions ont été détectés, les contacts sont résolus en utilisant la loi de Signorini $0 \leq \delta \perp \lambda \geq 0$. L'interaction avec les structures osseuse établit une relation orthogonale entre la réponse de force de contact λ et δ la distance d'interpénétration. Nous assurons que la condition du Signorini est remplie à la fin de chaque pas de temps en ajoutant un terme de contraintes dans la première équation.

Le liquide cérébro-spinal La principale cause de "Brain shift" est une perte de liquidecérébro-spinal (CSF) entourant le cerveau. La densité du CSF est similaire à l'eau ($\rho = 1007$ kg/m^3). Une perte du CSF conduit à un changement de pression à l'intérieur du crâne et provoque une déformation du cerveau. L'action de CSF sur le cerveau est modélisé avec une pression hydrostatique :

$$\mathbf{f}_{CSF} = \int_{S_e} \big(\rho\, g\, h + p(z_0)\big) \mathrm{d}\mathbf{S} \tag{2}$$

Fig.1 illustre les différentes composantes dans la simulation. La quantité du "Brain shift" est commandé par le niveau du liquide. Une perte de niveau du CSF h, et par la diminution des forces de fluide.

3.2 Approche de planification

Notre approche de planification préopératoire est basée sur une méthode contrainte de résolution géométrique dans des conditions statiques que nous avons précédemment publié dans [8].

Dans l'environnement statique : Pour mettre en œuvre une planification statique conditions $\mathbf{E_s}$, nous formalisons les règles chirurgicales en deux catégories de contraintes géométriques : contraintes strictes **HC** et contraintes souples **SC**. Alors que les **HC** expriment des règles strictes qui ne doivent pas être violés comme la traversée d'un vaisseau sanguin, les **SC** expriment des préférences telles que le maintien de la trajectoire le plus loin possible des ventricules. Pour résoudre **HC**, nous extrayons de la surface initiale de la peau $\mathbf{\Omega_0}$, la zone d'insertion faisables $\mathbf{\Omega_s}$ qui satisfait **HC**. Ceci est réalisé en éliminant du maillage de la peau des triangles qui sont invisibles à la cible. Par la suite, on calcule une trajectoire optimale en estimant sa qualité par

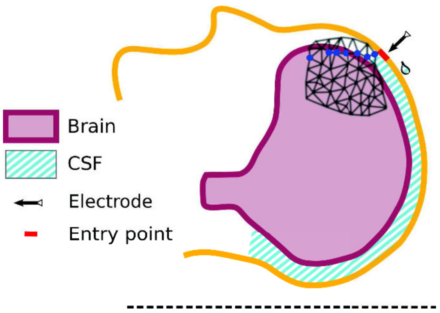

FIGURE 8 – Représentation schématique des points d'entrée (bleu) de la peau initiale de maillage S se trouvant à la même hauteur et susceptible de conduire à la mêmebrain shift maximale possible BS_h.

rapport aux **SC**. À cette fin, nous attribuons une fonction de coût f_i à chaque **SC**, et nous créons une fonction objective agrégative f composé de tous les **SC**.

$$f = \frac{\sum_{i=1}^{n} w_i . f_i}{\sum_{i=1}^{n} w_i} \tag{3}$$

Dans l'équation. 3, les poids w_i reflètent l'importance de chaque règle chirurgicale par rapport aux autres et sont déterminés par les chirurgiens. En minimisant f en utilisant une technique d'optimisation (Downhill Simplex), nous obtenons une trajectoire optimale (un point d'insertion et une direction).

Afin de réaliser une planification dans des conditions dynamiques $\mathbf{E_d}$, nous devons anticiper les potentielles déformations causées par le phénomène "brain shift" φ. Pour l'instant, il est impossible de déterminer dans une phase préopératoire l'ampleur exacte du "brain shift". Elle peut varier d'un niveau minimum φ_0 (correspondant à aucun brain shift) à un maximum φ_{max} (correspondant à la perte complète de CFS par le point d'entrée). Pour cette raison, notre objectif est de trouver une trajectoire sûre quel que soit l'intensité du «brain shift" de φ_0 à φ_{max} et incluant tous les niveaux intermédiaires possibles φ_i.

Alors que dans $\mathbf{E_s}$ la planification est réalisée sur le modèle statique initial $\mathbf{M_s}$, dans $\mathbf{E_d}$ il est calculé sur plusieurs modèles déformés $\mathbf{M_{d\varphi}}$ calculé en utilisant le framework de simulation biomécanique SOFA [1]. Plusieurs simulations correspondant à des niveaux (φ_0 to φ_{max}) sont calculés et sauvegardés dans une base de données de déformations spécifiques au patient. Nous avons accès à la base de données de simulations au cours du processus de planification en utilisant notre plugin de planification mis en œuvre dans MITK [16].

la méthode proposée consiste en deux étapes :

— Calculer la zone d'insertion possible dans des conditions dynamiques $\mathbf{\Omega_d}$.

— Calculer la trajectoire optimisée $\mathbf{\Omega_d}$.

Pour obtenir$\mathbf{\Omega_d}$ nous attribuons un niveau de hauteur h à chaque point d'entrée$p_i \in \mathbf{\Omega_0}$ (comme cela est illustré sur la figure 2). Pour chaque hauteur h, nous construisons son déformé modèle correspondant $\mathbf{M_{d}}_h$ en additionnant tous les modèles déformables $\mathbf{M_d}_{\varphi_0}$ to $\mathbf{M_d}_{\varphi_{max}}$ résultant de φ_0 to φ_{max}. Ensuite, nous vérifions si p_i satisfait à **HC** pour $\mathbf{M_{d}}_h$, si oui, on l'ajouter à $\mathbf{\Omega_d}$, et on l'exclut sinon. Dans une deuxième étape, nous appliquons l'optimisation Nelder-Mead méthode [13] sur $\mathbf{\Omega_d}$ pour trouver la meilleure trajectoire. À chaque itération, nous proposons une trajectoire candidate τ, nous obtenons le modèle $\mathbf{M_{d}}_h$ selon la hauteur de h du

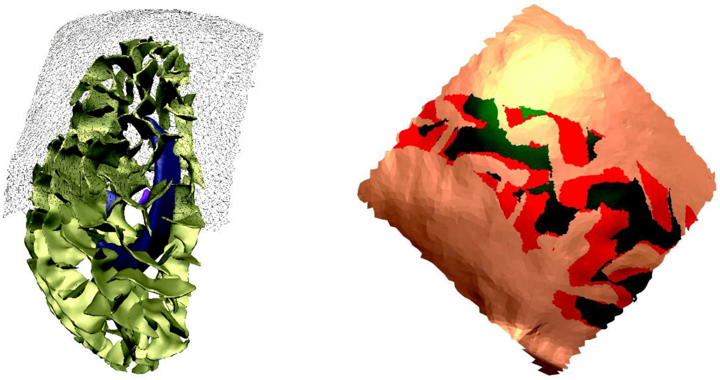

(a) Modèle 3D initial pour le solveur geometrique

(b) $\mathbf{E_d}$, $\mathbf{M_d}$: $\omega_\mathbf{s}$ en vert, et $\mathbf{\Omega_d}$ en vert et rouge

point d'entrée du candidat et nous évaluons $f(\tau)$ pour $\mathbf{M_d}_h$. Les itérations sont arrêtées lorsque la amélioration de f tombe sous un seuil ε, alors τ est considéré comme la trajectoire optimale.

3.3 Expérimentations

Nous avons testé notre méthode sur une modèle anonyme d'un patient réel. Le modèle 3D de cerveau 9a a été construit en utilisant le pipeline pydbs.

Le modèle est constitué de maillage de la surface des sillons, les ventricules, le noyau sous-thalamique, et un patch de la peau.

Tout d'abord, nous avons comparé les deux zones d'insertion possibles $\mathbf{\Omega_s}$ et $\mathbf{\Omega_d}$ calculée pour $\mathbf{E_s}$ et $\mathbf{E_d}$ respectivement. Les résultats obtenus sont présentés dans le tableau 1.

Table 1 – Zones d'insertions : tailles, temps de calcul, et le ration du couverture.

	$\mathbf{\Omega_0}$	$\mathbf{\Omega_s}$	$\mathbf{\Omega_d}$
# Triangles	67920	17408	7868
Comp. time (s)	-	12	36
$\mathbf{\Omega_0}$ coverage (%)	100	25.6	11.6

Deuxièmement, nous avons comparé les résultats d'optimisation pour $\mathbf{E_s}$ et $\mathbf{E_d}$. Le tableau 2 montre la performance de l'algorithme Nelder-Mead dans les deux cas $\mathbf{E_s}$ et $\mathbf{E_d}$. Nous avons rapporté à la valeur de f, la distance entre la trajectoire optimale et les obstacles (ventricules et sillons), le nombre d'itérations et le temps de convergence.

Une observation intéressante que nous obtenons est que les régions les plus sûres d'insertion dans des conditions statiques indiquées comme zones bleues sur Fig.4a peuvent être retirés de l'ensemble des trajectoires de sécurité en cas de "brain shift", comme le montre la figure 4b où certaines parties anciennement bleues sont rognées.

D'autres travaux pourraient être effectués sur le système tel que l'amélioration de la précision du modèle de "brain shift" en utilisant plus déformation complexe et modèles fluides, ou d'enquêter et comparer les différentes techniques d'optimisation.

TABLE 2 – La performance de Nelder-Mead en $\mathbf{E_s}$ et en $\mathbf{E_d}$

Nelder-Mead	$\mathbf{E_s}$	$\mathbf{E_d}$
eval(f) $[0, 1]$	0.28	0.38
dist. from ventricles (mm)	11.87	7.39
dist. from sulci (mm)	5.13	3.12
# of iterations	31	21
time (s)	0.034	0.258

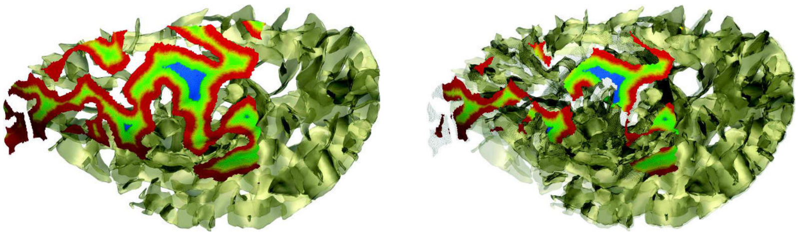

(a) $\mathbf{E_s}$, $\mathbf{M_s}$: $\omega_\mathbf{s}$ sur $\mathbf{\Omega_s}$

(b) $\mathbf{E_d}$, $\mathbf{M_d}$: $\omega_\mathbf{s}$ sur $\mathbf{\Omega_d}$

FIGURE 9 – (a) Carte de distance aux frontières de $\mathbf{\Omega_s}$, et (b) la même carte projetée sur $\mathbf{\Omega_d}$.

4 Optimisation pour la planification des trajectoires

La planification de trajectoire préopératoire pour la stimulation cérébrale profonde (DBS) est un problème d'optimisation multi-objectif consistant à rechercher le meilleur compromis entre de multiples contraintes de placement. Son automatisation est habituellement adressée en tournant le problème en mono-objectif grâce à une approche agrégative. Malgré son intuitivité, cette approche est connue pour son incapacité à trouver toutes les solutions optimales. Dans cette thèse, nous proposons une nouvelle approche basée sur la dominance multi-objectifs, et nous avons le comparé à une approche de somme pondérée.

4.1 Methode 1 : Front de Pareto ($\mathcal{M}_{PF}$)

la méthode $\mathcal{M}_{PF}$ que nous proposons est une méthode multi-objective basée sur un classement de Pareto. Elle consiste à analyser la non-domination mutuelle des points d'entrée des candidats dans une première série $\mathcal{S}$. Nous définissons la relation de *dominance stricte dom* entre deux individus x et y de l'espace de solution S$\mathcal{S}$ pour un ensemble de n fonctions objectif f_i comme la suit :

$$\forall \quad x, y \in \mathcal{S} \quad x \quad dom \quad y \quad \Longleftrightarrow \forall i \in [1..n] \quad , \quad f_i(x) < f_i(y)$$

Une solution x est *Pareto-optimale* si elle n'a pas été dominé par une autre solution dans l'espace des solutions $\mathcal{S}$.

$$x \in \mathcal{S} \quad \text{is } \textit{Pareto} \text{ optimal} \quad \Longleftrightarrow \quad \forall \quad y \in \mathcal{S} \quad , \quad \neg(y \quad dom \quad x)$$

L'ensemble des solutions Pareto-optimale est appelée un front de Pareto *Pareto front.* Notons $\mathcal{S}_{PF}$ le sous-ensemble de points de $\mathcal{S}$ qui appartient au front de Pareto. Sur le front, aucune solution ne domine une autre.

$$x \in \mathcal{S}_{PF} \quad \Longleftrightarrow \quad \forall \quad y \in \mathcal{S}_{PF} \quad , \quad \neg(y \quad dom \quad x) \quad \wedge \quad \neg(x \quad dom \quad y)$$

$\mathcal{S}_{PF}$ représente les points Pareto-optimales de $\mathcal{S}$ qui peuvent être atteints en utilisant $\mathcal{M}_{PF}$. Ils sont calculés en comparant le point de l'échantillonnage par paires et en ne conservant que les points correspondant à la propriété ci-dessus.

4.2 Method 2 : La somme pondérée ($\mathcal{M}_{WS}$)

La somme pondérée $\mathcal{M}_{WS}$ est une approche mono-objectif pour quantifier la qualité d'une solution basée sur la représentation de l'ensemble des n fonctions objective f_i par une seule fonction agrégative f à minimiser. Un poids w_i est associé à chaque f_i comme suite :

$$f(\mathbf{x}) = \sum_{i=1}^{n} w_i.f_i(\mathbf{x}), \quad \mathbf{x} \in \mathbb{R}^N$$

où : $0 < w_i < 1$ et $\Sigma w_i = 1$, et $\mathbf{x}$ représente la trajectoire associée à un point d'entrée du candidat.

Pour une combinaison fixe de poids $W = w_1, ..., w_n$, nous pouvons quantifier la qualité de chaque point d'entrée candidat $p_j \in \mathcal{S}$ de l'ensemble initial en évaluant $f(\mathbf{x_j})$, où $\mathbf{x_j}$ est la trajectoire correspondante à p_j. Ensuite, le point d'entrée optimal pour la combinaison W est un point de $\mathcal{S}$avec une valeur d'évaluation minimale de f.

Lorsque les poids sont variés w_i in W, différents points d'entrée de $\mathcal{S}$ minimisantes f peuvent être obtenus. Une exploration en faisant varier systématiquement un nombre élevé de différentes combinaisons de poids est l'approche le plus utilisée pour se rapprocher d'un front de Pareto : la couverture maximale de la méthode $\mathcal{M}_{WS}$ est le sous-ensemble $\mathcal{S}_{WS}$ de tous les points de $\mathcal{S}$ qui peut être trouvé comme optimale avec cette méthode.

4.3 Expérimentations

Une étude rétrospective a été réalisée sur 14 ensembles de données à partir de 7 patients ayant subi un procédure bilatéral de stimulation cérébrale profonde du noyau sous-thalamique (STN) pour traiter la maladie de Parkinson. Un pipeline expérimental a été mis en place et exécuté sur les scène 3D de données de patients. D'abord un discrétisation de l'espace de recherche S est fait. Ensuite, nous avons calculé les sous-ensembles$\mathcal{S}_{WS}$ et $\mathcal{S}_{PF}$ de points optimaux par les méthodes $\mathcal{M}_{WS}$ et $\mathcal{M}_{PF}$ respectivement. Enfin, un neurochirurgien a été demandé d'effectuer un test en 4 étapes comme indiqué dans la figure

- Étape 1 : "La planification manuelle $\mathcal{M}_{MP}$". Cette phase a consisté à sélectionner interactivement le point cible et le point d'entrée sur les images 2D T1/T2. La trajectoire choisie T_{MP} pourrait être visualisée et évaluée dans la vue 3D pour vérifier sa position était satisfaisante.
- Étape 2 : "La planification en utilisant la méthode $\mathcal{M}_{WS}$". Dans cette phase, le point cible choisi à l'étape 1 a été conservé, et le chirurgien a dû choisir un point d'entrée parmi celles proposées par la méthode $\mathcal{M}_{WS}$. La carte de couleur pourrait être utilisé pour aider le choix de la trajectoire T_{WS},

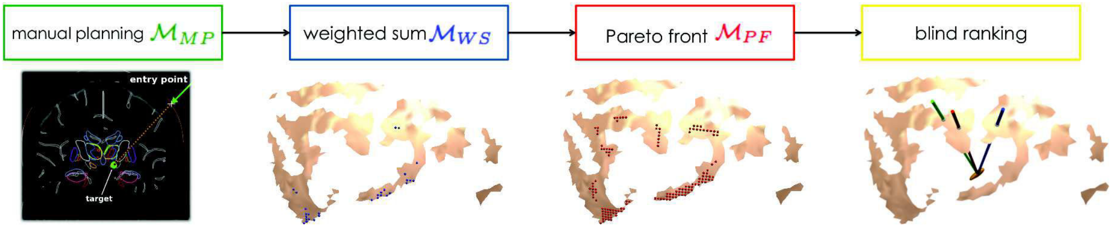

FIGURE 10 – Les quatre étapes de l'expérimentation

- Étape 3 : "La planification en utilisant la méthode $\mathcal{M}_{PF}$". Dans cette phase, le point cible choisi à l'étape 1 a également été maintenu, et le chirurgien a dû choisir un point d'entrée parmi celles proposées par la méthode $\mathcal{M}_{PF}$. Les sliders peuvent être utilisés pour aider le choix de la trajectoire $\mathcal{T}_{PF}$.
- Etape 4 : "Le classement des trajectoires ". Cette phase a consisté dans le classement des trois trajectoires $\mathcal{T}_{MP}$,$\mathcal{T}_{WS}$, et $\mathcal{T}_{PF}$ choisis dans les étapes 1-3. Le classement était aveugle et les trois trajectoires ont été assignés des couleur au hasard dont le chirurgien a classé selon leurs qualité d'après son expertise.

Pour tous les cas, $\mathcal{S}_{WS} \subset \mathcal{S}_{PF}$. Les moyennes cardinalités sont $|\mathcal{S}_{WS}| = 26$ et $|\mathcal{S}_{PF}| = 190$. Les ensembles $\mathcal{D}_{WS}$ était toujours vide, ce qui signifie que tous les points trouvé comme optimaux par $\mathcal{M}_{WS}$ sont également été proposés par $\mathcal{M}_{PF}$.

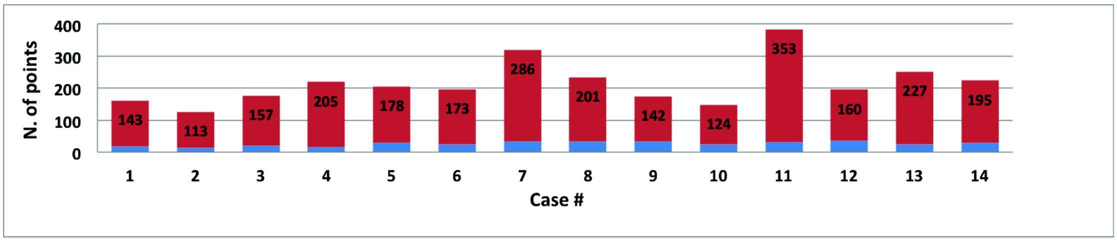

FIGURE 11 – Nombre de solutions trouvés par $\mathcal{M}_{WS}$ (en blue) et $\mathcal{M}_{PF}$ (en blue).

Afin de déterminer si les points manqués par $\mathcal{M}_{WS}$ étaient des points intéressants susceptibles d'être choisis par le chirurgien, nous avons analysé les données enregistrées pendant le test. Tout d'abord, nous avons pu observer que $\mathcal{M}_{MP}$ a été classé au premier rang dans 2/14 cas, la méthode $\mathcal{M}_{WS}$ au premier rang dans 5/14 cas, et la méthode $\mathcal{M}_{PF}$ au premier rang dans 6/14 cas. Dans le dernier cas, les points d'entrée choisis en utilisant $\mathcal{M}_{WS}$ et $\mathcal{M}_{PF}$ coïncidaient, de sorte les deux méthodes ont été également classées en première position.

Afin de voir si, dans ce genre de cas, des alternatives raisonnablement proches serait disponible en $\mathcal{S}_{WS}$, nous avons calculé les distances entre les points d'entrée sélectionné dans $\mathcal{S}_{PF}$ et le point le plus proche de $\mathcal{S}_{WS}$. Les résultats sont présentés sur la partie gauche de tableau 3. On peut observer que dans un cas sur six (#12), la distance est supérieur à 16 mm, ce qui signifie qu'aucun point a été proposé par $\mathcal{S}_{WS}$dans le région du point d'entrée sélectionné. Dans deux autres cas, la distance est supérieure à 4,8 mm, ce qui est encore loin de l'emplacement préféré. Pour les 3 autres cas, la distance est comprise entre 1,6 mm et 2,05 mm, ce qui peut correspondre à des solutions relativement raisonnables.

L'étude d'évaluation que nous avons mené en impliquant un classement aveugle, a souligné

Table 3 – Distances en mm entre les points d'insertion choisi par mes méthodes $\mathcal{M}_{PF}$ et $\mathcal{M}_{MP}$ et le point alternative le plus proche trouvé par une autre méthode

Distance	$\mathcal{M}_{PF}$ ranked first						$\mathcal{M}_{MP}$ ranked first	
to :	2	6	9	11	12	14	7	13
$\mathcal{S}_{WS}$	2.05	4.83	1.67	1.90	16.05	5.92	2.83	1.49
$\mathcal{S}_{PF}$	-	-	-	-	-	-	1.16	0.87

que les propositions supplémentaires peuvent souvent être choisis comme plus précis par un neurochirurgien, et que certains d'entre eux n'a pas eu d'alternative raisonnablement proche proposée par la méthode de la somme pondérée. Enfin, les temps enregistrés ont indiqué que l'assistance automatique était, en 12 cas de plus de 14, plus rapide et plus précise qu'une planification manuelle, qui confirme en outre l'intérêt global de l'aide automatique pour la planification préopératoire de trajectoires pour la stimulation cérébrale profonde.

5 Conclusions et Perspectives

Les objectifs de ce travail étaient tout d'abord de présenter de nouvelles méthodes de planification préopératoire de trajectoire pour la chirurgie guidée par l'image qui représentent des déformations intra-opératoire, et d'autre part d'introduire de nouvelles méthodes d'optimisation qui améliorent les techniques couramment utilisées dans les travaux connexes.

A la fin de cette thèse, nos objectifs ont été globalement respectées, et le travail accompli apporte deux contributions :

1. Nous avons présenté la première approche de planification automatique préopératoire de trajectoire pour MIS qui combinent des techniques d'optimisation basées sur la géométrie avec des simulations basés sur la physique. Nous avons expérimenté nos méthodes sur deux interventions chirurgicales différentes : pour la stimulation profonde du cerveau en neurochirurgie en tenant en compte le phénomène du "brain shift", et dans les procédures percutanées pour l'ablation des tumeurs hépatiques tenant en compte les déformations de l'aiguille flexible pendant le processus d'insertion, et la déformation du tissu mou pénétrés. Nous soulignons le fait que notre procédé est caractérisé par un certain niveau de généralité, de sorte qu'il peut être adapté à des procédures similaires.
2. Nous avons présenté une méthode d'optimisation efficace à base de Pareto multi-critères qui peuvent trouver des solutions plus optimales que l'état actuel de la technique dans les algorithmes d'optimisation des sommes pondérées.

La nature multidisciplinaire de ce travail nous a inspiré un certain nombre de futures perspectives à court ou à long terme.

- Des systèmes chirurgicaux pour la formation à la planification préopératoire : Notre système peut être personnalisé à court terme pour aider en tant que système de formation. LEs systèmes de formation de planification chirurgicale sont de plus en plus demandés dans les hôpitaux de nos jours et dans leurs centres de formation. Le système peut être utilisé par les étudiants stagiaires pour acquérir une expérience de planification, pour leur permettre de faire des erreurs sans nuire à un patient avant d'entrer dans la salle d'opération.
- Plus de modalités d'image : Dans notre travail, la planification a été réalisée sur images CT et MR. Nous pensons que l'emploi des techniques neuroradiologiques (y compris l'IRM

fonctionnelle et MR-tractographie) qui délivre une grande aide dans la planification neurochirurgicale préopératoire. Dans DBS, l'imagerie du tenseur de diffusion (DTI) est d'une importance vitale pour la planification de trajectoire, car elle permet la visualisation de tracts et d'aider la localisation de certaines fibres que les chirurgiens peuvent vouloir éviter avec la trajectoire d'accès de l'électrode.

- La planification avec plusieurs trajectoires : Une autre extension intéressante du système de planification est de résoudre le problème de la planification de multiples trajectoires. Dans le cas de cryoablation de la tumeur par exemple, il est assez fréquent que les chirurgiens placent plus d'une aiguille pour détruire une tumeur de taille en l'orientant dans des directions différentes.
- L'utilisation de systèmes experts : Malgré le système de planification commerciale pour la planification préopératoire existant, la décision et l'exécution encore découlent de l'homme et dépend de l'expérience et de la pratique chirurgien. Nous croyons que si l'expertise chirurgicale ont été introduits dans un algorithme de planification «intelligent», l'opération va se déplacer vers le milieu plus sûr. Une base de connaissances permet plus de chirurgiens de prendre part à la prise de décision réduisant ainsi le potentiel de polarisation et de la subjectivité d'un chirurgien.
- Combinaison avec système de commande guidée par l'image : Avec les progrès croissants dans la robotique médicale, nous proposons de coupler l'algorithme *Haystack* avec un système de contrôle pour valider ses résultats. Nous croyons que avec une instruction efficace, les robots aiguilles peuvent être utilisés pour mener à bien le processus d'insertion avec une précision significative par rapport à l'insertion manuelle.
- La réalité augmentée : Les techniques de réalité augmentée se familiarisent à la communauté chirurgicale. Elles pourraient être utilisées pour améliorer de nombreuses phases des interventions chirurgicales. Dans le système de formation proposé par exemple, les techniques de réalité augmentée peuvent être introduits pour enseigner les stagiaires au sujet d'éventuelles déformations. Les déformations calculées peuvent être superposées sur les images statiques du patient de donner des informations à titre informatif et visuel et aider le processus de prise de décision.

Noura HAMZE

Optimisation et planification préopératoire des trajectoires en conditions statiques et déformables pour la chirurgie guidée par l'image

Résumé

En chirurgie mini-invasive guidée par l’image, une planification préopératoire précise des trajectoires des outils chirurgicaux est un facteur clé pour une intervention réussie. Cependant, une planification efficace est une tâche difficile, qui peut être considérablement améliorée en considérant différents facteurs contributifs tels que les déformations biomécaniques intra-opératoires, ou en introduisant de nouvelles techniques d'optimisation.

Dans ce travail, nous nous concentrons sur deux aspects. Le premier aspect porte sur l'intégration de la déformation intra-opératoire dans le processus de planification de trajectoire. Nos méthodes combinent des techniques d'optimisation géométrique à base de simulations biomécaniques. Elles sont caractérisées par un certain niveau de généralité, et ont été expérimentées sur deux types d’interventions chirurgicales: les procédures percutanées pour l'ablation de tumeurs hépatiques, et la stimulation cérébrale profonde en neurochirurgie. Deuxièmement, nous étudions, mettons en œuvre, et comparons plusieurs approches d'optimisation en utilisant des méthodes qualitatives et quantitatives, et nous présentons une méthode efficace d'optimisation évolutionnaire multicritères à base de Pareto qui permet de trouver des solutions optimales qui ne sont pas accessibles par les méthodes existantes.

Mots clés :

Chirurgie guidé par l'image, résolution de contraintes géométrique, simulation biomécanique, optimisation multi-critères.

Résumé en anglais

In image-guided minimally invasive surgery, a precise preoperative planning of the surgical tools trajectory is a key factor to a successful intervention. However, an efficient planning is a challenging task, which can be significantly improved when considering different contributing factors such as biomechanical intra-operative deformations, or novel optimization techniques.

In this work, we focus on two aspects. The first aspect addresses integrating intra-operative deformation to the path planning process. Our methods combine geometric-based optimization techniques with physics-based simulations. They are characterized with a certain level of generality, and are experimented on two different surgical procedures: percutaneous procedures for hepatic tumor ablation, and in neurosurgery for Deep Brain Stimulation (DBS). Secondly, we investigate, implement, and compare many optimization approaches using qualitative and quantitative methods, and present an efficient evolutionary Pareto-based multi-criteria optimization method which can find optimal solutions that are not reachable via the current state of the art methods.

Keywords :

Image-guided surgery, geometric constraints solving, biomechanical simulation, multi-criteria optimization.